# "SCALE-UP AND MODELING OF FLOTATION COLUMNS USING SURFACE AREAS."

By

IAN MATTHEW FLI NT

B.Sc., The University of Toronto, 1983
B.A.Sc., The University of Toronto, 1986
M.A.Sc., The University of Toronto, 1989

A THESIS SUBMITTED IN PARTIAL FULFILMENT OF
THE REQUIREMENTS FOR THE DEGREE OF
DOCTOR OF PHILOSOPHY

In

THE FACULTY OF GRADUATE STUDIES

(Department of Mining and Mineral Process Engineering)

We accept this thesis as conforming
to the required standard

THE UNIVERSITY OF BRITISH COLUMBIA
October 2001

In presenting this thesis in partial fulfilment of the requirements for an advanced degree at the University of British Columbia, I agree that the Library shall make it freely available for reference and study. I further agree that permission for extensive copying of this thesis for scholarly purposes may be granted by the head of my department or by his or her representatives. It is understood that copying or publication of this thesis for financial gain shall not be allowed without my written permission.

Ian M. Flint

Department of Mining and Mineral Processing Engineering

The University of British Columbia
Vancouver, Canada

Date: Thursday, November 22, 2001

# Abstract

This research presents three models of froth flotation that recognize flotation as an interfacial phenomenon wherein the rate of solids-surface-area removal is related to the bubble-surface-area flux. These models use two "streams", air and liquid, within the vessel. The solids within the column are associated with one, or both, of these streams. The procedures and benefits of batch tests for flotation columns are also outlined. The first model uses this batch data and the simplex method of non-linear regression to determine four model parameters: a kinetic rate constant, maximum recovery, entrainment and carrying capacity. These parameters are then used in the second model in order to estimate continuous column performance. Within the continuous model, carrying capacity is determined by overflow bubble size; recovery within the froth zone is determined by loss of bubble surface area; and solids transfer from liquid- to gas-phase is estimated by kinetic relationships and the axial dispersion model. The prediction performance of the model is verified using both batch mechanical cell and column flotation cell batch data. The final model "framework" characterizes the effect of bubble residence time and bubble loading rates within a flotation cell using mechanistic bubble – particle collision and attachment relationships.

# Table of Contents

# List of Figures

# List of Tables

# Acknowledgements

Appreciation is given to the principle sponsors of this project for both funding and expert advice: Cominco Ltd., Teck Corp., INCO Ltd., and CANMET operating through MITEC. Thanks also to Andy Mular, Dr. Bern Klein and the faculty and staff of the University of British Columbia and to my colleages and students at Dalhousie University. For the year of 1994-1995 thanks is also extended to the British Columbia Science Council for funding. For 1999 thanks is extended to the University of British Columbia, and the Federal Human Resources Ministry. Other companies have generously provided ore, advice, assays, and funding for testing expenses. This list includes Process Research Associates, Klohn-Crippen Consultants, ALCAN, the Quinto Mining Corp., and Cominco Engineering Services Ltd. -- now Canadian Process Technology.

# Preface

This research presents three models for froth flotation. Most of the variables used within these models are similar to those used by other researchers. However, this research recognizes that flotation is an interfacial phenomenon wherein a solids-surface-area is attached to, and thus, removed by a bubble-surface-area. The rate of solids-surface-area removal is related to the bubble-surface-area flux. The one-dimensional equivalent to bubble surface area flux is the superficial bubble surface-area flux; "$\vartheta_B$" [$s^{-1}$] while the equivalent to solids-surface-area rate, attached to the bubble, is $\vartheta_{SB}$ [$s^{-1}$]. Also, the liquid stream is characterized by the superficial liquid flow rate ($J_l$ [cm $s^{-1}$]) and an associated superficial suspended-particle surface-area flux ($\vartheta_{SL}$ [$s^{-1}$]). The concentration of solids in the "liquid stream" is characterized by the specific solids surface or the concentration of solids-surface-area ($C_p$ [$cm^{-1}$]). Thus, these models used two "streams" within the vessel: bubble (air) and liquid. The solids within the column are associated with one or both of these streams.

Industrial-scale columns are currently designed using data gathered from either continuous column or "batch" mechanical-cell testing. A laboratory-scale column operating in "batch" offers many advantages over other testing methods. When compared to continuous column tests, "batch" columns use only a fraction of the feed material, have an equal residence-time of all particle sizes and densities, and have a slightly positive bias. Test work done to predict industrial-scale column performance using a laboratory-scale column, when compared to tests using "batch" mechanical-cells, eliminates differences in flotation due to impeller agitation and turbulence, reduces the effect of entrainment and allows for an estimate of carrying capacity.

"Batch" column testing is not yet practised due to a lack of procedures to run the test and models that relate the test results to continuous column performance. This thesis defines the necessary test procedures and introduces models that allow "batch" test data to be used to predict continuous column performance. The "batch" kinetic model is used to determine flotation parameters. The continuous, kinetic model uses the parameters determined in the

first model to predict continuous column performance. The final model is a mechanistic framework.

The empirical "batch" kinetic model determines four flotation related parameters: flotation rate constants ($k_{f(m,n)}$ [$s^{-1}$]), entrainment proportionality constants ($k_{e(m,n)}$), maximum recovery ($R_{\infty(m,n)}$) and the maximum solids-surface-area to bubble-surface-area ratio ($\phi_{SB}$). These parameters are estimated to minimize an objective function (Equation 1) in order to characterize the flotation time-recovery response of the test data.

$$\varepsilon_{m,n} = \sum_{i=1}^{L} \sqrt{\left( \vartheta_{S(O,i)} t_{(i)} - \vartheta^{*}_{S(O,i)} t_{(i)} \right)^2} \qquad \text{Equation 1}$$

Equation 1 uses the following symbols:

| | | |
|---|---|---|
| "$\varepsilon_{(m,n)}$" | | the "error" or difference between the predicted response and the test data, for each "m" (mineral) and "n" (size-class), |
| "L" | | the number of timed interval samples taken, |
| "$\vartheta_{S(O,i)}$" | [$s^{-1}$] | the model response overflow total superficial solids-surface-area flux, |
| "$\vartheta^{*}_{S(O,i)}$" | [$s^{-1}$] | the test data overflow total superficial solids-surface-area flux and |
| "$t_{(i)}$" | [s] | the time interval. |

The "batch" kinetic model can be used either with "batch" mechanical-cell data or column data. The use of mechanical-cells introduces unknown errors into the model since the mechanisms of flotation differ from those in columns. The "batch" kinetic model, as presented in this thesis, accounts for both entrainment and loading but not for the basic differences in collection between the mechanical-cells and columns. The "batch" kinetic model does not account for bubble loading differences caused by the short bubble residence-time of the "batch" mechanical-cell. In addition, this model quantifies bubble density and superficial surface-area removal rates.

The adjusted parameters determined in the "batch" kinetic model (Equation 1) are used in a continuous, column, kinetic model to predict performance. The continuous model uses hydrodynamic principles, mixing theory and mass balances. This model is an alternative to existing laboratory-scale, "batch", mechanical-cell and continuous, column, kinetic models.

This model uses the total superficial solids-surface-area flux ($\vartheta_{S(O,i)}$ [$s^{-1}$]) that is fundamental to flotation, rather than mass or volume. This value is determined by dividing the solids-surface-area rate [$cm^2\ s^{-1}$] by the cross-sectional area of the vessel [$cm^2$].

The continuous kinetic model uses superficial surface-area fluxes. A distinction is made between solids suspended in water and those attached to bubbles. Three hydrodynamic regions are used: the collection zone (between the feed port and spargers), the recollection zone (between the feed port and froth interface), and the froth zone. The collection and recollection zones are modeled using axial dispersion and carrying capacity, or loading, considerations. The froth zone accounts for loss of bubble surface-area. Solids bias is used throughout the model to predict the bulk transport of solids across zone boundaries (entrainment).

The mechanistic model framework has been developed in response to validity questions concerning that chemical rate analogy of flotation kinetics and conventional assumption that bubble residence time can be ignored. A bubble that has no residence-time cannot carry particles since no collisions will have occurred. Bubble load increases with bubble residence-time as more particles collide and attach. As such, the short residence-time of laboratory test units mean that maximum loading in test- and plant-scales may be different.

The mechanistic model uses descriptions of bubble-particle attachment, induction time, a solids packing factor, solids- and bubble-surface-area fluxes and specific surface (surface-area concentration), to predict solids-surface-area removal rates (Equation 2) and bubble loading (Equation 3).

Equation 2

$$\Delta \vartheta_{SB} = \vartheta_B C_p t_b \left(u_b + u_p\right) E_c \frac{\sin^2\left(\theta_e - \frac{2 t_i v_\theta}{d_p + d_b}\right)}{\sin^2 \theta_m}$$

Equation 3

$$\phi_{SB} = \frac{\Gamma}{2}\left[1 - \cos\left(\pi - \theta_i\right)\right]$$

Equation 2 calculates the change in superficial attached-solids surface-area flux ($\Delta\vartheta_{SB}$ [$s^{-1}$]) passing through a control volume. Within that control volume, "$\vartheta_B$" [$s^{-1}$] is the average superficial bubble-surface-area flux; "$C_p$" is the solids specific surface [$cm^{-1}$]; "$t_b$" [s] is the bubble residence-time; "$u_b$" [cm $s^{-1}$] is the bubble rise-velocity (assumes an upward flow); "$u_p$" [cm $s^{-1}$] is the particle settling-velocity (assumes a downward flow); "$E_c$" is the collision efficiency; "$\theta_e$" [radians] is the maximum angle of particle contact on the bubble; "$t_i$" [s] is the particle induction time;, "$v_\theta$" [cm $s^{-1}$] is the particle velocity along the bubble surface while in contact; "$d_p$" [cm] is the particle diameter, and "$d_b$" [cm] is the bubble diameter.

Equation 3 gives the bubble loading ($\phi_{SB}$ [dimensionless]); the ratio between particle-surface-area and bubble-surface-area, in terms of the solids packing ($\Gamma$ [dimensionless]) and the maximum angle of the solids-surface-area cap ($\theta_i$ [radians]).

# New Knowledge

This thesis develops three new models. The first two: the "batch" kinetic and continuous kinetic models, are designed to work together in order to use "batch" test data to predict continuous industrial-scale column performance. The third is a mechanistic model that could be adapted for either "batch"- or continuous column modeling. The following new information is presented in one or more of these models:

1. Development of test methods to obtain "batch" column data.
2. Development of the "batch" column model, as a whole, which is used to determine the flotation parameters for the continuous model.
3. Characterization of the solids as being part of, or being transferred by, either the liquid or gas phases.
4. The use of surface-area concentration, or specific surface area, to characterize solids concentrations in flotation.
5. A model of entrainment based upon the bulk transport of solids-surface-area within the liquid phase.
6. Incorporation of bubble loading and solids packing, expressed in relation to bubble surface, into both "batch"- and continuous kinetic models.
7. A froth-zone recovery model based on the bulk transport of water and the loss of bubble-surface-area.
8. The distinct treatment of the recollection zone as a unique mixing and collection environment.
9. The determination of solids residence-time in "batch" column tests.
10. Modeling of bubble loading in terms of bubble residence-time.
11. Determination of the maximum "batch" recycle rate.
12. Development of a wash-water system designed to minimize radial differences in wash-water rates,
13. Design of a test column with an adjustable feed port to enable the characterization of the recollection zone.

# 1 Introduction

## 1.1 Purpose

The purpose of this work is the development of equipment, procedures and models to allow the batch testing of columns to be used in the prediction of plant-scale continuous column performance.

## 1.2 Scope

### 1.2.1 Limitations

The emphasis of this thesis is column flotation. Dissolved air-, cavitation/nucleation-, and electro-flotation devices are not discussed. Mechanical-cells are reviewed only in the context of "batch" testing when they are used to determine column-modeling parameters. The chemistry of flotation is only mentioned as regards to induction time.

The primary emphasis is on rate constants, recovery equations, and the effect of particle size. The froth zone is treated in terms of bubble loading and the loss of bubble-surface-area. It is assumed that the "batch" column acts in a plug-flow manner. The continuous models use three stages: the froth, recollection and collection zones. Work by previous researchers is used, whenever possible, to formulate models, to predict the effect of variables, and for comparative data.

The mechanistic flotation model has been developed solely for "batch" operation. The model can be directly applied to continuous operation by means of subdividing the column into small zones along the axial dimension. Mixing, however, has not been accounted for. The basic strength of this description of flotation probably lies within its' future application within a model that accounts for liquid and bubble movement in both axial and radial dimensions.

### 1.2.2 Equipment Goals

The following objectives were considered to minimize error when designing the test equipment:

- Minimization of dead zones within the column
- Minimization of recycle volumes
- Minimization of required sample size
- Production of an even wash-water distribution in the froth zone
- Production of a variable feed port elevation

The equipment was designed to test small amounts of feed material. This allows multiple tests to be run or tests to be performed on core or small grab samples.

### 1.2.3 Modeling Goals

Three flotation models have been constructed each with a different purpose. The first is a "batch"-model that may be used with either "batch" mechanical-cell or column generated data. The second is a continuous-column model that uses the flotation parameters generated by the first model. The third, is highly mechanistic model that has been developed, but not yet tested, in order to predict solids removal as a function of bubble residence-time and induction time and to predict loading as a function of particle packing on the bubble.

#### 1.2.3.1 Batch Model

Currently, both laboratory-scale "batch" mechanical-cells and test- or pilot-scale continuous columns are used to predict performance of industrial-scale columns, or to provide sizing information. Mechanical-cell tests are both simple and inexpensive but error may be high due to entrainment or turbulent conditions. In contrast, continuous pilot- or laboratory-scale column tests offer the potential of more accurate sizing parameter determination but at

substantially higher costs. The "batch" model was developed in order to provide an alternative to these two types of tests and was designed with the following objectives:

- To generate flotation parameters, including kinetic rate constants, entrainment constants, maximum recovery and bubble loading,
- To reflect the surface transfer nature of flotation by using specific surface and surface-area fluxes within the model,
- To simplify data collection and model usage, and
- To estimate column flotation parameters from either "batch" column or "batch" mechanical-cell data

### 1.2.3.2 Continuous Column Model

Column sizing and performance models, already in existence, have been extensively modified to receive data from the laboratory-scale "batch" kinetic models developed in this thesis. In addition, the entrainment models of other researchers have been incorporated in order to simulate negative bias conditions. The continuous model also uses specific surface and surface-area fluxes.

### 1.2.3.3 Mechanistic Bubble Load Model

A mechanistic particle load (carrying capacity) model framework has been developed as an alternative to earlier models. These relationships remain untested, but present a method of predicting solids-surface-area removal dependent upon bubble surface flux. The mechanistic approach also characterizes the bubble load as a function of bubble residence-time and incorporates both induction time and particle packing on the bubble surface.

## 1.3 Batch Flotation

### 1.3.1 Mechanical Cell

Mechanical flotation cells form the bulk of flotation separation equipment on both industrial- and laboratory-scales. "Batch" mechanical-cells are the standard for laboratory test-work. A small flotation cell, typically between two (2) and five (5) liters in volume, is filled with slurry. Reagents are added and conditioned prior to the aeration that causes flotation. No new solids are placed into the system while the test is underway; air, however, is applied continuously, and water may be added to make-up the volume lost through flotation. Technically these tests are "batch" only with respect to the solids content.

### 1.3.2 Column Cells

#### 1.3.2.1 Introduction

A column flotation cell is a vertical device wherein slurry containing the minerals to be separated is passed through a column, from upper feed to lower underflow against a rising swarm of bubbles. Material that is collected by the bubbles, or entrained with overflow water, rises into a froth zone where a descending flow of water washes the entrained material back into the collection volume. This system takes advantage of the concentration gradient that exists as the newly formed bubbles are exposed to the lowest concentration of floatable particles at the base of the column (Rice et. al.; 1974).

Test columns have been used in solids batch for many years to either fill columns, or while the system is on stand-by to preserve feed. This mode of operation, however, has not been used to perform test work.

Industrial-scale columns range in area from 0.1 $m^2$ to 20 $m^2$ ("$A_c$") and between 3.0 and 18 m in total elevation ($h_{(v)}$). Application of these vessels include the flotation of such diverse minerals as: clay ("$d_p$" < 10 μm), potash ("$d_p$" > 4000 μm, "$\rho_s$" ≈ 1.7) and galena ("$\rho_s$" ≈ 6.5), and also the removal of micrometer sized organics in solvent extraction plants, newspaper de-

inking (Petri and Dobby; 1993), ion concentration (Walkowiak; 1991 and Mezhov et. al.; 1992), cell separation, biological waste material (Marti et. al.; 1994) and other environmental applications.

### 1.3.2.2 Sizing

Design of the earliest columns was based on "rules-of-thumb" residence-time and volume considerations. These columns were typically retrofit applications and were made with volumes equivalent to the mechanical-cells they replaced. Dobby's 1984 thesis, the first attempt to model flotation columns used in mineral processing, introduced mixing theory, bubble size and particle settling to the field. Two empirical sizing-parameters have been added since: from McGill University; area carrying capacity (Espinosa-Gomez, Yianatos, and Finch; 1988), and from CESL; the lip loading capacity as presented by Amelunxen (1990). To-date, models have assumed a fractional recovery through the froth zone. Additional work has been done on column froths in recent years; these studies, however, are beyond the scope of this thesis. The following are some of the parameters and variables that are important in the kinetic models presented:

- Rate constants, "$k_f$" [$s^{-1}$],
- Entrainment constant, "$k_e$" [dimensionless],
- Maximum recovery; "$R_\infty$" and
- Maximum and actual bubble load; "$\phi_{SB}$" [dimensionless].
- Bubble size at the sparger and in the overflow; "$d_{b(spa)}$", "$d_{b(O)}$" [cm],
- Air introduction rate; "$J_g$" [cm $s^{-1}$],
- Particle size; "$d_p$" [cm],
- Particle surface introduction rate; "$\vartheta_{SL(F)}$" [$s^{-1}$],
- Vessel type and physical dimensions,
- Wash-water introduction rate; "$J_{l(W)}$" [cm $s^{-1}$],
- Overflow water rate; "$J_{l(O)}$" [cm $s^{-1}$], and
- Overflow solids surface rate; "$\vartheta_{S(F)}$" [$s^{-1}$]

Current methods, as practiced by industry to collect flotation column scale-up data, are both time-consuming and expensive. Pilot-column testing is performed for accurate model parameter determinations. Both carrying capacities and rate constants are inferred from this data by adjusting the current continuous model parameters so that the model predicts the test results.

A bench-scale batch mechanical-cell is often used, rather than a continuous column, to reduce costs. Prediction error, however, is probably increased due to different bulk transport, collision and attachment environments. The use of batch mechanical-cell generated data means that an increased design safety factor must be used. Some column cell suppliers design column cells directly from batch mechanical-cell test results when carrying capacities are known and the particle size; "$d_p$", ranges between thirty (30) and seventy (70) micrometers. This type of estimation, however, cannot predict the behavior of middlings, locked, or entrained particles and ignores differences in the collision and attachment environments that exist between these vessels.

## 1.3.3 Hydrodynamic Zones

### 1.3.3.1 Introduction

Columns operated in either continuous- or batch have two distinct zones: the pulp and froth zones. The pulp zone is necessary for operation; the froth zone, however, may be omitted in certain applications such as scavenging operations. These zones are shown in Figure 1. Figure 1 also shows the sub-zones of the pulp-zone: the recollection, feed, collection and sparger zones.

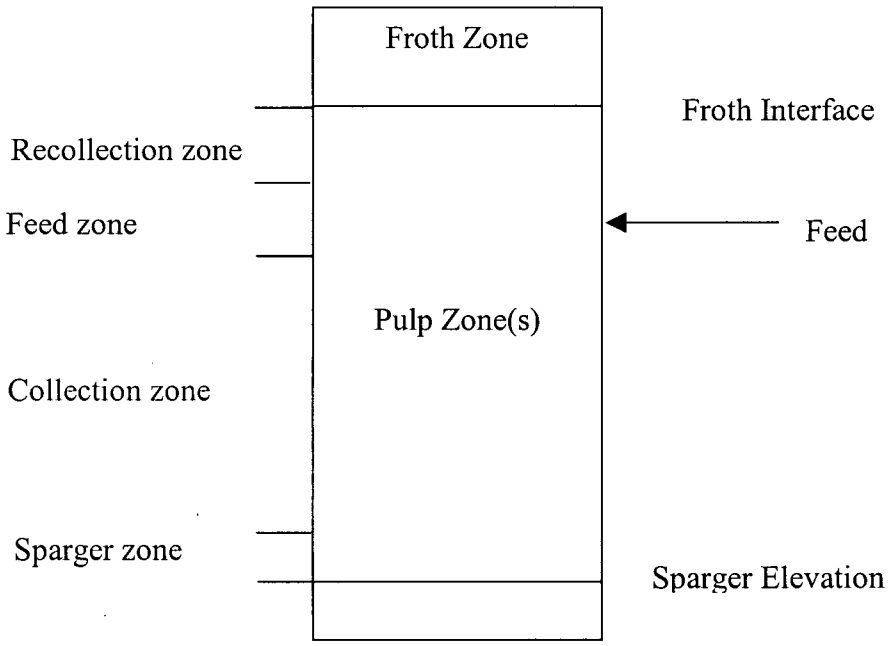


**Figure 1: Column hydrodynamic zones**

### 1.3.3.2 Pulp Zone(s)

The pulp zone is the volume between the froth-pulp interface and the lowest descent of bubbles produced by the spargers. The bubble-surface-area rate introduced at the sparger elevation, or the superficial bubble-surface-area flux ($\vartheta_{B(spa)}$ [$s^{-1}$]), does not carry any solids surface ($\vartheta_{SB(spa)}$ [$s^{-1}$] = 0). The sub-zones within the pulp "zone" are characterized, under

normal operation, by a continuous swarm of independently rising bubbles in quiescent slurry. Hydrophobic particles may collide and attach to these bubbles. Those solids that become attached are carried upwards ($\vartheta_{SB(x)}$ [$s^{-1}$] > 0) and eventually reach the interface between the pulp and the froth zone. The solids area that attaches to the bubbles is removed from liquid suspension ($\vartheta_{SL}$ [$s^{-1}$]). Hydrophilic particles that do not attach to the bubble phase fall through the collection zone and flow out the column underflow.

The pulp zone may be further divided into four sub-zones (Figure 1). The volume below the froth interface, and above the upper turbulence of the feed, is often called the "re-collection zone". The volume of moderately intense mixing where the feed is introduced may be treated separately and is termed the "feed zone". A similar zone may be defined around the spargers called the "sparger zone" and the remainder is the collection zone. Neither the "feed", nor the "sparger" zones are used in the models presented in this thesis.

#### 1.3.3.3 Froth Zones

The froth zone is primarily gas, with solids and liquid in the lamella between the bubbles. Wash-water, which may be added at the top of the column, filters down through this bed to remove entrained particles from the froth. Particles attached to a bubble will overflow the column unless bubble coalescence occurs which may force a fraction of the floated particles to return to the water phase in the froth.

The froth zone may be further subdivided into three sub-zones. The volume above an in-tank wash waster system is characterized by a dry, draining froth and may be termed the "dry froth zone", or "drainage zone". The volume under the wash-water addition system is a washed froth and can be termed the "wet froth zone" or "washing zone". The interface between pulp and froth zones may also be considered a separate zone. The models presented in this thesis consider the froth to be a single zone.

## 1.3.4 Column Flows

### 1.3.4.1 Liquid

Water flow rates within columns are commonly quoted as superficial velocities, which is the volumetric flow rate divided by the characteristic surface-area of the vessel. The characteristic column flows are feed slurry ($J_{sl(F)}$), overflow slurry ($J_{sl(O)}$), underflow slurry ($J_{sl(U)}$), wash-water ($J_{l(W)}$), and air flow ($J_g$) as shown in Figure 2. Wash-water is the water added either within or on top of the froth zone in order to provide a downward flow of water within the froth. Slurry flows ($J_{sl}$) are composed of the liquid and solids fractions represented by the superficial liquid flow rate ($J_l$ [cm $s^{-1}$]) and the superficial suspended solids-surface-area flux ($\vartheta_{SL}$ [$s^{-1}$]).

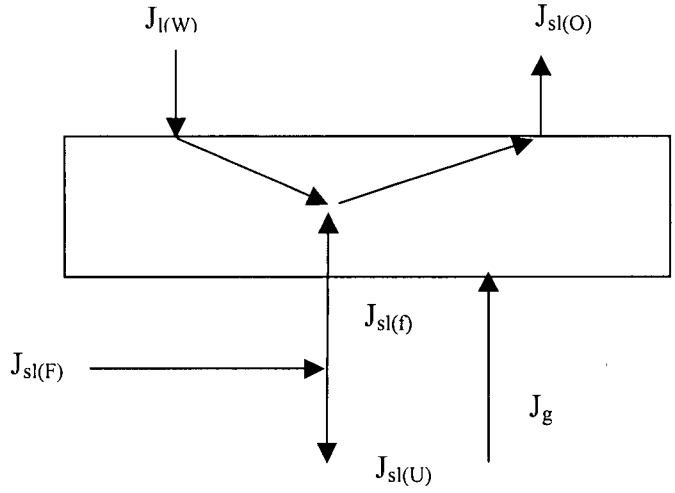


**Figure 2: Froth-zone water flow diagram**

Slurry bias ($J_{sl(f)}$) is the downward flow of slurry at the froth–pulp interface that can be determined as "$J_{sl(f)} = J_{l(W)} - J_{sl(O)} = J_{sl(U)} - J_{sl(F)}$". Slurry bias is quoted in terms of a slurry flux or superficial velocity. A positive bias is defined as a net downward flow of slurry, whereas a negative bias is an upward flow. Both states are shown in Figure 3. The purpose of the wash-water is to remove entrained material from the froth zone and return it to the collection zone.

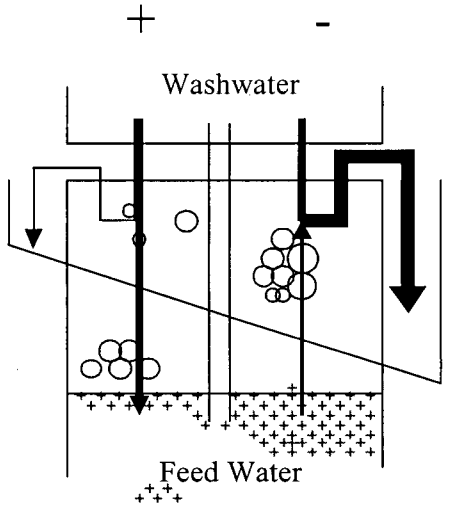


**Figure 3: Bias schematic wherein arrows show direction of water flow and width shows volume flow. The left side of the diagram shows positive bias conditions whereas the right shows negative bias conditions.**

An average positive bias across the entire column cross-section may contain within itself areas of substantial negative bias if wash-water addition is not uniform. Also, if channeling of the water occurs, large volumes of wash-water will descend through a small area thereby lowering the average bias throughout the remaining cross-sectional area.

### 1.3.4.2 Air

There are limits to the air rates that can be applied to a column. The maximum air rate is dependent upon many factors including slurry viscosity, density, and downward flow rates as well as the bubble-size distribution. In general, air cannot be added at a superficial rate greater than the bubble rise-velocity at any column elevation. The minimum amount of air that can be added is limited by the stability of the froth zone; lower rates result in a slower moving froth that may decrease the froth stability. The optimum air rate is the minimum rate that provides sufficient bubble surface area to remove the solids surface. Excess rate will increase the gas fraction contained within the vessel, and thus, reduce solids residence times. Typically, columns are designed with a maximum superficial air rate ($J_g$), at local pressure and temperature, of about 3 [cm $s^{-1}$] for slurry flotation. The column minimum superficial air

rate varies with column cell design, wash-water rate, reagents and froth height, however are usually in the range of 0.5 cm $s^{-1}$.

#### 1.3.4.3 Feed Flow

Columns usually receive slurry feed at a rate; "$J_{sl}$", of between 0.3 and 1.5 [cm $s^{-1}$] (volumetric feed rate divided by the column cross-sectional area). Specific designs can be made to shift this range. For example: a liquid flow increase reduces the maximum air rate. The practical feed-rate lower-limit must be high enough to prevent solids from settling out of suspension within the column or support piping. Particles settle within the slurry, thus solids residence-time will be less than slurry residence-time.

### 1.3.5 Mode of Operation

#### 1.3.5.1 Introduction

There are two general modes in which a flotation cell may work: batch and continuous. Batch means batch with respect to the solids only. Flotation, on a plant- or pilot-scale, is continuous. On a laboratory-scale, batch column flotation has been possible but, in the past, tests have been performed using continuous operation. Another operational mode variant is the "semi-batch" column wherein a positive bias is maintained by water addition and a surplus volume accumulates.

#### 1.3.5.2 Continuous-Mode

To-date, only continuous columns have been used for both test-work and industrial applications. Feed enters the column continuously and is met by a continual stream of rising bubbles in the column. Wash-water may or may not be used. Both overflow and underflow products are always being produced. Figure 4 is a schematic diagram of this mode of operation. Some solvent–liquid extraction columns collect the organic phase continuously on the top of the column but only dump it periodically.

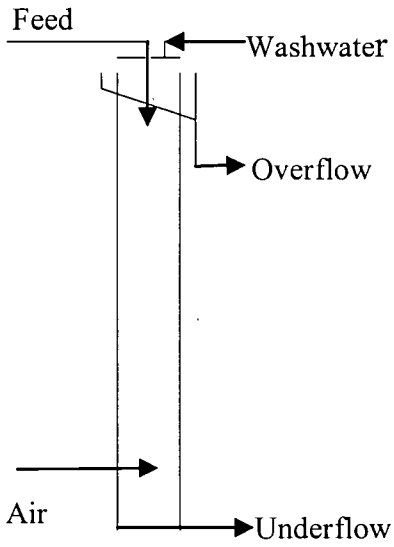


**Figure 4: Continuous column-cell operation**

### 1.3.5.3 Batch-Mode

A batch column receives an initial solids feed. Thereafter, the feed is recycled from the underflow to the feed. Wash-water is added to make up the volume lost to the overflow. This operation is actually "pseudo-batch" since both water and air are added to the system. To maintain a positive bias the slurry–froth interface level rises during a test.

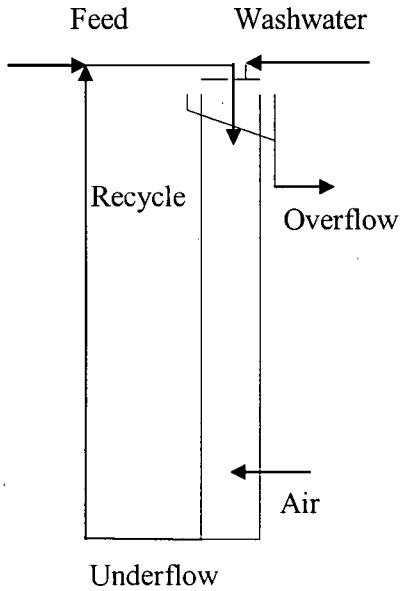


**Figure 5: Batch column-cell operation**

# 2 Background

## 2.1 Introduction

This section reviews information relevant to this research found in literature. The modeling theory presented: types, development and application of models, is used as a framework for the batch surface-area models. A selection of published flotation models are reviewed that pertain to column or batch flotation models and many of the relationships used in these models, such as carrying capacity, entrainment, rise or settling velocities, the axial dispersion model, kinetics and collection efficiencies are reviewed.

## 2.2 Modeling Theory

### 2.2.1 Introduction

Simulation, or modeling, of flotation vessels is complex because of the large number of process variables involved (Lynch et. al.; 1981 and Frew and Davey; 1988). Process conditions and mineral kinetics do play an important role (Schuhmann; 1942), and should be considered in a working model. The parameters of many models, such as most macro-phenomenological kinetic models, deal with many process variables as groups. Therefore, little information about the process itself can be inferred (Reuter and van Deventer; 1992). There are three aspects of flotation that must be taken into consideration when models are constructed and used: equipment, operational and chemical factors.

**Equipment Factors**

- Cell design, type
- Configuration
- Control
- Froth removal and depth

**Chemical**

- Reagents
- Dissolvable species
- Ionic concentration

**Operations**

- Mass flow rates
- Minerals, liberation
- Particle size
- Pulp density
- Solids densities
- Air flow

There must be an understanding of the advantages and disadvantages of columns, in comparison to other flotation vessels, in order to identify proper applications. A good mathematical model is an important tool for systematic and consistent process analysis (Sastry; 1990). A good model can assist in each of these aspects. Modeling and simulation can give the following:

- A structured understanding and definition of a process,
- A basis for planning, evaluation, optimization, and process control,
- A training tool for operational staff and
- A minimization of experimental costs.

In order to achieve these goals, the model must fit the experimental data independently of the process and also be accurate.

The purpose of a model is to represent a "real" process, or an assembly of elements linked together. These elements may be as small as a unit operation or encompass an entire processing plant. A model is an approximation of the "real" system that is neither complete nor exact. There are two types of models: physical and symbolic (Jacoby and Kowalik; 1980). These models and their inter-relationships are shown in Figure 6 (Sastry; 1990)

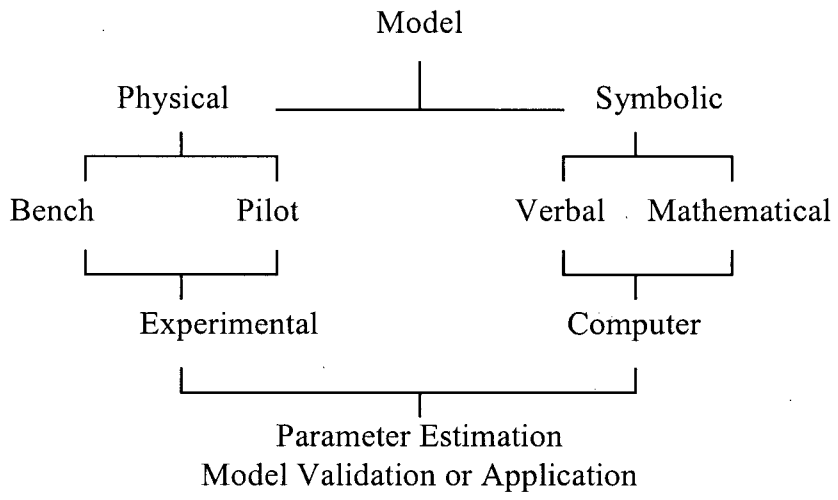


**Figure 6: Types of models and their components from Sastry (1990).**

### 2.2.2 Physical Models

Physical models, scale models, drawings and diagrams are concrete representations of the "real" system. Scale models are used for experimentation and the gathering of information that concerns the "real" system. Common scale models include bench- and pilot-scales. Szekely et. al. (1987) state that for meaningful information on the "real" system scale models must be constructed and used appropriately, including considerations of geometric, dynamic, kinematic and process similarity. The batch column is a scale model.

### 2.2.3 Symbolic Models

Symbolic, or process models, may be either verbal or mathematical. A verbal model may be either knowledge or fuzzy logic based such as Reuter and van Deventer (1992). These models are "symbolic statements of [the] structure and behavioral aspects of the real process" (Sastry; 1990). There is a link between physical and symbolic models because investigation of the physical leads to knowledge used to construct and verify the symbolic. Simulations using symbolic models are used to plan laboratory- and pilot-scale testing and are helpful to plan or modify "real" systems.

### 2.2.4 Mathematical Models

Mathematical models may be stochastic or deterministic in nature, or may be comprised of elements of both. Stochastic models use probability, or chance, and are rarely used in mineral processing with the exception of the modeling of specific phenomena such as particle-bubble attachment. Deterministic models, using either empirical or mechanistic methods, assume a consistent, repeatable behavior. Empirical models are based on statistical correlation between causal elements and results, while phenomenological (mechanistic) models relate the mechanics of the process mathematically to the result. In mineral processing, phenomenological models are not usually linked directly to the basic chemistry or physics of the system, but are empirical models of sub-processes; thus most of these models must be considered to be semi-empirical in nature or empirical on a basic level. Mechanistic models

have the potential to be more accurate when extrapolating from known performance relationships (Box et. al.; 1978).

### 2.2.5 Development

Model development is an iterative procedure used to maximize utility and accuracy while minimizing research costs. One possible development flowchart involves the following five step iterative process (based on Sastry; 1990).

1. Determine the scope and purpose of the model. Possible objectives are to understand the fundamentals of the process, to determine scale-up criteria and to optimize existing circuits. These models may also be used in the design and execution of test work and the design of full-scale processes.
2. Collect information: existing knowledge should be surveyed including a description of mechanistic information, experimental data of others, and prior models. A determination should be made whether more experimentation is needed based on the collected information.
3. Experimentation: A test work program should be designed and carried out to determine any information missing from the collection stage.
4. Model Development: The model is composed of an axiomatic and mechanistic description of the process. The following elements are used:

    - State variables and parameters are defined.
    - Laws of conservation are identified.
    - Mathematical model equations along with inferential, analytical or numerical solutions are developed. Also, all sub-processes that cause changes within the vessel are characterized either mechanistically or empirically.
    - All necessary equations including a clear statement of interdependence of variables and parameters are introduced.
    - All initial and boundary conditions are defined.

5. Evaluation: Model predictions are compared to "real" system performances to assess their validity. This comparison often includes estimation of parameters and an assessment of accuracy, stability and applicability. If these results lie within acceptable boundaries, the model is complete; otherwise, an analysis must be conducted to determine the causes of error and the model development cycle repeated from the information collection stage.

The end result will be a model that characterizes a "real" system; an input stream enters the process vessel which then performs some action(s) related to the process conditions that are present in order to produce one or more output streams. The model will be composed of input variables that affect a mechanistic or empirical representation along with process variables and parameters to give responses that predict column performance.

### 2.2.6 Applicability

Models are imperfect representations of "real" systems. As such, error is present as a result of the process description or through the mathematical equations and solutions that characterize the process. Experimental, assay or sampling error may also exist or the input parameters may be inaccurately estimated. The following restrictions also apply to models:

1. The model can only be used within the range of conditions under which it was developed. As such, all assumptions used in the model processes or sub-process must be taken into consideration. A model is only as good as the hypothesis it is built around.
2. The model is limited by the understanding of the processes involved.
3. Solutions, analytical or numerical, may not be possible for some complex equations.
4. The experimental results that a simulation is based upon may be of limited use due to errors. According to Blau et. al. (1972) the statistical confidence limits must be narrow enough to correctly assess the outcome of the model.

Villeneuve et. al. (1995) describe two uses of models:

1. Those models that are used to predict industrial-scale equipment performance typically are concerned with component recovery and are often used during operation to perform material balances, minimize circulating loads, and determine the best operating conditions of a vessel or circuit

2. Those models that are used to size and configure equipment.

### 2.2.7 Determination of Model Parameters

The traditional method of flotation kinetics and performance evaluation has been through bench-scale tests (physical models), performed over a sufficient time period to determine final recovery values. This type of test gives a single point on a time-recovery curve that can be used to estimate the kinetic rate constant if both entrainment and maximum recovery are assumed. According to Bushell (1962), and Klimpel (1980), this assumption is unjustified when relating bench-scale tests to full-scale mechanical-cells. In order to minimize time-dependency error, a full time–recovery curve is needed (Dowling et. al.; 1986).

The confidence in this method of sizing parameter determination may be further eroded when comparing different types of machines as is the case when batch mechanical-cell rougher results are used to predict full-scale column performance. In order to use this information an assumption must be made of time-recovery equivalency between these tests and the "real" flotation systems.

## 2.3 Current Flotation Models

### 2.3.1 Introduction to Kinetic Models

The mechanisms governing flotation in either mechanical-cells or columns are not fully known. As a result, mathematical models cannot be formulated directly from theory. Thus, to some extent, all current models are empirical. These models may or may not be based on the kinetic flotation rate.

The kinetic models currently available typically consider the froth as a simple zone wherein an experimentally determined fraction of the solids particles are rejected and returned to the pulp zones. While there are insights into the actions occurring, these may not be modeled. Performance may be significantly different between laboratory-, pilot-, and industrial-scale units depending on froth stability, mixing and residence-times.

Batch mechanical cell models are considered because they form the basis of the batch column cell model developed in this research.

### 2.3.2 Batch Mechanical-Cell Kinetic Models

#### 2.3.2.1 Introduction

The mechanical flotation cell can be treated as a single entity (single stage), or as a multistage system wherein two or more entities (Harris; 1978) are joined to form a complete, coherent system. In two stage models the pulp and froth stages are treated separately. In models with more than two stages, the froth and pulp are subdivided into additional stages.

#### 2.3.2.2 Single Stage

The USIM PAC simulators of mechanical-cells use either (1) sub-populations of each mineral including non-floating, slow and fast floating components (Fichera and Chudacek; 1991, Mehrotra and Podmanabhan; 1990, and Kelly and Carlson; 1991), or (2) a distribution of

kinetic rate constants with particle size. The flotation rate constant of single stage models is a composite of many mechanisms including flotation, drop-back, and operator technique. The mechanical-cell is assumed to be a perfect mixer. The total recovery predicted by these equations may be modified by an entrainment factor such as that of Kirjavainen (1992).

### 2.3.2.3 Two Stage

#### 2.3.2.3.1 **Introduction**

Arbiter and Harris (1961) propose a two-stage mechanical-cell kinetic model. Harris and Rimmer's (1966) version of this model is shown in Figure 7.

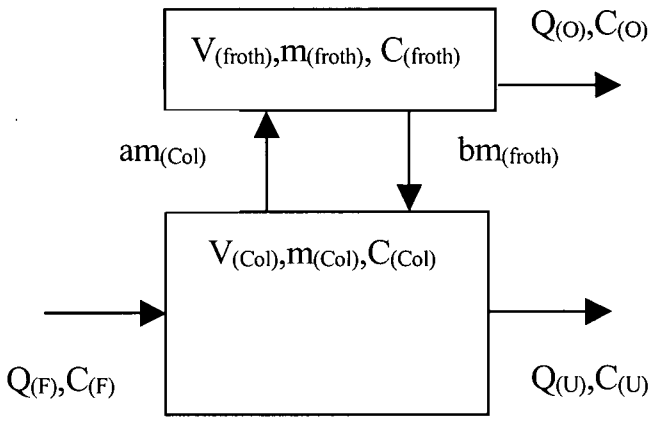


**Figure 7: Two-stage flotation model of Harris and Rimmer (1966)**

In Figure 7, "Q" [$cm^3\ s^{-1}$] is the volumetric flow rate; "C" is the component concentration (where the units depend on the type of concentration); "a" [$s^{-1}$] is the transport rate from pulp to froth; "b" [$s^{-1}$] is the transport rate from froth to pulp; "m" [g] is the component mass and "V" [$cm^3$] is the stage volume. The subscripts used in Figure 7 are "F" (feed), "U" (underflow), "O" (overflow), "Col" (collection zone) and "froth" (froth zone).

Neither the Arbiter and Harris (1961) or Harris and Rimmer (1966) models describe inter-stage water or gas flow. The Harris and Rimmer (1966) model assumes that each pulp stage is perfectly mixed. This assumption is valid for smaller sized particles considering that mechanical-cell test units operate with Reynolds' numbers on the order of 10,000 (Arbiter and

Harris; 1961). In the Harris and Rimmer (1966) model mass is assumed to flow into, and out of, each stage from the other.

2.3.2.3.2 **Pulp Stage**

The pulp stage is modeled using continuously stirred tank reactor (CSTR) kinetics wherein mass recovered is a function of the mineral/particle-size rate constant and residence-time under perfectly mixed conditions. Input to the system is from a feed stream and "drop-back" is from the froth stage. The pulp stage balance is found in Equation 4 (Harris; 1978).

$$\frac{\partial m_{(Col)}}{\partial t} = Q_{(F)}C_{(F)} - \frac{m_{(Col)}}{t_{(Col)}} + bm_{(froth)} - am_{(Col)} \qquad \text{Equation 4}$$

In Equation 4 the symbols used are the same as in Figure 7. In the pulp stage, the mass balance consists of mass entering via new feed (assuming continuous operation), minus the mass removed to the froth, plus any mass returned to the pulp stage from the froth.

Sastry and Fuerstenau (1970) performed an analysis of the flotation column. They assumed axially dispersed plug-flow of both liquid and gas stages.

2.3.2.3.3 **Froth Stage**

The froth mass flow rate balance of Harris (1978) is shown as Equation 5.

$$\frac{\partial m_{(froth)}}{\partial t} = -\frac{m_{(froth)}}{t_{(froth)}} + am_{(Col)} - bm_{(froth)} \qquad \text{Equation 5}$$

In Equation 5, the change in froth solids mass with time ($\partial m_{(froth)}/\partial t$) is the amount of solids entering from the pulp stage minus the mass leaving with the overflow and returning to the pulp stage.

There are many froth stage models including those by Moys (1989), Cutting et. al. (1986), and Ross (1991b). Bisshop and White (1976) claim that the most important rate recovery factor is the froth residence-time.

#### 2.3.2.3.4 **Stage Interactions**

Sadler (1973) used a single-stage, gamma distributed, first-order rate coefficient model and a bubble-surface-area model to describe flotation. The transfer of floatable mineral from the froth back to the pulp is related to bubble-surface-area and loading density.

If a constant volume is maintained then "$Q_{(F)}=Q_{(O)}+Q_{(U)}$". At steady state both "$\partial m_{(froth)}/\partial t$" and "$\partial m_{(Col)}/\partial t$" are zero, thus, Equation 5 and Equation 4 simplify to Equation 6.

$$\frac{m_{(Col)}}{m_{(froth)}} = \frac{b}{a} + \frac{1}{at_{(froth)}} \qquad \text{Equation 6}$$

Equation 6 is the inverse of Woodburn et. al.'s (1976) *enhancement factor*. When Equation 6 is converted to concentration terms it is the inverse of Schuhmann's (1942) *coefficient of mineralization*.

Transient conditions of two-stage models have been investigated by Harris and Rimmer (1966). Their observations show that there may be a delay in overflow at the start of flotation due to the accumulation of mass in the froth. Harris and Chakravarti (1970) noted that multistage models are equivalent to single stage models with a time delay used to account for accumulation of mass. Harris (1978) further states that "it is the generality of the [two stage] equation that succeeds, not the model from which it is derived".

Water transport between stages is an important aspect of the two stage model as seen by Schuhmann's (1942) and Woodburn et. al.'s (1976) works. The concentrate removal rate (Harris and Raja; 1966), water flow rates (entrainment), and airflow rates are also important (Sadler; 1973 and Flint; 1974).

#### 2.3.2.4 Multi Stage

Harris (1978) mathematically modeled a three-stage system and showed that, at steady state, the model reduces to the two-stage equations, although the rate constants are a composite of the three-stage rates. An example of a three-stage system is that of Hanumans and Williams (1992) who modeled the froth stage as two separate zones.

### 2.3.3 Column Kinetic Models

#### 2.3.3.1 Introduction

Column kinetic models of other researchers form the basis of the continuous kinetic model developed in this thesis. There are three common kinetic models of column flotation. The first is a widely used model by Dobby (1984) and Finch and Dobby (1990). The second is a variation of the first by Yoon and Luttrell at Virginia Polytechnical Institute (Yoon; 1993, Yoon and Luttrell; 1989 and Yoon et. al.; 1991). The third, also a variant of the first, is by Alford (1992). All three of these kinetic models use the axial dispersion theory in the pulp zone. Both the Finch and Dobby model and the Yoon and Luttrell model assign a recovery to the froth zone or incorporate froth-zone affects into the pulp stage model. Alford uses a single-stage model. The mixing parameter is the Peclet number "Pe" or its' inverse "Np". When the Peclet number approaches infinity, a plug flow condition exists. A Peclet number that approaches zero represents perfect mixing.

#### 2.3.3.2 Single Stage

The JKMRC model (Alford; 1992) is a single stage equivalent of the Dobby and Finch's (1990) two-stage model. This model assumes that froth depth and wash-water rate have an insignificant effect on the flotation rate parameter. In addition, Alford (1992) uses an empirical modification of the rate constant to compensate for air rates and viscosity (Equation 7).

$$k_{f(m,n)} = C_{1(m,n)} \left(J_g^*\right)^{0.75} \left(\frac{\mu_l}{\mu_{sl}}\right)^{a_1} R_f$$ Equation 7

$$k_f = \frac{1.5 J_g E_k}{d_b}$$ Equation 8

Equation 7 is an empirical equation that is similar to Equation 8 (Jameson et. al.; 1977). Equation 7 uses water viscosity ($\mu_l$ [g $cm^{-1}s^{-1}$]) and slurry viscosity ($\mu_{sl}$) but is only valid when the Peclet number is low and there is a high froth recovery. Also in Equation 7 "$C_{1(m,n)}$" is a dimensionless characteristic of the mineral and particle size as well as a function of sparger characteristics and frother concentration. "$R_f$" is the recovery through the froth zone.

In Equation 8, "k" [$s^{-1}$] is the kinetic rate constant; "$J_g$" is the superficial gas velocity [cm $s^{-1}$]; "$d_b$" [cm] is the bubble diameter and "$E_k$" [dimensionless] is the collection efficiency.

The adjusted gas velocity of Equation 7 is found in Equation 9. This equation attempts to compensate for the gas velocity term of Equation 7 by using loading and column diameter (Alford; 1992).

$$J_g^* = J_g - \frac{b_1 A_C J_g^{0.75}}{m_O}$$ Equation 9

In Equation 9, "$b_1$" [g $cm^{-2}$] is independent of mineral and particle size. Also, in Equation 9, "$m_O$" [g] is the mass of floatable particles that are in the overflow stream; "$A_c$" [$cm^2$] is the column cross-sectional area and "$J_g$" [cm $s^{-1}$] is the superficial gas velocity.

Referring to Equation 7, Alford (1992) uses Equation 10 to predict the "$C_{1(m,n)}$" value.

$$C_{1(m,n)} = C_{1(m)} d_p^{a_2} e^{-a_3 d_p}$$ Equation 10

The model parameters of Equation 10 are determined by curve-fitting techniques and are applied for "scale-up" with the axial dispersion model. Alford's (1992) curve fitting was done to minimize the chi-squared statistic using the Levenberg-Marquardt method (Kojovic; 1988, as referred to by Alford; 1992). Redundancy is a requirement of this method and Box and Draper (1987) recommend that the number of observations be five to ten times the number of estimated parameters.

The Alford (1992) JKMRC model is an empirical simplification of the Dobby model that assumes the froth and pulp zone cannot be, or need not be, separated. This model also assumes that baffles do not reduce mixing and that the effect of variations in froth depth and bias, within the range used by the model, have minimal impact upon performance.

#### 2.3.3.3 Two Stage - Finch and Dobby Model

The development of the Finch and Dobby type model began with Dobby's 1984 Ph.D. thesis. Since that time it has been refined by many others. The purpose of the Finch and Dobby model is to determine modeling parameters from continuous pilot-scale column tests and then to use these parameters to predict the performance of continuous industrial-scale columns. This model was not designed to use parameters determined in batch mechanical-cell tests, although with modifications it has been used for that purpose.

Dobby and Finch's two-stage model is based on axial dispersion model and kinetics. No comprehensive froth model is given and recovery through this stage is set as an input value. An assumption is made that performance is dictated within the collection zone. The model takes into consideration solids loading of bubbles through a carrying capacity term at the top of the collection zone, solids overloading in the froth, misalignment of the column and baffling and uses mineral and size-class rate constants (Castillo; 1988).

The Dobby and Finch model is similar to that of Harris and Rimmer (1966) in that both are two–stage. The first stage is the collection, or pulp zone. Feed to this section is composed of vessel feed and drop-back from the froth zone and includes water flow terms. Recovery is calculated in the collection zone by using a dispersion model with a cap on recovery as

dictated by carrying capacity constraints. Entrainment of non-attached particles, either within the bubble wake or within the boundary layer, is neglected under a positive bias assumption. The collection rate is assumed to be first-order with respect to concentration. Material not floated in the collection-zone flows with the underflow stream.

Recovery in the Dobby and Finch (1986a) collection-zone model is a function of rate constants, particle retention time and mixing. In this model, the solids are assumed to have the same axial dispersion as the liquid. The equations in Table 1 are used to simulate column performance.

**Table 1: Castillo (1988) version of the Finch and Dobby Model**

| | Description | Units | Definition | |
|---|---|---|---|---|
| $A_C$ | Area | $cm^2$ | $4A_c = \pi d_C^2$ | A |
| $d_{Ce}$ | Column diameter | cm | $A_c = d_{Ce} Nb$ | B |
| $h_{(Col)}$ | Collection height | cm | $h_{(Col)} = h_{(V)} - h_{(f)} - h_{(spa)}$ | C |
| $Q_{sl}$ | Volumetric rate | $cm^3\ s^{-1}$ | $Q_{sl} = \frac{1}{t}\left[\frac{m_{SL(F)}}{\rho_{SL(F)}} + \frac{m_{SL(f)}}{\rho_{SL(f)}} + \frac{m_{LL(F)} + m_{LL(f)}}{\rho_L}\right]$ | D |
| $u_l$ | Interstitial liquid flow rate | $cm\ s^{-1}$ | $u_l = Q_{sl}\frac{(1-\varepsilon_g)}{A_C}$ | E |
| $t_l$ | Liquid retention time | s | $t_l = \frac{h_{(Col)}(1-\varepsilon_g)}{J_{sl}}$ | F |
| $u_p$ | Particle settling-velocity | $cm\ s^{-1}$ | $u_p = \frac{g d_p^2 (\rho_p - \rho_{sl})(1-\varepsilon_s)^{2.7}}{18\mu_{sl}(1+0.15\,\mathrm{Re}_p^{0.687})}$ Masliyah (1979) | G |
| $t_p$ | Particle retention time | s | $t_p = t_l \frac{u_l}{u_l + u_p}$ | H |
| Di | Dispersion Dobby (1984) | $cm^2\ s^{-1}$ | $Di = 0.0547 d_{Ce} J_g^{0.3}[1 + (1100\alpha d_{Ce})]^2$ | I |
| Np | Dispersion | --- | $Np = \frac{Di}{h_{(Col)}(J_l + u_p)}$ | J |
| Np | Dispersion number | --- | $N_p = \frac{1}{Pe} = \frac{0.05471 d_C J_g^{0.3}}{\left(\frac{J_{sl}}{1-\varepsilon_g} + u_p\right) h_{(Col)}}$ | K |
| Pe | Peclet number Levenspiel 1972 | ---- | $Pe = 18.28\frac{h_{(Col)}}{d_C}\left[\frac{J_{sl}}{1-\varepsilon_g} + u_p\right] J_g^{-0.3}$ | L |
| R | Recovery | --- | See Table 3 | M |
| $Re_p$ | Reynolds' number | --- | $\mathrm{Re}_p = \frac{d_p u_p \rho_l (1-\varepsilon_s)}{\mu_l}$ | N |

In Table 1, "$m_{SL}$" [g] is the feed solids mass suspended in the liquid, "$m_{LL(s)}$" [g] is the liquid mass in the liquid phase in the feed; "$\rho_{SL}$" [g $cm^{-3}$] is the suspended solids density; "$\rho_L$" [g $cm^{-3}$] is the liquid density; "Np" is the dispersion number (inverse Peclet number); "Nb" is the number of baffles; "$J_l$" [cm $s^{-1}$] is the superficial liquid flow rate and "$\alpha$" is the column misalignment in radians. The subscripts used are "F" (feed) and "f" (drop-back).

The particle Reynolds' number ($Re_p$ -- Table 1-N) and particle settling-velocity ($u_p$ [cm $s^{-1}$] -- Table 1-G) calculations use the solids fractional holdup within the liquid phase ($\varepsilon_s$). This solids holdup can be calculated using Equation 11.

$$\varepsilon_s = \frac{V_s}{V_s + V_l} \qquad \text{Equation 11}$$

In Equation 11, "$V_s$" [$cm^3$] is solids volume; "$V_l$" [$cm^3$] is the liquid volume and "$\varepsilon_s$" [dimensionless] is the volumetric solids holdup. Table 2 shows typical velocity ranges as stated by Dobby and Finch (1986a). Columns may be run under negative bias conditions.

**Table 2: Typical flows**

| Symbol | Description | Units | Minimum | Maximum |
|---|---|---|---|---|
| $J_g$ | Superficial gas velocity | cm $s^{-1}$ | 1.0 | 3.0 |
| $J_{sl}$ | Superficial slurry velocity | cm $s^{-1}$ | 0.5 | 2.0 |
| $J_b$ | Superficial bias velocity | cm $s^{-1}$ | 0.1 | 0.5 |

Vessel recovery is calculated using Table 3 limited by the carrying capacity.

**Table 3: Recovery equations**

| Symbol | Description | Units | Definition | Source |
|---|---|---|---|---|
| $R_{S(v)}$ | Vessel recovery | --- | $R_{S(v)} = \frac{R_{S(Col)}R_{S(froth)}}{R_{S(Col)}R_{S(froth)} + 1 - R_{S(Col)}}$ | Dobby (1986a) |
| $R_{S(Col)}$ | Collection-zone recovery | --- | Wehner - Wilhelm | Levenspiel (1972) |
| $R_{S(froth)}$ | Froth-zone recovery | --- | 0.5<br>$0.4 \rightarrow 0.8$ | Castillo (1988)<br>Falutsu (1989a) |
| $m_o/t$ | Overflow solids flow rate | $g\ s^{-1}$ | | |
| $Ca_{(max)}$ | Maximum carrying capacity | $g\ cm^{-2}\ s^{-1}$ | $Ca_{(\max)} = b_{12}\rho_{s(O)}d_{80(O)}$ | Espinosa, Yianatos and Finch (1988) |
| Ca | Carrying capacity | $g\ cm^{-2}\ s^{-1}$ | $Ca = \frac{m_O}{A_c t}$ | |

The total vessel recovery ($R_{s(v)}$) is calculated when determining overflow recovery. Then the solids flow rate in the overflow ($m_O/t$" [$g\ s^{-1}$]) is calculated using the feed data and recovery. The actual carrying capacity (Ca [$g\ cm^{-2}s^{-1}$]) is then calculated and compared to the maximum carrying capacity ($Ca_{(max)}$). If "Ca" is greater then "$Ca_{(max)}$", recovery ($R_{s(v)}$) is decreased and these calculations are repeated. Material rejected from the froth zone is then calculated, added to the feed (for collection zone purposes only), and the entire model is iterated. Note: "$d_{80}$" size is quoted in cm.

The second stage, or froth zone, assumes a certain recovery of material presented to it from the collection stage. The material recovered then becomes overflow product while everything else is returned to the collection zone through drop-back (Table 3).

Carrying capacity is determined using the relationship of Espinosa-Gomez, Finch and Yianatos (1988) as shown in Equation 12.

$$Ca_{(\max)} = b_{12}\rho_{s(O)}d_{80(O)} \qquad \text{Equation 12}$$

In Equation 12, "$Ca_{(max)}$" [g $cm^{-2}sec^{-1}$] is the maximum area carrying capacity; "$\rho_{s(O)}$" [g $cm^{-3}$] is the overflow solids density and "$d_{80(O)}$" [cm] is the overflow particle size at which 80% of the particle mass is smaller than. The value of "$b_{12}$" [$s^{-1}$] depends upon the units used in the equation. Use of this model involves the minimization of error between actual and predicted performance by the adjustment of model parameters.

### 2.3.3.4 Two Stage - VPI Model

Yoon et. al. (1991, 1993) also model columns using axial dispersion and the Wehner and Wilhelm (1956) equation. In their calculations, the Peclet number (Pe [dimensionless]) is calculated using the empirical relationship found in Equation 13.

$$Pe = 0.6\left[\frac{h_{(col)}}{d_c}\right]^{0.63}\left[\frac{J_{sl}}{J_g\left(1-\varepsilon_g\right)}\right]^{0.5} \qquad \text{Equation 13}$$

Equation 13 uses collection-zone height ($h_{(Col)}$ [cm]), column diameter ($d_c$ [cm]), superficial slurry velocity ($J_{sl}$ [cm $s^{-1}$]), superficial gas velocity ($J_g$ [cm $s^{-1}$]), and fractional gas-holdup ($\varepsilon_g$ [dimensionless]). Yoon et. al. (1991, 1993) uses Jameson et. al's (1977) relationship, found in Equation 8, to further relate the flotation rate parameter ($k_f$ [$s^{-1}$]) to the mechanistic collection process using a probability factor that is equivalent to Dobby's (1984) collection efficiency "$E_k$". Yoon's carrying capacity limitation is the maximum solids-surface-area removed as a bubble-surface-area percentage. Furthermore, a maximum gas rate is used that is determined by coalescing and slugging factors. Similar equations can be derived from Dobby (1984) and the bubble size and flooding patterns from Flint (1989).

### 2.3.3.5 Summary

The simplifications and empirical nature of the single-stage JKMRC model (Alford; 1992) make this model difficult to convert for use with bubble loading and particle surface-area. The VPI model follows the form of the Finch and Dobby model with modifications to the mixing terms. However, more data is available on the Finch and Dobby model and it is more widely used. Thus, the Finch and Dobby continuous kinetic column model is used as a basis of the continuous kinetic surface-area model in this research.

## 2.4 Carrying Capacity

### 2.4.1 Introduction

"Carrying capacity" is a term used in most continuous column flotation models to indicate the relationship between solids removal rates and the size of the flotation vessel: "carrying capacity" is the maximum amount of material that can be removed per time from a flotation vessel. Early work by Espinosa-Gomez, Yianatos and Finch (1988) relates carrying capacity to column cross-sectional area (Ca [g $cm^{-2}sec^{-1}$]) while work by Amelunxen (1990) relates carrying capacity to lip length ($C_L$ [g $cm^{-1}sec^{-1}$]).

### 2.4.2 Cross-Sectional Area "Carrying Capacity"

Espinosa-Gomez, Yianatos and Finch (1988) determined a relationship between floated material and column size. In this relationship mineral size ($d_{80}$) and solids density multiplied by a proportionality constant give the area carrying capacity (Ca [g $cm^{-2}sec^{-1}$]) as shown in Equation 14 and used previously as Equation 12.

$$Ca_{(max)} = b_{14}\rho_{s(O)}d_{80(O)} \qquad \text{Equation 14}$$

In Espinosa-Gomez's (1988) work, the proportionality constant, "$b_{14}$" was determined to be 0.00113 [$s^{-1}$]. Work by Finch and Dobby (1990), extended the particle size limit to about 100 μm but the authors that an uncertainty of about 30% and a "$b_{14}$" value of 0.00803 [$s^{-1}$]. In Equation 14, "$d_{80}$", the 80% passing size, is the particle size [cm] and "$\rho_p$" is the particle density [g $cm^{-3}$].

Not all parameters that affect "Ca" may be included in Equation 14 since the value predicted by this relationship drops below expected values when the gas rate ($J_g$ [cm $s^{-1}$]), is below 1.5 (Castillo; 1988). Ityokumbul and Trubelja (1998) have pointed out that carrying capacity depends on gas velocity. Other studies by Amelunxen (1990) and Sastri (1996) have also

found this equation lacking. Xu (1987) estimated the gas carrying capacity (Ca) as the relationship shown in Equation 15. This equation is the same as Equation 14 when the proportionality constant, "$b_{14}$" [$s^{-1}$], is replaced by "$\pi J_g/(2d_b)$" and "$d_{80}$" [cm] is replaced with "$d_p$" [cm].

$$Ca = \frac{\pi}{2}\frac{J_g d_p \rho_{s(O)}}{d_b} \qquad \text{Equation 15}$$

In Equation 15, "$J_g$" [cm $s^{-1}$] is the superficial gas rate; "$d_b$" and "$d_p$" [cm] are the bubble and particle diameters respectively, and "$\rho_{s(O)}$" [g $cm^{-3}$] is the average overflow solids density. This equation should only be used when mono-dispersed particles are assumed.

Xu (1987) calculates the bubble density as shown in Equation 16 by assuming that the maximum loading on the bubble is 50% ["$\phi_{SB}$" = 0.5] and that particle diameter is much smaller than bubble diameter ($d_p << d_b$).

$$\rho_b = \frac{\pi}{2}\frac{d_p \rho_{s(O)}}{d_b} \qquad \text{Equation 16}$$

In Equation 16 "$\rho_b$" [g $cm^{-3}$] is the bubble density; "$d_p$" [cm] is the particle diameter; "$d_b$" [cm] is the bubble diameter and "$\rho_{s(O)}$" [g $cm^{-3}$] is the average attached solids density.

Xu (1987) combines Equation 15 and Equation 16 to give the relationship shown in Equation 17.

$$Ca = \rho_b J_g \qquad \text{Equation 17}$$

In Equation 17, "Ca" is the area carrying capacity [g $cm^{-2}s^{-1}$]; "$J_g$" [cm $s^{-1}$] is the superficial gas velocity and "$\rho_b$" [g $cm^{-3}$] is the bubble density.

Ityokumbul and Trubelja (1998) propose the relationship shown in Equation 18 for area "carrying capacity" (Ca) when a mono-dispersed solid is assumed.

$$Ca = b_{18}\frac{240J_g}{d_b}\rho_{s(O)}d_p \qquad \text{Equation 18}$$

Equation 18 is similar to Equation 14 when "$b_{18}$" is equivalent to $b_{14}[240J_g/d_b]$ and "$d_{80}$" is equivalent to "$d_p$". Flotation occurs in slurries of poly-dispersed solids, thus, a value must be determined for particle size such as the "$d_{80}$" term of Espinosa-Gomez, Yianatos and Finch (1988). Ityokumbul and Trubelja (1998) experimentally determined the value of "$\phi_{SB}$" at 0.5, which is similar to that assumed by Xu (1987).

### 2.4.3 Lip Loading

Amelunxen (1990) presented a second empirical "carrying capacity" relationship after finding that "Ca" [g $cm^{-2}s^{-1}$] decreases for column diameters greater than one meter. This relationship assumes that the total froth-zone lip-length is a constraining factor. Amelunxen's (1990) lip loading; $C_L$ [g $cm^{-1}s^{-1}$], uses slurry mass rather than only solids mass (Equation 19) for zinc.

$$C_L = b_{19}d_C^{a_{19}} \qquad \text{Equation 19}$$

Equation 19 is an empirical equation where the constant "$b_{19}$" and the exponent "$a_{19}$" (determined to be 0.3 for sphalerite) are determined strictly by regression analysis. Both the proportionality constant "$b_2$" and the exponent "0.3" vary depending on the operation in question.

### 2.4.4 Summary

Neither the simplification of carrying capacity found in Equation 14 nor the empirical lip loading relationship (Equation 19) include all variables necessary to describe maximum loading of bubbles. The expanded area carrying capacity relationship described by Equation 15 is more comprehensive. The area carrying capacity relationship shown in Equation 17 uses

the bubble density as calculated in Equation 16 which assumes that the bubble size is much larger than the particle size.

### 2.4.5 Bubble Loading

Flotation is an interfacial phenomenon wherein a solids-surface-area is attached to, and thus, removed by a bubble-surface-area. The rate of removal of solids-surface-area is related to the bubble-surface-area flux as shown, through regression, by a modified form of Ityokumbul and Trubelja's (1998) relationship (Equation 20). Bradshaw and O'Connor (1996) report similar results using pyrite.

$$R_S = b_{20}\left(\frac{S_{B(O)}}{S_{SB(O)}}\right)^{a_{20}} \qquad \text{Equation 20}$$

In Equation 20, "$R_S$" [dimensionless] is the solids recovery; "$S_{B(O)}$" [$cm^2$] is the total surface-areas of bubble, "$S_{SB(O)}$" [$cm^2$] is the total surface of particles attached to the bubbles in the overflow, "$b_{20}$" is determined to be 0.4445 and "$a_{20}$" is determined to be 1.05. This equation, however, should work just as well with surface-area per time or surface-area flux ($\vartheta_B$ [$s^{-1}$] and $\vartheta_{SB}$ [$s^{-1}$]). The superficial bubble-surface-area flux (Xu; 1987) is the bubble-surface-area passing through the column per time and cross-sectional area ($\vartheta_B$ [$s^{-1}$]) as shown in Equation 21 (modified from Xu; 1987). "$\vartheta_{SB}$" [$s^{-1}$] attached superficial total-solids surface-area rate.

$$\vartheta_{B(x)} = 6\frac{J_g}{d_{b(x)}} \qquad \text{Equation 21}$$

In Equation 21,"x" indicates any elevation.

## 2.5 Entrainment

### 2.5.1 Introduction

Entrainment is the non-selective recovery, to the overflow, of both hydrophobic and hydrophilic solid particles and occurs in most flotation vessels. An adequate model of entrainment must be incorporated in order to model flotation properly. The entrainment recovery is influenced by many factors, but water flow between flotation stages is generally recognized as the medium for gangue transport (Harris et. al.; 1963, Jowett; 1966, Sadler; 1973, Flint; 1974, Bisshop and White; 1976, and Moys; 1978). Some variables that affect the rate of solids entrainment are: pulp density (Kirjavainen; 1989), particle size (Trahar and Warren; 1976; Bisshop and White; 1976), particle shape (Kirjavainen and Laapas; 1988), and froth properties such as stability, drainage (Subrahmanyam and Forssberg; 1988, Ross; 1990b and Ross; 1991a), removal rate (Flynn and Woodburn; 1987), and froth residence-time (Bisshop and White; 1976, Moys; 1984 and Ross; 1990c).

### 2.5.2 Entrainment in Flotation Columns

Under normal industrial-scale column operating and design conditions, overflow entrainment is minimal and is usually ignored. However, entrainment can become important if any of the following operation conditions exist:

- Close to neutral or negative bias,
- High concentration ratios, or
- Variable or cyclical flows.

As in the mechanical-cell, flotation column entrainment rate is assumed to be proportional to the overflow feed water recovery rate. This rate is determined by two factors: the relative water magnitudes required to transport the froth compared to the quantity of wash-water used, and the mixing that occurs in the froth zone.

Column wash-water addition rates are usually known. The volume of water, however, used to transport the froth to the overflow is often unknown but can be estimated using empirically derived relationships. The flow magnitude is dependent on the quantity, hydrophobicity, size and shape of floating particles, on the reagent suite used in the process, and on the bubble quantity and size distribution. Operating variables such as interface level and variability also have an impact.

At best, wash-water introduced into the froth would replace an equivalent volume of feed water. Industrial-scale column froths, however, do not occur in a plug flow environment and bias may not be consistent throughout the cross-section. Some areas of negative bias may occur even when the average bias is positive. Factors that affect mixing in the froth zone are: radial pulp-zone bubble distribution, placement of internal baffles, wash-water distributor design, wash-water rate, and operational practices.

The results of both Maachar (1992), and Pal and Masliyah (1990) show that gas rate has a significant impact on feed-water recovery. Water content in the froth increases with increasing gas rate since water enters the froth zone with the rising bubbles. As more froth-zone feed-water is recovered bias decreases and entrainment increases.

Bias increases in a linear fashion with wash-water rate within the range tested by Maachar (1992) and Pal and Masliyah (1990). An increase in bias, when all else is held constant, results in diminished feed water in the overflow (Maachar; 1992). A higher average bias rate is more likely to ensure that there is a positive bias throughout the froth zone. At very high wash-water rates, the wash-water may channel or froth destruction may occur.

## 2.5.3 Feed Water Recovery Entrainment Models

### 2.5.3.1 Introduction

Many entrainment models have been published. Three have been presented here in order to illustrate the different methods used. These are the models of Ross (1990b), Trahar (1981) and Kirjavainen (1992) and Warren (1985).

### 2.5.3.2 Ross (1990b)

Ross (1990b) uses transfer functions to characterize the entrainment and total rates of overflow solids production -- shown in modified form in Equation 22 and Equation 23, respectively. Ross assumes that only entrainment occurs at the end of a batch flotation test of sufficient residence-time (no flotation). This assumption means that the transfer function "X" approaches "Y" with sufficient residence-time.

$$\frac{m_{SL(O)}}{m_{SL(z)}} = X(t)\frac{m_{LL(O)}}{m_{LL(z)}} \qquad \text{Equation 22}$$

$$\frac{m_{SB(O)} + m_{SL(O)}}{m_{SL(z)}} = Y(t)\frac{m_{LL(O)}}{m_{LL(z)}} \qquad \text{Equation 23}$$

The transfer function, "X(t)" [dimensionless] characterizes the solids in the overflow carried by suspension in the liquid phase, and "Y(t)" [dimensionless] characterizes the solids in the overflow carried both in suspension and attached to bubbles. In Equation 22 and Equation 23 "m" is the mass of solids to the overflow (O) or within a zone (z). That mass (m) may be either that of the solids (S) or liquid (L) associated with either the liquid phase (L) or attached to the bubbles phase (B). The pulp density in a flotation column is not constant; thus, the proper values of solids and water concentrations may not be known. The ratio of "$m_{ll(O)}$" to "$m_{ll(z)}$" is the recovery of feed water to the overflow in a continuous system.

### 2.5.3.3 Trahar (1981)

Trahar determines the relationship between solids and water recovery, on mineral and size-class base, by measuring solids and water recovery with and without collectors – the

difference between these two tests is assumed to be the true flotation rate. Recovery without collector is assumed to be due only to entrainment. This test assumes that tests with, or without collectors, have the same water recovery which may not be the case.

#### 2.5.3.4 Warren (1985) and Kirjavainen (1992)

Warren relates solids to water recovery by a series of tests that vary the ratio of water to solids recovery by altering froth height and removal rates. The procedure assumes that the function slope is the rate of entrainment and the intercept, at zero water recovery, is the rate of true flotation (Equation 24: Warren; 1985, and Villeneuve et. al.; 1995) for each counter: mineral (m) and size-class (n).

$$R_{S(m,n)(i)} = R_{Sf(m,n)(i)} + \beta_{(m,n)(i)} R_{l(i)} \qquad \text{Equation 24}$$

In Equation 24, "$R_S$" is the total vessel solids recovery; "$R_{Sf}$" is the solids recovered by flotation; "$R_l$" is the water recovery and "$\beta$" is a mineral, size, and shape-dependent constant. All variables in Equation 24 are dimensionless. A proper time interval must be chosen because the relationship between the degree of entrainment and the water recovery may deteriorate with time (Warren; 1985).

Villenueve et. al. (1995), based on work by Kirjavainen (1992), use a simple proportionality with water recovery to estimate recovery by entrainment. The mineral recovery relationship used is Equation 24 when the recovery of solids due to flotation ($R_{Sf(i)}$) is assumed zero. The slope of this relationship, "$\beta_{m,n}(t)$", is calculated by Kirjavainen (1992) using Equation 25.

$$\beta_{(m,n)(i)} = \frac{\left[R_{l(i)}\right]^{0.7}}{\left[R_{l(i)}\right]^{0.7} + b_{(m)}\left(\frac{m_{S(O)(m,n)}}{\mu_{sl}}\right)^{0.5}} \qquad \text{Equation 25}$$

In Equation 25, "$R_l$" [dimensionless] is the water recovery to the overflow; "m" [g] is the mass of solids; "$\mu_{sl}$" [g $cm^{-1}s^{-1}$] is the slurry viscosity and "b" [$s^{-1}$] is a mineral constant.

Kirjavainen (1992) obtains the slurry viscosity using the relationship found in Equation 26 where "b" is a mineral specific constant (Kirjavainen; 1992). The value for quartz, for example, is 1.83.

$$\mu_{sl} = \mu_l + b\varepsilon_s(1-\varepsilon_s)^{-4} \qquad \text{Equation 26}$$

In Equation 26, "$\mu_{sl}$" is the slurry viscosity; "$\mu_l$" is the water viscosity; "$\varepsilon_s$" is the solids holdup and the proportionality constant and the constant "b" has the units of viscosity [g $cm^{-1}s^{-1}$].

#### 2.5.3.5 Summary

The model of Ross (1990b) assumes that the material recovered after a long flotation residence time is due only to entrainment. This is not necessarily true. The entrainment predicted by Trahar (1981) may not be valid since solids may stabilize the froth. Subrahmanyam and Forssberg (1988) use Trahar's method but Ross (1991) states that this method underestimates entrainment. The number of tests needed to determine entrainment using Warren's (1985) method is a deterrent to this method's use. Also, the varying removal rates and froth depths of Warren's method could change the entrainment rate (Flynn and Woodburn; 1987). Kirjavainen's (1992) model for $\beta$ uses a mineral constant that may not be known.

The method of Ross (1990b) was chosen to determine an initial, temporary value. Only an approximation is needed of the entrainment in order to use a minimization routine. This method eliminated the need for special mineral constants and extensive test work.

### 2.5.4 Moys and Finch (1991) – Feed Water Recovery

Water recovery is recognized as a key variable in the entrainment of solids in flotation. The amount of feed water recovered to the overflow can be calculated using a temperature balance on the feed, wash-water and overflow as shown in Equation 27 (Moys and Finch; 1991). Uribe-Salas et. al. (1990) use similar tests with conductivity.

$$\frac{Q_{l(F,O)}}{Q_{l(W,O)}} = \frac{T_{(O)} - T_{(W)}}{T_{(F)} - T_{(W)}} \qquad \text{Equation 27}$$

In Equation 27, "$Q_{l(FO)}$" [$cm^3\ s^{-1}$] is the volumetric, overflow, water flow originating in the feed and "$Q_{l(WO)}$" [$cm^3\ s^{-1}$] is the total volumetric, overflow water. Also, "T" is temperature of the overflow (O), feed (F) and wash-water (W). In this equation, the ratio of feed water that goes to the overflow to the total feed water equals the ratio of overflow to feed temperatures when both temperatures have the wash-water temperature subtracted from them. Maachar et. al. (1992) proves that the temperature method of determining overflow feed water recovery has a very close correlation to the results of tracer tests.

## 2.6 Gas Phase

### 2.6.1 Introduction

There are four gas phase "characteristics" that are important in flotation: bubble flow regime, bubble rise velocity, maximum gas rate and superficial bubble surface area flux.

### 2.6.2 Bubble Flow Regime

In the gas phase, the bubble flow regime, surface-area-flux and size are important because flotation is a separation based on the removal of solid-surface-area on a bubble-surface-area. A column collection-zone typically operates in the "bubbly flow" regime. Kumar et. al. (1976) further divide the "bubbly regime" into the "dispersed regime" -- where bubbles flow freely (gas holdup, $\varepsilon_g < 0.10$), and the "fluidized regime" -- where bubbles rise as swarms ($0.10 < \varepsilon_g < 0.25$). As the gas rate is increased, the "bubbly flow regime" homogeneity is lost and larger bubbles, spherical caps, and slugs are formed. As a result, mixing increases (Rice and Littlefield; 1987) gas holdup decreases and the flow regime becomes heterogeneous or "churn-turbulent" (Shah et. al.; 1982, Kasireday and Al Taweel; 1989 and Finch and Dobby; 1990). The optimum gas rate for flotation occurs prior to the transition to "churn-turbulent flow". Finch and Dobby (1991) present the transition gas rates at various bubble sizes and flow rates (from other sources). This information is reproduced as Table 4.

**Table 4: Transition Gas Rates from various sources (Finch and Dobby; 1991)**

| $d_b$ (mm) | Kasireday (1989) | Mankosa (1990) | Dobby (1986a) | Finch (1990) | Xu (1991) |
|---|---|---|---|---|---|
| $J_{sl} = 0.4$ | $J_g$ cm/s | $J_g$ cm/s | $J_g$ cm/s | $J_g$ cm/s | $J_g$ cm/s |
| 1.0 | 1.9 | >2 | 1.5 | 2.9 | 2.5 |
| 0.6 | 1.1 | 1.5 | 1.0 | 1.3 | 1.4 |
| 0.2 | <0.1 | | <0.2 | | 0.17 |
| $J_{sl} = 1.0$ | $J_g$ cm/s | $J_g$ cm/s | $J_g$ cm/s | $J_g$ cm/s | $J_g$ cm/s |
| 1.0 | 1.5 | >2 | 1.4 | 2.5 | 2 |
| 0.6 | 0.8 | 1.2 | 0.7 | 1.0 | 1 |
| 0.2 | 0.005 | | <0.1 | | 0.04 |

These various sources show that maximum gas rate decreases with bubble size. Note that reagent conditions are not stated.

Zuber and Hench (1962) found the transition at gas holdups of between 20% and 25%. Lockett and Kirkpatrick (1975) state that the transition is due to liquid circulation patterns and the presence of large bubbles. Operational deficiencies, such as the generation of a wide size distribution of bubble sizes or the liquid flow patterns may reduce the air rate at which regime transition occurs (Xu et. al.; 1989)

### 2.6.3 Bubble Rise-velocity

Bubble rise-velocity affects bubble residence-time, gas holdup, kinetics of bubble-particle interactions and many other factors that impact on the outcome of a flotation separation. Upward bubble "swarm" rise-velocity ($u_b$ [cm $s^{-1}$]) can be estimated by using Equation 28 -- from Yianatos (1986).

$$u_b = \frac{J_g}{\varepsilon_g} + \frac{J_l + J_s}{1 - \varepsilon_g} \qquad \text{Equation 28}$$

In Equation 28, "$J_g$", "$J_l$", and "$J_s$" are the gas, liquid and solids superficial flow rates [cm $s^{-1}$] respectively and "$\varepsilon_g$" is the gas holdup [dimensionless]. Yianatos, Finch, Dobby and Xu (1988) use a modification of the Masliyah (1979) hindered settling relationship shown in Equation 29 (from Finch and Dobby; 1990) to calculate bubble "swarm" rise-velocity.

$$u_b = \frac{g d_b^2 (\rho_{sl} - \rho_b)(1 - \varepsilon_g)^{n-1}}{18\mu_l (1 + 0.15\,\mathrm{Re}_b^{0.687})} \qquad \text{Equation 29}$$

In Equation 29, "g" [cm $s^{-2}$] is gravitational acceleration; "$d_b$" [cm] is bubble diameter; "$\rho_{sl}$" [g $cm^{-3}$] is slurry density; "$\rho_b$" [g $cm^{-3}$] is bubble density; "$\mu_l$" [g $cm^{-1}s^{-1}$] is liquid viscosity and "$Re_b$" is the bubble Reynolds' number [dimensionless].

Equation 29 assumes that bubbles act as solid spheres (Flint and Howarth; 1971). In the previous equation "m", a dimensionless number found as a function of Reynolds' number, takes the form illustrated in either Equation 30 ($1 < Re_b < 200$) or Equation 31 ($200 < Re_b < 500$). Both of these equations are from Richardson and Zaki (1954).

$$m = \left(4.45 + 18\frac{d_b}{d_c}\right)\mathrm{Re}_b^{-0.1} \qquad \text{Equation 30}$$

$$m = 4.45\,\mathrm{Re}_b^{-0.1} \qquad \text{Equation 31}$$

In Equation 30 and Equation 31 "m" is the function of Reynolds' number used in Equation 29, "$d_b$" [cm] is the bubble diameter, "$d_c$" [cm] is the column diameter, and "$Re_b$" [dimensionless] is the bubble Reynolds' number.

The use of two parallel "m" relationships, as used by Finch and Dobby (1990), and whose usage depends upon the Reynolds' number, causes an incongruency when calculations are switched from one function to the other at "$Re_b$"=200. The differences between the two equations are minimal when "$d_c >> d_b$" which is usually the case in industrial-scale columns. Under these circumstances, the 200 – 500 Reynolds' number form can be used throughout. In

a 15 cm diameter column, however, assuming a 0.1 cm bubble, the difference between the two equations will be on the order of 10%. Under these conditions, it may be possible to scale each equation so that no incongruence occurs.

Reynolds' number is an index that characterizes the system turbulence. The general equation defining Reynolds' number is found in Equation 32. This dimensionless number can be described as "a ratio of inertial to viscous forces" (Roberson and Crowe; 1965.)

$$\mathrm{Re} = \frac{VD\rho}{\mu} \qquad \text{Equation 32}$$

In Equation 32,"D" [cm] is the particle (droplet) diameter; "V" [cm $s^{-1}$] is the velocity of that particle; "$\rho$" [g $cm^{-3}$] is the particle-to-liquid density difference and $\mu$ [g $s^{-1}cm^{-1}$] is the liquid viscosity.

Bubbles, in flotation columns, are typically between 0.8 and 2.0 mm. The Reynolds' number for this bubble size range is between approximately 120 and 750. For particles up to 1 mm the Reynolds' number is expected to be between 20 and 650. These numbers should only be used as an approximate guide since they have been generated without regard to three-phase density. There are many variations on the general Reynolds' number equation. Some of these are presented in Table 5.

**Table 5: Reynolds' number general equation functions**

| Author | Symbol | V | D | $\rho$ | $\mu$ | Description |
|---|---|---|---|---|---|---|
| Finch and Dobby 1990 | $Re_p$ | $u_p$ | $d_p$ | $(\rho_p-\rho_{sl})(1-\varepsilon_g)$ | $\mu_{sl}$ | particle |
| Smith and Reuther 1986 | $Re_p$ | $J_g$ | $d_p$ | $\rho_l$ | $\mu_l$ | particle |
| Finch and Dobby 1990 | $Re_b$ | $u_b$ | $d_b$ | $\rho_l-\rho_b$ | $\mu_{sl}$ | 2 phase bubble |
| Finch and Dobby 1990 | $Re_b$ | $u_b$ | $d_b$ | $(\rho_{sl}-\rho_b)(1-\varepsilon_g)$ | $\mu_{sl}$ | 3 phase bubble |
| Smith and Reuther 1986 | $Re_g$ | $J_g$ | $d_c$ | $\rho_l$ | $\mu_l$ | column |

The Reynolds' number of a mechanical-cell is described by Schubert and Bischofberger (1978).

Many functions have been described that relate the terminal bubble rise-velocity of a single bubble ($u_T$ [cm $s^{-1}$]) to that in a "swarm" (Lockett and Kirkpatrick; 1975, Shah et. al.; 1982). One such relationship, by Wallis (1962), is shown as Equation 33.

$$u_b = u_T(1-\varepsilon_g)^{m-1} \qquad \text{Equation 33}$$

In Equation 33, "$u_b$" [cm $s^{-1}$] is the bubble-swarm rise-velocity; "$u_T$" [cm $s^{-1}$] is the bubble rise-velocity and "$\varepsilon_g$" is the gas holdup [dimensionless]. Equation 29 is based on Equation 33 and the bubble rise-velocity of Schiller and Naumann (1933), as shown in Equation 34.

$$u_T = \frac{g d_b^2 \left(\rho_l - \rho_g\right)}{18\mu_l \left(1 + 0.15\,\mathrm{Re}_b^{0.687}\right)} \qquad \text{Equation 34}$$

Equation 34 is a two-phase relationship that does not account for solids. As such, water viscosity ($\mu_l$ [g $cm^{-1}s^{-1}$]) and liquid density ($\rho_l$ [g $cm^{-3}$]) are used along with gas density ($\rho_g$ [g $cm^{-3}$], assumed zero) and the bubble Reynolds' number ($Re_b$). Terminal bubble rise-velocity ($u_T$ [cm $s^{-1}$]) is about twenty-one (21) for bubble sizes between 0.15 and 0.10 cm (Clift et. al.; 1978). This bubble velocity relationship is valid for bubble sizes ($d_b$ [cm]), smaller than 0.20. There are three unknowns in the drift-flux calculation used in flotation vessel models: bubble size ($d_b$ [cm]), gas holdup ($\varepsilon_g$) and rise-velocity ($u_b$ [cm $s^{-1}$]). Three equations that may be used to determine these unknowns are Equation 28, Equation 29 and the Reynolds' number calculated using the method found in Equation 32.

### 2.6.4 Maximum Gas Rate

The maximum gas rate determines, in part, the maximum superficial bubble surface area flux through a flotation column. When Equation 28 and Equation 33 are combined the following "drift-flux relationships" (Xu et. al.; 1991) for maximum gas rate (Equation 35) and liquid velocity (Equation 36) are obtained.

$$J_g = u_T \varepsilon_g \left(1-\varepsilon_g\right)^{m-1} - J_l \frac{\varepsilon_g}{1-\varepsilon_g}$$ Equation 35

$$J_l = u_T \left(1-\varepsilon_g\right)^{m} - J_g \frac{1-\varepsilon_g}{\varepsilon_g}$$ Equation 36

### 2.6.5 Superficial Bubble-Surface-Area Rate

The superficial bubble-surface-area rate is used throughout this research. This is the surface area of bubble that passes through a cross-section of the column, divided by the time interval and the cross-sectional area.

Gorain et. al. (1999) determined that the kinetics of flotation, as represented by the flotation rate constant ($k_f$ [$s^{-1}$]), can be determined by the empirical, superficial bubble-surface-area rate, relationship of Equation 37 where"P" is the mineral floatability and "$R_{S(froth)}$" is a froth recovery factor.

$$k_f = P \vartheta_B R_{S(froth)}$$ Equation 37

Gorain et. al. (1999) assumes that bubble size, thus superficial bubble-surface-area rate ($\vartheta_B$ [$s^{-1}$]), can be determined for mechanical-cells by empirical correlations using peripheral impeller speed ($N_s$ [cm $s^{-1}$]), superficial gas velocity ($J_g$ [cm $s^{-1}$]), impeller aspect ratio (impeller diameter divided by impeller height) and particle size distribution ($d_{80}$ [cm]) or 80% passing size. This relationship is found in Equation 38 where the model parameters "a" through "e" are determined empirically for every flotation system. This system does not account for reagent dosage.

$$\vartheta_B = a N_s^b J_g^c A_s^d d_{80}^e$$ Equation 38

When the bubble size is known the superficial bubble-surface-area rate ($\vartheta_B$ [$s^{-1}$]) is defined by Gorain et. al. (1999) as Equation 39 (also presented as Equation 21).

$$\vartheta_B = 6\frac{J_g}{d_b}$$ Equation 39

In Equation 39, "$J_g$" [cm $s^{-1}$] is the superficial gas velocity and "$d_b$" [cm] is the bubble diameter. Equation 39 is used extensively in this research when modeling flotation with surface areas.

## 2.7 Settling Velocity

### 2.7.1 Introduction

Column flotation occurs in a hindered settling environment. Settling velocity is an important criterion in column flotation since particles are not agitated; thus, increased settling velocity reduces residence times for larger particles. Furthermore, flotation systems are suspensions of typically non-spherical solid particles in water.

### 2.7.2 Settling Velocity of a Sphere in Water

Settling velocity calculations are usually based on the non-linear Navier-Stokes' equations that describe laminar flow past a spherical particle. Reynolds' number (Re) is a key dimensionless number in settling velocity equations (Torobin and Gauvin; 1959 and Slattery; 1972). When "Re" is small (Re <0.5, Roberson and Crowe; 1980), the Navier – Stokes' inertial term can be neglected and therefore results in the linear "Creeping Flow Equation" (Happel and Brenner; 1964) or "Stokes' flow". At high Reynolds' numbers (Re>1000), the viscous forces can be neglected and the Navier – Stokes' equation is reduced to Euler's equation. Within flow of intermediate Reynolds' number, both the viscous and inertial components of the Navier-Stokes' relationship have an effect on the settling velocity.

### 2.7.3 Settling Velocity of Spheres in Suspensions

The slurry in which the particles are settling may vary greatly in solids content. Often the volume of solids exceeds that required to specifically use the solids settling in water relationships. Shah et. al. (1982), Muroyama and Fan (1985), Masliyah (1979) and Concha and Almendra (1979a,b) have investigated a wide variety of these variables.

For settling in a slurry Zuber (1964), Happel and Brenner (1964), Barnea and Mizahi (1973) and Concha and Almendra (1979a,b) espouse a system where the same equations are used for water settling but the suspension properties are used rather than those of the water. When determining the settling velocity of spherical particles in a mono-dispersed system at low

Reynolds' numbers, Masliyah's (1979) relationship shown in Equation 40 can be used. When the liquid fraction approaches unity Equation 40 becomes Stokes' equation.

$$u_p = \frac{g d_p^2 \left(\rho_p - \rho_l\right)}{18 \mu_l} \varepsilon_l f\left(\varepsilon_l\right) \qquad \text{Equation 40}$$

Where $f(\varepsilon_l)$ is determined by Equation 40.

**Equation 40 – Symbol definitions**

| Symbol | Description | Source | |
|---|---|---|---|
| $f(\varepsilon_l)$ | Liquid Fraction | $\varepsilon_l^{2.7}$ -Richardson and Zaki (1954) | $\left[1+\left(1-\varepsilon_l\right)^{\frac{1}{3}} e^{\frac{5(1-\varepsilon_l)}{3\varepsilon_l}}\right]^{-1}$ Barnea and Mizrachi (1973) |

In Equation 40 "g" [cm $s^{-2}$] is the acceleration due to gravity; "$d_p$" [cm] is the particle diameter; "$\rho_p$" [g $cm^{-3}$] is the particle density; "$\rho_l$" [g $cm^{-3}$] is the liquid density; "$\varepsilon_l$" is the fractional liquid hold-up and "$\mu_l$" [g $cm^{-1}$ $s^{-1}$] is the liquid viscosity.

Masliyah (1979) uses the method of Wallis (1969) (momentum and drag forces) to estimate and predict particle hindered settling velocities (Equation 41). The Reynolds' number term of this equation may be neglected at very low Reynolds' number values. Otherwise, the Reynolds' number relationship shown in Equation 42 can be used.

$$u_p = \frac{g d_p^2 f\left(\varepsilon_l\right)\left(\rho_p - \rho_l\right)\left(1-\varepsilon_g\right)}{18 \mu_l \left(1+0.15 \mathrm{Re}_p^{0.687}\right)} \qquad \text{Equation 41}$$

$$\mathrm{Re}_p = \frac{d_p u_p \varepsilon_l \left(\rho_p - \rho_{sl}\right)}{\mu_{sl}} \qquad \text{Equation 42}$$

In Equation 41 and Equation 42, "$d_b$" [cm] is the bubble diameter; "g" [cm $s^{-2}$] is the gravitational acceleration; "$Re_p$" is the particle Reynolds' number; "$u_p$" [cm $s^{-1}$] is the particle settling-velocity; "$\mu_l$" [g $cm^{-1}s^{-1}$] is the fluid viscosity; "$\mu_{sl}$" [g $cm^{-1}s^{-1}$] is the slurry viscosity; "$\varepsilon_l$" is the volumetric, two-phase, fraction of water; "$\rho_p$" [g $cm^{-3}$] is the particle density; "$\rho_l$"[g $cm^{-3}$] is the liquid or water density; "$\rho_{sl}$" [g $cm^3$] is the effective slurry density and "$\varepsilon_g$" is the fractional gas-holdup.

The hindered settling-velocity of Smith et. al. (1985) is a function of slurry liquid and gas fractions (Equation 43).

$$u_p = 1.44 u_T^{0.78} J_g^{0.25} \varepsilon_l^{3.5} \qquad \text{Equation 43}$$

In Equation 43, "$u_p$" [cm $s^{-1}$] is the hindered settling-velocity of a spherical particle; "$u_t$" [cm $s^{-1}$] is the particle settling-velocity; "$J_g$" [cm $s^{-1}$] is the superficial gas velocity and "$\varepsilon_l$" is the volumetric two-phase liquid fraction.

### 2.7.4 Non-Spherical Particle Velocity

The solids suspended in flotation applications are typically not spherical. As such, the non-spherical nature must be incorporated into the flotation model in order to limit residence time error. Concha and Barrientos (1986) (who have in turn used work by Christiansen and Barker (1965), Pettyjohn and Christiansen (1948), Swanson (1967), Swanson (1978), Wadell (1932) and Wadell (1934)), use Equation 44 to model non-spherical settling-velocity. This equation is acceptable for Reynolds' numbers under 100 and the equation becomes more accurate as the Reynolds' number approaches zero.

$$u_n = \frac{u_s}{f_A f_B f_C f_D^2} \qquad \text{Equation 44}$$

Equation 44 - Symbol Definitions

| Symbol | Units | Description | Source |
|---|---|---|---|
| $\lambda$ | | Dimensionless Density | $\rho_p\rho_{sl}^{-1}$ |
| $\rho_p$ | g $cm^{-3}$ | Particle Density | |
| $\rho_{sl}$ | g $cm^{-3}$ | Slurry Density | |
| a | | Constant | 5.42 |
| b | | Constant | 4.75 |
| $f_a$ | | Sphericity Function "A" | $(a-b\psi)(a-b)^{-1}$ |
| $f_b$ | | Sphericity Function "B" | $0.843f_A\log(15.385\psi)$ |
| $\psi$ | | Sphericity | |
| $f_c$ | | Sphericity Function "C" | $\lambda^m$ |
| $f_d$ | | Sphericity Function "D" | $\lambda^{-(m/2)}$ |
| m | | Constant | -0.0145 |
| $u_n$ | cm $s^{-1}$ | Non-spherical settling-velocity | |
| $u_s$ | cm $s^{-1}$ | Spherical hindered particle settling-velocity | |

Particle sphericity ($1 \geq \psi \geq 0$) is defined as the ratio of minor to major axis or, as the surface-area of spherical particle to actual particle-surface-area when both the sphere and particle have the same volume. The symbol "$u_s$" [cm $s^{-1}$] is spherical particle settling-velocity and "$u_n$" [cm $s^{-1}$] is the equivalent non-spherical velocity. The effective diameter is the diameter of a sphere that gives the same volume as the non-spherical particle.

## 2.8 Mixing

### 2.8.1 Introduction

An important criterion for determining flotation vessel performance is the residence time of particle populations. However, when mixing occurs in the vessel there will be a distribution of residence times. One extreme of mixing is "plug flow" wherein all particles of the same settling velocity have the same residence time. The opposite extreme is "perfect mixing" wherein all particles have the same residence times. Mixing relationships compensate for variations in residence time when conditions within the vessel lie between these end-points.

Most mixing models have been developed for reactors with one input and one output. A flotation column, in terms of solids flow, has one input and two outputs; thus, the models used may be expected to suffer from increased error. The three-phase slurry nature (solid, liquid, and gas) also introduces error. Flotation models may predict performance but they cannot be used to generate definitive numbers.

Non-ideal flow can be caused by channeling, recirculation, or stagnant zones within the vessel. Laboratory-scale columns act essentially as "plug-flow" units. As the vessel diameter increases, more mixing occurs so that large industrial-scale columns may perform somewhat like a stirred tank, albeit not a perfect mixer. The performance of these columns, in terms of short-circuiting and residence-times, falls between these two conditions.

Three mixing models have been used to scale-up flotation columns from laboratory-, or pilot-scale to industrial-scale. These include the axial dispersion model (Levenspiel; 1972 and Dobby; 1984) which has been thoroughly tested on columns, the tanks-in-series model (Goodall and O'Connor; 1991a,b), and the sedimentation-convection model (Ityokumbul; 1992).

## 2.8.2 Tanks-in-Series

Mills and O'Connor (1990) use the tanks-in-series model. It has not, however, seen general use. The model assumes that all mixing conditions between "plug-flow" and the "CSTR" can be modeled by a number of CSTR's in series. For practical purposes, plug flow exists when more than 10 CSTR's in series are used, and very little change occurs from six (6) to ten (10) reactors. Laplante et. al. (1988) argues that the added flexibility of the tank-in-series model is unnecessary since the axial distribution calculations provide a good fit to the data.

## 2.8.3 Axial Dispersion Model

### 2.8.3.1 Introduction

The most common method of accounting for mixing with a flotation column is the axial dispersion model. This is a one-dimensional model that assumes uniform radial-dispersion and velocity profiles. According to Levenspiel and Fitzgerald (1983) the axial dispersion model describes a "diffusion like process... superimposed on plug flow", which gives a Gaussian-shaped residence-time distribution (RTD) curve. Levenspiel and Fitzgerald (1983) also states that a Gaussian-convective model should be used when some elements always move either more slowly or quickly than others. The dispersion model is used when all elements move essentially at the same rate. Also, the axial dispersion model should only be used when modeling small deviations from plug flow.

According to Bischoff and Levenspiel (1962a,b) errors increase in the axial dispersion model predictions as the vessel dispersion number increases beyond 0.2. O'Connor (1991) has shown that this error may not be significant in the case of low aspect ratio columns where the dispersion number is often greater than 0.3. In addition, when considering all phases, columns are three input – two output vessels, not the single input output devices for which the axial mixing equations were developed.

Despite Levenspiel's warning, the most common model used for column flotation is the axial dispersion model (Dobby; 1984). Mavros et. al. (1989) and Goodall and O'Connor (1991a,b)

have criticized this model for being non-realistic in larger columns. The models based on axial dispersion, however, do perform well.

### 2.8.3.2 Peclet Number and Residence-time Distribution

The basic differential equation for a column residence-time distribution (RTD) is based on Equation 45 (Ostergaard and Michelsen; 1969). The Peclet number (Pe) is the only parameter in the model subject to geometrical and operating parameters. A probability term must also be incorporated (rate constants), in order to predict recoveries. When "Pe" is infinite, there is negligible dispersion and the vessel flow is "plug-flow". On the opposite extreme, a zero "Pe" indicates a large dispersion and perfect mixing conditions.

$$\frac{\partial E}{\partial \theta} = \frac{1}{Pe}\frac{\partial^2 E}{\partial Z^2} - \frac{\partial E}{\partial Z} \qquad \text{Equation 45}$$

In Equation 45, "E" is the normalized concentration; "Pe" is the Peclet number; "Z" is the normalized axial distance and "θ" is normalized time.

### 2.8.3.3 Boundary Conditions

The solution to the differential equation (Equation 45) depends on the boundary conditions set. Given the nature of the flotation process, however, error introduced by using inappropriate boundary conditions may not be significant (Mavros 1993a,b) when compared to other variables. Two boundary conditions are generally used: "open–open" or "closed–closed", although it is possible to have "open–closed" or "closed–open". "Open" means that fluid may cross the boundary more than once and "closed" means that fluid may only cross once.

Injection of tracer into the feed can be considered "closed". However, tracer under positive bias conditions is recycled through the froth zone resulting in an "open" system if the pulp-froth interface is defined as the control volume boundary. Tracer detection usually occurs at the column underflow and overflow. Flow in the underflow is quite rapid in comparison to the column interior, thus, it may be considered a "closed" system. Flow in the overflow is over a weir, and cannot return to the column, thus, is also a "closed" boundary. Therefore, if the column, as a whole, is defined as the control volume the "closed-closed" solution applies. If

only the column collection-zone is used, however, it can be argued that an "open-closed" solution is necessary. Ityokumbul (1988) has correlated the Peclet Number (Pe < 2) from closed and open solutions. Levenspiel (1972) presents solutions for both the "open-open" and "closed-closed" boundary conditions of Equation 45.

The Peclet number can be determined using moment matching (Finch and Dobby; 1990, Leverspiel; 1972), or a direct search, least squares method as used by Ityokumbul et. al. (1988). Both Ityokumbul et. al. (1988) and Finch and Dobby (1990) state that the "closed-closed" solution better suites the conditions found in most column flotation RTD studies. Other forms of the "closed-closed" solution are found in Shinju Nagata (1975), Froment and Bischoff (1979), Ityokumbul et. al. (1988), and Abouzeid (1989)

### 2.8.3.4 Estimation of Peclet Number using Column Variables

The Peclet number can be estimated through empirical models such as Levenspiel's (1972) relationship found in Equation 46.

$$Pe = \frac{uh}{Di} \qquad \text{Equation 46}$$

In Equation 46, "u" [cm $s^{-1}$] is characteristic velocity, usually liquid flow; "h" [cm] is vessel or characteristic length, and "Di" [$cm^2$ $s^{-1}$] is the dispersion number. An alternative Peclet number approximation based on dispersion numbers is given by Smith et. al. (1986).

Column performance is not highly sensitive to the exact "Pe" value because the Peclet number values in full-scale columns tend to be less than four (4). Indeed, Luttrell et. al. (1988) suggested that the value of four (4) be used in all full-scale applications and Newall et. al. (1989) and Espinosa-Gomez et. al. (1989) have suggested that perfect mixing be used.

Recent work by Mankosa et. al. (1992) expands Levenspiel's (1972) relationship specifically for flotation columns. This group performed a dimensional analysis to quantify axial mixing variables including geometry, flows (Mavros 1993a,b), and holdups. Mankosa et. al. (1992) found that the variables with the most effect on the Peclet number are column diameter and

superficial liquid flows. They postulate that the Peclet number can be described by Equation 47. The form of this equation is supported by analysis of currently available data obtained by Mavros (1993a,b).

$$Pe = f\left[\left(\frac{d_c}{h_{(z)}}\right),\left(\frac{J_g}{J_l}\right),\left(\varepsilon_g\right)\right] \qquad \text{Equation 47}$$

In Equation 47, "$d_c$" [cm] is the column diameter; "$h_{(z)}$" [cm] is the zone height; "$J_g$" [cm $s^{-1}$] is the superficial gas velocity; "$J_l$" [cm $s^{-1}$] is the superficial liquid velocity and "$\varepsilon_g$" is the fractional gas-holdup. The later three terms are averages within the zone.

Mankosa et. al. (1992), Mavros and Daniilidou (1993) and Xu and Finch (1991a,b) have determined equations for the Peclet number based on function presented in Equation 47.

Mavros and Daniilidou (1993) present extensive RTD data that indicates that gas velocity affects mixing within flotation columns. Their work builds on that of Ohki and Inoue (1970). Subramanian and Tien (1975) found that the amount of mixing was affected by the bubble-forming device, gas velocity and bubble size. The relationship in Equation 48 may be used when all other factors are held constant.

$$Di = 2.048 + 2039J_g \qquad \text{Equation 48}$$

Reith et. al. (1968) concluded that the major cause of column dispersion is bubble movement. For example, Ohki and Inoue (1970) found that dispersion was proportional to $J_g^{1.2}$.

Column diameter has long been known to effect mixing in vessels as illustrated by the work of Argo and Cova (1965). Deckwer et. al. (1974) experimented with different diameter columns to define the effect of diameter on mixing. Shah, Stiegel and Sharma (1978) conclude that "Di" is a function of column diameter and is essentially independent of other properties such

as viscosity, velocity, density and surface tension. This function is illustrated in Equation 49 below.

$$Di = bd_x^{a_1} J_g^{a_2} \qquad \text{Equation 49}$$

**Table 6: Symbol Definitions for Equation 49 and Equation 50**

| Symbol | Units | Description | Source |
|---|---|---|---|
| $d_x$ | cm | Column Diameter | Shah et. al. (1982) |
| | | Column Diameter | Magnussen and Shumacher (1978) |
| | | Bubble Diameter | Rice and Littlefield (1987) |
| b | | 1 | Shah et. al. (1982) |
| | | 1 | Magnussen and Shumacher (1978) |
| | | $0.35g^{(1/3)}$ | Rice and Littlefield (1987) |
| $a_1$ | | $1.0 \rightarrow 1.5$ | Shah et. al. (1982) |
| | | 1.0 | Magnussen and Shumacher's (1978) |
| | | 1.333 | Rice and Littlefield (1987) |
| $a_2$ | | $0.3 \rightarrow 2.0$ | Shah et. al. (1982) |
| | | 0.23 | Magnussen and Shumacher's (1978) |
| | | .333 | Rice and Littlefield (1987) |

Magnussen and Shumacher's (1978) experiments used columns between four (4) and 100 cm in diameter with air rates between one (1) and ten (10) [cm $s^{-1}$] in a countercurrent flow mode (Dobby and Finch; 1985a,b). Dobby (1984) took previous data and approximated the effect of diameter on the dispersion coefficient (Di [$cm^2$ $s^{-1}$]) (shown in Equation 50).

$$Di = ad_c \qquad \text{Equation 50}$$

In Equation 50, "$d_c$" [cm] is the equivalent column diameter in meters and "a" [cm $s^{-1}$] is a proportionality constant set at 0.063. Akita and Yoshida (1973) determined that square

columns could be considered to have a diameter that gives the same column cross-sectional area.

Mixing in a column depends on the vertical alignment. Tinge and Drinkenburg (1986) showed that mixing may increase by an order of magnitude with small deviations from vertical. Their correlation is shown in Equation 51 where "Dα" is the misaligned dispersion coefficient.

$$D\alpha = Di\left(1 + C_{\alpha} d_c \alpha\right)^2 \qquad \text{Equation 51}$$

In Equation 51, "Di" [$cm^2\ s^{-1}$] is the dispersion number; "$C_\alpha$" is a constant valued equal to approximately 1100 [$cm^{-1}$]; "$d_c$" [cm] is the column diameter and $\alpha$ is the non-vertical displacement in radians. Xu (1987) concludes that the affect of non-vertical alignment is usually minimal.

## 2.8.4 Solids Distribution

### 2.8.4.1 Introduction

Solids distribution varies depending on the bubble flow-regime: "bubbly" or "churn-turbulent". Within these regimes the effect of gas velocity on solids distribution is minimal (Murray and Fan; 1989). Other variables such as liquid density, viscosity, and surface tension effect solids-distribution. Axial solids-distribution may result from entrainment and "de-entrainment" of solids in bubble wakes. Murray and Fan (1989) suggest that a bubble and its' wake rise at the same rate. Wake shedding disengagement is believed to be the "de-entrainment" mechanism.

Both the axial dispersion and sedimentation dispersion models can be used by continuous-column models to characterize mixing. The latter is espoused by authors such as Cova (1966), Suganuma and Yamanishi (1966), Imafuku et. al. (1968), Farkas and Lablond (1969), Kato et. al. (1972), Kojima et. al. (1984), Smith et. al. (1986), and Smith (1985). The sedimentation-dispersion model uses two parameters: axial solids-dispersion and solid settling-velocity.

Most continuous column models use the axial-dispersion model. This model considers that three distinct phases are important: gas or bubbles, bubble wakes, and suspended particulates. Dobby and Finch (1985a,b), and others such as Rice et. al. (1974), Kho and Sohn (1989), Yianatos and Bergh (1991), Clingan and McGregor (1987), Finch and Dobby (1990) and Adel et. al. (1991) have used the axial-dispersion model to predict solids dispersion. This model has been questioned by authors such as Ityokumbul (1992), Mavros et. al. (1989), Mills and O'Connor (1990) and Goodall and O'Connor (1991a,b). The McGill University research team, Xu and Finch (1991a) and Xu and Finch (1991b), have shown that careful attention to boundary conditions and the use of a good least-squares fit allows adequate modeling of the RTD over many mixing conditions when using the axial-dispersion model. Kho and Sohn (1989) state that the solids and liquid dispersion coefficients are approximately equal when the solids particles are smaller than 150 μm.

### 2.8.4.2 Axial Solids Dispersion Model

The equivalent solids Peclet number ($Pe_p$) to Levenspiel's (1972) liquid number is presented in Equation 52 (Xu and Finch; 1992)

$$Pe_p = \frac{(J_l + u_p)h_{(z)}}{Di} \qquad \text{Equation 52}$$

In Equation 52, "$J_l$" [cm $s^{-1}$] is the superficial liquid velocity; "$u_p$" [cm $s^{-1}$] is the particle settling-velocity; "$h_{(z)}$" is the zone height and "Di" is the dispersion number.

Particle settling-velocity is greater than zero ($u_p > 0$), thus, in the previous equation the particle Peclet number is greater than the liquid Peclet number ($Pe_p > Pe$) as stated by Ityokumbul (1992). To determine the exact values of $Pe_p$ the solids settling characteristics must be known.

Yianatos et. al. (1986a) states that the Masliyah (1979) settling velocity equation is valid as long as the solids concentration in the bubble wake is equal to that in the downward flowing liquid. Xu and Finch (1992) assume this state when particles are less than 150 μm in diameter. This upper size limit assumes a mineral density that is not stated. A more complex solution to "$u_p$" is needed when modeling particles greater than this size. Xu and Finch (1992) avoid "$u_p$" [cm $s^{-1}$] by using the ratio of particle to liquid residence-times, as shown in the Equation 53.

$$\frac{\tau_p}{\tau_l} = \frac{J_l}{J_l + u_p} \qquad \text{Equation 53}$$

Both the particle residence-time ($\tau_p$ [s]) and the liquid residence-time ($\tau_l$ [s]) can be determined from residence-time distribution tests using liquid or solid tracers. When the particles are infinitely small, the particle and liquid residence-times will be equal and the "Pe" ratio will be unity. Increasing the particle size increases "$Pe_p$" and thus decreases the "Pe" ratio (Yianatos and Bergh; 1991 and Xu and Finch; 1992). Xu and Finch (1992) also found that dispersion increases with particle size as shown in Table 7.

**Table 7: Solids dispersion data from various sources.**

| Material | Average Particle Size | Mean Residence (min). | Peclet Number | Particle Slip Velocity | Axial Dispersion |
|---|---|---|---|---|---|
| Set I Y&B | | | | | |
| Liquid | | 20.1 | 0.82 | | 1.37 |
| -38 um | 19 | 19.87 | 0.82 | 0.04 | 1.23 |
| -75 + 38 μm | 56.5 | 16.49 | 0.81 | 0.31 | 1.58 |
| -150 + 75 | 112.5 | 10.70 | 1.08 | 0.87 | 1.71 |
| Set II Y&B | | | | | |
| Liquid | | 15.45 | 1.02 | | 1.05 |
| -38 um | 19 | 14.09 | 1.25 | 0.04 | 0.81 |
| -75 + 38 μm | 56.5 | 12.57 | 1.16 | 0.31 | 1.10 |
| -150 + 75 | 112.5 | 8.54 | 1.67 | 0.87 | 1.10 |
| total solids | | 12.06 | 1.18 | | |
| X&F | | | | | |
| Liquid | | 11.66 | 3.13 | | 0.40 |
| -38 um | 19 | 8.45 | 3.85 | 0.08 | 0.34 |
| -53 + 38 μm | 45.5 | 8.23 | 3.57 | 0.38 | 0.45 |
| -75 + 53 μm | 64 | 7.88 | 3.85 | 0.65 | 0.49 |
| -106 +75 | 90.5 | 6.67 | 4.45 | 1.07 | 0.50 |
| -150 + 106 | 128 | 5.79 | 5.56 | 1.65 | 0.51 |
| Total solids | | 6.85 | 4.17 | | |

Y&B refers to Yianatos and Bergh (1991) and X&F refers to Xu and Finch (1992).

## 2.8.5 Conclusions

This research uses the axial dispersion model to account for vessel mixing. The method was chosen because it is currently the most widely used method in existing flotation column models and because it has been proven to give accurate predictions of performance. The best method of calculating the Peclet number has not been assessed since validity of the data used as a basis of comparison is unknown. However, this research uses the work of Xu and Finch (1992) to determine the solids Peclet number based on Equation 50 without incorporating any adjustments for misalignment. Other methods could also have been used.

## 2.9 Macro-Phenomenological Kinetics

### 2.9.1 Introduction

Flotation rate constant or kinetic models use "macro-phenomenological kinetics". This concept dates back to Garsia-Zuniga (1935) and Schuhmann (1942) who noted that the "specific flotation rate has the same dimensional significance as the specific reaction rate for a first-order chemical reaction". Flotation kinetics refers to the rate at which the flotation process occurs and is a function of system chemistry, such as collector absorption and electrochemistry (Woods; 1976, Woods; 1984 and Chander; 1985), and on the physics of collection (Schulze; 1984). The flotation rate constant ($k_f$ [$s^{-1}$]) is the speed of substance flotation and has been regarded as analogous to chemical reaction rate constants. Jameson et. al. (1977) and Ityokumbul (1992) have drawn attention to the fact that flotation is actually more closely related to interface mass or heat transfer than to chemical kinetics.

The present knowledge of flotation means that "global" kinetic systems are usually used. These systems are empirical models that have been used extensively to size and predict the behavior of flotation machines. Villeneuve et. al. (1995) has called these empirical models the kinetic macro-phenomenological approach to flotation modeling. The rate constant determined by one model can be significantly different from those obtained by other models. Thus, rate constants determined using one model may not be suitable for use with other models.

"Macro-phenomenological" models group both physical and chemical sub-processes into one parameter -- the kinetic rate constant ($k_f$ [$s^{-1}$]). This parameter gives the speed at which the separation progresses only within the given conditions; it does not give information on the effect of any subsystem variability that was not specifically tested.

## 2.9.2 Reaction Order

Flotation is a time, rate-recovery process -- the cumulative recovery of a component mineral depends on the flotation time when operated under non-loaded or "free" floating conditions. Thus, both recovery and rate functions are required to describe the flotation time-recovery profile. Flotation models (Dowling et. al.; 1986) describe recovery as an exponential function of time. Gaudin (1957) suggests that first-order rate-constants describe flotation when gas rate, agitation, and reagents are constant. Under these conditions, the number of bubbles will be approximately constant. Equation 54 may be used to represent this relationship (Szatkowski; 1987):

$$dC_p = kC_bC_p^a dt \qquad \text{Equation 54}$$

In Equation 54 the bubble concentration ($C_b$) may be variable but is usually assumed constant (Arbiter and Harris; 1976). Also in Equation 54 "$C_p$" is the particle concentration. The type of concentration [either "$C_b$" or "$C_p$"] is not specified, although it may be by number, volume, mass, bubble-surface-area or particle-surface-area. The order of "a" is assumed to be unity.

Nguyen et. al. (1998) has proven, from a mechanistic approach, that the rate equation is first-order. The second-order models, as reviewed by Dowling et. al., (1986) and Yuan et. al. (1996), are not usually needed to model flotation in mineral processing applications; higher order empirical models, however, do exist. These higher order models generally follow the form of Equation 54 but use an order; "a", greater than unity. The order has been found to be two, which suggests both bubble and particle effects, by many researchers including Arbiter (1951), Horst (1958) and Hukki (1953). Fichera and Chudacek (1992) state that these models are purely empirical, having no mechanistic basis, and generally have been rejected in favor of first-order models.

### 2.9.3 Non-Floating Particles

A recovery model can only predict the recovery of those mineral particles that are floatable. Identical particles of one mineral, however, may vary in hydrophobicity with a population being un-floatable. This distribution of floatability may be attributed to oxidation (Morris; 1952), insufficient collector adsorption (Bushell; 1962), or other effects. Bushell (1962) accounts for non-floating particles by subtracting the final underflow concentration ($C_{(U)}$) from the feed initial concentration ($C_{(F)}$). The total floatable components recovery is usually incorporated into the kinetics equation using a maximum recovery term. The maximum recovery ($R_\infty$) is found by dividing material floated over a long residence-time ($C_{(O)}$), by the material in the feed ($C_{(F)}$). This method does, however, have significant problems since re-floating of material often results in an additional non-floating portion within a population that has previously floated. As such, there have been suggestions by Szatkowski (1987) and Jowett and Safvi (1960) that the effect may be due to pulp density changes, changes in the flotation chemistry, or due to initial entrainment of the non-floatable population.

## 2.9.4 Flotation Phases

### 2.9.4.1 Introduction

The usual description of flotation, as described in the recovery equations normally used within the industry, give a response curve similar to line (a) of Figure 8 from Szatkowski (1987). Curve (b) on this figure represents a common flotation response. Szatkowski (1987) has divided the flotation response into three phases: hindered flotation, free flotation (Tomlinson and Flemming; 1963), and what is termed here as depleted flotation. These stages are represented in Figure 8 as "A", "B" and "C" respectively.

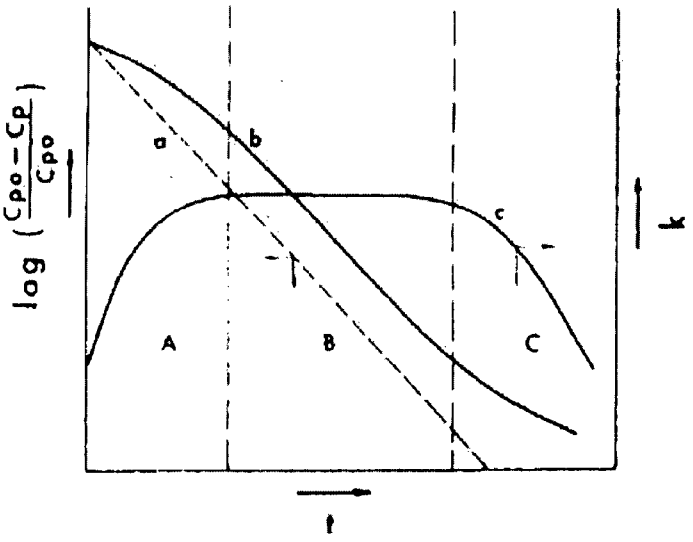


**Figure 8: Phases of flotation from Szatkowski 1987**

### 2.9.4.2 Hindered Flotation

Hindered flotation (Tomlinson and Fleming; 1965) generally occurs at the beginning of a batch flotation test -- especially when there is a high overflow recovery. This type of flotation is characterized by a sub-optimal flotation rate, as predicted by kinetic models, and by limitations in the bubble-surface-area available for collection (Szatkowski; 1987). When there is limited bubble-surface-area available for flotation, the flotation rate will be proportional to

the bubble-surface-area flux and independent of particle concentration. This type of flotation is said to be carrying capacity limited.

When small bubbles are generated within the flotation vessel, it is possible to load these bubbles so that they fall rather than rise. This phenomenon restricts recovery. The bubble size at which this restriction occurs can be estimated by determining loaded bubble densities (Szatkowski and Freyberger; 1985b).

#### 2.9.4.3 Free Flotation

Free flotation characterizes the kinetics of most flotation tests. In this type of flotation the probability of collision and attachment between particle and bubble govern the kinetics of separation. Most kinetic models describe this type of flotation.

#### 2.9.4.4 Depleted Flotation

Flotation of particles at low concentrations after a significant residence-time in a batch, laboratory-scale unit, may express much slower kinetics than earlier flotation. This slow kinetic response may be caused by many factors including the distribution of particles sizes, surface coverage by collectors (Imaizumi and Inoune; 1965, Bushell; 1962), or liberation. In effect, the faster floating material is removed during the initial flotation phases. The kinetics may also be hindered by the collapse of poorly mineralized bubbles within the froth zone (Mori et. al.; 1986).

### 2.9.5 **Model Stages**

The kinetic rate constant parameter's value depends on the flotation model form. In mechanical-cells, the model of origin may be either single or double stage. Single stage models describe the entire flotation cell using a single empirical equation. In double phase models the pulp and froth phases are considered separately.

## 2.9.6 Recovery Models

### 2.9.6.1 Introduction

Recovery models are intended for use in either single stage, or pulp stage models under free - floating conditions, for either batch- or continuous operation. All the models described here are empirical. Under "hindered" conditions flotation is zero order; this condition is dealt with in these models by carrying capacity limitations. Otherwise, these relationships assume that there is excess bubble-surface-area; that the flotation is "free" or "unhindered" and therefore first-order. The recovery form of the kinetics equation generally takes the form of Equation 55 where the recovery is a function of rate constant ($k_f$ [$s^{-1}$]), residence-time ($t_p$ [s]) and vessel mixing ($Pe_p$ [dimensionless]).

$$R = R_\infty f\left(k_f, t_p, Pe_p\right) \qquad \text{Equation 55}$$

### 2.9.6.2 Rate Constants

Gaudin (1957) states that the rate of flotation is expected to remain constant throughout a test if all particles are homogeneous in terms of size, shape, and surface characteristics. Since these factors may not be constant, the rate of flotation may deviate from first-order when these factors are not considered.

Kelsall (1961) hypothesized that particles could be characterized as either fast or slow floating. The asymptote (slow float) is subtracted from the time-recovery curve to obtain a curve of greater slope (fast float). Many researchers, such as Bushell (1962) and Villeneuve et. al. (1995) have used a model of flotation recovery which incorporates slow and fast floating components. An example of this model, expressed in terms of recovery, is found in Equation 56 (Dowling et. al.; 1986). Arbiter and Harris (1976), Lynch et. al. (1981) and Yalcin (1992) have used forms of this recovery equation.

$$R = \left(R_\infty - \phi\right) f\left(k_{s,f}, t_p, Pe_p\right) + \phi f\left(k_{f,f}, t_p, Pe_p\right) \qquad \text{Equation 56}$$

In Equation 56, "$\phi$" is the fraction of fast floating material; "*f*" is a function; "$k_{f,s}$" [$s^{-1}$] is the slow floating rate constant and "$k_{f,f}$" [$s^{-1}$] is the fast floating rate constant. Some authors have described a continuous distribution of flotation rates. However, Sutherland (1948) concludes that it is more practical to use discrete rates due to difficulties in finding an appropriate continuous function.

A single distributed system, or floatability model, uses one function to describe a particular mineral species. This one function considers particle size distribution together with particle shape, surface properties and other characteristics that effect flotation rates. This approach was taken by Imaizumi et. al. (1965) and shown to be effective by Woodburn et. al. (1965) in the analysis of either batch- or continuous flotation. This approach is also espoused by others such as Huber-Panu et. al. (1976) who used both floatability and size distribution, and others such as Kapur and Mehrotra (1973), Kelsall (1961), Lynch et. al. (1974) and Klimpel et. al. (1979).

Mica and Fuerstenau (1968) and King (1974) have used multidimensional distribution functions. Huber-Panu et. al. (1976) reviews a number of double distributed parameter models. These models determine independent functions by mineral and size-class.

#### 2.9.6.3 Residence-time

The residence-time used to determine recovery is dependent on the mode of operation. In batch flotation, the residence-time is approximately the test elapsed time. When the recovery model is single stage; that is the entire cell is treated as a unit, there is often a delay in the onset of flotation after test initiation test as the froth zone becomes mineralized. A time delay term can be subtracted from the residence-time to model this behavior. In continuous operation, the residence-time is the average retention time of a particle in the flotation environment.

### 2.9.6.4 Mixing Kinetics

The mixing characteristics within a flotation vessel are critical in predicting recovery. The two extremes of mixing are plug flow and perfect mixing. Both of these conditions, as well as intermediate mixing, have been used to describe flotation conditions. In addition, other empirical formulas have been used.

Plug flow is the condition wherein a slug of fluid passes through the vessel without mixing: (Pe = ∞); in this type of flow the reactant composition, or the solids particles concentration, is dependent on position. Material passes unmixed through the vessel meaning that all material present at any specified point will have had the same residence-time. A bench-scale, batch, mechanical-cell or a "plug-flow" continuous cell can be modeled by the recovery given in Equation 57.

$$f\left(k_f, t_p, Pe_p\right) = 1 - e^{-k_f t_p} \qquad \text{Equation 57}$$

Yuan et. al. (1996) calls this model the "classical first-order model"; it originates with the work of Garsia-Zuniga (1935), Sutherland (1948) and others.

A fully mixed system, described as a "continuously stirred tank reactor" (CSTR), is a vessel wherein the concentration of particles is independent of position (Pe = 0). In effect, feed added to the vessel is immediately distributed throughout the vessel. This model has been applied to flotation recovery by Yuan et. al. (1996), Dowling et. al. (1986), Finch and Dobby (1990) and others and is described by Equation 58.

$$f\left(k_f, t_p, Pe_p\right) = 1 - \frac{1}{\left(1 + k_f t_p\right)} = \frac{k_f t_p}{1 + k_f t_p} \qquad \text{Equation 58}$$

The continuous mechanical-cell, with the exception of some stratification of particle size with depth, is almost a perfectly mixed vessel where the underflow is considered to have the same composition as the contents of the cell itself. In contrast, mixing in other continuous vessels

can vary from "plug flow" to perfectly mixed. Columns, depending on their diameter, height, air rates and air distribution, fall between these two extremes. The Wehner and Wilhelm (1956) solution to the residence-time differential equation (Equation 45), valid under any entrance and exit conditions, is presented again here as Equation 59.

$$f\left(k_f, t_p, Pe_p\right) = 1 - \frac{4a_{Pe}e^{\frac{Pe}{2}}}{\left(1+a_{Pe}\right)^2 e^{\frac{a_{Pe}Pe}{2}} - \left(1-a_{Pe}\right)^2 e^{\frac{-a_{Pe}Pe}{2}}} \qquad \text{Equation 59}$$

In Equation 59 "$a_{Pe}$" is a function of rate constant ($k_f$ [$s^{-1}$]), residence-time ($t_p$ [s]) and Peclet number (Pe) as shown in Equation 60.

$$a_{Pe}^2 = 1 + \frac{4k_f t_p}{Pe_p} \qquad \text{Equation 60}$$

Under plug flow conditions, Equation 59 simplifies to Equation 57, while under perfectly mixed conditions it simplifies to Equation 58.

Many other kinetic models exist. Dowling (1986) compares thirteen models. This selection includes some of those presented earlier and some second order models. All models compared by Dowling (1986) give a good fit with the experimental data; however, large differences were found in model confidence limits.

## 2.9.7 Determination of Macro-Phenomenological Rates

### 2.9.7.1 Introduction

Traditionally, laboratory-scale, mechanical flotation devices have been used to generate kinetic data. Column rates have been estimated using batch, bench-scale mechanical-cell, or continuous pilot-scale column tests. In each case, test results are then used in a model to determine the appropriate rate constants.

### 2.9.7.2 Mechanical-Cell Rate Determination

There are two tests generally used to determine the flotation rates of mechanical-cells. The first (1) takes a single cumulative overflow sample at a long residence-time, a feed sample and remainder sample. The test is run over a period of time long enough to float most of the material. The plug flow recovery relationship (Equation 57) is then used to determine the rate for that particular time-recovery point. Maximum recovery and entrainment are neglected or assumed. This type of test can lead to large errors but can be used successfully when quick approximations of rates are required.

The second (2) type of test generates a time-recovery plot and is known as a "time-recovery" or "release" test. In this test, a number of timed overflow samples are taken and a cumulative recovery is plotted with time. A time-recovery relationship is generated that allows a more accurate maximum recovery determination, delays in flotation, and other such errors. Entrainment may also be estimated if water recovery is recorded. Again, the plug flow recovery relationship (Equation 57) is used and the model parameters are generated to minimize the error between predicted and measured results (Yuan et. al.; 1996) by non-linear regression (quasi-Newton or Simplex) usually using a cumulative recovery based objective function.

### 2.9.7.3 Column Flotation Rate Determination

Column flotation rate constants have been more difficult to determine. Typically, a batch, bench-scale mechanical-cell test is done to estimate the flotation rate followed by a pilot-scale test program that generates a series of time-recovery points. Finch and Dobby (1990) and others employ a method whereby the parameters of a column model are adjusted to give a response approximately equal to the test results.

## 2.9.8 Interface Mass Transfer

Dobby and Finch (1986b) recognize the interface mass transfer characteristics of flotation by noting that the "*full loading of bubbles is a possible limitation in flotation columns*". This flotation limitation has been termed carrying capacity. Jameson et. al. (1977) has questioned the validity of the chemical rate analogy of flotation kinetics since the flotation process is more closely related to interface mass transfer (Ityokumbul; 1992). Ityokumbul (1992) uses adsorption, or interface mass transfer, as an analogy to bubble loading (Equation 61). Bubble surface does not play a role in restricting particle removal unless more than about 50% of the bubble surface is covered (Ityokumbul; 1992) since the particles are swept to the bubble rear (Brown; 1965).

$$\frac{d\phi_{SB}}{dt} = k\phi_{SB,\max}C \qquad \text{Equation 61}$$

Within Equation 61 "C" is a concentration. Since there are many mineral particles with varying size and composition, Equation 61 can be modified to account for each mineral (m) and size-class (n) fraction resulting in Equation 62. Equation 62 is similar to King's (1974) relationship of bubble loading.

$$\frac{d\phi_{SB}}{dt} = \phi_{BS,\max}\sum\left(k_{(m,n)}C_{(m,n)}\right) \qquad \text{Equation 62}$$

Equation 62 "$\phi_{SB}$" [dimensionless] is the surface coverage of solids on the bubble determined by the ratio of solids- to bubble-surface-area.

The use of this equation is dependent on knowing the relationship between concentration and column flotation vessel height. As such, it must be coupled with a model that is able to predict concentration with height.

## 2.10 Micro-Phenomenological Models

### 2.10.1 **Introduction**

The flotation process is one in which a particle is collected on a bubble surface and the bubble is subsequently separated from the pulp in a froth. Models that account for the collision, attachment and detachment between particles and bubbles during the flotation process are termed "micro-phenomenological". The total rate of flotation can be modeled using a "micro-phenomenological" approach, or as the product of various sub-processes. Schuhmann (1942) states that "Q", the specific rate of flotation, can be described in terms of the probabilities of collision and attachment to bubbles according to Equation 63.

$$Q_{Sch} = P_c P_a F_{Sch} \qquad \text{Equation 63}$$

In Equation 63; "$Q_{Sch}$" is the specific rate of flotation; "$P_c$" is the probability of collision; "$P_a$" is the probability of attachment and "$F_{Sch}$" is Schuhmann's froth factor. Sutherland (1948) describes possible variables involved in flotation. Trahar and Warren (1976) also list sub-processes that effect the overall kinetics of flotation including particle-bubble collision, adhesion and detachment.

In order to use macro-phenomenological models, many variables must be determined using prior knowledge, held constant during test work, or factored into the model. These variables act on sub-processes that affect the overall response and most of these are still poorly understood quantitatively.

## 2.10.2 Collection Efficiency

Without considering the froth zone, the mechanics of flotation kinetics are characterized by collection efficiency, which itself is composed of bubble-particle collision, attachment and detachment (Schuhmann; 1942, Sutherland; 1948 and Tomlinson and Fleming; 1963). This concept is a refinement of the direct-encounter hypothesis of Gaudin (1932) which states that "attachment of particles to air bubbles occurs as the result of direct collisions of particles with bubbles". Dobby (1984) states that the rate constant is related to the system collection efficiency ($E_k$) (Flint and Howarth; 1971, Reay and Ratcliff; 1973 and Jameson et. al.; 1977). Equation 64 may be used to determine "$E_k$". Many authors use probabilities; "P", rather than efficiencies; "E".

$$E_k = E_c\, E_a\, (1\text{-}E_d) \qquad \text{Equation 64}$$

In Equation 64 the subscripts represent: "c" = collision, "a" = attachment, and "d" = detachment. Collection efficiency is described by Schulze (1977a,b) as the formation of a thin liquid film (attachment) upon approach of a particle and bubble (collision), formation of a three-phase contact (attachment) and the stability of that aggregate (detachment). An alternative definition of collection efficiency is the number of particles that are carried into the froth on the bubble surface compared to the number of particles swept up by the cross-sectional bubble area.

## 2.10.3 Collision Efficiency

### 2.10.3.1 Introduction

Bubble-particle collision is determined by system hydrodynamics including particle and bubble velocities. A body in flowing water is subjected to dynamic forces such as viscous, pressure and buoyant or weight forces. Those forces acting normal to the flow stream are called "lift", while those acting parallel are "drag".

At Reynolds' numbers under 0.5, the coefficient of drag ($C_D$) can be predicted directly using the Stokes' relationship between Reynolds' number and $C_D$ [$C_D = 24/Re$]. This region is often called the Stokes' flow regime and is characterized by laminar flow and an absence of wakes behind the object. At very high Reynolds' numbers (>10,000) the flow regime is termed "potential flow" wherein the liquid streamlines separate from the object and no wake is formed. The bubble-particle collisions typical in flotation systems occur in the region between Stokes' and potential flow; the intermediate flow regime. This flow regime is characterized by the presence of bubble wakes.

Researchers have generally recognized that collision can occur by three mechanisms. The first (1) is interception where a particle stays with the water streamline. The second and third involve the particle departing from the water streamlines under (2) inertial or (3) gravitational influences. For collision to occur by any of these mechanisms the particle must approach within one particle radius of the bubble.

From these types of collision, it is intuitive that the collision efficiency is greater for "potential" flow than Stokes' flow since there is a higher streamline curvature. Also, very fine particles follow the streamlines and collision can only occur by interception. The following assumptions apply to collision models unless otherwise stated:

- Fine particles are assumed allowing inertial forces to be neglected
- Flow is in the bubbly flow regime (Luttrell; 1986, Xu et. al.; 1989 and Yianatos and Finch; 1990)
- Collisions in the turbulent region behind the bubble and diffusion are ignored.
- Spherical bubbles rise and spherical particles fall within a pulp.
- Collision is defined as an approach to within the distances that surface forces begin to act (Schulze; 1989, Derjaguin and Dukhin; 1960/61). (About 1000 nm).
- Bubbles diameters are between 0.5 and 1.5 mm, and the bubbles are regarded as rigid spheres (Leja; 1982).

### 2.10.3.2 Empirical Models

One type of empirical model is presented by Sutherland (1948) -- variations have since been presented by others. This model uses potential flow and assumes that collision occurs when a particle approaches within one particle radius of the bubble (interceptional). Both the gravitational and inertial forces are neglected. The probability of collision is assumed proportional to the ratio of particle to bubble diameters. Sutherland's relationship and variations are presented as Equation 65 using the constants in Table 8.

$$E_c = b d_p^{a_1} d_b^{a_2} \qquad \text{Equation 65}$$

**Table 8: Constants of Sutherland type $E_c$ equations**

| Author | "b" | "$a_1$" | "$a_2$" |
|---|---|---|---|
| Sutherland (1948) | 3 | 1 | - $a_1$ |
| Reay and Ratcliff (1973) | 1 | 2 | - $a_1$ |
| Anfruns and Kitchener (1976, 1977) | 1 | $1.5 > a_1 > 2$ | - $a_1$ |
| Jameson et. al. (1977) | 1 | 2 | -1.69 |
| Derjaguin (1986) | $1.5 + \frac{\rho_p - \rho_l}{\rho_l}$ | 2 | - $a_1$ |
| Yoon (1993) | $1.5+0.267Re_b^{0.72}$ | 2 | - $a_1$ |

Reay and Ratcliff (1973) include the particles swept out by the bubble cross-sectional area and account for gravitational effects but not for inertia (as proposed by Levich; 1962). A Stokes' flow region is assumed with particles ranging in size from three (3) to twenty (20) micrometers and bubbles on the order of 0.1 cm.

Nguyen et. al. (1998) graphically compares five collision models with experimental data as shown in Figure 9. These models include that of Sutherland (1948), Weber and Paddock (1983), Finch and Dobby (1990), Schulze (1989), and Nguyen and Kmet (1994).

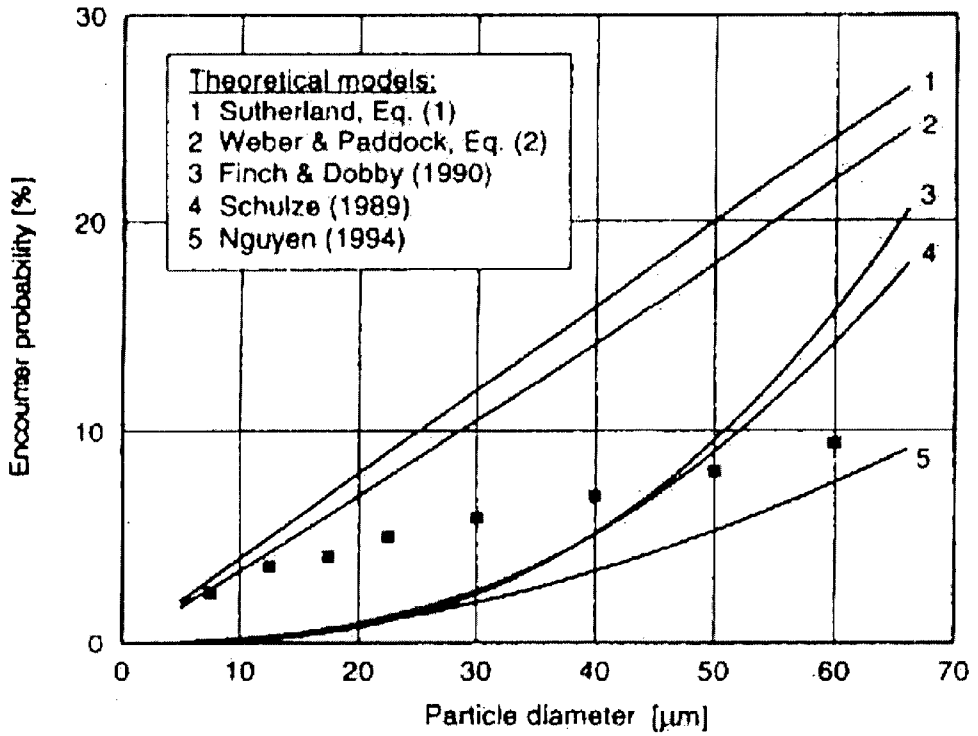


**Figure 9: Collision model and experimental comparison. Bubble diameter of 750 micrometers rising at 2 cm/s from Nguyen et. al. (1998)**

These models may not account for particle and bubble trajectories under different flow conditions, interactions between bubbles and particles, or variations in hydrophobicity -- all of these conditions can be found in column flotation vessels. Trahar and Warren (1976) compare the calculated Sutherland model results with the data from Broken Hill Mines as shown in Figure 10. The results presented in Figure 10 show that the Sutherland model can be used

with particles up to about 20 micrometers, depending on particle settling-velocity, or as long as the particle settling-velocity falls within the Stokes' region.

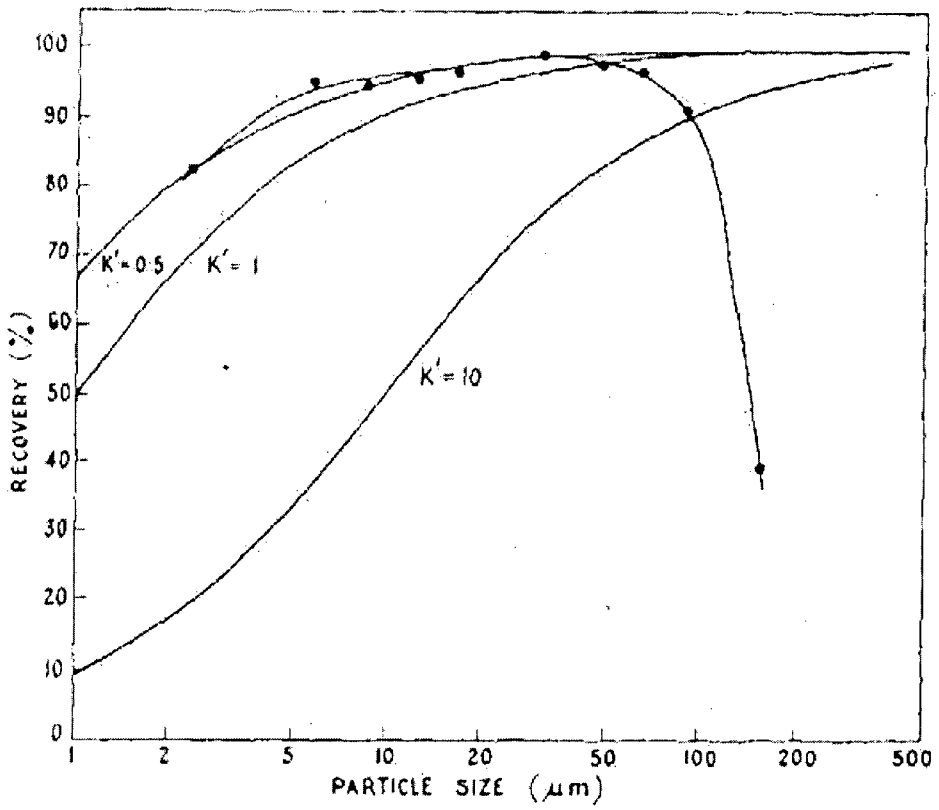


**Figure 10: Recovery response to particle size, as calculated from Sutherland (1948), and experimental data from Cameron et. al., (1971). From Trahar and Warren (1976)**

## 2.10.3.3 Semi-Empirical Models

### 2.10.3.3.1 **Introduction**

Bubble - particle collisions are determined by zone hydrodynamics including the velocities of both particle and bubble. Many authors have contributed models of these events including Sutherland (1948), Plate and Schulze (1991), Schulze et. al., (1989) and Dobby and Finch (1986a). Nguyen and Kmet (1992) illustrate the collision process as shown in Figure 11. In this diagram, a rising bubble with radius "$R_b$" [cm] sweeps out a particle of radius "$R_p$" [cm]. All particles within a critical radius from the bubble centerline ($R_c$ [cm]) will collide with the

bubble. Those at the critical radius will follow a "grazing particle trajectory". Particle velocity is represented by the term "$v_p$" [cm $s^{-1}$]. "$\theta$" [radians] is the angle from the forward stagnation point to the particle along the bubble circumference. At the point of collision, this angle is "$\theta_T$", which cannot be greater than the collision angle "$\theta_C$". This simplified model assumes that the bubbles are rising, and the particles are falling on the vector parallel to the gravitational direction. An example of particle divergence from water streamlines is illustrated in Figure 12 from Reay and Ratcliff (1973). This diagram shows the particle divergence from the water streamlines caused by either inertia or gravity. It is also possible for a particle to bounce on the bubble as shown in Figure 13 -- from Schulze (1992).

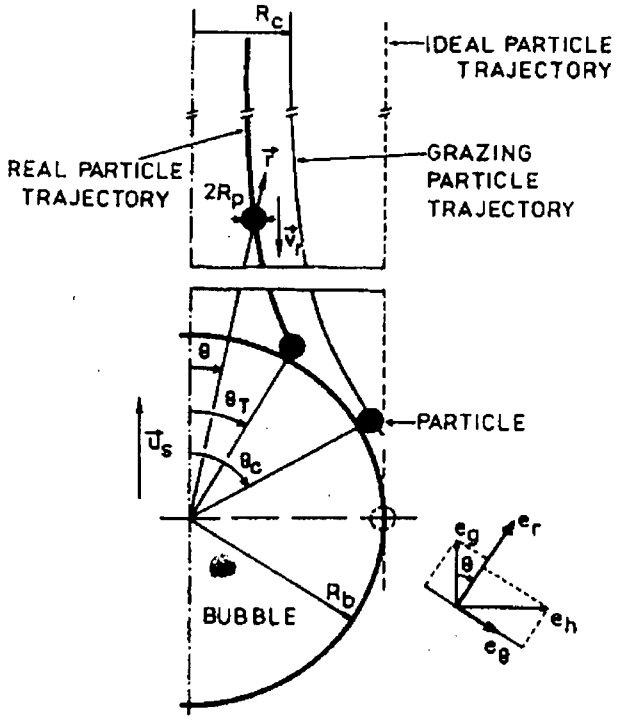


**Figure 11: Nguyen and Kmet (1992) depiction of particle - bubble collision.**

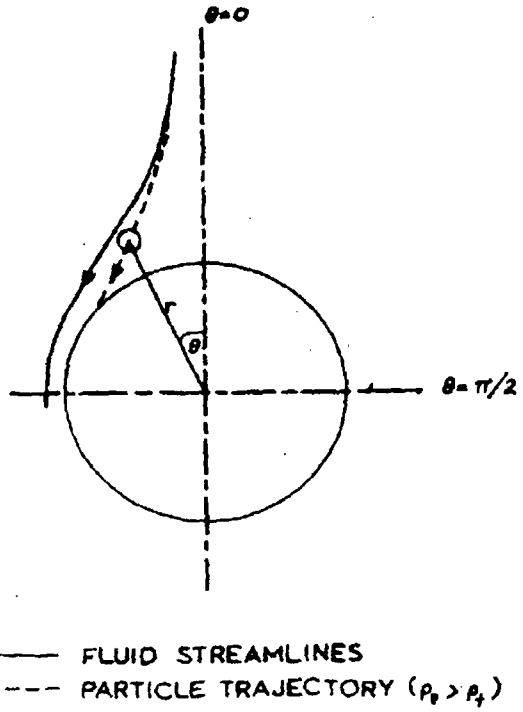


**Figure 12: Reay and Ratcliff (1973) depiction of particle behavior in water streamlines around a moving bubble.**

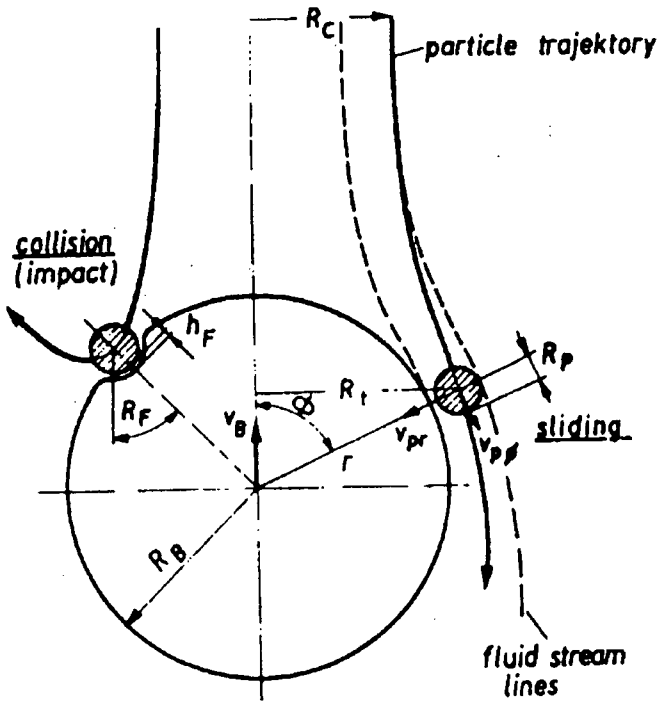


**Figure 13: Particle - bubble collision by sliding or by bounce from Schulze (1992) or Schulze et. al. (1989).**

#### 2.10.3.3.2 **Dobby and Finch's Model**

In Dobby and Finch's (1986a) model an assumption is made that the angle between bubble and particle movement is between 0 and 45°. When the Stokes' number is low (Sk<0.1) the collision efficiency is estimated using independent gravitational and interceptional contact. When the Stokes' number is higher, an additional term is introduced to account for interactions and inertial contact.

Stokes' number (Sk) is the ratio of inertial to drag forces. This number has typically been assumed to be zero in flotation models. According to Dobby and Finch (1987) a zero (0) Stokes' number is not always valid. Stokes' number (Sk) is calculated using Equation 66

$$Sk = 0.111 \mathrm{Re}_b \frac{\rho_p}{\rho_l} \left( \frac{d_p}{d_b} \right)^2 \qquad \text{Equation 66}$$

The symbols used in Equation 66 are the particle diameter ($d_p$ [cm]), bubble diameter ($d_b$ [cm]), liquid density ($\rho_l$ [g $cm^{-3}$]) and particle density ($\rho_p$).

#### 2.10.3.3.3 **Low Stokes' Number Model**

Weber and Paddock (1983) estimate collision efficiency ($E_c$) as the sum of collisions due to gravity ($E_{cg}$) and interception contact ($E_{ci}$) as shown in Equation 67.

$$E_c = E_{cg} + E_{ci} \qquad \text{Equation 67}$$

Weber and Paddock (1983) have investigated interception collision and estimated its' value using Equation 68.

$$E_{ci} = \frac{1.5\left(1+\frac{u_p}{u_b}\right)\left(\frac{d_p}{d_b}\right)^2}{1+0.1875\,\mathrm{Re}_b\left(1+0.249\,\mathrm{Re}_b^{0.56}\right)}$$

Equation 68

In Equation 68, "$E_{ci}$" [dimensionless] is the interception collision efficiency; "$u_p$" [cm $s^{-1}$] is the particle settling-velocity; "$u_b$" [cm $s^{-1}$] is the bubble rise-velocity; "$d_p$" [cm] is the particle diameter; "$d_b$" [cm] is the bubble diameter and "$Re_b$" is the bubble Reynolds' number (as calculated in Equation 32 and Equation 42).

Reay and Ratcliff's (1973) gravity collision ($E_{cg}$) relationship is found in Equation 69 (constrained by $0 < Re_b < 300$).

$$E_{cg} = \frac{u_p}{u_b}\frac{\left(1+\frac{d_p}{d_b}\right)^2 \sin^2\theta_c}{\left(1+\frac{u_p}{u_b}\right)}$$

Equation 69

In Equation 69, "$E_{cg}$" [dimensionless] is the gravitational collision efficiency and "$\theta_c$" [radians] is the maximum angle of collision that results in attachment as determined by Equation 70. Nguyen et. al. (1998) calls the compression angle the collision angle, or the maximum angle at which a particle will collide with the bubble. Woo (1971) gives "$\theta_c$" as a number of empirical relationships, the form of which depends on "$Re_b$", as shown in the following set of equations (Equation 70) while Nguyen et. al. (1998) states that "$\theta_c = \arccos(-Re_b)$".

**Equation 70: Woo (1971)**

| Reynolds' Number Constraint | Equation |
|---|---|
| $0.1 < Re_b < 1.0$ | $\theta_c = 90.0 - 2.51\ \mathrm{Log}(100\ Re_b)$ |
| $1.0 < Re_b < 20$ | $\theta_c = 98.0 - 12.49\ \mathrm{Log}(10\ Re_b)$ |
| $20 < Re_b < 400$ | $\theta_c = 78.1 - 7.371\ \mathrm{Log}\ (Re_b)$ |

2.10.3.3.4 **Intermediate Stokes' Number Model**

Dobby and Finch (1986a) opted to use Equation 71 after Weber (1981). To calculate the collision efficiency under intermediate Stokes' number (Sk) conditions.

$$E_c = 1.627\left(E_{cg} + E_{ci}\right)\frac{\mathrm{Re}_b^{0.06}\, Sk^{0.54} u_b^{0.16}}{u_p^{0.16}} \qquad \text{Equation 71}$$

In Equation 71, "$E_{cg}$" is the gravitational- and "$E_{ci}$" is the interceptional-component of the collection efficiency ($E_c$). Also, "$Re_b$" is the bubble Reynolds number; "Sk" is the Stokes' number, "$u_b$" [cm $s^{-1}$] is the bubble rise-velocity and "$u_p$" [cm $s^{-1}$] is the particle settling-velocity.

The particle settling-velocity is estimated by Masliyah's (1979) hindered settling-velocity method. There are some questions as to the applicability of Weber (1981) and Weber and Paddock (1983), when applied to flotation processes. They assume a $(\rho_p - \rho_l)/\rho_l$ on the order of 0.1 which allows the interception angle of the streamlines with the bubble to be approximately equal to the collision angle ($\theta_c$).

## 2.10.4 Attachment Efficiency

### 2.10.4.1 Introduction

Attachment is strongly dependent on the surface chemistry of both the particles and bubbles. The attachment sub-process involves many complex interactions that are not well understood (Nguyen et. al.; 1998). Models that attempt to describe this sub-process include Sutherland (1948), Dobby and Finch (1986a), Crawford and Ralston (1988), Ye and Miller (1989), Yoon and Luttrell (1989), Finch and Dobby (1990), Yoon and Yordon (1991), Schulze (1992) and Nguyen et. al., (1997). Nguyen (1993) has analyzed some of these models using experimental data and has determined that the model of Finch and Dobby gives a better fit than those of Yoon although some of the experimental data from Hewitt (1994) are not described well by either model.

### 2.10.4.2 Induction Time

The induction time concept was developed by Sven-Nilsson (1934) who included only film thinning time ($t_f$ [s]), and by many others referred by Nguyen et. al. (1998) that include Eigeles (1939), Glembotsky (1953) and Eigeles (1964).

Sutherland (1948) defines induction time as the finite time of contact between bubble and particle needed to cause attachment. Sven-Nilsson (1934) defines induction time as the time elapsing between apparent contact (bubble deformation) and true contact (formation of three-phase interface). The separating factors, or the disjoining pressure (Derjaguin and Kussakov; 1939), is the result of hydration effects, van der Waal's forces and the electrical double-layer effect.

For attachment to occur, the time of particle contact with the bubble, contact time ($t_c$ [s]) must be greater than the induction time ($t_i$ [s]); the time required for the particle to become attached to the bubble after collision (Derjaguin and Durhin; 1960-61). The induction time itself has three components: the time taken for the water film to thin ($t_f$ [s]), the time needed for thin

film rupture ($t_r$ [s]) and the time needed for establishment of three-phase contact ($t_{tpc}$ [s]). For attachment to occur contact time must be greater than the induction time (Equation 72).

$$t_c \geq t_f + t_r + t_{tcp} \qquad \text{Equation 72}$$

Induction time is a material dependent constant (Rasemann; 1988) that depends on hydrophobicity or contact angle (Laskowski; 1986). Jowett (1980) has linked induction time to mineral recovery and surface chemistry in flotation systems. The connection between particle size and induction time as referred to by Nguyen (1998), where induction time increased with an increase in particle size (Quartz - Dodecylamine system with particles between 150 and 300 micrometers). Other references relating particle size to induction time are found in Jowett (1980), Yordon and Yoon (1986), and Ye et. al. (1989). Particle shape is also significant as described by Anfruns and Kitchener (1977) -- angularity decreases induction time.

Induction time is also dependent on bubble size. Smaller bubbles have a higher internal pressure that may thin the hydrated layer (Klassen and Mokrousov; 1963 and Dobby; 1984). An increase in contact angle is assumed to add to this effect resulting in reduced induction times. Stechemesser et. al. (1980) gives the usual induction time range as being between three (3) and thirty (30) milliseconds. While the median induction time is usually used, this parameter is actually an exponential, gamma or Weibull distribution (Rasemann; 1988).

### 2.10.4.3 Contact Time

Contact time is the length of time that a particle and bubble remain in contact between initial collision and when the particle is swept away from the bubble by departing streamlines (Figure 14). Contact time may also be called sliding time. In Figure 14 a particle with initial position [2] contacts the bubble at $(R_b,\theta_T)$ then slides along the bubble until the water streamlines part from that bubble.

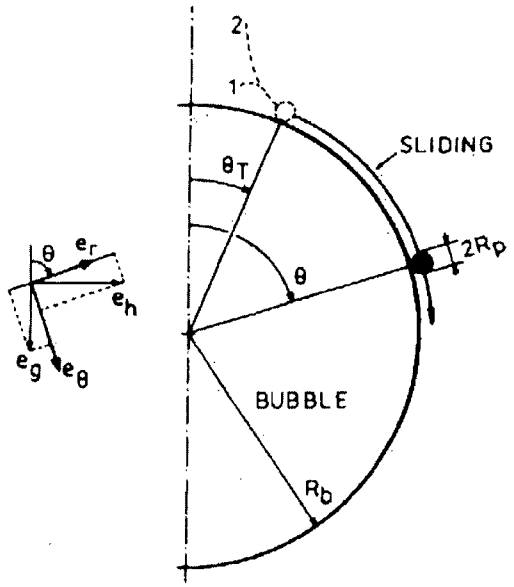


**Figure 14: Sliding action between bubble and particle from Nguyen 1993.**

In Figure 14, "$e_g$" is the unit vector opposite the gravitational direction; "$e_h$" is the unit vector normal to the gravitational direction and "$e_r$" is the unit vector in the radial direction. Also, "$R_b$" is the bubble radius; "$R_c$" is the radius of collision and "$R_p$" is the particle radius.

Contact time is a function of the travel distance on the bubble surface and the speed at which a particle travels along that surface (sliding time, "$t_s$" [s]) or the equivalent time of contact due to particle bouncing ($t_b$ [s]). Contact occurs at a distribution of locations.

### 2.10.4.4 Model of Finch and Dobby

Dobby (1984) calculates a collision angle and an initial particle velocity to predict a particle sliding velocity. The particle travels along the bubble until the streamlines force it away. This departure occurs after the point that the streamlines are most compressed. This model assumes that the particle slides along the bubble after collision, a phenomenon that has been photographed by Schulze and Gottschalk (1981) and according to Klassen and Mokrousov (1963) -- by Bogdanov. Sliding time varies depending on location of collisions and relative particle - bubble velocities. The distribution angle on the bubble at which particles collides can be determined by a trajectory model. The approximation of this model used by Finch and Dobby (1990) is shown in Equation 73.

$$n_\theta = \frac{\sin^2 \theta}{\sin^2 \theta_c} \qquad \text{Equation 73}$$

In Equation 73 "$n_\theta$" is the fraction of particles that collide between the bubble stagnation point and "$\theta$". The maximum contact angle is that at which the particle settling-velocity and liquid velocity radial components are equal and opposite (Finch and Dobby; 1990). (Equation 74)

$$\theta_m = 9 + 8.1\ \rho_p + \theta_c(0.9\text{-}0.09\rho_p) \qquad \text{Equation 74}$$

The particle velocity over the bubble surface is a function of particle settling-velocity relative to the bubble, local liquid flows and location on the bubble surface. Seeley et. al. (1975) determined that there is a large tangential velocity gradient on the bubble upper surface.

Dobby and Finch (1986a,b) use a vorticity ($\xi_s$), defined as the surface tangential velocity gradient, to model the particle velocity over the bubble (Equation 75, from Woo (1971)). They use Woo (1971) to predict vorticity for $0.2<Re_b<400$ at angles to $84^o$. The Woo (1971) correlations to determine this vorticity are found in Table 9 and Table 10.

$$\xi_s = b_1 + b_2\theta + b_3\theta^2 + b_4\theta^3 \qquad \text{Equation 75}$$

**Table 9: Vorticity ($\xi_s$) correlation for $20<Re_b<400$**

| Parameter | Equation |
|---|---|
| $b_1$ | $-0.010822-7.273\times10^{-4}Re_b+1.735\times10^{-6}Re_b^2-2.046\times10^{-9}Re_b^3$ |
| $b_2$ | $-0.0745+3.013\times10^{-3}Re_b-7.402\times10^{-6}Re_b^2-8.931\times10^{-9}Re_b^3$ |
| $b_3$ | $-4.276\times10^{-4}Re_b-1.977\times10^{-7}Re_b^2-6.52\times10^{-11}Re_b^3$ |
| $b_4$ | $-1.103\times10^{-6}-1.032\times10^{-7}Re_b+1.397\times10^{-10}Re_b^2-1.334\times10^{-13}Re_b^3$ |

**Table 10: Vorticity ($\xi_s$) correlation for $0.2<Re_b<20$**

| Parameter | Equation |
|---|---|
| $b_1$ | $-1.217\times10-3-1.745\times10-3Re_b+5.143\times10^{-4}Re_b^2-1.165\times10^{-6}Re_b^3$ |
| $b_2$ | $0.02859+9.229\times10^{-3}Re_b-3.85\times10^{-4}Re_b^2+9.19\times10^{-6}Re_b^3$ |
| $b_3$ | $-4.06\times10^{-5}-5.857\times10^{-5}Re_b+1.62\times10^{-6}Re_b^2-2.992\times10^{-8}Re_b^3$ |
| $b_4$ | $-9.61\times10^{-7}-2.54\times10^{-7}Re_b+1.74\times10^{-8}Re_b^2-5.1\times10^{-10}Re_b^3$ |

Equation 76 determines the velocity at which the particle slides over the bubble surface.

| Conditions | Equation |
|---|---|
| $\frac{d_p}{d_b} \prec 0.03$ | $v_\theta = 0.07\xi_s u_p \frac{d_p}{d_b} + u_p \sin\theta$ |
| $\frac{d_p}{d_b} \geq 0.03$ | $v_\theta = 0.07\xi_s u_p \left[\frac{\left(d_p - 0.03d_b\right)}{d_b} + \frac{0.03d_a}{d_p}\right] + u_p \sin\theta$ |

**Equation 76: Particle sliding velocity**

Finch and Dobby (1990) calculate the sliding time ($t_s$ [s]) using Equation 77.

$$t_s = \frac{(\theta_m - \theta)\left(d_p + d_b\right)}{\upsilon_\theta}$$ Equation 77

In Equation 77 "$\theta_m$" is the maximum contact angle; "$\theta$" is the angle of contact; "$d_p$" [cm] is the particle size; "$d_b$" [cm] is the bubble size and "$v_\theta$" [cm $s^{-1}$] is the particle settling-velocity along the bubble surface. Particles will attach when the sliding time ($t_s$ [s]) is greater than the induction time ($t_i$ [s]). The point where these two times are equal is "$\theta_a$". This value may be determined by Finch and Dobby's (1990) relationship as shown in Equation 78:

$$\theta_a = \theta_m - \frac{114.59 v_\theta t_s}{d_b + d_p} \qquad \text{Equation 78}$$

In Equation 78 "$\theta_a$" is the maximum angle at which a particle can collide with the bubble in order to attach to that bubble.

Equation 79 is then used to calculate the attachment efficiency:

$$E_a = \frac{\sin^2 \theta_a}{\sin^2 \theta_c} \qquad \text{Equation 79}$$

## 2.11 Summary

This section has reviewed existing literature concerning elements of current flotation models that can be used directly or modified for use in the models developed in this research. Many elements of the surface-area model developed in the research are not covered in current literature and are the subject of the discussion section.

The structure and mathematics of a batch column model are not found in current literature. Furthermore, the entrainment, maximum recovery, kinetic rate and carrying capacity relationships surveyed required modification for use in the surface-area models; specifically, in the case of the batch model, modified to give initial estimates. Additional relationships are also required such as an estimate of the active flotation residence time and the calculation of specific surface or surface area density.

The continuous surface-area model uses the form of the Finch and Dobby continuous flotation column model modified and enhanced for surface area. Additional modifications required include the separate treatment of solids associated with the liquid and gas phases, the use of flotation kinetics and bubble loading as the means of transfer between phases, determination of surface area fluxes with axial location, and the subdivision of the "pulp" zone into collection and re-collection zones. None of these relationships are covered, in detail, in the current literature.

The micro-phenomenological relationships form the basis of the mechanistic model frame-work. However, determination of induction time, solids packing, critical solids load angle, the effect of bubble residence time on bubble loading, the relationship between induction time and solids surface coverage, surface loading rates, and attached surface area fluxes are not covered in detail by current literature.

# 3 Apparatus

## 3.1 Introduction

This section describes the equipment used to generate the data for this research and includes batch column and mechanical-cells. The batch flotation test column was designed to minimize the time and cost of test work while maintaining accuracy. The piping, pumps, and control system have been designed for simplicity, portability and flexibility.

The small column size allows tests to be performed with as little as five kilograms of sample. Thus, the cost of obtaining samples is greatly reduced, when compared to hundreds of kilograms used for continuous pilot column tests. Variability in the ore can be easily assessed because many samples can be tested. The small sample size allows testing for variations with in a production stream; and thus, this procedure may accurately determine flotation potential across a wide range of operational conditions. The ability to operate with small samples also means that more tests can be performed on a fixed sample size that can be used to statistically validate the results.

A single test takes about 30 minutes to complete, not including sample preparation. This means that tests run in parallel to an operating circuit can quickly estimate the effect of changing flotation parameters and operational variables.

## 3.2 Test Column

### 3.2.1 **Introduction**

The batch column was designed based on information gathered in the literature review, and from plant design and operation experience. The design follows a classic column configuration with the exception of feed port and wash-water addition systems. A sketch of the design is found in Figure 15

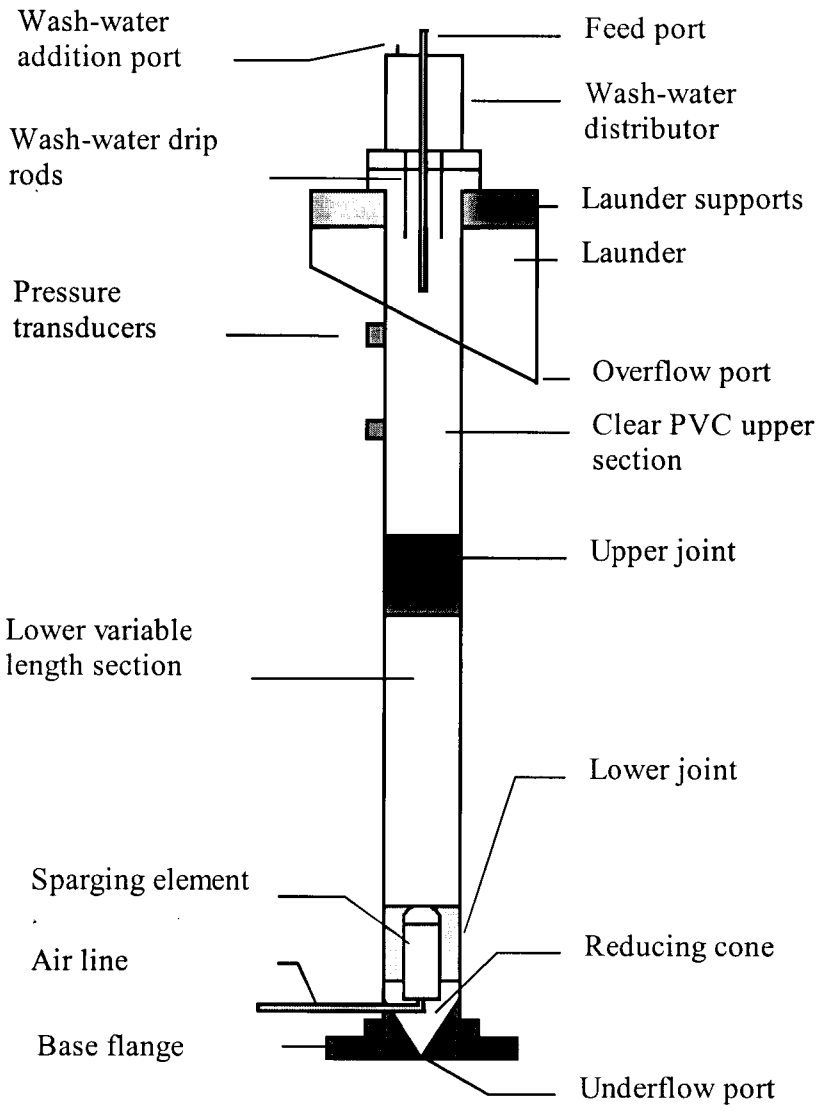


Figure 15: Batch column schematic drawing

### 3.2.2 Column Body

The column body is the reactor vessel that contains the collection, recollection and froth zones. The column body contains the sparger mounting, the slurry exit-cone, the overflow collection launder, and mounts for both the wash-water distributor and feed line. The material of construction is PVC. The minimum height ($h_{(v,min)}$) has been designed at 77.5 [cm]. Additional sections can be added to increase this height. The vessel diameter ($d_v$) is 10.2 [cm].

The base cone gives a smooth transition from column inside-diameter to underflow nipple outside diameter across a 10.2 cm distance or at a cone angle ($\theta_{cone}$) of approximately $\pi/4$ radians.

The batch column is fed from the top of the column through an adjustable pipe that descends through the froth zone. This design allows the recollection-zone dimensions to be changed between tests, or within, tests.

### 3.2.3 Control System

There is no control system on the column. The interface level is maintained at a specific height by the wash-water split between overflow and bias. A specific level is maintained in the column depending on initial level, wash-water rate, froth stability, and flotation rate and was observed through the transparent column.

### 3.2.4 Wash-Water Distributor

The wash-water distributor provides water to the top of froth zone. This flow filters through the froth bubbles and washes entrained material back into the collection zone. Three methods exist to add wash-water to the froth: submerged, spray and directed drips. The submerged system leads to excessive froth break-up and is impractical in a 10.2 cm diameter column. The spray system, often called the overhead-shower system cannot guarantee an even distribution at this diameter because the system uses too few orifices and results in large quantities of wash-water in the overflow. There are two types of "drip" systems: (i) the traditional system in which water flows through a pipe into the froth zone (Figure 16), and (ii)

a system that is of new design in which the water flows along a rod (Figure 17). The rod system is used throughout these tests because it provides a good water distribution that neither breaks the froth nor leads to a large crown of froth above the column lip. The rod system avoids the build-up of froth around the pipes that adversely affects the pipe drip system.

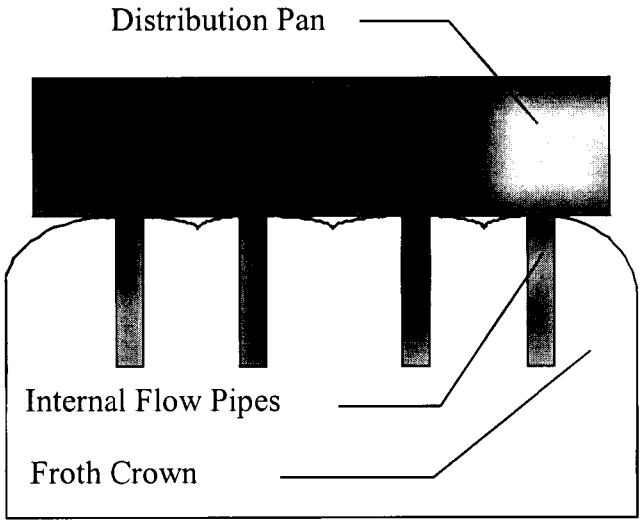


Figure 16: Internal flow pipe wash-water distributor

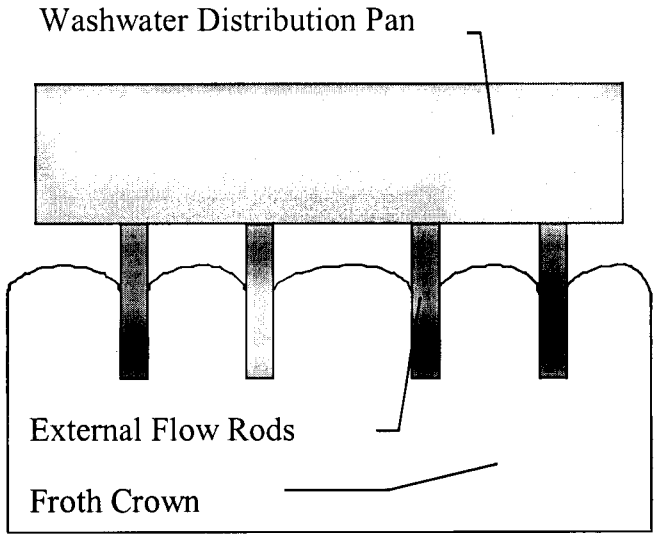


Figure 17: External flow rod wash-water distributor

In the rod system, plastic rods extend from a water distribution tank into the froth zone. The rod diameter is smaller than the distribution tank orifices. The rods are welded off center, into the tank orifices to create a gap through which the water can flow. Water, delivered down the outside of the rods also serves to clean the rods and prevent the build-up of a solids crown. The rod system results in a quiescent froth zone with little bubble breakage.

The current design uses four holes with drip rods and one hole in the center into which the feed pipe is mounted (Figure 18).

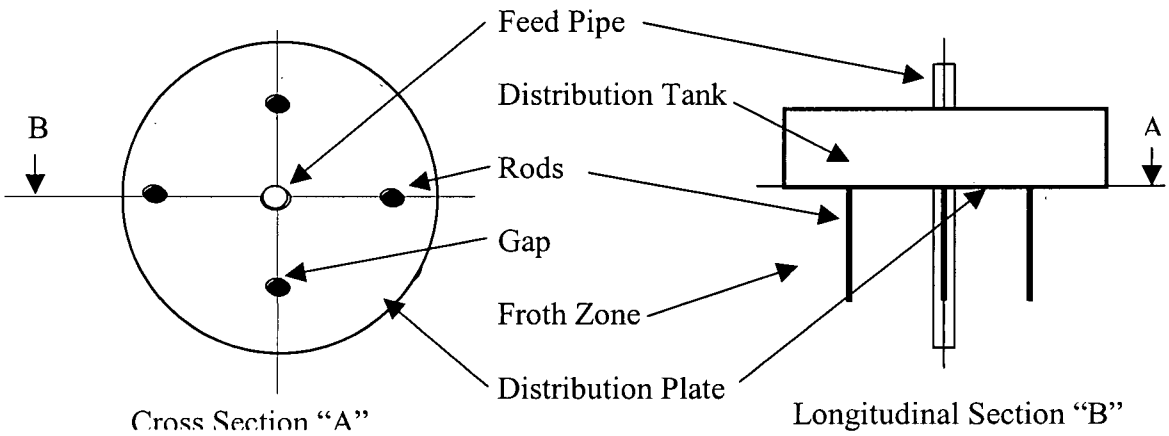


Figure 18: Wash-water rod pattern

Since a crown of froth is expected to build-up above the column lip, the wash-water distribution tank was suspended 7.5 cm above the column lip. The wash-water distributor is placed on the external launder support flanges, so that it does not interfere with froth flow.

### 3.2.5 **Launder**

The column launder collects material that passes over the column lip and directs it to an overflow pipe. The launder has a width of 30.5 cm and is mounted with supports to the column (Figure 19). The launder base has a slope of $\pi/6$ radians.

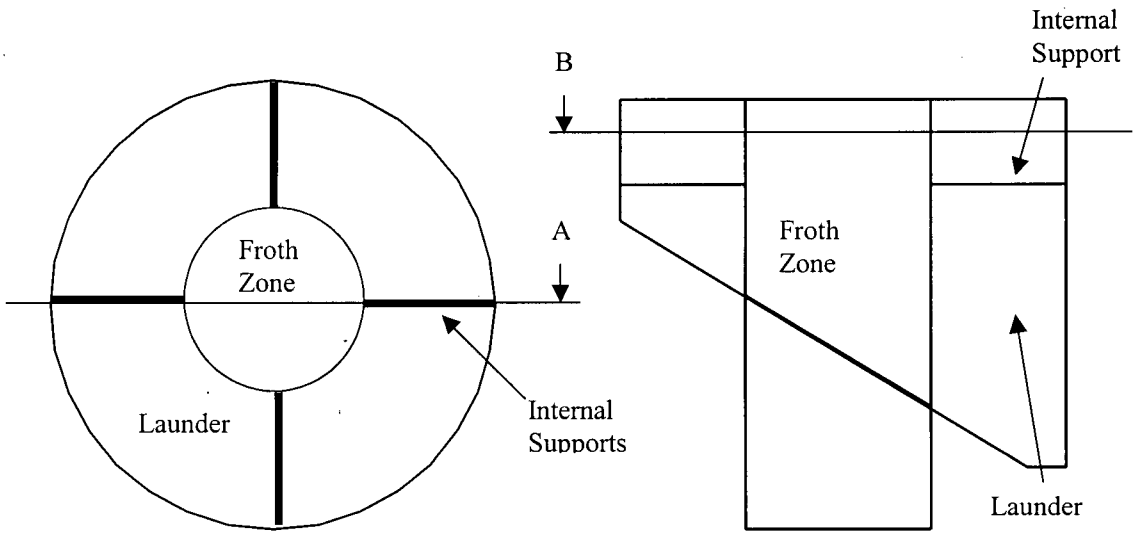


Figure 19: Launder system

### 3.2.6 Sparger

The sparger creates bubbles for the flotation process. The sparger design, along with other system conditions like reagent dosage, air rate, and hydrodynamics, determines both bubble-size distribution and air-flow distribution over the column cross-sectional area. Porous spargers are typically of three media: sintered stainless-steel, perforated-rubber sleeves, and filter-cloth socks. The sparger used in this research was made of rubber.

The active diameter that generates bubbles ($d_{spa}$) is approximately 3.4 cm. When mounted in the column, there is a distance of 3.4 cm on either side of the sparger (Figure 20). The sparger produces bubbles along 7.5 cm of its' height at a superficial gas rate ($J_g$) of 3 cm $s^{-1}$. This height gives a ratio of sparger to column-surface-area of approximately one (sparger = 81 $cm^2$, column = 78 $cm^2$).

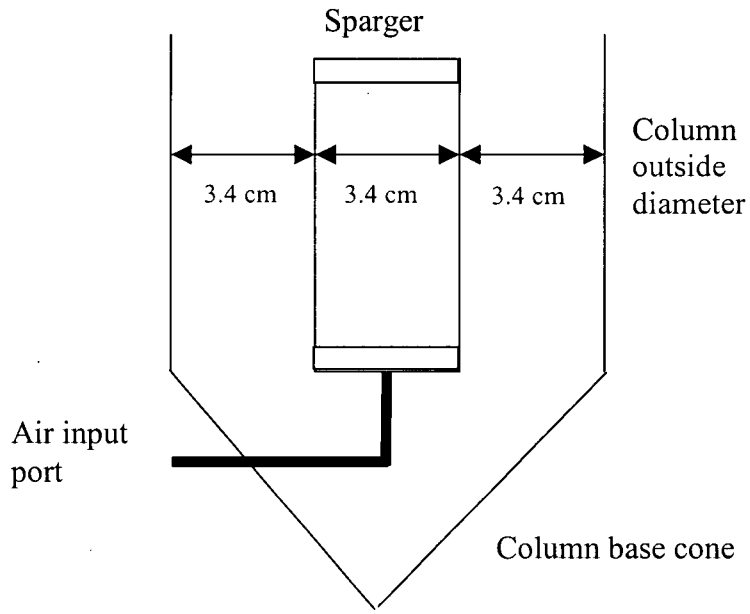


**Figure 20: Sparger System**

## 3.3 Batch Mechanical-Cell Tests

Two batch mechanical-cell flotation devices were used. A custom built mechanical-cell with a flotation chamber of 18,000 $cm^3$ was used for testing the Quinto Mines graphite ore. The INCO tests used a standard Denver laboratory-scale unit operating with a 2,200 $cm^3$ flotation chamber.

## 3.4 Continuous Columns

Data was collected from two continuous columns. The Quinto pilot-scale column was 40.6 cm in diameter ($d_c$) and 488 cm in height ($h_{(v)}$) with the air injection spargers mounted at the 20 cm elevation ($h_{(spa)}$). Wash-water was added through an overhead shower system. Table 11 shows the operating conditions of the pilot column.

**Table 11: Operating Conditions of the Quinto Pilot Column (Graphite)**

| | |
|---|---|
| Lip elevation; "$h_{(v)}$" [cm]<br>Feed port elevation; "$h_{(F)}$" [cm] | 488<br>433 (variable) |
| Sparger elevation; "$h_{(spa)}$" [cm]<br>Vessel diameter; "$d_c$" [cm]<br>Bubble size; "$d_b$" [cm] | 20<br>40.6 – no baffles in pulp zones<br>Unknown (0.15 assumed) |
| Gas holdup; "$\varepsilon_g$"<br>Superficial gas velocity; "$J_g$" [cm $s^{-1}$]<br>Froth depth; "$H_f$" [cm] | Unknown (0.10 assumed)<br>1.5<br>50 – 55 |
| Bias; "$J_b$" [cm $s^{-1}$]<br>Wash-water; "$J_{lw}$" [cm $s^{-1}$]<br>Feed rate; "$J_f$" [cm $s^{-1}$] (slurry) | Unknown<br>0.066<br>1.0±0.1 |

The Quinto column was assumed to have a bubble size; "$d_b$", of 0.11 cm at the sparger. This bubble size is based on CESL sparger performance curves (CESL; 1998) and sparger test work (Flint; 1989) for air injection spargers operating at 15 ppm of MIBC. A 15% reduction in surface area is assumed to occur through the froth zone that is consistent with carrying capacity limitations of Espinosa-Gomez (1988) and others.

The INCO matte separation #2 copper cleaner column operating data was obtained. This is a 1.8 m diameter column. The high copper content stream of this cleaner is called the MK

product. The physical characteristics and operating conditions of this column are shown in Table 12.

**Table 12: Typical Operating Conditions of INCO #2 Column**

| | |
|---|---|
| Lip elevation; "$h_{(v)}$" | 1160 cm |
| Feed port elevation; "$h_{(F)}$" | 885 cm |
| Sparger elevation; "$h_{(spa)}$" | 75 cm |
| Vessel diameter; "$d_c$" | 183 cm baffled into four equal sections |
| Bubble size; "$d_b$" | 0.2 cm (Wilson, 1990) |
| Gas holdup; "$\varepsilon_g$" | 0.20 – 0.25 |
| Superficial gas velocity; "$J_g$" | 3.1 cm/s |
| Froth depth; "$H_f$" | 60 – 240 cm |
| Bias; "$J_b$" | Slightly positive in terms of liquid flow |
| Wash-water; | 1400 – 3900 $cm^3/s$ (0.15 cm/s) |
| Feed solids mass | 5600 – 8300 g/s |
| Overflow | 3300 – 6100 g/s |
| Underflow | 2800 – 5600 g/s |

The overflow bubble size was not measured in the INCO #2 column data of Wilson (1990). Wilson's (1990) work uses a collection zone bubble size of 0.2 cm based on drift flux analysis performed during column operation. The size of 0.2 cm represents a minimum bubble diameter in the overflowing froth as this number represents a zero bubble coalescence condition. Assuming a 15% reduction in surface area through the froth zone an appropriate bubble size would be 0.24 cm, this number however, represents a bubble loading of greater than one.

# 4 Procedures

## 4.1 Laboratory Batch Mechanical-Cell

### 4.1.1 Introduction

During flotation the following elements must be present:

- The peripheral impeller velocity must remain constant in mechanical-cells. (Peripheral impeller speed has an impact both on the bubble size distribution and on the suspension of solid particles. The batch test impeller velocity should be the same as that of the full-scale equipment to be modeled (Gorain et. al.; 1999)).
- The air rate must remain constant.
- The mechanical froth removal method must be consistent. (Variations in removal within, or between, tests will change the froth residence-time and liquid overflow rates.)
- The pulp and froth volumes must be constant or known. Gorain et. al. (1999) have shown that large froth depths affect vessel kinetic performance but, also, that little or no effect is found when shallow froths are maintained.
- The initial and interval sampling timing must be accurate.
- There must be constant feed between repeat tests.
- The feed and tailings rates within, and between, continuous tests must be constant.
- Reagent concentrations must be constant between tests.
- Flotation must occur over a time interval of sufficient length to ensure total flotation of floatable material (batch).

The bubble size ($d_b$ [cm]) and superficial bubble-surface-area flux ($\vartheta_B$ [$s^{-1}$]) through the vessel must remain constant and be approximately the same value as will be present in the continuous, industrial-scale, unit to be modeled.

## 4.1.2 Feed Material

### 4.1.2.1 INCO Matte

The first test material used was matte from the INCO Coppercliff plant in Sudbury Ontario, feed to the #2 column (second copper cleaner), that was composed of approximately 80% to 85% chalcocite ($Cu_2S$) and 15% to 20% heazelwoodite ($Ni_3S_2$) with minor amounts of silicates, metallic copper and nickel. The chalcocite is floated from the "gangue" material. An average of 82% of the feed mass is floatable: thus, this system may be subject to carrying capacity limitations. A flotation stage block-diagram for this separation is shown in Figure 21.

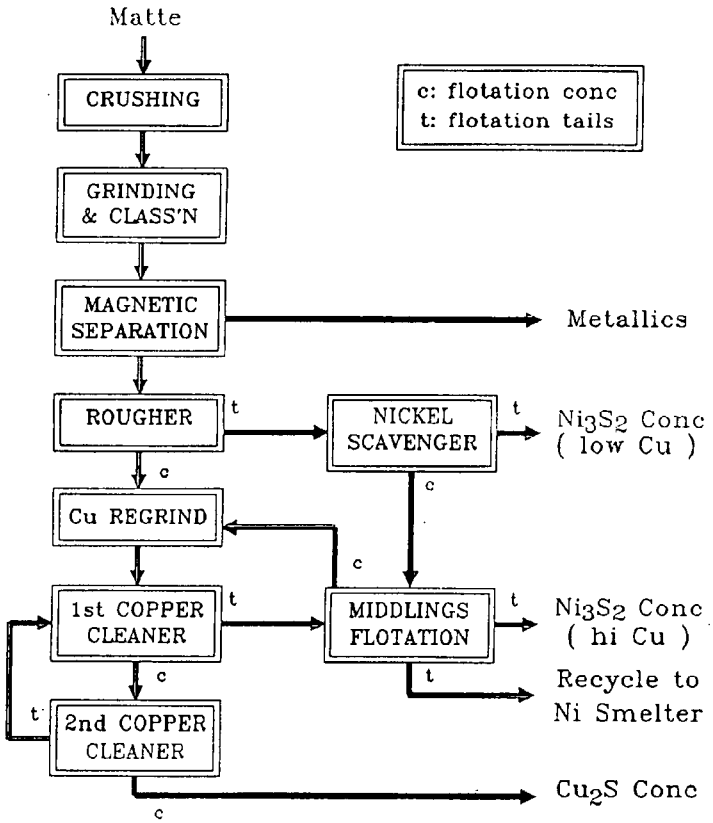


Figure 21: Stages of INCO Matte Separation Flotation from Wilson 1990.

The test material was transported from INCO Coppercliff to the University of British Columbia in a filtered and frozen state. The reagents, already present in the solids, were diphenol guanadine (DPG) and methyl isobutyl carbinol (MIBC), both of which are hydrophobic and stable over the short period of time in the frozen state. These samples were frozen for a period of 10-12 days. One sample was taken over a short period of time, and

therefore does not reflect the variations found within that feed both in terms of mineral grades and particle size distribution. The time delay effects, while frozen and during the six-hour thaw, on the oxidation and reagents are not known and therefore represent a possible source of error.

The #2 copper cleaner feed is very consistent and is composed of essentially two minerals. The copper mineral floats whereas the nickel mineral does not. The copper mineral is a high percentage of the feed "mass".

Performance data readings from the Outokumpu Courier 300 OSA system in the INCO Coppercliff matte plant, are reproduced in the results appendix (Wilson; 1990). The copper product, or overflow from the industrial-scale column, as determined by the OSA system is shown in Table 57. The amount of overflow solids was estimated from the Wilson (1990) data using the copper and nickel recoveries and the overall overflow product density. Underflow results are not given by Wilson (1990), but were calculated from bias and recovery data. These calculated mineral and element values, plus flow conditions, are shown in Table 58 (Appendix II). Typical INCO #2 column operating performances is given in Table 13.

**Table 13: Typical Performance of the INCO #2 Column**

| | Copper Grade | | Nickel Grade | |
|---|---|---|---|---|
| Stream | Maximum | Minimum | Maximum | Minimum |
| Feed | 67% | 60% | 12% | 6% |
| Overflow | 75% | 70% | 3% | 5% |
| Underflow | 65% | 55% | 20% | 10% |

The INCO feed material was screened to determine its size class distribution using 144, 74 and 44 micrometer screens. This distribution is shown in Figure 22. This figure also shows the Rosin-Rammler relationship of the data. The mass data from which the INCO size distribution is derived is found in the data appendix, section 10.2.

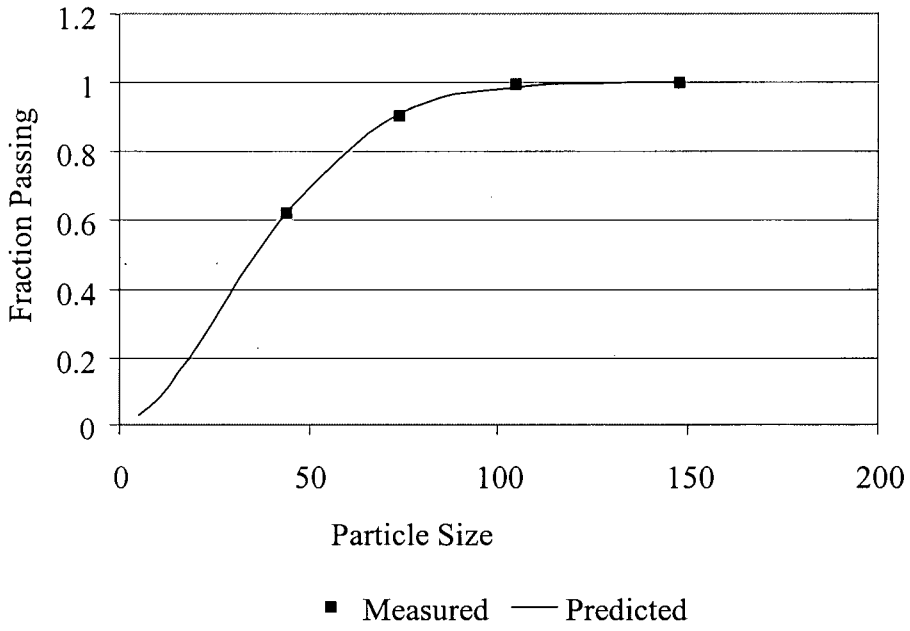


**Figure 22: INCO #2 copper cleaner column feed particle size distribution showing screen fractions as data points and the Rosin-Rammler relationship where $\bar{x}_i$ = 44.58 micrometers and β = 1.312.**

The Rosin-Rammler relationship assumes the relationship shown in Equation 80 between particle size and the fraction of material less than that size.

$$\bar{y}_i = 1 - e^{-\left(\frac{x_i}{\bar{x}_i}\right)^{\beta}} \qquad \text{Equation 80}$$

In Equation 80 "$\bar{y}_i$" is the weight passing or the weight of all material of less size, "$x_i$" is the size, "$\bar{x}_i$" is a reference size, or the size modulus, which may be an indicator of the average particle size, and "β" is the distribution modulus. In the case of the INCO #2 copper cleaner column feed, "$\bar{x}_i$" was determined to be 44.58 micrometers and "β" to be 1.312.

The size class distribution determined for the overflow of test #1 is shown in Figure 23. The Rosin Rammler relationship parameters ofr the INCO overflow size distribution was $\bar{x}_i$ = 37.9 and β = 1.34 .

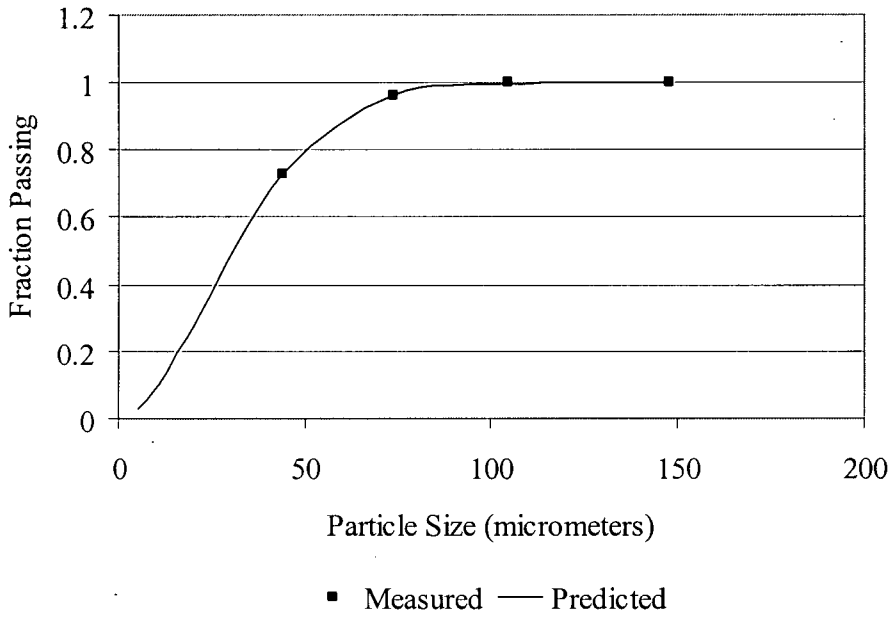


**Figure 23: INCO #2 copper cleaner overflow particle size distribution showing screen fractions as data points and the Rosin-Rammler relationship where $\bar{x}_i$ = 37.9 micrometers and β = 1.34.**

### 4.1.2.2 Quinto Graphite

A series of tests were run at Quinto Mining Corp., located in Lumby B.C., using the batch test column, a batch mechanical-cell and a 40.6 cm diameter pilot-scale column. The objective of these tests was to maximize single stage recovery while producing a concentrate grade of 30% graphitic carbon. The average grinding circuit composition output is shown in Table 14.

**Table 14: Quinto Mines Grinding Circuit Output**

| Mineral | Feed Grade | Size Range (μm) |
|---|---|---|
| Graphite | 2% | 0.5 – 10 |
| Mica (muscovite) | 22% | 2.0 – 30 |
| Pyrite | 8% | 60 - 150 |
| Silica ($SiO_2$) | 50% | 75 - 200 |
| Calcite | 18% | 50 - 120 |

Quinto muscovite occurs as very fine particles which is known as sericite.

The graphite found within the feed is attached physically to approximately twice the mass, or more, of mica either on the surface or between the mica "sheets" or lamella (Figure 24). This physical association means that about 6% of the feed mass is floatable and that the maximum grade may be as low as 30% cG (graphitic carbon).

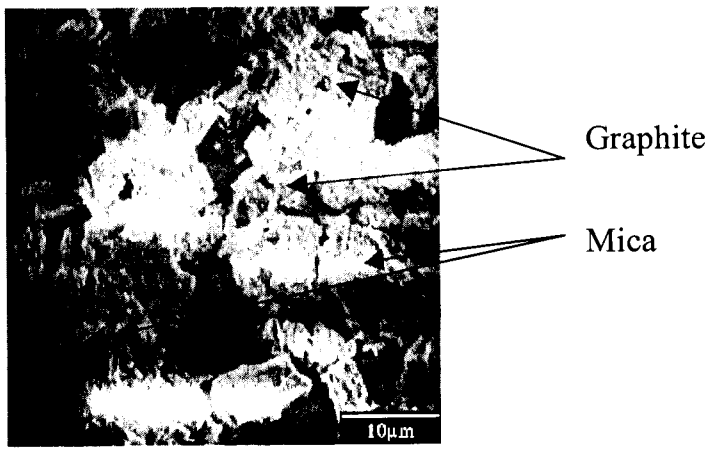


**Figure 24 – SEM image of the Quinto ore including graphite and mica**

The results of a size class distribution performed on the pilot column overflow material is shown in Figure 25 (Malvern Instruments MASTER particle sizer M3.1). The Rosin – Rammler relationship parameters for the Quinto overflow distribution was size $\bar{x}_i$ = 12.181 and $\beta$ = 1.503. The non-linear correlation coefficent eta squared, $\eta^2 = 0.997$ ($\eta^2 >= r^2$, $\eta^2 = r^2$ when relationship is linear.)

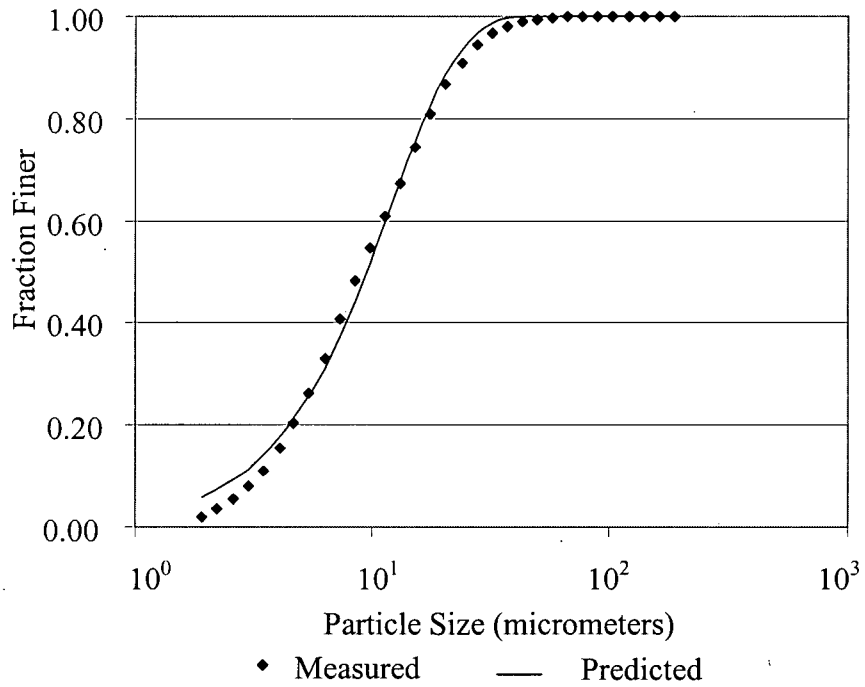


**Figure 25: Quinto graphite pilot column overflow particle size distribution showing size fractions as data points (■), the Rosin-Rammler relationship where $\bar{x}_i$ = 12.181 micrometers and $\beta$ = 1.503.**

In the graphite/mica circuit, frother and fuel oil (as a promoter) are added to float the fine graphite in conventional mechanical-cells. Multiple scavenger stages are used with a total residence-time of approximately 30 minutes. The product target grade is about 30% graphite and 70% mica which has yet to be achieved. Pyrite recovery to the graphite concentrate is minimal. The pilot plant was operated with a target of 35% solids at the sample point. Actual samples were 31.6% and 35.9% respectively.

Feed material for the batch column test was taken from the feed to the Quinto pilot column (Figure 26).

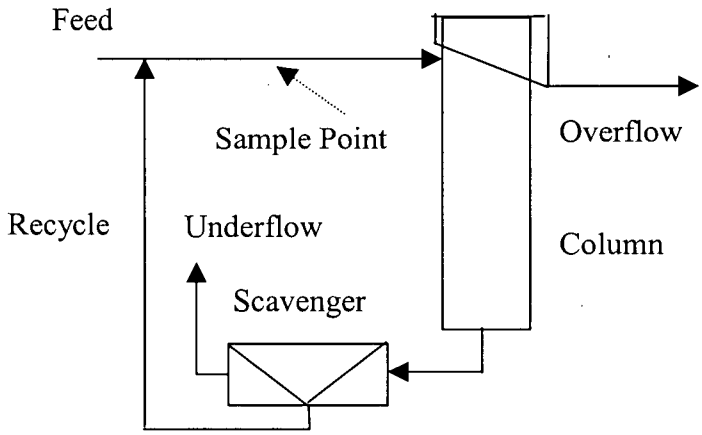


**Figure 26: Quinto pilot plant graphite circuit and test column sample location**

## 4.1.3 Mechanical-Cell Base Line Tests

### 4.1.3.1 Introduction

The batch, mechanical-cell tests can be done using any batch cell as long as the following information is known: vessel height ($h_{(v)}$ [cm] or $L_z$ [cm]), cross-sectional area (A [$cm^2$] or $L_xL_y$ [$cm^2$]), liquid volume ($V_l$ [$cm^3$]), solids volume ($V_{p(m,n)}$ [$cm^3$]), gas holdup ($\varepsilon_g$ [dimensionless]) and particle size ($d_{p(m,n)}$ [cm]). A time-recovery test must be run wherein the initial vessel conditions are known; this knowledge must include the particle-surface-area concentration (specific particle-surface-area) by mineral and size-class ($C_{p(m,n)}$ [$cm^{-1}$]), and froth depth ($h_{(f)}$ [cm]). For each timed sample, the overflow solids-surface-area flux ($\vartheta_{S(O,l)}$ [$s^{-1}$]), overflow bubble-surface-area flux ($\vartheta_{B(O,l)}$ [$s^{-1}$]), and water content ($v_{Ol(i)}$ [$cm^3$]) must be known. Water is added to the vessel in order to maintain the froth-pulp interface a constant elevation.

### 4.1.3.2 INCO Matte

The batch mechanical-cell tests were conducted in a Denver laboratory mechanical-cell with a 2.2 L tank. 2.0 L ($V_l + V_p$) of slurry was added with a total of 900 g of feed (approximately 12% moisture) making a feed pulp density of approximately 30% (w/w) solids. No additional reagents were added. The solids were kept at room temperature for six hours before use and were essentially at room temperature when slurried. The material was agitated for 2.0 minutes before turning on the air.

The practice of using frozen filtered solids, without the addition of reagents has been demonstrated to produce consistent results by INCO. However, this practice introduces an error that would not be present if the test had been done on site.

The concentrate was collected at the 0.5, 1.0, 2.0, 4.0, 8.0, and 16.0 minute intervals ($t_{(i)}$ [s]). Pulp level was maintained throughout these tests by the addition of makeup water.

Bubble size was measured visually by comparison to a grid suspended above the overflow lip. No water was added to the concentrate as launder water. A tailings sample was taken and the remainder was set aside. The samples were then weighed wet, filtered, dried, and re-weighed to obtain water and solid, overflow rates. A sub-sample was taken of each product before screening to obtain +150, -150/+74, -74/+44, and –44 micrometer fractions. The size distribution of the overflow is presented in Figure 23. Essentially no material was recovered in the +150 micrometer fraction. Each product and size fraction was then assayed for nickel and copper. The assays were then used to calculate percentages of mineral products: chalcocite and heazelwoodite. The discrepancies between the sum of these products and 100% is called "other" and is composed of all residual minerals. Chalcocite ($Cu_2S$) was assumed to be composed of 88.9% copper and 11.1% sulfur with a mineral density of 5.6 (Sinkankas; 1964). Heazelwoodite is a nickel sulfur mineral ($Ni_3S_2$). A 73.55% nickel grade was assumed for haezelwoodite based on obtaining 0% of "other" in the purest sample as opposed to the 73.3% obtained by atomic weights. This grade difference may be due to minor amounts of metallic nickel being present in the ore. These minerals are natural mixtures, thus, are not always exact in their composition.

#### 4.1.3.3 Quinto Graphite

The batch, mechanical-cell tests were conducted in a large laboratory-scale mechanical-cell with a one cubic foot capacity. An 11,000 gram sample of ground and dried ore (< 10% moisture) was used to create a feed pulp. Dowfroth 250C frother was added to all tests at 10 ppm along with 50 ppm fuel oil. The material was agitated for 2.0 minutes before turning on the air. All tests were done in the Quinto Corporation pilot plant.

During the tests, a feed sample was taken before applying air. The concentrate was collected at the 1.0, 2.0, 4.0, 8.0, 16.0 and 25.0 minute intervals. Bubble size was measured visually by comparison to a grid suspended above the overflow lip. No water was added to the concentrate as launder water; however, the pulp level in the cell was maintained by adding water to the cell throughout the tests. A tailings sample was taken and the remainder was set aside. The samples were then weighed wet, filtered, dried and re-weighed to obtain water and solid overflow rates. The size distribution of the overflow product is shown in Figure 25. A double loss on ignition assay was done to determine the graphitic carbon; "cG", content. The

following densities were assumed: Calcite; 2.71, Graphite; 2.23, Mica; 2.76, Pyrite; 5.02 and Silica; 2.65.

In both the INCO and Quinto tests, bubble measurement error is significantly higher in the early stages of a flotation test. At the start of the tests, the overflow flow rate was higher; thus, less time is available for the assessment. Bubbles were measured on the top of the flotation cell and not on the fast-moving bubbles overflowing the lip.

## 4.2 Laboratory-Scale Batch Column

### 4.2.1 Equipment

The batch flotation column, described in section 3.2 was used to collect the test data. During these tests, feed was added 20 cm from the column lip using the adjustable height feed pipe. No launder water was added. Wash-water was added by a drip system using five rods. Level was not actively maintained. Wash-water, added to the system, overflowed the column and resulted in a positive bias as solids were displaced and the froth slowly became shallower. This column was used on both INCO matte and Quinto feeds.

### 4.2.2 Procedures

A 10 L slurry sample containing approximately 30% solids was prepared by (a) adding water to 4300 g of previously frozen INCO # 2 column feed (about 12% moisture) or (b) taking approximately 4300 g of feed solids from the Quinto graphite circuit (as a slurry). (Note: test #1 feed solids was 3572.4 g). No additional reagents were added to the INCO material, although 10 ppm DOW250C and 50 ppm fuel oil was added to the Quinto feed material (both the column and pilot plant).

The slurry was agitated to maintain the suspension and then pumped into the column. The underflow line was constricted with a valve and allowed to return to the feed tank until the column was filled to 90% of the estimated collection-zone volume or 122.5 cm from the column base. The INCO tests used an initial froth zone height of 20 cm whereas the Quinto tests were done with 10 cm due to physical setup restrictions within the Quinto pilot plant. The height difference was achieved by the use of a 10 cm collar. The feed pump input hose was then connected to the column underflow leaving 560 $cm^3$ volume of slurry in the feed tank; this remainder formed the feed sample.

The slurry was allowed to circulate for ten minutes to promote even solids mixing. Air was then applied at "$J_g$" = 1.5 [$cm\ s^{-1}$], a rate that formed approximately 10% gas holdup. Wash-water ($Q_w$) was added at a rate of approximately 10 $cm^3\ s^{-1}$ (INCO) or 2.5 $cm^3\ s^{-1}$ (Quinto), as determined by rotameter, and adjusted downward as the level in the column started to

increase. Overflow was continuously sampled over specific intervals. In both sets of tests, the interface level in the column slowly approached the overflow lip as the test progressed.

Overflow bubble diameter was measured visually as the bubbles descended the outside of the column but only on sections that were moving slowly. The University of Cape Town bubble size analyzer was tried but did not work. Bubble size affects the bubble surface area flux through the column that, in the model, is independent of flotation kinetics (flotation rate constant and maximum recovery) and vessel entrainment. Thus, error in the bubble size will only affect the bubble loading parameter.

Initial test timing started when the first froth overflowed. At the end of both tests the column was emptied and the entire contents formed the tailings sample. For both series of tests each sample was weighed wet and dry. An assay was performed on each product for graphitic carbon (Quinto) or nickel and copper (INCO).

All tests were run with a recycle rate; "$J_{sl}$" of 3.0 [cm $s^{-1}$], in order to minimize the difference between elapsed time and flotation residence-time and to allow the bubbles to have a longer residence-time.

The batch mechanical-cell and batch column and continuous column tests results are found in the results appendix (section 10).

## 4.2.3 Surface Area Determination

### 4.2.3.1 Particle Surface Area

#### 4.2.3.1.1 Introduction

Throughout these tests surface area was determined by taking the geometric average between the largest and smallest particle sizes within a size class as shown in Equation 81.

$$d_p = \sqrt{d_{p(\min)} d_{p(\max)}} \qquad \text{Equation 81}$$

In Equation 81, "$d_p$" [cm] is the geometric particle diameter, "$d_{p(min.)}$" [cm] is the smallest size in a size class and "$d_{p(max.)}$" [cm] is the maximum size in a size class. Within the "pan" fraction; the smallest size fraction, the minimum particle size was estimated. Within the largest size fraction the upper size was assumed to be twice that of the lower size.

The mass of mineral in one size fraction; "m" [g] is determined using Equation 82 (where $\rho$ [g $cm^{-3}$] is the solids density).

$$m = \rho V \qquad \text{Equation 82}$$

The volume; "V" [$cm^3$] of collection of "n" particles of diameter "$d_p$" [cm] is determined using Equation 83 (spherical), Equation 84 (cubic) Equation 85 (tabular).

Spherical $$6V_{spherical} = n\pi d_p^3 \qquad \text{Equation 83}$$

Cubic $$V_{cubic} = n\bar{x}_p^3 \qquad \text{Equation 84}$$

Tabular $$V_{tabular} = n\bar{x}_p\bar{y}_p\bar{z}_p \qquad \text{Equation 85}$$

Equation 84 can be used to calculate the volume of the INCO particles, while Equation 85 with "x" = "y" and "z" = 2 can be used for the Quinto mica.

Combining the appropriate volume equation with Equation 86, Equation 87 or Equation 88 (total surface area) gives the surface area in a size fraction (Equation 89, Equation 90 and Equation 91). Multiplication of this surface area by the grade of mineral in the size class will give a specific mineral surface area.

Spherical $$S_{spherial} = n\pi d_p^2$$ Equation 86

Cubic $$S_{cubic} = 6n\bar{x}_p^2$$ Equation 87

Tabular $$S_{tabular}=2n\left(\bar{x}_p\bar{y}_p+\bar{x}_p\bar{z}_p+\bar{y}_p\bar{z}_p\right)$$ Equation 88

Spherical $$S_{spherical} = \frac{6m}{\rho d_p}$$ Equation 89

Cubic $$S_{cubic} = \frac{6m}{\rho\bar{x}_p}$$ Equation 90

Tabular $$S_{tabular} = \frac{2m}{\rho}\left[\frac{\bar{x}_p\bar{y}_p+\bar{x}_p\bar{z}_p+\bar{y}_p\bar{z}_p}{\bar{x}_p\bar{y}_p\bar{z}_p}\right]$$ Equation 91

In Equation 86, "S" [$cm^2$] is the solids surface area, "n" is the number of particles and "$d_p$" [cm] is the average particle diameter. In Equation 89, "m" [g] is the mass of contained solids and "ρ" [g $cm^{-3}$] is the solids density.

The surface area rate; "S/t" [$cm^2$ $s^{-1}$] is the surface area that passes a reference plane with time. The superficial surface area flux; "ϑ" [$s^{-1}$] is the rate divided by the cross sectional area of the reference plane.

#### 4.2.3.1.2 **INCO**

The lower size; "$d_{p(min)}$" [cm] in the INCO pan fraction was assumed to be 20 micrometers (0.0006 fractional passing) as illustrated in Figure 22. There is a sharp increase in the number of particles larger than 20 micrometers present in the sample according the Rosin – Rammler curve (Section 4.1.2.1). With this lower size, the average particle size; $\bar{x}_i \cong d_p$, determined is shown in Table 15 (feed) and Table 16 (overflow) using both geometric mean and Sauter mean diameter (Rosin-Rammler distribution) methods for each size class. The mass and density (5.5 g $cm^{-3}$) of the material in the size class is then used to calculate the surface area's (using both geometric and SMD means)

Table 15: Surface area calculations for INCO feed particles

| Screen Size | Mean (cm) | | mass | Surface ($cm^2$) | | |
|---|---|---|---|---|---|---|
| cm | Geometric | SMD | g | Geometric | SMD | Difference |
| 0.0144 | | | | | | |
| 0.0105 | 0.0125 | 0.0113 | 5 | 438 | 483 | -9.3% |
| 0.0074 | 0.0088 | 0.0081 | 70 | 8,660 | 9,400 | -7.9% |
| 0.0044 | 0.0057 | 0.0052 | 224 | 42,800 | 46,600 | -8.2% |
| 0.0020 | 0.0030 | 0.0029 | 496.5 | 182,600 | 189,900 | -3.8% |

Table 16: Surface area calculations for INCO total overflow particles

| Screen Size | Mean (cm) | | mass | Surface ($cm^2$) | | Difference |
|---|---|---|---|---|---|---|
| cm | Geometric | SMD | g | Geometric | SMD | |
| 0.0144 | | | | | | |
| 0.0105 | 0.0125 | 0.0111 | 0.1 | 9 | 10 | -10.0% |
| 0.0074 | 0.0088 | 0.0080 | 21.4 | 2,650 | 2,900 | -13.8% |
| 0.0044 | 0.0057 | 0.0052 | 134 | 25,600 | 28,200 | -9.2% |
| 0.0020 | 0.0030 | 0.0028 | 422 | 155,200 | 162,900 | -4.7% |

#### 4.2.3.1.3 **Quinto**

The lower size; "$d_{p(min)}$" [cm] within the overflow fraction this was assumed to be 4.7 micrometers because the Malvern particle size analyzer measures a significant number of particles along their minor axis, which in the case of Quinto mica is between 1 and 4 micrometers (from SEM pictures). The resulting geometric and Sauter mean diameters (Section 12.2) are shown in Table 17. The Sauter mean diameter does not realistically represent the particle size. However, when these particle sizes are converted to surface areas (Equation 91 and Equation 89) these is little difference between the methods of calculation.

Table 17: Surface area calculations for Quinto total overflow particles

| Size | Diameter (cm) | | Volume | Surface ($cm^2$) | | |
|---|---|---|---|---|---|---|
| cm | Geometric | Sauter | $cm^3$ | Geometric | Sauter | Difference |
| 0.00669 | 0.00720 | 0.01066 | 0.08 | 42 | 42 | -1.13% |
| 0.00577 | 0.00621 | 0.00922 | 0.08 | 48 | 49 | -0.91% |
| 0.00498 | 0.00536 | 0.00797 | 0.23 | 168 | 170 | -0.72% |
| 0.00429 | 0.00462 | 0.00689 | 0.45 | 391 | 393 | -0.54% |
| 0.00371 | 0.00399 | 0.00595 | 0.75 | 754 | 758 | -0.43% |
| 0.00320 | 0.00345 | 0.00515 | 0.83 | 961 | 963 | -0.29% |
| 0.00276 | 0.00297 | 0.00445 | 1.65 | 2,227 | 2,231 | -0.18% |
| 0.00239 | 0.00257 | 0.00385 | 2.63 | 4,100 | 4,105 | -0.11% |
| 0.00205 | 0.00221 | 0.00332 | 3.31 | 5,980 | 5,978 | 0.03% |
| 0.00177 | 0.00190 | 0.00286 | 4.43 | 9,317 | 9,312 | 0.05% |
| 0.00153 | 0.00165 | 0.00247 | 4.89 | 11,881 | 11,868 | 0.10% |
| 0.00132 | 0.00142 | 0.00213 | 5.19 | 14,603 | 14,579 | 0.17% |
| 0.00114 | 0.00123 | 0.00184 | 5.04 | 16,427 | 16,393 | 0.21% |
| 0.00098 | 0.00106 | 0.00159 | 4.51 | 17,072 | 17,025 | 0.27% |
| 0.00085 | 0.00091 | 0.00137 | 4.96 | 21,747 | 21,693 | 0.25% |
| 0.00073 | 0.00079 | 0.00119 | 5.56 | 28,251 | 28,155 | 0.34% |
| 0.00063 | 0.00068 | 0.00102 | 5.79 | 34,144 | 34,030 | 0.33% |
| 0.00054 | 0.00058 | 0.00088 | 5.19 | 35,574 | 35,431 | 0.40% |
| 0.00047 | 0.00050 | 0.00076 | 4.21 | 33,426 | 33,319 | 0.32% |
| 0.00041 | 0.00044 | 0.00066 | 3.83 | 34,935 | 34,824 | 0.32% |
| 0.00035 | 0.00038 | 0.00057 | 3.23 | 34,133 | 33,971 | 0.47% |
| 0.00030 | 0.00032 | 0.00049 | 2.33 | 28,767 | 28,635 | 0.46% |
| 0.00026 | 0.00028 | 0.00042 | 1.80 | 25,839 | 25,737 | 0.40% |
| 0.00022 | 0.00024 | 0.00036 | 1.43 | 23,887 | 23,751 | 0.57% |
| 0.00019 | 0.00020 | 0.00031 | 1.28 | 25,002 | 24,893 | 0.43% |

### 4.2.3.2 Bubble Surface Area

#### 4.2.3.2.1 **Introduction**

The bubble surface area rate, or the surface area that passes a specific plane per unit time, can be determined using Equation 92.

$$\frac{S_B}{t} = \frac{6Q_g}{d_b} \qquad \text{Equation 92}$$

In Equation 92 "$S_B$" [$cm^2$] is the bubble surface area, "t" [s] is a time interval, "$Q_g$" [$cm^3\ s^{-1}$] is a volumetric gas flow rate, and "$d_b$" [cm] is the average bubble diameter.

#### 4.2.3.2.2 **INCO**

The INCO #2 column overflow bubble size was not measured by Wilson (1990). Within Wilson's (1990) work average bubble size within the collection zone was estimated to be 0.2 cm based on drift flux analysis. As the bubble size overflowing the froth zone must be greater than or equal to that in the collection zone, thus, 0.2 cm represents the minimum overflow bubble diameter. The 0.2 cm size represents a bubble loading of 0.85. A bubble size of 0.24 cm (15% reduction in surface area) results in a solids load on the bubble of greater than one [1], thus, this number represents a bubble size that is too large. The bubble size used in the continuous model was 0.2 cm that represents the minimum size predicted by the Wilson (1990) data. This bubble size may be too large since a bubble load of 0.85 is large when compared to the accepted maximum of 0.5.

#### 4.2.3.2.3 **Quinto**

Frother levels in the Quinto column were used in order to give an estimated bubble size; "$d_b$", of 0.11 cm at the sparger based on CESL (1998) and sparger test work (Flint; 1989) for an air injection sparger. A 15% reduction in surface area is assumed to occur through the froth zone that is consistent with carrying capacity limitations of Espinosa-Gomez (1988) and others. This results in a bubble size of 0.15 cm.

# 5 Discussion

## 5.1 Model Introduction

Three models are presented: a batch kinetic model, a continuous column kinetic model and a mechanistic pulp-zone model framework. The following assumptions are made concerning the flotation environment in all three models:

1. There are minimal changes in temperature within the system and the changes that do occur do not affect the flotation process. No changes in state occur.
2. There are no chemical reactions or dissolution that may cause a change in the mass of solids present in the system.
3. Particle size is preserved within the flotation vessel.
4. A fraction of the particles within each population, represented by a maximum recovery, is assumed to have a specific induction time with no variations. Other particles within that population are assumed not to float.

The **batch kinetic model** adjusts the parameters of an objective function in order to minimize error between test data and the objective function response. The purpose of this model is to estimate the kinetic rate constant ($k_{f(m,n)}$ [$s^{-1}$]), entrainment constant ($k_{e(m,n)}$ [dimensionless]), maximum recovery ($R_{\infty(m,n)}$ [dimensionless]), and a carrying capacity or bubble load ($\phi_{SB}$ [dimensionless]), for the flotation of a suite of minerals under specific conditions. These parameters are then used in the continuous model to predict full-scale performance. The batch kinetic model uses bubble-surface-area and solids-surface-area rather than traditional volumes and weights. The use of surface area allows direct modeling of the interfacial nature of flotation.

The **continuous kinetic model** uses the parameters estimated in the batch model to estimate continuous, full-scale recovery performance for the purpose of sizing industrial flotation equipment or to predict the effect of circuit modifications. This is a one-dimensional model wherein the vessel is divided into three physical zones: collection, recollection and froth zones. The recollection zone is the pulp zone above the feed port elevation and the collection

zone is pulp zone below this elevation. Superficial bubble, attached-solids and suspended solids surface-area fluxes are used throughout.

The third model is a **"mechanistic" bubble-loading model** framework that may be used to model pulp phase flotation using induction time and packing factors rather than kinetic rates and carrying capacity. This could allow the calculation of bubble loading with time, and thus, model the effect of bubble residence-time on carrying capacity. The model links the flotation chemistry, using induction time, with the flotation process.

## 5.2 Variables

Most of the variables used in these models are similar to those used by other researchers. However, unlike other models, two "streams" are used within the vessel: bubble (air) and liquid. The solids within the column are associated with one or both of these streams.

In addition, the bubble stream is characterized by the superficial bubble-surface-area flux ($\vartheta_B$ [$s^{-1}$]), as used by Gorain et. al. (1999), and an associated superficial attached-particle surface-area flux ($\vartheta_{SB}$ [$s^{-1}$]). These variables are not directly observed, but calculated knowing particle or bubble size and volume flow rates (section 4.2.3). Gorain et. al. (1999) justified using the bubble surface-area flux statistically by showing that this characterization is an accurate predictor of flotation performance. The solids association, as an "area flux", with the bubbles is new to this research and is made to simplify calculations of bubble loading and to make a clear distinction between solids in suspension and those attached to the bubbles. This characterization of the solids allows pulp density, bubble loading and bubble velocity to be determined easily with axial location.

The liquid stream is characterized by the superficial liquid flow rate ($J_l$ [cm $s^{-1}$]) and an associated superficial suspended-particle surface-area flux ($\vartheta_{SL}$ [$s^{-1}$]). The concentration of solids in the "liquid stream" is characterized by the specific solids surface or the concentration of solids-surface-area ($C_p$ [$cm^{-1}$]).

## 5.3 Batch Kinetic Model

### 5.3.1 Introduction

The batch kinetic model estimates the parameters used in the continuous flotation model. The resulting values are valid only within the conditions tested. The batch kinetic model is empirical in nature and is an adaptation of current batch kinetic models for mechanical-cells. The following assumptions are made concerning factors that affect flotation:

1. The entire cell is considered as one unit,
2. The initial conditions are known including liquid, solids, reagents, agitation and air addition rates and no solids mass, volume or surface area is gained or lost,
3. Any water lost to the overflow is replaced to maintain overall volume,
4. Temperature is assumed to be constant,
5. Batch tests are performed using discrete timed samples.
6. Maximum bubble loading ($\phi_{SB}$) is assumed to remain constant. In "reality" loading may vary with time as the solids composition in the vessel change.
7. The floatable solids-surface-area concentration ($C_{pf}$ [$cm^{-1}$]), or floatable solids specific surface is assumed to be constant with axial and radial location but not with time. The average specific surface ($C_p$ [$cm^{-1}$]) within a time interval is used to represent that entire time interval for the purposes of entrainment. For kinetic purposes, the solids-surface-area concentration is the initial value minus the average entrained value for the timed sample. There is a unique specific surface ($C_p$ [$cm^{-1}$]) for each mineral and size-class.
8. The assumption is made that all bubbles are the average size or that minimal error is introduced by assuming an average. Bubble surface area was calculated according to section 4.2.3.2.
9. The batch flotation vessel is assumed to behave as a plug flow vessel with time.
10. Average particle size is assumed to be the geometric mean of the upper and lower sizes within the size class and particle surface area is determined according to section 4.2.3.1.

### 5.3.2 Model Structure

The batch flotation model uses a single "stage"; it combines the pulp and froth zones into a single zone. The single stage model simplifies testing procedures but restricts tests to shallow froths. Gorain et. al. (1999) indicates that shallow froths have limited impact on recovery of a float vessel.

### 5.3.3 Model Description

The batch model parameters are determined by minimizing the difference between the model response and the data from laboratory-scale time–recovery tests. The objective function used in this model is presented in Equation 93.

$$\varepsilon_{m,n} = \sum_{i=1}^{L} \sqrt{\left(\vartheta_{S(O,i)(m,n)} t_{(i)} - \vartheta^{*}_{S(O,i)(m,n)} t_{(i)}\right)^2} \qquad \text{Equation 93}$$

In Equation 93 the error term ($\varepsilon_{(m,n)}$) is dimensionless and the time interval ($t_{(i)}$ [s]) is the individual interval elapsed time (i).

The objective function uses the total overflow superficial solids-surface-area flux calculated from test data ($\vartheta^{*}_{S(O,i)}$ [$s^{-1}$]) and the response predicted by the model ($\vartheta_{S(O,i)}$ [$s^{-1}$]), along with the time interval ($t_{(i)}$ [s]). Three parameters arrays (m,n) are used in the objective function: (1) flotation rate constants, (2) entrainment parameters and (3) maximum recovery due to flotation. In addition a carrying capacity parameter is also used. Alternative objective functions may be used such as those that incorporate cumulative solids overflow surface, surface recovery or cumulative surface recovery.

To use the objective function (Equation 93) the overflow surface-area fluxes are calculated. Within the model, the solids-surface-area of each timed interval is the sum of both floating and entrained solids surfaces: "$\vartheta_{S(O,i)} = \vartheta_{SL(O,i)} + \vartheta_{SB(O,i)}$". The solids entrainment ($\vartheta_{SL(O,i)}$ [$s^{-1}$]) is determined by Equation 94 (modified from Warren; 1985) but is only valid under negative bias conditions (i.e. when water, originating in the feed makes up, part, or all of the overflow water). Under positive bias condition, the liquid superficial velocity; "$J_l$" [cm $s^{-1}$] is positive

(water flows downward), meaning that no suspended solids flow to the overflow. The floating solids ($\vartheta_{SB(O,i)}$ [$s^{-1}$]) is determined by Equation 95 (modification of the plug flow kinetic equation, Equation 57) after accounting for restrictions of bubble loading: "$\vartheta_{B(O,i)}\ \phi_{SB} \geq \vartheta_{SB(O,i)}$".

$$\vartheta_{SL(O,i)} = k_e J_{l(O,i)} \left( \frac{C_{p(i)} + C_{p(i+1)}}{2} \right) \qquad \text{Equation 94}$$

$$\vartheta_{SB(i)} t_{(i)} = \left[ C_{pf(i)} h_{(z)} - \vartheta_{SLF(i)} \frac{t_{(i)}}{2} \right] \left( 1 - e^{-k_{f(i)} t_{(i)}} \right) \qquad \text{Equation 95}$$

Where

"$C_p$" [$cm^{-1}$] is the specific solids-surface-area,

"$C_{pf}$" [$cm^{-1}$] is the specific floatable solids-surface-area: $C_{pf(1)} = C_{p(1)}\ R_\infty$,

"$h_{(z)}$" [cm] is the flotation zone height,

"$J_{l(O)}$" [cm $s^{-1}$] is the liquid superficial overflow velocity,

"$k_e$" [dimensionless] is the entrainment parameter,

"$k_{f(i)}$" [$s^{-1}$] is the flotation rate constant,

"$R_\infty$" [dimensionless] is the maximum recovery of floatable mineral parameter,

"$t_{(i)}$" [s] is the sample time interval,

"$\phi_{SB}$" [dimensionless] is the ratio of maximum solids-surface-area to bubble-surface-area,

"$\vartheta_B$" [$s^{-1}$] is the bubble-surface-area flux,

"$\vartheta_{SB}$" [$s^{-1}$] is superficial attached-solids surface-area flux,

"$\vartheta_{SLF}$" [$s^{-1}$] is the superficial, floatable, suspended-solids surface-area flux, and

"$\vartheta_{SL}$" [$s^{-1}$] is the superficial suspended-solids surface-area flux.

Equation 94 is derived in the entrainment section (5.3.9.4) of this model, whereas Equation 95 is derived in the kinetic relationship section (5.3.11.1).

The four parameters are adjusted using a "downhill" simplex method (non-linear regression) to minimize error between objective function response and test data. The purpose of this numerical manipulation is to find the minimum of a multidimensional function as first outlined by Nelder and Mead (1965). A simplex is a geometric figure of N dimensions and N+1 points with interconnecting segments. This figure is a triangle in two dimensions and a tetrahedron in three dimensions. In multidimensional space, it is not possible to bracket a minimum, and thus, the minimum located by this procedure may be a local minimum.

Initial parameter values are estimated. The simplex routine then changes the values (reflections) of one dimension (one parameter) by a set amount and determines if the function results in a lower value. If a lower value does result, that dimension is maintained otherwise the original value is used. If the initial reflection does not return a lower value the step is performed with the opposite sign. This reflection is repeated with all dimensions. Performing one reflection with each dimension is called a step. Upon subsequent steps, a reflection that does not return a lower value results in the reflection size being reduced. If this operation still does not result in a reduction, the reflection sign is also changed. If changes to both the sign and reflection size do not result in a decrease in the function value the next dimension is determined without change of the original value but with a reflection size reduction. Once the overall change in the function value is less than a specified tolerance the function ends and returns the values of each dimension.

The down-hill simplex method of non-linear regression will find local, or absolute minimums depending on the shape of the n-space and the initial parameter values. Thus, the initial parameter value estimations are important.

Each time-recovery test should include at least five samples (one degree of freedom) although error is reduced as the number of samples increase; a minimum of six samples is recommended. Repeated tests are necessary to statistically justify the results (Box and Draper; 1987).

Each timed sample must include grades for each mineral and size-class along with the amount of water recovered to the overflow and an overflow bubble size estimation. The model can be used without size-class information, but is more useful with it. All particles are assumed liberated. Particle density and the aspect ratio (ratio between mineral particle major axis and minor axis, or sphericity) must also be known to properly estimate the particle settling-velocity ($u_p$ [cm $s^{-1}$]). Remainder mass and assays are required.

This model uses surface-area throughout. Particle-surface-area is assumed to report to the overflow stream by flotation or entrainment. The superficial attached-solids surface-area flux ($\vartheta_{SB}$ [$s^{-1}$]) is assumed limited to a specific fraction of the available superficial bubble-surface-area flux ($\vartheta_B$ [$s^{-1}$]) – this limitation is dictated by carrying capacity. Flotation is characterized by the flotation rate constant ($k_f$ [$s^{-1}$]). Each mineral and size-class is divided into the surface-area that is floatable and unfloatable by the maximum recovery. Carrying capacity is described by the maximum particle-bubble surface-area ratio (Cg [dimensionless]). Entrainment is estimated by the entrainment factor ($k_e$ [dimensionless]).

### 5.3.4 Liberation

Laboratory flotation tests assume that the material is liberated. When the secondary minerals are locked within the primary mineral without surface exposure, there will be no difference in flotation between the pure primary mineral and the non-liberated particle. In cases where the secondary mineral is showing, flotation rates may be affected resulting in a higher or lower effective rate constants depending on the probability of collision and attachment. The presence of non-liberated particles will result in increased error in both the entrainment and rate parameters.

### 5.3.5 Vessel Mixing

Both the mechanical-cell and column laboratory-scale units behave as plug flow vessels when operated in batch, with respect to time. Test-scale mechanical-cells, behave as "plug-flow" vessels because they are well agitated, thus, particle concentration is dependent on time and not axial or radial location. The continuous recycle, in the batch column, provides a concentration independent of axial or radial location but not with time.

The batch column system operates as a perfectly mixed unit, with respect to constant concentration at any location, when the column has no height. As the column height increases there will be a concentration gradient along it's length as material is removed from the system. As such, to approximate constant concentration height should be as short as possible.

As the recycle rate in the column increases the concentration gradient within column become less and the column will operate closer to constant concentration with respect to location. Thus, the column should be operated with as high a recycle rate as possible.

Bubble loading occurs with bubble residence time. To test bubble loading the bubble residence times should be either sufficient to fully load the bubble or approximately equal to the bubble residence time of industrial columns. Bubble residence time is increased with column height.

The column height was designed using a target bubble residence time half that of an industrial column. Bubble size distribution was assumed with an average size of 0.11 cm with three standard deviations falling between 0.07 and 0.15 cm (CESL; 1998, and Flint; 1989). An average sized bubble will have a residence time of approximately 30 seconds over a 135 cm distance when gas holdup is 0.10 and three-phase density is 1.0. This residence time is approximately half that in an industrial column with a collection zone height of 600 cm and a slurry velocity of 1.0 cm/s.

### 5.3.6 Column Dead Zone

Batch column construction includes a small dead volume below the sparging element. This zone is shown in Figure 27.

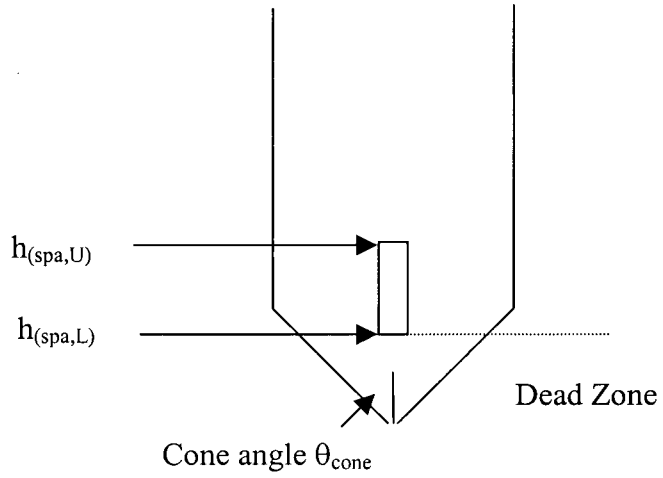


**Figure 27: Dead-zone volume design**

In Figure 27, "$h_{(spa,U)}$" [cm] is the upper sparger elevation; "$h_{(spa,L)}$" [cm] is the lower sparger elevation and "$\theta_{cone}$" [radians] is the column-base cone-angle. The column diameter at the sparger base ($d_{c(spa,L)}$ [cm]) can be determined using Equation 96 (assuming a base cone).

$$d_{c(spa,L)} = 2h_{(spa,L)} \sin\theta_{cone} \qquad \text{Equation 96}$$

The dead volume ($V_d$ [$cm^3$]) is the cone volume under the sparger as determined by Equation 97.

$$V_d = \frac{\pi}{12} h_{(spa,L)} d^2_{c(spa,L)} \qquad \text{Equation 97}$$

Equation 97 is specific for the cone angle of the test column. Other relationships are required for different column designs. The vessel dead volume is subtracted from total vessel volume in the residence time calculations.

## 5.3.7 Column Residence-time

The residence-time of all solids in the mechanical flotation cell is the time elapsed since the start of flotation. In the batch flotation column, there is both an active floating volume and a recycle volume. The ratio between the active residence-time and the elapsed time can be determined using Equation 98.

$$\frac{t}{t_{(i)}} = \frac{\left[\frac{\left(h_{(v)} - h_{(f)} - h_{(spa)}\right)\left(1-\varepsilon_g\right)}{J_l + u_p}\right]_1}{\left[\frac{\left(h_{(z)} - h_{(f)} - h_{(spa)}\right)\left(1-\varepsilon_g\right)}{J_l + u_p}\right]_1 + \left[\frac{h_{(r)}}{J_r - u_p}\right]_2 + \left[\frac{V_d}{A_c J_l}\right]_3}$$

Equation 98

Equation 98 consists of three residence-times demarked as subscript "1" through "3". Residence-time "1" is the active system residence-time wherein bubbles and solids are colliding. Residence-time "2" is the recycle line residence-time. Time "3" is the dead-volume residence-time ($V_d$ [$cm^3$]) within the column -- a function of sparger placement and system geometry (Equation 97).

In Equation 98, "t" [s] is the active residence-time; "$t_{(i)}$" [s] is the elapsed time; "$h_{(v)}$" [cm] is the total vessel axial elevation; "$h_{(spa)}$" [cm] is the elevation of the lowest decent of bubbles originating from the sparger; "$h_{(r)}$" [cm] is the recycle line length; "$h_{(f)}$" [cm] is the froth – pulp interface elevation; "$J_l$" [cm $s^{-1}$] is the superficial liquid velocity in the vessel; "$J_r$" [cm $s^{-1}$] is the superficial velocity in the recycle line and "$u_p$" [cm $s^{-1}$] is the particle settling-velocity with respect to the liquid.

The ratio of active residence-time to elapsed time (Equation 98) is shown in Figure 28 for various slurry flow rates (downward) and particle settling velocities. This example assumes that the collection-zone height ($h_{(Col)} = h_{(v)}-h_{(f)}$) is 150 cm; the gas holdup is 10% ("$\varepsilon_g$" = 0.1); the recycle line length ($h_r$) is 200 cm; the sparger height ($h_{(spa,U)}-h_{(spa,L)}$) is 4 cm; the vessel diameter ($d_v$) is 10.2 cm and the recycle tube inside diameter is 0.95 cm.

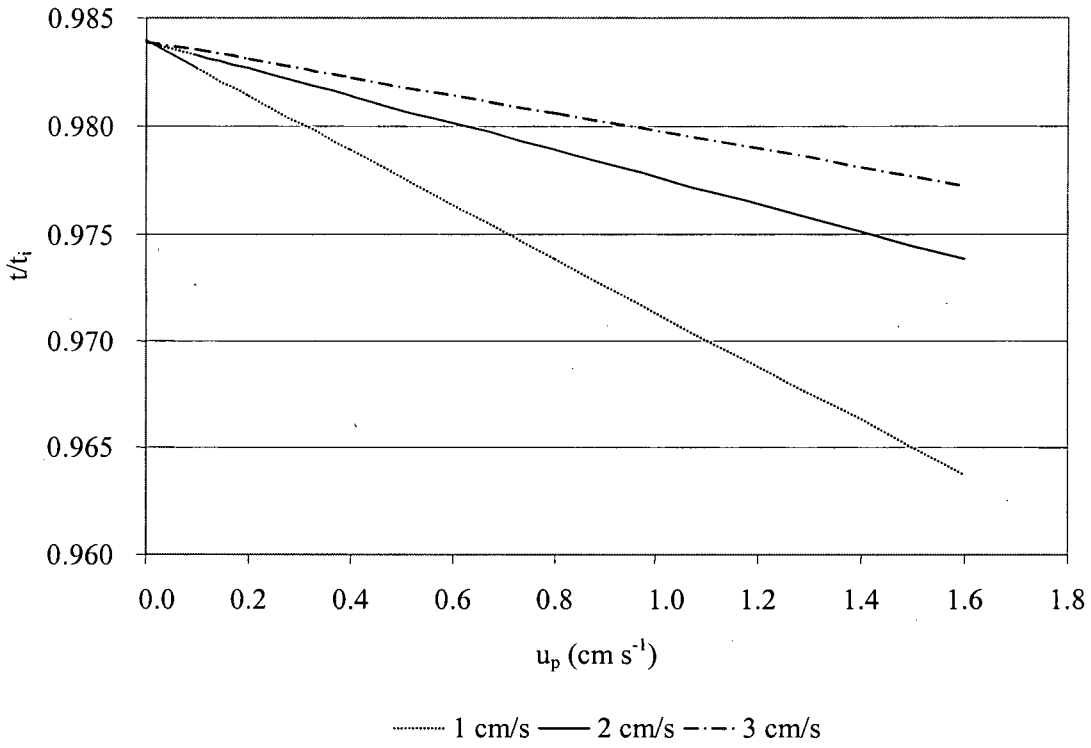


**Figure 28: Ratio of active residence-time (t [s]) to elapsed test time ($t_i$ [s]) for typical particle settling velocities ($u_p$ [cm $s^{-1}$]) and downward slurry velocities (1, 2, and 3 cm $s^{-1}$).**

Under the conditions tested, as described, within the column model, $0.985 \geq t/t_{(i)} \geq 0.98$. When measurement error is taken into account, the difference between $t/t_{(i)}$ and 1 is small; thus, "t" can be considered to be "$t_{(i)}$" with minimal error.

## 5.3.8 Column Maximum Recycle Rate

Maximum batch column recycle rate, or downward column slurry flow, is determined by the rate at which bubbles no longer ascend through the vessel. As such, "$J_{sl(max)}$" must be less than "$u_b$" [cm $s^{-1}$]. The maximum superficial slurry velocity occurs within the sparger element elevation. The superficial slurry velocity at this point is determined by the ratio of column area to the minimum column area ($A_{cm}$) as shown in Equation 99

$$J_{sl(spa,A_{cm})} = J_{sl}\frac{A_c}{A_{c(spa,A_{cm})}} \qquad \text{Equation 99}$$

In Equation 99 "$J_{sl}$" [cm $s^{-1}$] is the slurry superficial velocity; "$A_c$" [$cm^2$] is the column cross-sectional area and "$A_{cm}$" [$cm^2$] is the minimum column cross-sectional area.

The maximum slurry velocity can be determined if the assumption is made that the downward slurry velocity must be lower than the minimum bubble rise-velocity. The maximum downward slurry velocity will occur within the sparger elevation in most test columns. A maximum slurry velocity estimation can be made using Equation 100.

$$J_{sl(\max)} \le \frac{\pi}{4}\frac{u_b}{A_c}\left[\left(2h_{(spa,x)}\sin\theta_{cone}\right)^2 - d_{spa}^2\right] \qquad \text{Equation 100}$$

In Equation 100 "$u_b$" [cm $s^{-1}$] is the bubble rise-velocity; "$A_c$" [$cm^2$] is the column cross-sectional area; "$h_{(spa,x)}$" [cm] is the elevation between the upper and lower sparger elevations; "$\theta_{cone}$" [radians] is the conical column base angle and "$d_{spa}$" [cm] is the outside sparger diameter. This calculation is based upon column base geometry and will vary from column to column. Equation 100 assumes that a single bubble size exists. If the bubble size distribution is known, the rise velocity can be adjusted to reflect the smaller bubble sizes. This equation assumes a single, vertically mounted, sparger in a conical shaped column base. The elevation used ($h_{(spa,x)}$ [cm]) is the elevation with the smallest cross-sectional area as determined by Equation 101.

$$A_{cm} = \frac{\pi}{4}\left(d_{c(x)}^2 - d_{spa(x)}^2\right)\left(1-\varepsilon_g\right) \qquad \text{Equation 101}$$

## 5.3.9 Entrainment

### 5.3.9.1 Factors and Error

This model only assesses entrainment differences between minerals and size-classes that are constant with time under the test operating conditions. The characteristics of minerals that effect this entrainment are differences in size, shape and density. These factors can be analyzed using the data from properly conducted time-recovery tests. This model assumes that entrainment can be represented as a parameter array ($k_e$ [dimensionless]), corresponding to each size-class and mineral fraction.

All other factors are discounted since constant test conditions and operations were maintained. The entrainment factor is assumed to remain constant with time, and thus, time dependent variables such as change in slurry density, slurry viscosity, and froth characteristics are ignored. Changes in conditions with time may cause the entrainment parameter to also change with time.

Operational error such as variations in air rate, reagents, agitation, froth depth and removal rates are ignored. Change in these variables may result in different entrainment factors between tests, or within a test, if operation is are not kept constant.

The entrainment parameters calculated by this model are dependent upon the conditions of flotation such as the suspension viscosity and the hindered settling velocities that exist within the cell. Therefore, the entrainment parameters determined must be considered an "average" value over the test duration. These values may not hold when flotation conditions are significantly different; thus, extrapolation using this parameter must be done with care.

### 5.3.9.2 Mechanical-Cell Model

Laboratory mechanical-cells are almost perfect mixers. Bubble size within these cells is difficult to assess. Also, little axial stratification of solids occurs; there is approximately the same concentration of large and small particles along the cell vertical axis. Thus, there will be little difference in the entrainment caused by feed water or water originating in bubble wakes. In addition, wash-water is usually not added to the froth of these cells. Thus, there should be no need to quantify the water source in the froth zone. The feed water source is important in larger pilot- or industrial-scale units and must be understood in order to properly scale the results to larger mechanical-cells.

The water content in a vessel ($V_{l(v)}$ [$cm^3$]) may not be constant. Water was added throughout the tests in order to maintain cell volume. The vessel water content was not constant since solids volume was removed throughout the test (conservation of volume). "$V_{l(v,i)}$" [$cm^3$] can be estimated by determining the pulp zone volume and the volume fraction of solids within the pulp as shown by Equation 102.

$$V_{l(v,i)} = (L_x - h_{(f,i)})L_y L_z \phi_{l(i)} \qquad \text{Equation 102}$$

In Equation 102 "$L_x$" [cm] is the cell vertical axis length; "$L_y$" [cm] is length and "$L_z$" [cm] is depth. The "$L_yL_z$" term is replaced by cross-sectional surface-area in non-rectangular vessels. "$h_{(f,i)}$" [cm] is the distance from the cell lip to the top of the pulp-zone elevation (also in Equation 102), and "$\phi_{l(i)}$" is the average volume fraction of water in the cell during time "i". The water fraction ($\phi_{l(i)}$) becomes larger as flotation removes solids from the vessel.

### 5.3.9.3 Flotation Columns

Flotation columns are characterized by the addition of wash-water to the froth zone ($J_{IW}$ [cm $s^{-1}$]). This model has been developed for column tests that are run with a slightly positive bias, but should be accurate for larger positive bias or a negative bias. Although the average froth-zone bias may be positive, this bias may not exist throughout the vessel cross-section. Localized flows, in both time and space, may provide negative bias conditions for particles to become entrained. In general, mixing within a properly designed and aligned laboratory-scale column is minimized in both the pulp and froth phases; thus plug flow conditions can be assumed in laboratory-scale columns. The test equipment had a good cross-sectional distribution of wash-water (by visual inspection); no swells, uneven flows, or stagnant areas were observed in the froth surface.

### 5.3.9.4 Determination of Entrainment

The same equations can be used to estimate both column and mechanical-cell entrainment. According to Warren (1985), the entrainment recovery of a solid is proportional to the water recovery, the solids concentration and a constant that is dependent upon mineral characteristics and particle size. That constant in this model is the dimensionless "$k_e$" as shown in Equation 103.

$$\vartheta_{SL(O,i)} = k_e J_{l(O,i)} \left( \frac{C_{p(i)} + C_{p(i+1)}}{2} \right) \qquad \text{Equation 103}$$

Equation 103 is derived by assuming that the overflow superficial suspended-solids surface-area flux ($\vartheta_{SL(O,i)}$ [$s^{-1}$] -- average throughout a timed sample) is proportional to the specific solids surface in the vessel and the vessel superficial overflow-water rate. The superficial solids-surface-area flux is defined as the rate at which solids surface-area passes an elevation divided by the vessel cross-sectional area. "$k_e$" [dimensionless] is the proportionality constant of this relationship. The concentration of surface-area used in Equation 103 is the average within that time interval. The non-floating solids entrainment ($\vartheta_{SLN}$ [$s^{-1}$]) is calculated using

non-floatable specific surface ($C_{pn}$ [$cm^{-1}$]). The floatable component equivalent, ($\vartheta_{SLF}$ [$s^{-1}$]), is calculated using the floatable specific surface ($C_{pf}$ [$cm^{-1}$]). Total entrainment is the sum of floatable and non-floatable components.

In order to determine an initial entrainment parameter value ($k_e$), for the simplex routine, the assumption of Ross (1990b) is used. The overflow solids are composed of both floating ($\vartheta_{SB(O)}$) and entrained solids ($\vartheta_{SLN(O)} + \vartheta_{SLF(O)}$). Using Ross' approach, after a long residence-time, the flotation product to overflow is reduced to zero ($\vartheta_{SB(O,L)} = 0$) and no floatable material remains within the vessel. Thus, $\vartheta_{S(O,L)} \cong \vartheta_{SL(O,L)}$ where L indicates the last sample. The initial entrainment proportionality constant ($k_e$) can determined with these assumptions (Equation 104).

$$k_e \approx \frac{2\vartheta_{S(O,L)}}{\left(C_{p(L)} + C_{p(r)}\right) J_{l(O,L)}} \qquad \text{Equation 104}$$

In Equation 104, "$C_{p(r)}$" is the remainder fraction, or the solids specific surface remaining in the cell at the end of the test. In a flotation column, the overflow superficial liquid rate ($J_{l(O)}$ [cm $s^{-1}$]) must be broken into water that originates in the feed ($J_{lF(O)}$ [cm $s^{-1}$]) and the flow that originates in the wash-water ($J_{lw(O)}$ [cm $s^{-1}$]) since entrainment is only a function of the former. This value is not known in a column test since wash-water is added to the froth. Both "$k_e$" and the superficial wash-water rate ($J_{lw(O)}$ [cm $s^{-1}$]) are unknown, and thus, Equation 104 cannot be solved without further information. The initial "$k_e$" value of a column, run with an average positive bias, assumes that the volume of water originating in the feed which reports to the overflow ($J_{lF(O)}$ [cm $s^{-1}$]) is zero. This assumption may not be valid when wash-water is not distributed well, if a negative bias is run, or if the froth depth changes cyclically. Adjustments are expected to this initial value in the simplex - least squares minimization routine. A more rigorous test would also measure the temperature of the vessel water, wash-water and overflow products (Uribe-Salas et. al.; 1990: Equation 27) to enable a liquid mass balance to be performed, and thus, to determine "$J_{lw(O)}$" [cm $s^{-1}$] – the wash-water flow to the overflow.

There may be considerable error in determining the initial entrainment parameter of a floatable mineral since the assumption that the last sample contains only entrained solids may not be valid. Thus, if there is a similar non-floating mineral, its' entrainment parameter may be used to estimate the floating materials entrainment.

Larger particles will be entrained less than smaller particles since they have a larger settling velocity and their momentum is independent of the water flow. Thus, a greater initial entrainment parameter estimate for a larger particle size is probably in error. In this case, the estimate from the smaller particle size-class could be used.

The surface-area flux response in a test wherein the only surface reporting to the overflow is by entrainment will look somewhat like Figure 29 (as predicted by Equation 103). This figure uses the data of INCO "batch mechanical-cell test #1 (details in the results appendix) with all kinetic terms set to zero.

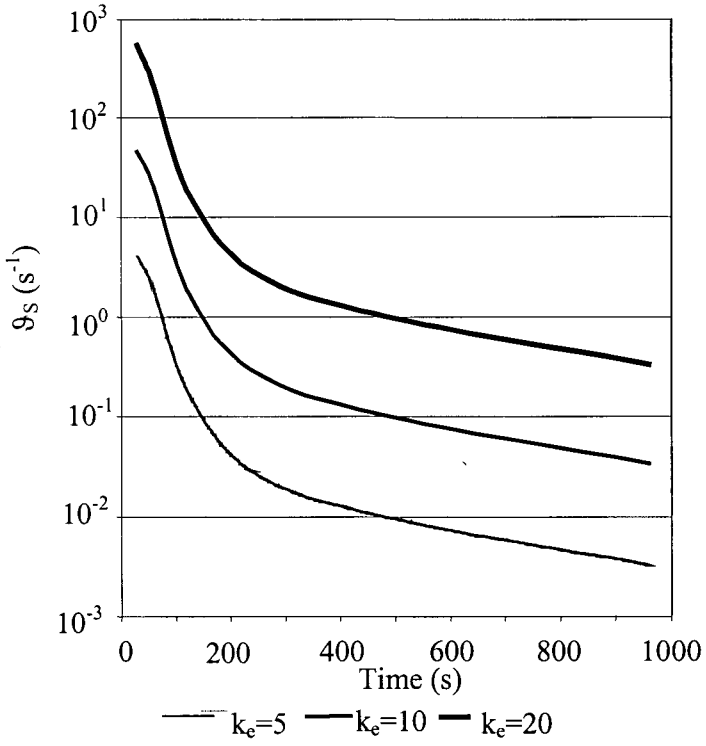


**Figure 29: Example entrainment without kinetic flotation**

### 5.3.10 Specific Surface

The specific solids surface ($C_{p(0)}$ [$cm^{-1}$]) is calculated according to Equation 105. In Equation 105, "$S_{SL(0)}$" [$cm^2$] is the total initial solids-surface-area contained within the zone, "A" [$cm^2$] is vessel cross-sectional area and "$h_{(z)}$" [cm] is the total zone elevation.

$$C_{p(0)} = \frac{S_{SL(0)}}{Ah_{(z)}} \qquad \text{Equation 105}$$

The solids surface area contained within a zone; "$S_{SL(0)}$" is calculated by setting the mass; "m" [g] of Equation 89 to the mass of the size class contained within the vessel at t = 0. The specific surface-area floatable component ($C_{pf}$ [$cm^{-1}$]) is calculated using Equation 106 and the non-floating component ($C_{pn}$ [$cm^{-1}$]) is calculated using and Equation 107.

$$C_{pf(0)} = C_{p(0)}R_{\infty} \qquad \text{Equation 106}$$

$$C_{pn(0)} = C_{p(0)}\left(1 - R_{\infty}\right) \qquad \text{Equation 107}$$

In Equation 106 and Equation 107, "$R_{\infty}$" is the maximum recovery. Subsequent values of specific surface ($C_{p(i+1)}$ [$cm^{-1}$]) can be determined using Equation 108 and Equation 109 for floatable and non-floatable components respectively.

$$C_{pn(i+1)} = C_{pn(i)} - \frac{\vartheta_{SLN(O,i)}t_{(i)}}{h_{(z)}} \qquad \text{Equation 108}$$

$$C_{pf(i+1)} = C_{pf(i)} - \frac{\left(\vartheta_{SLF(O,i)} + \vartheta_{SB(O,i)}\right)t_{(i)}}{h_{(z)}} \qquad \text{Equation 109}$$

Where "$\vartheta_{SLN(O,i)}$" [$s^{-1}$] is the overflow superficial, non-floating, suspended-solids surface-area flux; "$\vartheta_{SLF(O,i)}$" [$s^{-1}$] is the overflow superficial, floating, suspended-solids surface-area flux and "$\vartheta_{SB(O,i)}$" [$s^{-1}$] is the overflow superficial attached-solids surface-area flux while "$t_{(i)}$" is the elapsed sample time.

## 5.3.11 Flotation

### 5.3.11.1 Kinetic Relationship

Kinetic relationships are used to predict the transfer of solids-surface-area from the liquid phase ($\vartheta_{SLF(i)}$ [$s^{-1}$]) to the bubble phase ($\vartheta_{SB(i)}$ [$s^{-1}$]).

This model uses a plug flow relationship wherein the overflow-surface-area is predicted using the kinetic first-order relationship shown in Equation 110 (presented earlier as Equation 95).

$$\vartheta_{SB(i)} t_{(i)} = \frac{S_{SB(i)}}{A} = \left( C_{pf(i)} h_{(z)} - \vartheta_{SLF(O,i)} \frac{t_{(i)}}{2} \right) \left( 1 - e^{-k_{f(i)} t_{(i)}} \right) \qquad \text{Equation 110}$$

In Equation 110, "$\vartheta_{SB}$" [$s^{-1}$] is the superficial surface-area flux of solids attached to the bubbles and "$\vartheta_{SLF}$" [$s^{-1}$] is the superficial surface-area flux of floatable solids removed by suspension in water), "S" is the surface area, "$C_{p(i)}$" [$cm^{-1}$] is the surface-area concentration or solids specific surface of floatable solids in the zone, "$h_{(z)}$" [cm] is active zone axial length and "$t_{(i)}$" [s] is the elapsed interval time.

Equation 110 is derived from Equation 57. The concentration of solids in the active flotation volume is the specific floatable surface through the height of the volume, "$C_{pf(i)}h_{(z)}$" [dimensionless]. This concentration is modified to account for entrainment by subtracting half the suspended floatable solids that move by bulk transport to overflow.

Carrying capacity may limit the solids-surface-area floated. Equation 110 is only valid when flotation is "free" or "unhindered", otherwise, the model will overestimate the material floated. In this model, the output value of Equation 110 is "capped" by carrying capacity considerations. Under "hindered" conditions, the initial flotation rate constant values may be significantly different than those obtained later in the test. In order to obtain an accurate rate, those time intervals that are "hindered", must be excluded from flotation rate constant ($k_f$ [$s^{-1}$]) estimation.

In addition, Equation 110 does not calculate total solids overflow unless the solids-surface-area of entrained material is added. The initial specific floatable solids surface ($C_{pf(0)}$ [$cm^{-1}$]) is determined by multiplying the total, initial, specific solids surface ($C_{p(0)}$ [$cm^{-1}$]) by the maximum recovery ($R_\infty$) as shown in Equation 106 and Equation 107.

### 5.3.11.2 Maximum Floatable Surface-Area

The maximum floatable solids-surface-area is expressed as a maximum recovery; ($R_\infty$ [dimensionless]). The solids-surface-area available for flotation is assumed to be a set fraction ($R_\infty$) of the total solids-surface-area (Equation 111). The equation estimates the maximum recovery as being the total solids-surface-area recovered, or that could have been recovered, divided by the initial surface-area contained within the zone.

$$R_\infty \approx \frac{\sum_{i=1}^{L}\left[\left(\vartheta_{SB(O,i)} + \vartheta_{SLF(O,i)}\right)t_{(i)}\right]}{C_{p(0)}h_{(z)}} \qquad \text{Equation 111}$$

In Equation 111, "$\vartheta_{SB(O,i)}$" [$s^{-1}$] is the overflow superficial attached-solids surface-area flux (interval "i"); "$\vartheta_{SLF(O,i)}$" [$s^{-1}$] is the overflow superficial, floatable, suspended-solids surface-area flux (interval "i"); "$C_{p(0)}$" [$cm^{-1}$] is the solids-surface-area concentration within the cell at the beginning of the test, and "$h_{(z)}$" [cm] is the zone axial dimension.

Floated solids-surface-area and entrained floatable solids-surface-area rates may not be known. A crude initial value of maximum recovery can be determined by assuming that entrainment is not present in any but the last sample, and that the last sample consists only of entrained surfaces. This simplifies Equation 111 into Equation 112.

$$R_\infty \approx \frac{\sum_{i=1}^{L-1}\left[\vartheta_{SB(O,i)}t_{(i)}\right]}{C_{p(0)}h_{(z)}} \qquad \text{Equation 112}$$

Within a size class, errors in particle size determination do not effect the maximum recovery estimation since this value is a ratio of floatable surface area to entire surface area.

### 5.3.11.3 Rate Estimation

Equation 110 can be rearranged to isolate the rate constant as shown in Equation 113.

$$k_{(i)}t_{(i)} = -\ln\left[1 - \frac{\vartheta_{SB(O,i)}t_{(i)}}{C_{pf(i)}h_{(z)} - 0.5\vartheta_{SLF(O,i)}t_{(i)}}\right] \qquad \text{Equation 113}$$

In Equation 113, "$\vartheta_{SB}$" [$s^{-1}$] is the superficial attached solids surface-area flux and "$\vartheta_{SLF}$" [$s^{-1}$] is the superficial suspended solids surface-area-flux that are removed from the vessel by entrainment during the timed sample "i". Also in Equation 113, "$C_{pf(i)}$" [$cm^{-1}$] is the floatable surface-area concentration in the vessel; "$h_{(z)}$" [cm] is the zone axial dimension and "$t_{(i)}$" [s] is the sampled interval elapsed time.

An initial rate constant estimate ($k_f$ [$s^{-1}$]) can be calculated assuming entrainment of both floatable and non-floatable surfaces are zero for each sample. The average rate can then be determined over the "L-1" samples using Equation 114 (assuming that the rate constant remains constant throughout the test). "L-1" samples are used under the simplifying assumption that no entrainment occurs with the exception of the last sample that includes only entrained material.

$$k_f t_{(L-1)} = -\ln\left[1 - \frac{\sum_{j=1}^{L-1}\vartheta_{SB(i)}t_{(i)}}{C_{p(0)}h_{(z)}}\right] \qquad \text{Equation 114}$$

The flotation rate constant ($k_f$ [$s^{-1}$]) is assumed to remain constant. This assumption is only valid if the induction time of all particles within the floating population is the same at all times throughout the test. A distribution of induction times does exist in "real" flotation systems. Thus, this model is only an approximation of a "real" system.

### 5.3.11.4 Errors Factors in Rate Estimation

Delays in the onset of flotation can be incorporated into the model by assigning a positive value to the test start time ($t_0 > 0$). The time of flotation initiation ($t_0$) may be greater than one or more of the test time intervals ($t_n$). This manipulation results in a loss of degrees of freedom; additional samples or repeat tests may be required. This type of delay could be caused by testing error, by solids buildup to form a stable froth (froth mineralization) prior to an affective overflow product being produced, or to "crowding" effects wherein a mineral species with limited flotation ability do not report to the overflow until later in a test. The effect of delay on the floated solids-surface-area rate is shown in Figure 30. The solids-surface-area recovery decreases as the concentration of floatable solids within the vessel becomes depleted. When a delay in flotation occurs, an apparent lowering of this rate appears in the initial sample interval(s).

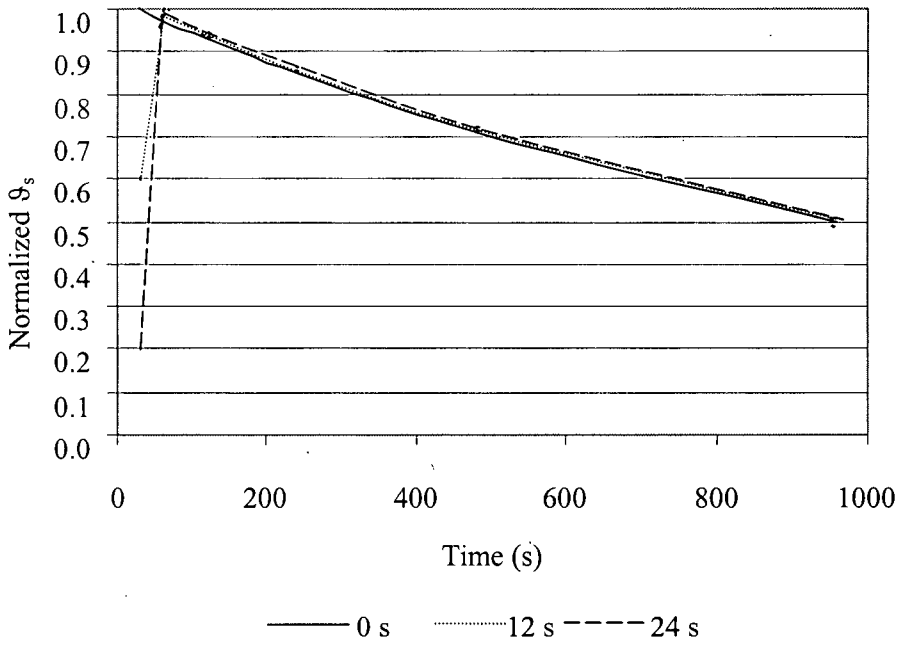


**Figure 30: Illustration of the effect of delays in flotation time on the floated solids-surface-area flux. Delays of 0, 12 and 24 seconds are shown.**

Within a size class, errors in particle size determination do not affect the rate constant since the rate is a function of recovery which is a ratio of surface area removed and that initially present.

## 5.3.12 Carrying Capacity

### 5.3.12.1 Introduction

The kinetic equations used in section 5.3.11 assume an excess bubble surface under conditions of uninhibited flotation or "free" flotation. This assumption may not always hold. "Hindered" flotation occurs when available bubble-surface-area limits flotation. This model accounts for "hindered" flotation by capping the surface floated to a maximum, or to a carrying capacity.

Flotation is essentially a surface-area phenomenon; a solids-surface-area is carried by a bubble-surface-area to the vessel surface and is removed. Thus, the maximum flux of solids-surface-area depends, in part, upon bubble-surface-area flux and maximum particle load. The bubble-surface-area flux is a function of both the number of bubbles and the size distribution of those bubbles. Bubble size is a function of agitation, air rate, and reagent dosage within a mechanical-cell batch flotation test. In flotation columns agitation is not a factor; the sparging system and reagents, however, are important. The bubble-surface-area flux can be estimated with bubble size distribution knowledge.

A bubble that has no residence-time cannot carry particles. More particle collisions occur with increased residence-time. The increased residence-time results in increased bubble loading. Loading rate will slow when bubble loaded area increases, as the "cap" of free bubble surface shrinks and particle sliding distance is reduced. As this occurs, attachment becomes less probable until at an infinite time the bubble is fully loaded.

Within a batch mechanical-cell, the average bubble residence-time within the pulp zone is on the order of one second depending on the slurry conditions, size of flotation vessel, and the bubble size produced. This low residence-time means that bubbles may not be fully loaded as they pass into the froth zone, or as they pass into the overflow. The vessel is still "hindered", however, because particles do not have the chance to load the bubble. The bubble-surface-area flux used, or available, may be lower than the maximum.

Bubble loading will occur over a period of time. Thus, the bubble residence-time is an important factor in determining the amount of solid that is carried. As such, the maximum

load of bubbles in a laboratory-scale batch mechanical-cell will probably be lower than that in a laboratory- or industrial-scale column unit.

### 5.3.12.2 Loading

Maximum solids-surface-area removed by flotation is related to bubble-surface-area as shown in Equation 115, although the system kinetics may result in lower removal rates.

$$\vartheta_{B(i)}\phi_{SB} \geq \vartheta_{SB(i)} \qquad \text{Equation 115}$$

Where "$\vartheta_{SB(i)}$" [$s^{-1}$] is the superficial attached-solids surface-area flux, "$\vartheta_{B(i)}$" [$s^{-1}$] is the superficial bubble-surface-area flux and "$\phi_{SB}$" is the ratio of loaded solids surface area to bubble surface area. This definition of loading uses the total particle surface-area rather than the cross-sectional area.

A generally accepted maximum solids-surface to bubble-surface load ($\phi_{SB}$) is 0.50 (Jameson et. al.; 1977) although tests results may indicate higher or lower values. Mechanistically, the loading value will be dependent upon the particle major axis cross-sectional area and a packing factor that, in turn, depends on particle shape, size distribution and hydrophobicity. An illustration of the particle major axis is shown in Figure 31.

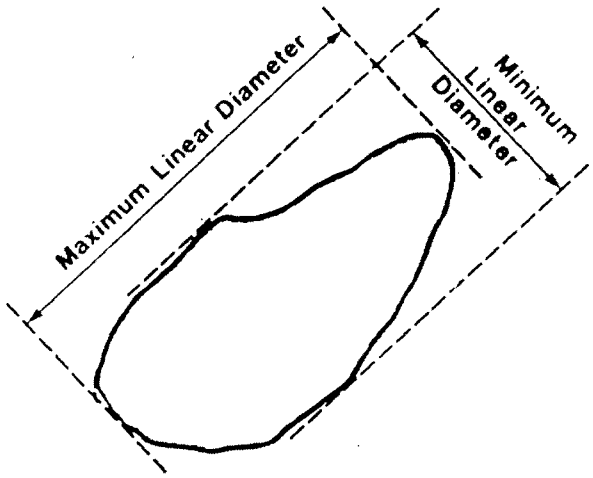


**Figure 31: Particle major (maximum linear diameter) and minor (minimum linear diameter) axis illustration (Kelly and Spottiswood; 1982)**

"$\vartheta_B$" [$s^{-1}$] is the superficial bubble-surface-area rate. The value of "$\vartheta_B$" is a function of the bubble size distribution and the number of bubbles. The size of bubbles is not that of the bubbles in the flotation pulp, but rather of those that pass the upper zone boundary. In a laboratory-scale mechanical flotation vessel, the size and distribution of these bubbles are usually unknown, but can be approximated visually or by measuring bubble sizes from photographs. Within a flotation column, the size of bubbles within the pulp zones can be estimated by various techniques.

Taking the volume of a sphere to be $\pi d_b^3/6$ and the surface area to be $\pi d_b^2$, the superficial bubble-surface-area flux from the pulp into the froth can be calculated using Equation 116 (presented earlier as Equation 21).

$$\vartheta_{B(i)} = \frac{6J_{g(i)}}{d_{b(i)}} \qquad \text{Equation 116}$$

In Equation 116, "$d_b$" [cm] is the average bubble diameter and "$J_g$" [cm $s^{-1}$] is the superficial gas velocity.

The total superficial total-solids surface-area flux achieved through flotation for each timed sample is the sum of all mineral and size-class areas as found in Equation 117.

$$\vartheta_{S(O,i)} = \frac{6}{t_{(i)}} \sum_{h=1}^{m} \sum_{j=1}^{n} \frac{m_{(h,i,j)}}{\rho_{p(h)} d_{p(j)}} \qquad \text{Equation 117}$$

In Equation 117, "$\vartheta_{S(O,i)}$" [$s^{-1}$] is overflow superficial total-solids surface-area flux (interval "i") for mineral (m) and size-class (n); "m" [g] is the mass recovered to the overflow during sample "i"; "$\rho_{p(h)}$" [$g/cm^3$] is the particle density (varies with mineral), and "$d_{p(j)}$" [cm] is the particle diameter (varies with size-class).

The overflow superficial total-solids surface-area rate determination is shown in Equation 118 along with the components that make this overflow.

$$\vartheta_{S(O,i)} = \vartheta_{SB(O,i)} + \vartheta_{SLF(O,i)} + \vartheta_{SLN(O,i)} \qquad \text{Equation 118}$$

In Equation 118, "$\vartheta_{S(O,i)}$" [$s^{-1}$] is overflow superficial total-solids surface-area rate (interval "i"). The other superficial rates within this equation are the solids attached to the bubble overflow "$\vartheta_{SB(O,i)}$" [$s^{-1}$], solids entrained from the floatable solids fraction "$\vartheta_{SLF(O,i)}$" [$s^{-1}$] and solids entrained from the non-floatable solids fraction "$\vartheta_{SLN(O,i)}$" [$s^{-1}$].

All calculations using the superficial bubble-surface-area flux ($\vartheta_B$ [$s^{-1}$]) assume that the distribution of bubble sizes, by number, is approximately "normal" in nature with an average bubble size ($d_b$ [cm]) and a standard deviation ($\sigma$). An error of less than 2% is incorporated into the model when $\sigma <= 0.1$, while a $\sigma = 0.15$ gives an additional error of about 3.5%. Error increases rapidly if the curve is not "normal".

The loading of each sample ("$\phi_{SB(i)}$) can be determined using the relationship found in Equation 119 (a rearrangement of Equation 115).

$$\phi_{SB(i)} = \frac{\vartheta_{SB(i)}}{\vartheta_{B(i)}} \qquad \text{Equation 119}$$

In Equation 119, "$\vartheta_{SB(i)}$" [$s^{-1}$] is the sample overflow superficial attached-solids surface-area flux and "$\vartheta_{B(i)}$" [$s^{-1}$] is the superficial bubble-surface-area flux .

The particle-surface-area floated is the sum of all mineral and size-class float surfaces as predicted by kinetics as shown in Equation 120.

$$\vartheta_{SB(i)} = \sum_{k=1}^{m} \sum_{j=1}^{n} \vartheta_{SB(i,j,k)} \qquad \text{Equation 120}$$

In Equation 120, "i" is the sample; "$\vartheta_{SB(i)}$" [$s^{-1}$] is superficial attached-solids surface-area rate of particles (for all minerals (m) and size-classes (n)). The interval bubble load is then calculated using Equation 119. When the model predicts flotation loading greater than the

maximum load ($\phi_{SB(max)}$) each mineral, size-fraction, floated solids-surface-area is scaled by the ratio of maximum load to sample load ($\phi_{SB(max)}/\ \phi_{SB}$).

The maximum loading by solids on the bubbles will be at least as large as the maximum loading of the test timed intervals (Equation 121). There will be differences due to the kinetics of solids-surface-area attachment or to insufficient bubble residence-time. Significant unaccounted for entrainment will artificially increase this value.

$$\phi_{SB} \geq \max\left(\phi_{SB(i)}\right) \qquad \text{Equation 121}$$

Errors in bubble size measurement do affect the value of the bubble loading parameter. Bubble loading is proportional to bubble diameter, assuming a constant gas flow rate and superficial attached solids surface area flux, as shown mathematically in Equation 122 and graphically in Figure 32.

$$\phi_{SB} \propto d_b \qquad \text{Equation 122}$$

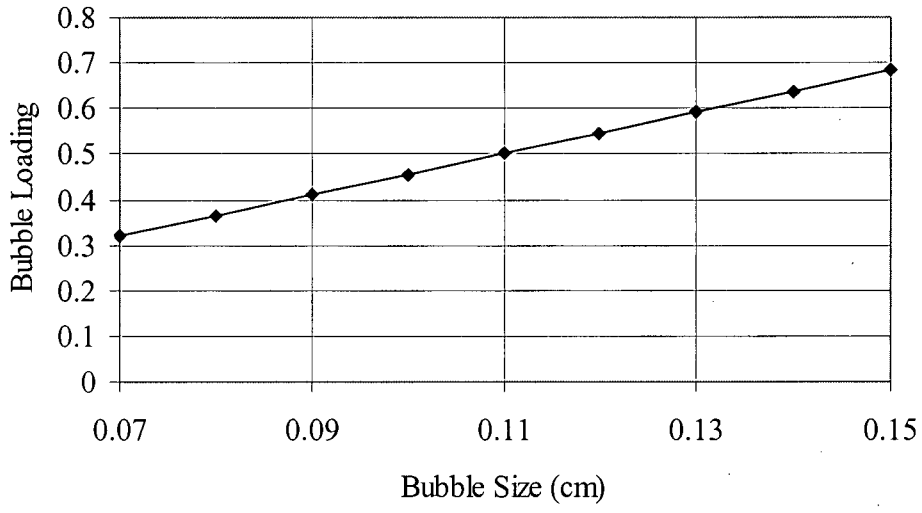


**Figure 32: Response of bubble loading to bubble diameter**

Figure 32 assumes a superficial attached solids surface area flux of 45 [$s^{-1}$] and a superficial gas velocity of 1.5 [cm $s^{-1}$].

### 5.3.12.3 Flotation Under Loading Constraints

The carrying capacity model predicts the total particle-surface-area that can be removed by a specific bubble-surface-area. The model does not predict the composition of solids on the bubble. The percentage of mineral and size-classes floated may be different under loaded and unloaded conditions. This model assumes that the flotation of all minerals is scaled equally in order to match kinetic surface-area predictions with the loading maximum when kinetics predict removal rates greater than the carrying capacity.

The difference between "hindered", or carrying capacity limited, and "free" flotation, is illustrated in Figure 33. During hindered flotation the surface removal rate of solids is dependant on the bubble flux. If the bubble flux is constant then the solids surface-area flux plots as a straight line with time. This continues until such time as the rate is lower than the carrying capacity at which time "free" flotation occurs.

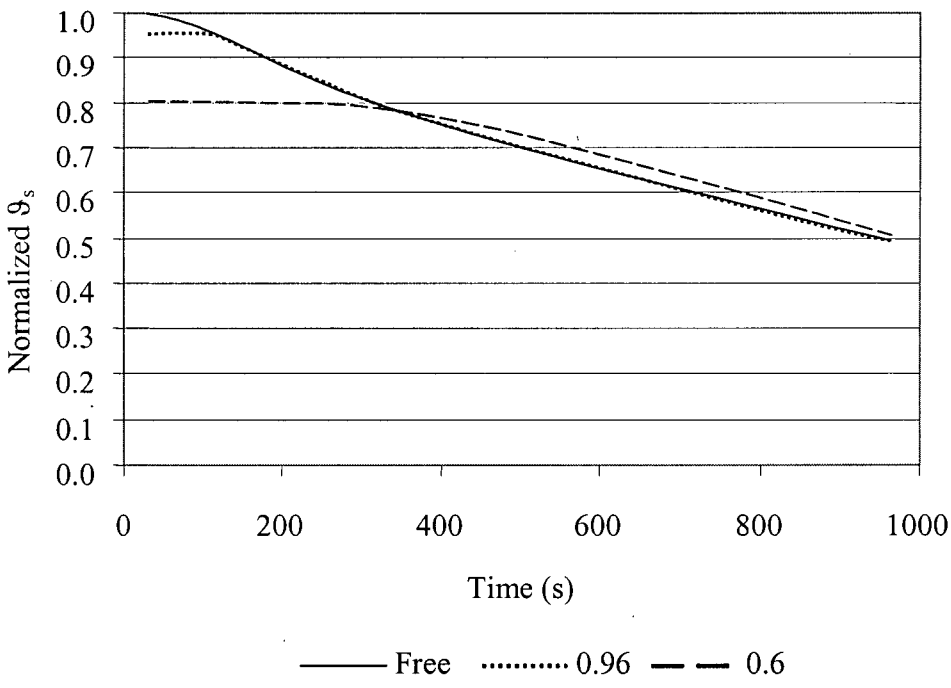


**Figure 33: Normalized solids surfaces area flux with time under "free" flotation and "hindered" conditions wherein the maximum load is 0.96 and 0.8 of the maximum "free" surface-area flux.**

Under "hindered" flotation conditions the bubble load will be at its' maximum. Thus, a plot of load versus time should show an initial flat response until such time as the "free" flotation condition is achieved. This response is illustrated using a theoretical example of a flotation test that is loading limited as shown in Figure 34.

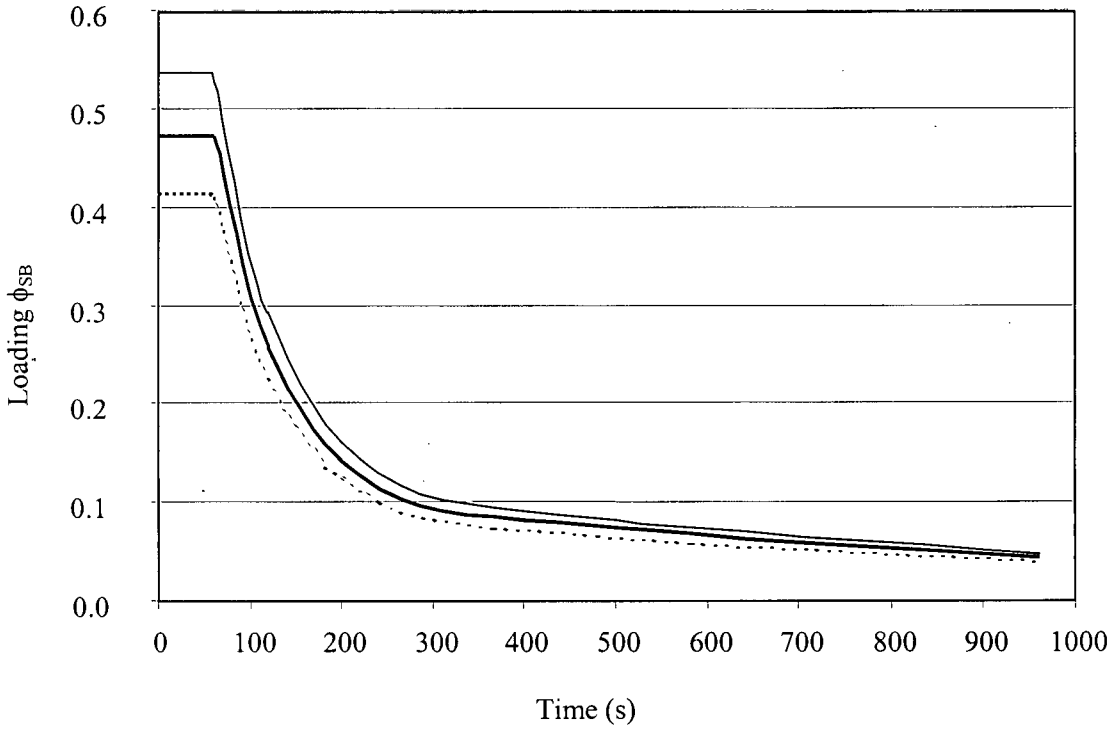


**Figure 34: Example of a load limited flotation response. Y-axis is the ratio of solids to bubble surface-area and the X-axis is time in seconds.**

### 5.3.12.4 Bubble Size Error

INCO mechanical-cell test data analysis results indicate a minimum value for maximum bubble loading of about 47%. The bubble loading relationship over time of this test is shown in Figure 35.

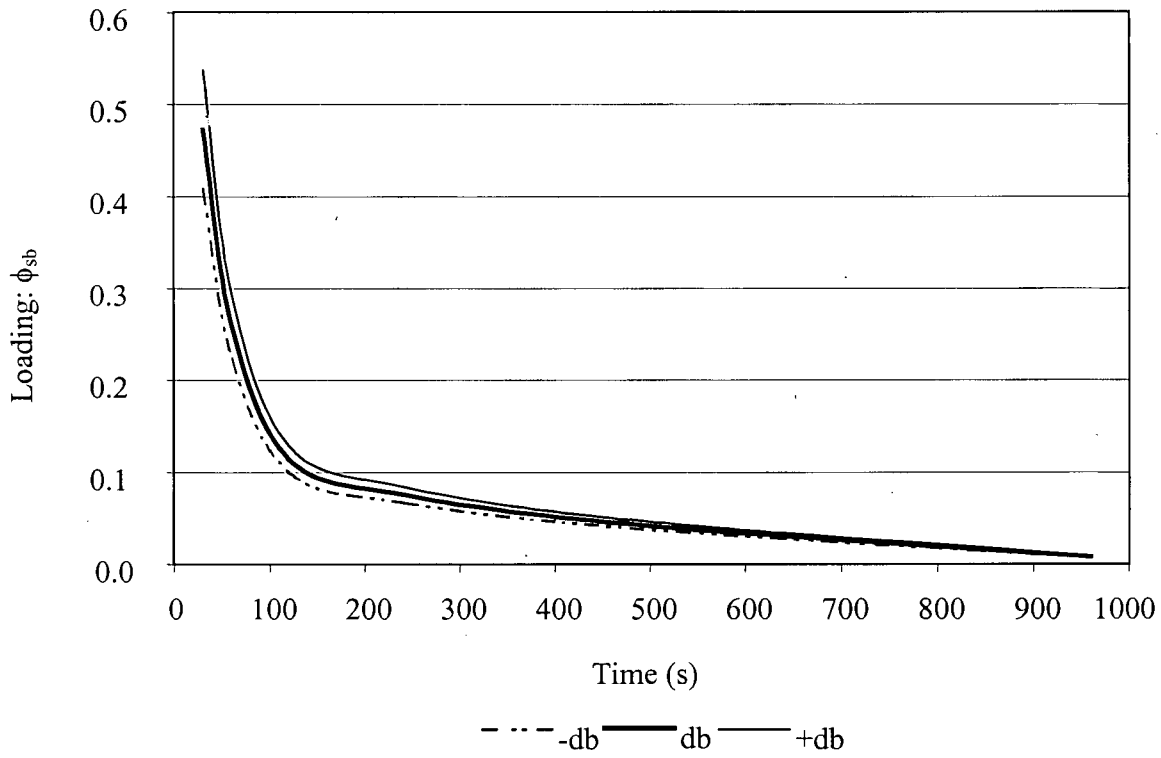


**Figure 35: Illustration of how error in bubble measurement affects loading. Loading with time in INCO batch mechanical-cell tests. The "Y" axis is the ratio of solids to bubble-surface-area and the "X" axis is time in seconds. The +/- "$d_b$" curves indicate the possible error due to bubble size estimation.**

Also shown in Figure 35 is a bubble measurement error estimation. This error is significant and impacts on the results from the solids-surface-area maximum bubble load ($\phi_{SB}$) calculation. Figure 35 shows the effect of the error spread; "$-d_b$" is the measured bubble size minus the probable error; "$+d_b$" is the measured bubble size plus the probable error. Thus, the curves of Figure 35 show the expected bubble load ("$d_b$") -- the possible load due to error.

### 5.3.13 Application of the Batch Model

There are four parts to the kinetic batch flotation model; each of which is composed of a number of steps.

Part 1: Flotation time – recovery test, perform the following:

1. Obtain a solids feed sample.
2. Record the volume of water added and the total volume of slurry.
3. Record (and maintain at a constant rate) the air flow rate and level of agitation.
4. Perform a time-recovery test run under the conditions to be investigated. Repeat tests should be performed to minimize error and confirm the consistency of the results.
5. Obtain an overflow sample for each timed interval.
6. Maintain the interface level through water addition.
7. Obtain a remainder sample from the contents left in the vessel.
8. Determine the overflow bubble size throughout the test.
9. Determine the water in the overflow by difference between wet and dry product weights.
10. Determine the dry solids weight in the overflow in each sample.
11. Screen into appropriate size-classes.
12. Assay for elements appropriate to determine mineral components.

Part 2: Flotation, time – recovery test calculations -- calculate the following values (for mineral, size-class and interval were appropriate):

1. Mass of mineral equivalents ($m_{p(i)(m,n)}$ [g])
2. The solids-surface-area ($S_{p(i)(m,n)}$ [$cm^2$]) for each overflow sample based on size fraction masses.
3. The overflow superficial bubble-surface-area flux ($\vartheta_{B(O,i)}$ [$s^{-1}$]) (Equation 116)
4. The overflow superficial total-solids surface-area flux ($\vartheta_{S(O,i)(m,n)}$ [$s^{-1}$]) (Equation 117), and

5. The cell specific surface ($C_{p(0)(m,n)}$ [$cm^{-1}$]) (Equation 105).

Part 3: Initial parameter values estimations:

1. Surface-area loading ($\phi_{SB}$) using Equation 121 and Equation 119
2. Entrainment parameter ($k_e$) using Equation 104
3. Maximum recovery ($R_\infty$) using Equation 112
4. Flotation rate constant ($k_f$) using Equation 114

Part 4: Objective Function Minimization

The objective function response is the difference between a "predicted" overflow superficial total-particle surface-area flux ($\vartheta_{S(O,i)(m,n)}$ [$s^{-1}$]) and the test flux. This flux is the sum of the overflow superficial attached-solids surface-area flux ($\vartheta_{SB(O,i)(m,n)}$ [$s^{-1}$]) and overflow superficial suspended-solids surface-area ($\vartheta_{SL(i)(m,n)}$ [$s^{-1}$] -- entrainment). Minimization of this response is achieved by adjustment of the four model parameter values determined in Stage 3 using a "down hill" simplex method. The following steps are used in this model:

1. Assign overflow superficial total-solids surface-area overflow flux ($\vartheta^*_{S(O,i)}$ [$s^{-1}$]) values from test work values.
2. Estimate floatable solids specific surface ($C_{pf(0)}$ [$cm^{-1}$]) (Equation 106).
3. Estimate non-floatable solids specific surface ($C_{pn(0)}$ [$cm^{-1}$]) (Equation 107).
4. for i = 1 to L "$C_{pn(i)}$" = "$C_{pn(0)}$"
5. for i = 1 to L "$C_{pf(i)}$" = "$C_{pf(0)}$"
6. Estimate the overflow superficial suspended-solids surface-area flux ($\vartheta_{SL(O,i)}$ [$s^{-1}$]) (Equation 103).
7. Estimate the overflow superficial attached-solids surface-area flux ($\vartheta_{SB(O,i)}$ [$s^{-1}$]) (Equation 110).
8. Estimate the solids loading ($\phi_{SB}$) (Equation 116).

9. Adjust overflow for "hindered" flotation. If "$\phi_{SB}$" > "$\phi_{SB(max)}$" then "$\vartheta_{SB(O,i)}$" is modified using the ratio of maximum of predicted load. All minerals and size-classes should be scaled equally.
10. Estimate non-floatable solids specific surface ($C_{pn(i)}$ [$cm^{-1}$]) (Equation 108).
11. Estimate floatable solids specific surface ($C_{pf(i)}$ [$cm^{-1}$]) (Equation 109).
12. Estimate overflow superficial total-solids surface-area ($\vartheta_{S(O,i)}$ [$s^{-1}$]) as "$\vartheta_{SB(O,i)}$" + "$\vartheta_{SL(O,i)}$".
13. Iterate from (6) while "$C_{pn(i)(1)}$" or "$C_{pf(i)}$" change more than a tolerance
14. Calculate the objective function using Equation 93
15. Iterate from (6): modify model parameters according to downward simplex and iterate while objective function response changes more than a tolerance.

Note: this function must be run simultaneously for each mineral and size-class in order to obtain the bubble loading.

### 5.3.14 Model Validation

The batch kinetic model is an empirical model. As such, it is only valid within the range of conditions under which it has been tested. Tests were performed on feed to the INCO Coppercliff #2 copper column (matte) to determine the ability of the objective function to match performance in a high solids-surface-area recovery application of relatively large particles with a sphericity close to one. Tests were also done on the Quinto graphite product that has a low feed grade, small particle size, and high aspect ratio. Additional tests should be considered to further verify this function including conditions such as ore that contains more than one floating mineral, very course particles sizes or a wide range of particle sizes, very low feed grades, and other conditions. A series of batch tests must be compared with the performance of full-scale flotation equipment working on the same ore under the same conditions to obtain a valid assessment of the model. In order to improve model accuracy better techniques of overflow bubble size measurement and particle size determination must be achieved.

### 5.3.15 INCO Batch Mechanical-Cell Tests

Initial parameter values for the batch mechanical-cell model where determined from test results. These values were adjusted to minimize the difference between test data and model response based on an equal weighting of all four batch mechanical-cell tests. The resulting flotation parameters are shown in Table 18.

**Table 18: Mechanical-cell test parameters to minimize error**

| | -44 μm | -74/+44 μm | +74 μm |
|---|---|---|---|
| Chalcocite | | | |
| Kinetic rate, "$k_f$" | 0.004 $s^{-1}$ | 0.001 $s^{-1}$ | 0.0004 $s^{-1}$ |
| Maximum recovery, "$R_\infty$" | 78.2% | 20.2% | 12.0% |
| Entrainment factor, "$k_e$" | 2.27 | 3.18 | 1.40 |
| Heazelwoodite | | | |
| Kinetic rate, "$k_f$" | 0.0004$s^{-1}$ | 0.001$s^{-1}$ | 0.0004 $s^{-1}$ |
| Maximum recovery, "$R_\infty$" | 31.0% | 16.0% | 5.3% |
| Entrainment factor, "$k_e$" | 0.48 | 0.44 | 0.31 |
| Other | | | |
| Kinetic rate, "$k_f$" | 0.0044 $s^{-1}$ | 0.0017 $s^{-1}$ | 0.0004 $s^{-1}$ |
| Maximum recovery, "$R_\infty$" | 100% | 65% | 4.5% |
| Entrainment factor, "$k_e$" | 0.44 | 0.0 | 0.15 |

The initial entrainment analysis of a floating mineral is subject to considerable error. When a similar non-floating mineral is found in the system, the entrainment parameter calculated for that mineral may be substituted for the floating mineral. Chalcocite is the floating mineral but is also similar in particle size, density and mineral particle shape to the haezelwoodite. Thus, it is reasonable to assume that the entrainment rates of these two minerals should be similar.

In addition, entrainment is closely related to settling velocity. Thus, a dense mineral with the same dimensions as a light mineral should have a lower entrainment rate and the entrainment parameter should increase with a decrease in particle size. This is shown in the entrainment parameter of both the heazelwoodite and other. However, this trend it not clear in the chalcocite data. Also, the chalcocite entrainment parameter is significantly higher than the other two streams which is inconsistent with the similarities of chalcocite and haezelwoodite. The large differences in entrainment parameter between chalcocite and heazelwoodite indicate that the curve fitting techniques used may suffer from significant error. This brings into question that validity of using batch mechanical cell tests to predict column cell performance or use of the model to separate entrainment and flotation effects.

In Table 18 the rate constant, "$k_f$" of the chalcocite increases as particle size is reduced. This is expected if the optimum size for flotation falls closer to the –44 than the –74/+44 size fraction. This optimum size is also supported by the drop in maximum recovery with increasing particle size.

The rate of heazelwoodite flotation; "$k_f$" for the –74/+44 and +74 μm fractions appears to be the same as the chalcocite although the maximum recoveries are much lower. This may indicate a high degree of locking between these minerals within those size classes. The rate constant for heazelwoodite in the smallest size fraction is much smaller than the chalcocite possibly indicating better liberation.

The "other" material, that floats, seems to have flotation characteristics similar to chalcocite in all size fractions, however the maximum recovery quickly drops off with size. This may indicate that the other material, that is small in size, is associated with the chalcocite whereas the largest sizes are essentially liberated and that the flotation characteristics of chalcocite dominate. While this is possible, any conclusions based on the "other" mineral must be looked at knowing that this fraction contains significant errors since it is calculationed from the subtraction of two larger numbers (heazelwoodite and chalcocite fractions) that each contain error.

The bubble size measured in the batch mechanical cell tests varied from 0.22 to 0.30 cm (see results appendix). . This is consistent with a 0.2 cm collection zone bubble size (as determined by Wilson; 1990) after coalescence through the froth zone.

Analysis of test data indicates a calculated minimum value for maximum bubble loading of about 0.47. The bubble loading relationship over time of this test is shown in Figure 36.

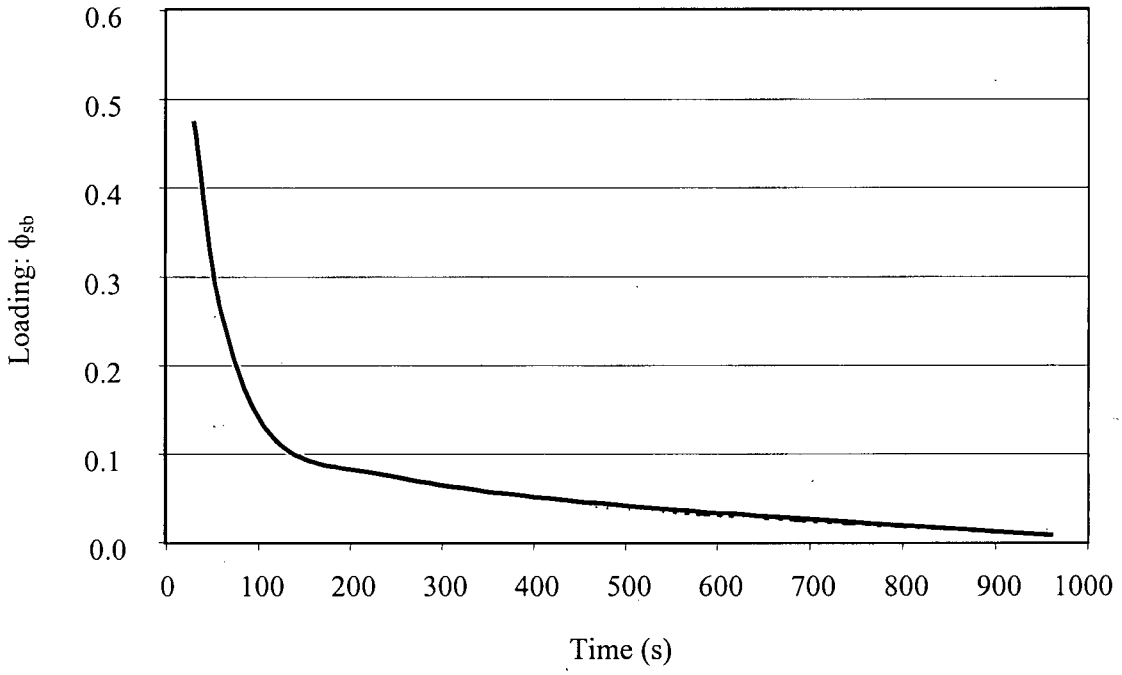


**Figure 36: Loading with time in batch mechanical-cell #1. The "Y" axis is the ratio of solids to bubble surface-area and the "X" axis is time in seconds (similar to Figure 35).**

Figure 36 shows a sharp reduction of bubble loading at the beginning of the test. This reduction indicates that loading limits were probably not approached. Loading would have remained constant for a time interval, before dropping, if the overflow production rate was limited (Figure 34).

An example comparison between test data and performance predicted by the model (model response) is shown in Figure 37 for the chalcocite –44 μm fraction. This figure shows the superficial total-solids surface-area flux. This type of presentation allows a comparison on a

time basis without influence from previous time data. Figures showing the test data and predicted values (model responses) for other minerals and size-classes can be found in the "results" appendix.

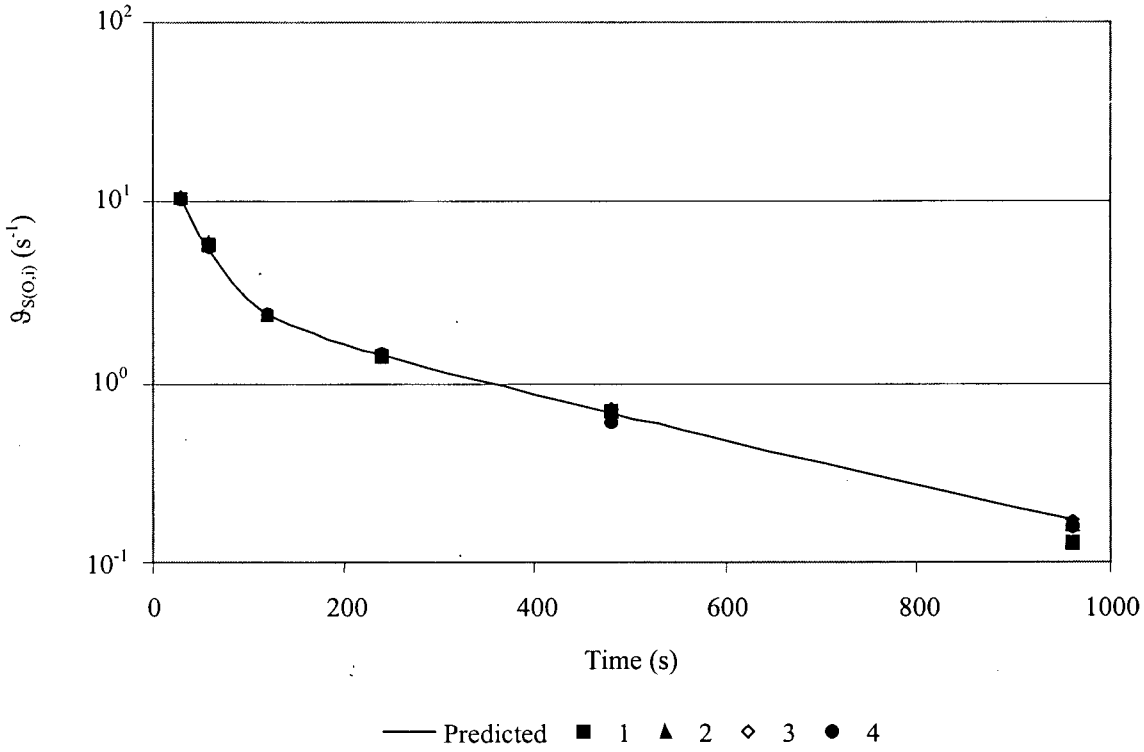


**Figure 37: Model performance on –44 μm chalcocite showing all four tests and the predicted surface-area flux (model response) on a semi-log plot. X-axis is time in seconds while Y-axis is overflow superficial total-solids surface-area rate ($s^{-1}$).**

The closeness of fit between the test data and the model response, which includes entrainment (Figure 37), is significantly better than the model that discounts entrainment (Figure 79). Neither model response nor test data overflow superficial total-solids surface-area fluxes as straight line on the semi-log plot as shown in Figure 37.

Figure 38 shows the model response constituent parts: flotation and entrainment.

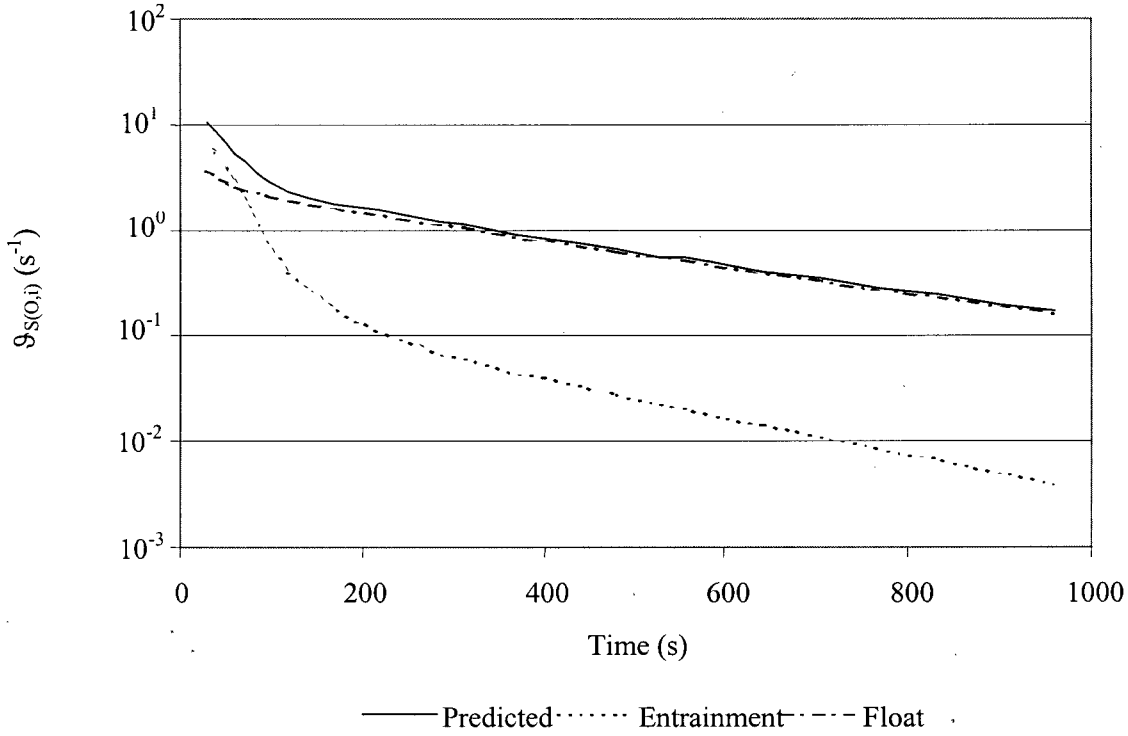


**Figure 38: Model performance on –44 μm chalcocite showing all four tests and the predicted surface-area flux (model response) on a semi-log plot showing both predicted entrainment and flotation components. X-axis is time in seconds while Y-axis is overflow superficial total-solids surface-area overflow rate ($s^{-1}$).**

The predicted high entrainment rate seen in Figure 38 in the first samples is a result of the overflow liquid flow rate values and initial specific solids surface ($C_p$" [$cm^{-1}$]).

An alternate presentation of this data is shown in Figure 39 where cumulative recovery of the same fraction (INCO chalcocite, -44 micrometer) is plotted against time.

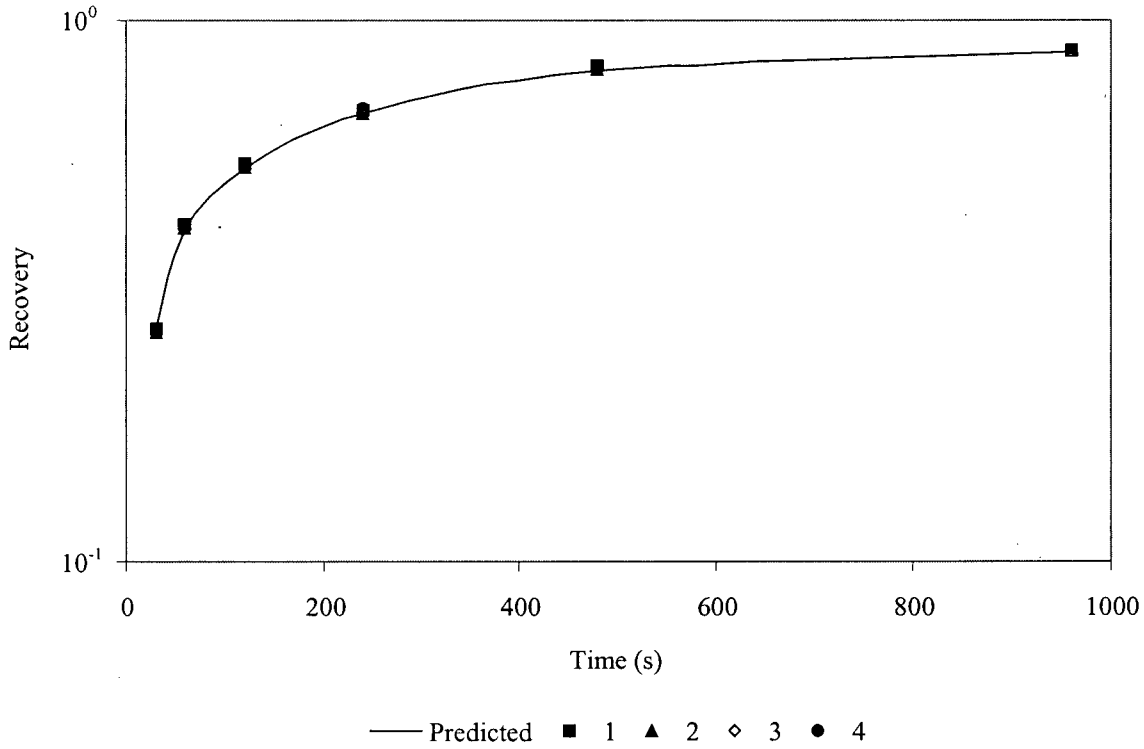


**Figure 39: Model performance comparison on –44 μm chalcocite showing all four tests and the predicted cumulative recovery (model response).**

This model minimizes one rate constant over all test intervals. The single rate constant is a simplification and not an exact "real" system representation since there may be a distribution of reagent surface-area concentrations or floatabilies within each particle population. The model, when using this average flotation rate, may under estimate the solids-surface-area flux in the early intervals and over estimate it in the later intervals. As such, entrainment may be overestimated.

### 5.3.16 Example – INCO Batch Column Application

The flotation model parameters determined by error minimization for the batch column flotation tests (composite data) are shown in Table 19.

**Table 19: Batch column test parameters to minimize error**

| | -44 μm | -74/+44 μm | +74 μm |
|---|---|---|---|
| Chalcocite | | | |
| Kinetic rate, "$k_f$" | 0.0046 $s^{-1}$ | 0.0055 $s^{-1}$ | 0.0057 $s^{-1}$ |
| Maximum recovery, "$R_\infty$" | 80.0% | 83.0% | 85.0% |
| Entrainment factor, "$k_e$" | | | |
| Heazelwoodite | | | |
| Kinetic rate, "$k_f$" | 0.0040 $s^{-1}$ | 0.0036 $s^{-1}$ | 0.0035 $s^{-1}$ |
| Maximum recovery, "$R_\infty$" | 31.0% | 45.5% | 52.4% |
| Entrainment factor, "$k_e$" | | | |
| Other | | | |
| Kinetic rate, "$k_f$" | 0.0047 $s^{-1}$ | 0.0047 $s^{-1}$ | 0.0042 $s^{-1}$ |
| Maximum recovery, "$R_\infty$" | 69.9% | 96.0% | 4.5% |
| Entrainment factor, "$k_e$" | | | |

In Table 19 the chalcocite kinetic rate constant increases with particle size. This is contrary to the findings of the mechanical cell. This is possible since the high agitation levels of the mechanical cell are absent, thus, bubble particle detachment is lower. The ability of the quiescent flotation column to float larger particles is further supported by the much larger maximum recovery shown in the chalcocite larger particle size fractions.

Heazelwoodite rate constants are approximately equal in each size class, with a slight reduction as size increases. However, these values are significantly higher than the mechanical cell rates (Table 18). These characteristics may be the result of non-liberated chalcocite on haezelwoodite remaining on the bubble or they may be explained by inaccurate

descriptions of the mechanical cell data by over stating the entrainment considerations. Either mechanism could also explain the increased maximum recovery of the column over the mechanical cell.

No entrainment was detected for any of the mineral size classes. This differs significantly from the mechanical cell generated data (Table 18).

The bubble size detected in the column overflow ranged from 0.24 to 0.28 cm which is consistant with a the 0.2 cm diameter bubble in the INCO #2 column after loss of surface area through coalescence in the froth zone.

A comparison between the test data and the performance predicted by the model is shown in Figure 40 for the chalcocite –44 micrometer fraction. This figure shows the overflow superficial total-solids surface-area rate ($\vartheta_{s(O)}$ [$s^{-1}$]) plotted against time on a log-linear scale. This type of presentation allows a comparison on a time basis without influence from previous time interval data. Figure 40 is a plot of the "–44" micrometer chalcocite particles-surface-area flux response. The test data model response for the other minerals and size-classes are shown in the "results" appendix.

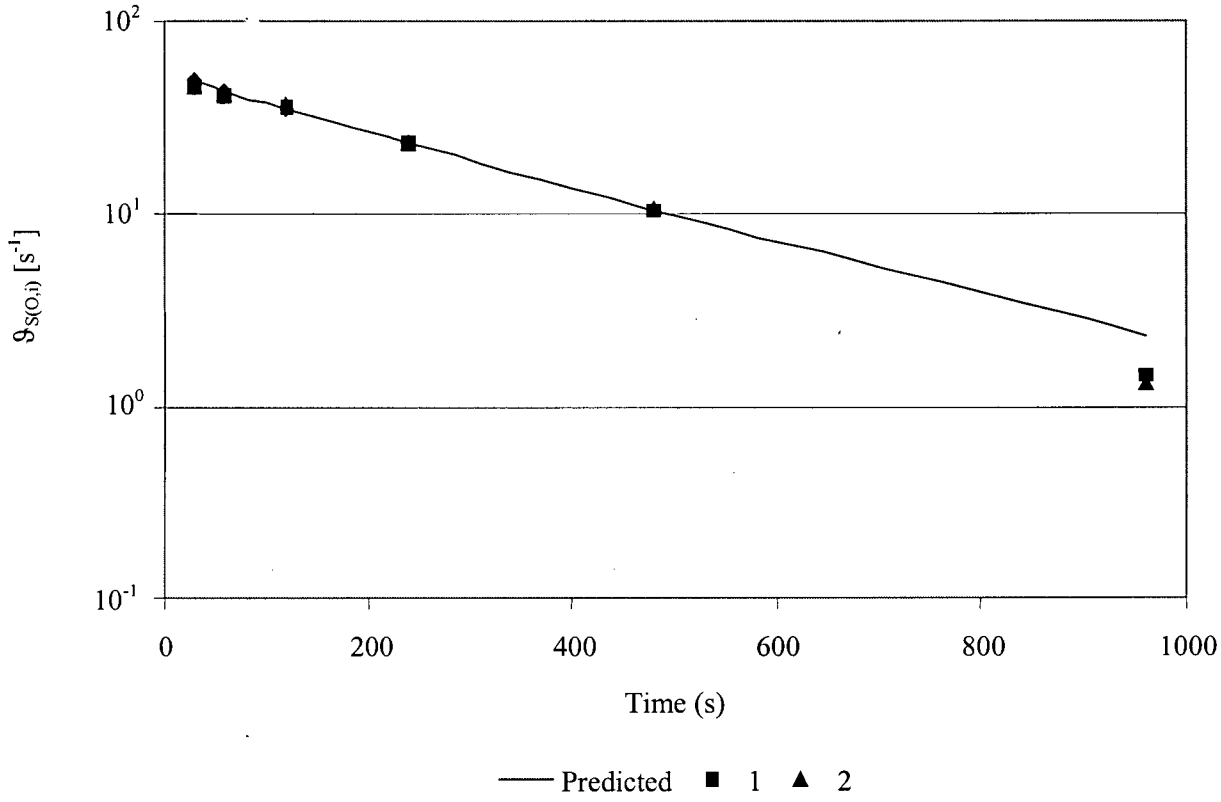


**Figure 40: Model performance on –44 μm chalcocite, batch column, showing both tests and the predicted surface-area flux (model response) on a semi-log plot. X-axis is time in seconds while Y-axis is overflow superficial total-solids surface-area rate ($s^{-1}$).**

Figure 40 shows that the model response is a good fit to the test data and that both are straight lines on the log–normal plot. There is some deviation between the test data and the model response at the "i"= 960 [s] test interval. This deviation may be due to either test error or to "depleted" flotation conditions. The same model response and test data are plotted on a "traditional" time-recovery curve in Figure 41.

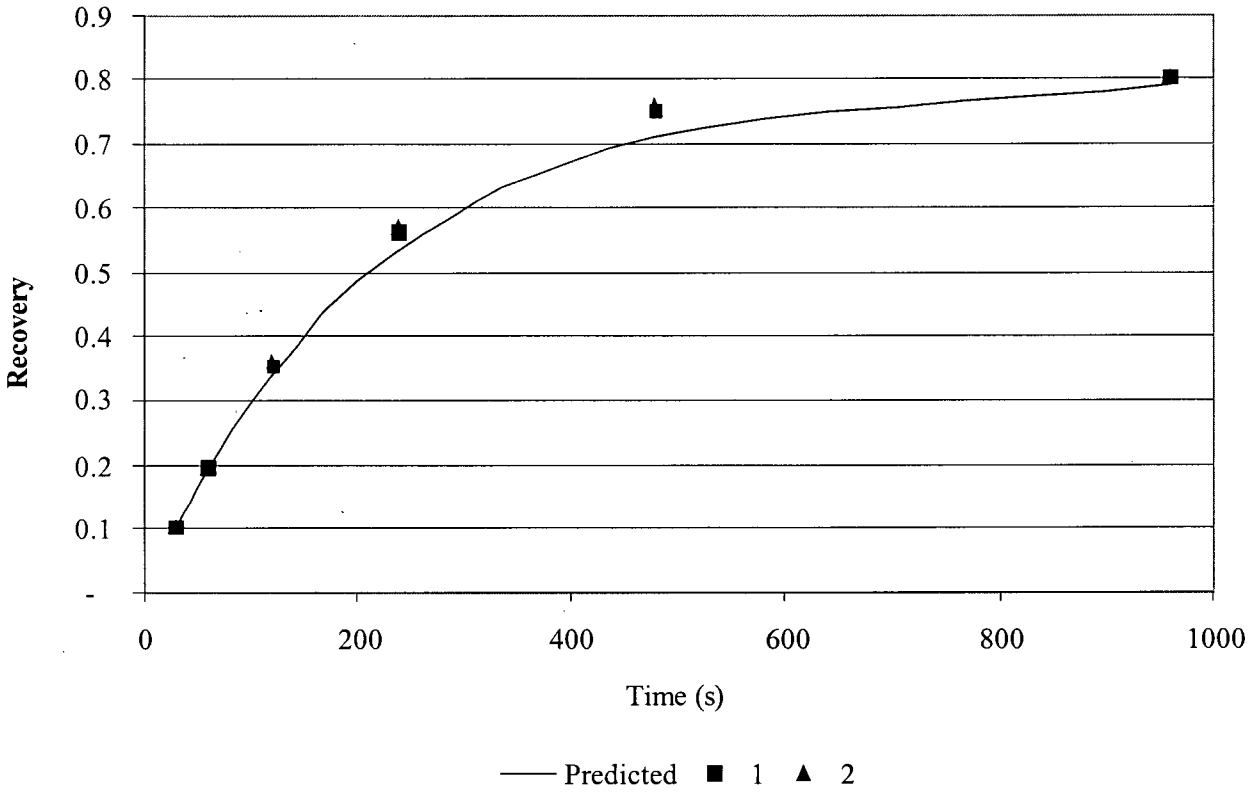


**Figure 41: Model performance comparison using –44 μm chalcocite, batch column, showing cumulative recovery with time for the predicted or model response and test data points.**

### 5.3.17 Quinto Batch Mechanical-Cell

The model flotation parameters shown in Table 20 were calculated, including entrainment, and adjusted to minimize the model objective from the Quinto batch mechanical cell tests.

**Table 20: Graphite mechanical-cell test parameters to minimize error.**

| | Graphite | Other |
|---|---|---|
| Kinetic rate, "$k_f$" | 0.0008 $s^{-1}$ | 0.0004 $s^{-1}$ |
| Maximum recovery, "$R_{max}$" | 48.8% | 24.0% |
| Entrainment factor, "$k_e$" | 53.5 | 11.4 |

The kinetic rate for the Quinto "other" material is approximately the same as the rate determined for the INCO "other" material. The Quinto entrainment factor is significantly higher than the INCO factor as expected since the Quinto material is very fine (Figure 25) and consists of platelike mica material.

A comparison between the model response and the test data for Quinto graphite is shown in Figure 42. This figure shows the graphite superficial total-solids surface-area rate ($\vartheta_s$ [$s^{-1}$]) using a log-normal scale, plotted against time.

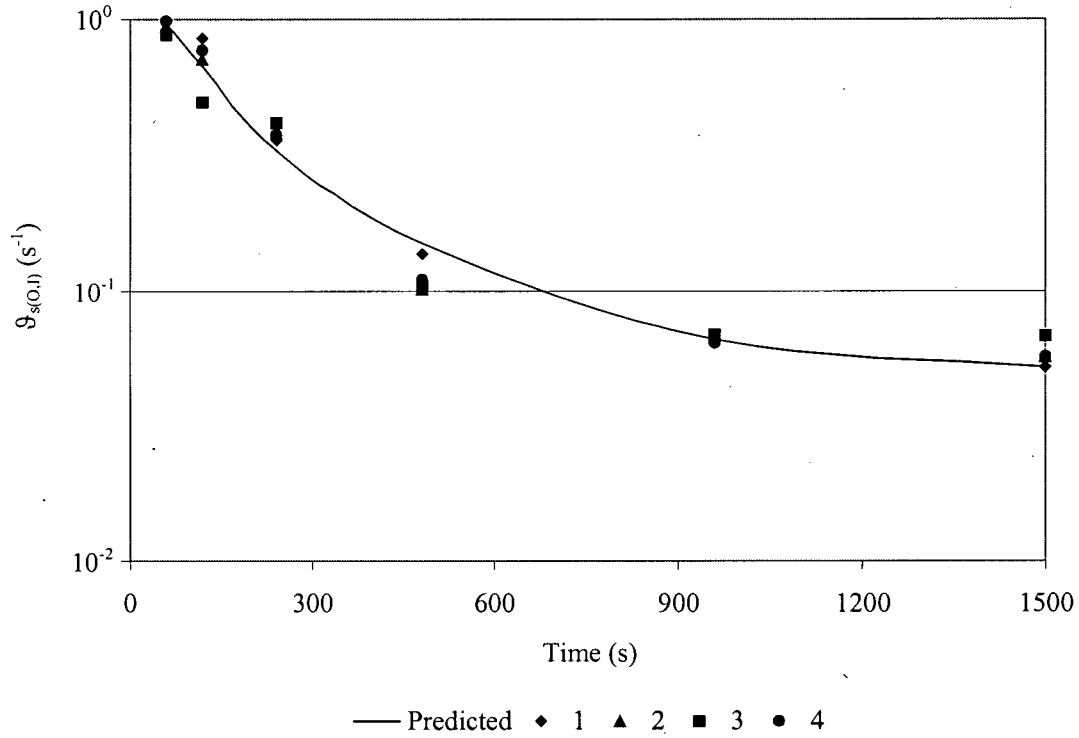


**Figure 42: Model performance for the Quinto graphite fraction showing all four batch mechanical-cell tests and the predicted surface-area flux on a semi-log plot. X-axis is time in seconds while Y-axis is overflow superficial total-solids surface-area rate ($s^{-1}$).**

The "other" material in the graphite float responds as shown in Figure 43.

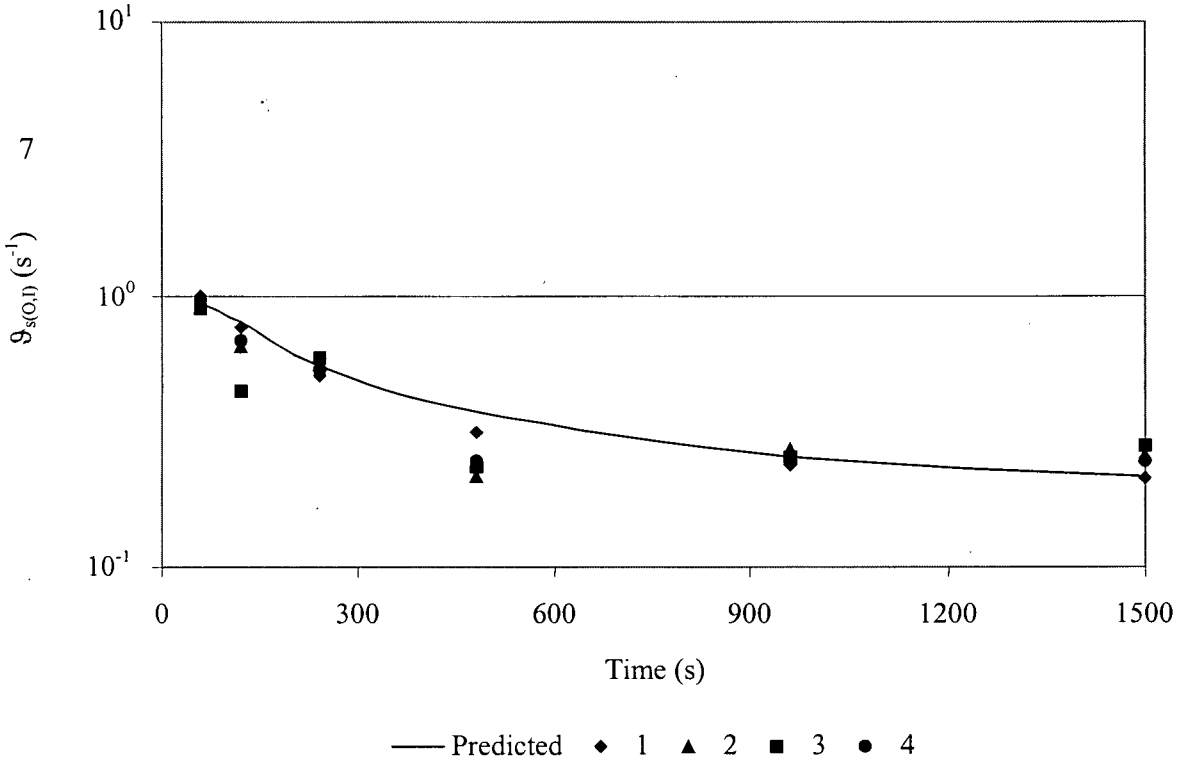


**Figure 43: Model performance without entrainment for the Quinto "other" fraction showing all four batch mechanical-cell tests and the predicted surface-area flux on a semi-log plot. X-axis is time in seconds while Y-axis is overflow superficial total-solids surface-area overflow rate ($s^{-1}$).**

The model response compares well to the test data for both the graphite (Figure 42) and the "other" components (Figure 43). Neither curve is a straight line on the log – normal plot.

### 5.3.18 Quinto Column

The flotation parameters obtained by minimizing the objective function using Quinto ore tested in the batch test column are found in Table 21.

**Table 21: Graphite Column Test Parameters to Minimize Error.**

| | Graphite | Other |
|---|---|---|
| Kinetic rate, "$k_f$" | 0.0061 $s^{-1}$ | 0.0006 $s^{-1}$ |
| Maximum recovery, "$R_{max}$" | 100% | 10.0% |
| Entrainment factor, "$k_e$" | 0.32 | 0.21 |

A comparison between the model response and test data for this graphite is shown in Figure 44. This figure shows the superficial total-solids surface-area rate ($\vartheta_s$" [$s^{-1}$]) using a log scale plotted against time.

The column kinetic rate for graphite is larger than that determined for the batch mechanical cell tests. If is unlikely that this is caused by different mechanisms of collision between these two cells since that turbulent conditions found in the mechanical cell are better at colliding small particles with bubbles. Therefore, the low mechanical cell results must be caused by attributing part of the floating graphite to entrainment.

The "other" material within the Quinto ore is composed of mica, calcite and quartz. The mica is very small and is often physically attached to the graphite. The 10% mica recovery can be attributed to that attached graphite.

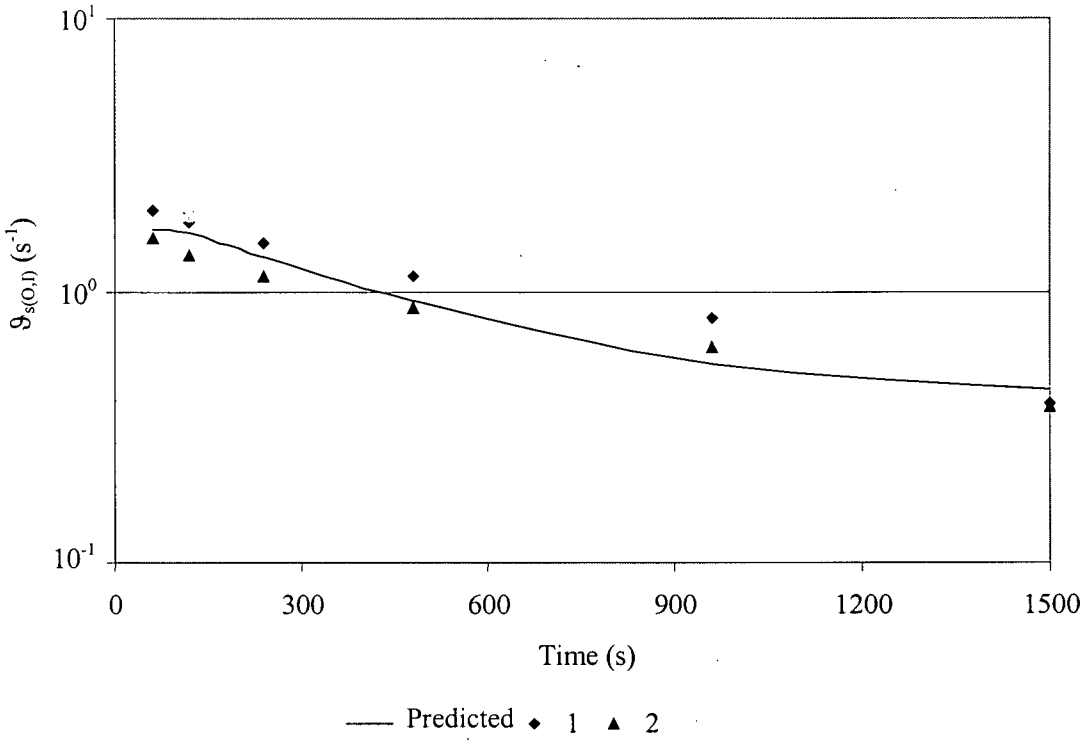


**Figure 44: Model performance for the Quinto graphite fraction showing both column batch tests and the predicted surface-area flux on a semi-log plot. X-axis is time in seconds while Y-axis is overflow superficial total-solids surface-area rate ($s^{-1}$).**

The comparison between the model response and test data for "other" material in the graphite float is shown in Figure 43. The model response accurately predicts the test data.

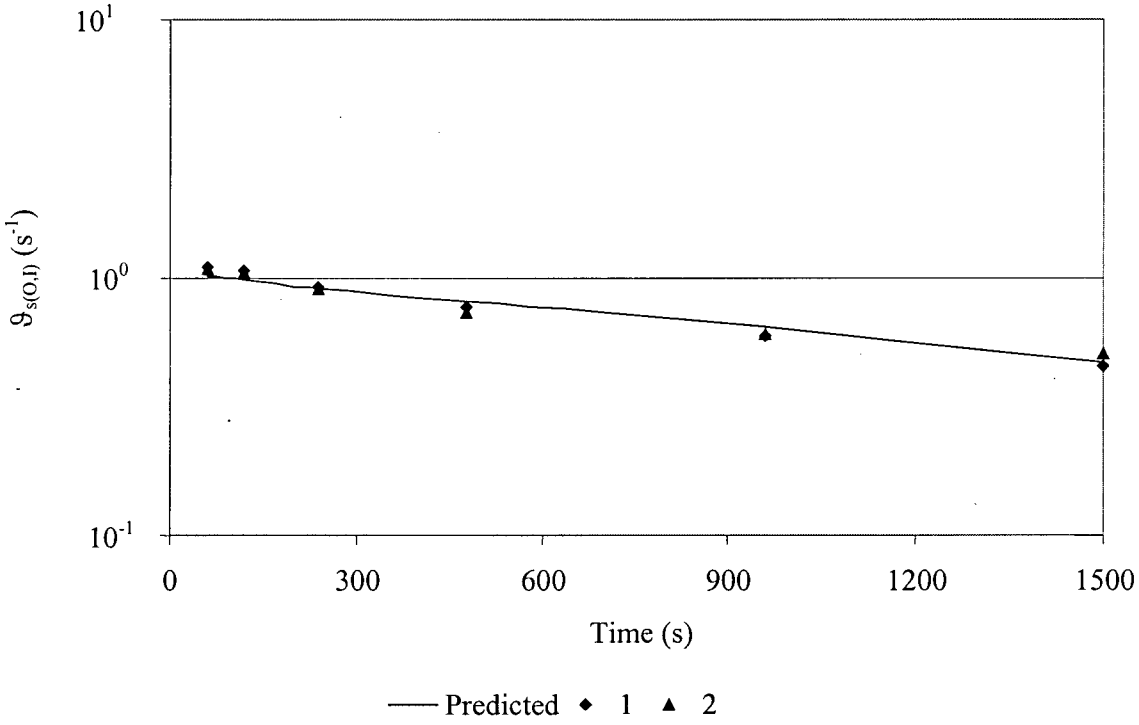


**Figure 45: Model performance without entrainment for the Quinto "other" fraction showing both column batch tests and the predicted surface-area flux on a semi-log plot. X-axis is time in seconds while Y-axis is overflow superficial total-solids surface-area rate ($s^{-1}$).**

### 5.3.19 Batch Model Sensitivity

Variations in surface area due to calculation errors do not affect rate constants, maximum recovery or the entrainment parameter. These three parameters are defined in terms of recovery which remains constant with changes in particle size due to error measurement. Bubble loading changes since this parameter is the ratio between attached solids surface area and bubble surface area fluxes.

### 5.3.20 Batch Model Summary

The response of the batch kinetic model, which incorporates kinetic rate constants, entrainment, and maximum recovery, accurately predicts the batch laboratory-scale tests performed using bubble and particle surface area concentrations and fluxes in both flotation column and mechanical cells. A minimum value of bubble loading was determined. However, since the tests done did not test full loaded ("hindered" flotation conditions), this bubble loading value is probably lower than the maximum possible loading. The flotation parameters generated are not sensitive to surface area errors, however, such errors will affect the bubble loading parameter.

## 5.4 Continuous Column Kinetic Model

### 5.4.1 **Introduction**

The continuous kinetic model is a one-dimensional model that predicts bubble loading (carrying capacity) and solids removal rates in continuous column flotation systems using kinetic flotation rates. The following assumptions are made:

1. The column is at steady state, feed is added though the feed port, and wash water may be added to the froth. Solids attached to the bubbles exit the column through the overflow stream along with any solids carried by bulk transport in the water. All other solids exit the column suspended in the underflow water flow.

2. Continuous column operation is modeled with three flotation zones: froth, re-collection and collection zones. These zones encompass the entire vessel cross-sectional area with distinct lower and upper boundaries

3. The bubble loading factor ($\phi_{SB}$ [dimensionless]) is assumed to be constant throughout the vessel height.

4. The floatable solids-surface-area concentration or specific solids area, "$C_p$" [$cm^{-1}$], is assumed to be constant with time but not with vertical height (position).

5. All bubbles are assumed to be the average size within the pulp zones. Hydrostatic forces decrease with vertical height from the column base so bubble size will vary between and within the collection and re-collection volumes.

6. Kinetics are determined by mineral and size fraction rate constants ($k_{f(m,n)}$ [$s^{-1}$]).

7. Mixing is taken into consideration using the Peclet number (Pe, used in the axial dispersion equations).

8. This model does not consider the water found in the wake behind moving bubbles. This water volume is dependent upon the bubble Stokes' number. Bubbles that fall within the Stokes' (low Reynolds' number) or Euler's flow (high Reynolds' number) regions will have insignificant water entrained within their wake. Those within the transition region (between low and high Reynolds' numbers) will have entrained wake water. This wake water also carries suspended solids with the bubbles, through the re-collection zone into the froth zone. Water then drains, as a bias flow, from the froth zone. This flow will affect the flow of entrained solids through all cell zones. It will also affect the liquid flow balance within each zone.

## 5.4.2 Model Structure

The continuous flotation model separates the column into three "stages" as described in Table 22 and shown in Figure 46.

**Table 22: Continuous model stage locations.**

| Zone | Location | Description |
|---|---|---|
| Froth | "$h_{(O)}$" → "$h_{(f)}$" | Froth phase primarily consisting of bubbles. |
| Recollection | "$h_{(f)}$" → "$h_{(F)}$" | Zone above the feed port |
| Collection | "$h_{(F)}$" →"$h_{(spa)}$" | Main flotation zone, between sparger and feed port |

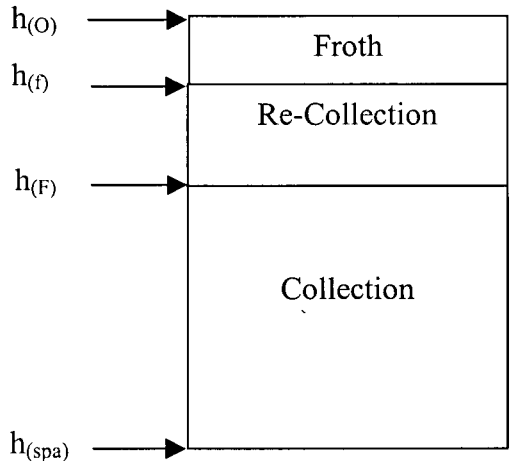


**Figure 46: Model stage locations**

The following elevations (h [cm]) are found in Figure 46: overflow (O), froth-pulp interface (f), feed (F), and sparger (spa). All elevations are measured from the column base elevation. Usually the overflow elevation is also the total vessel height; "$h_{(v)}$".

Two streams are considered in each column zone: the bubble stream (B) and the liquid stream (L). Each of these streams will have an associated solids content. The surface-area, volume and mass of each phase (gas -- including collected solids and liquid -- including suspended solids) is calculated for the top, bottom and average of each zone. Both the suspended and

collected solids are calculated as superficial surface-area rates ($\vartheta$ [$s^{-1}$]) similar to the "$J_B$" term used by Gorain et. al. (1999). The symbol "$\vartheta$" is used here for all superficial area flow rates to differentiate them from the volume superficial rates. Slurry density, bubble density, bubble size, phase holdups and particle settling velocities are calculated within each zone using the average phase holdups within that zone. All flows are considered positive downward. Solids attached to bubbles are considered to be part of the "gas" phase.

The overall column solids flow diagram, taking the entire vessel as a "black box", is shown in Figure 47. ($\vartheta_{SL,(froth,U)}$ only exists under negative bias conditions)

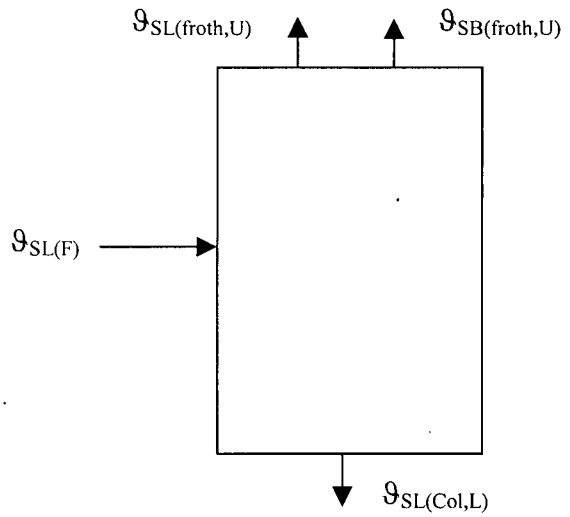


**Figure 47: Total column solids flow**

The solids balance around the column is shown in Equation 123. The overall recovery to the overflow can be calculated using Equation 124.

$$\vartheta_{SL(F)} = \vartheta_{SL(Col,L)} - \vartheta_{SL(froth,U)} - \vartheta_{SB(froth,U)} \qquad \text{Equation 123}$$

$$R_{S(O)} = \frac{\vartheta_{SL(froth,U)} + \vartheta_{SB(froth,U)}}{\vartheta_{SL(F)}} \qquad \text{Equation 124}$$

## 5.4.3 **Froth Zone**

### 5.4.3.1 Introduction

The froth-zone model accounts for the difference in bubble size between its' axial boundaries, thus, determines the loss of bubble-surface-area. The froth zone extends from the froth-pulp interface ($h_{(f)}$ [cm]) to the overflow lip elevation ($h_{(O)}$ [cm]) ($h_{(f)} = h_{(froth,L)}$ and $h_{(O)} = h_{(froth,U)}$). The loss of bubble-surface-area may force solids from the bubble phase to the liquid phase. Bias in the zone then determines the direction of liquid flow, thus the direction of the particles. The superficial surface rates passing the froth boundaries are shown in Figure 48.

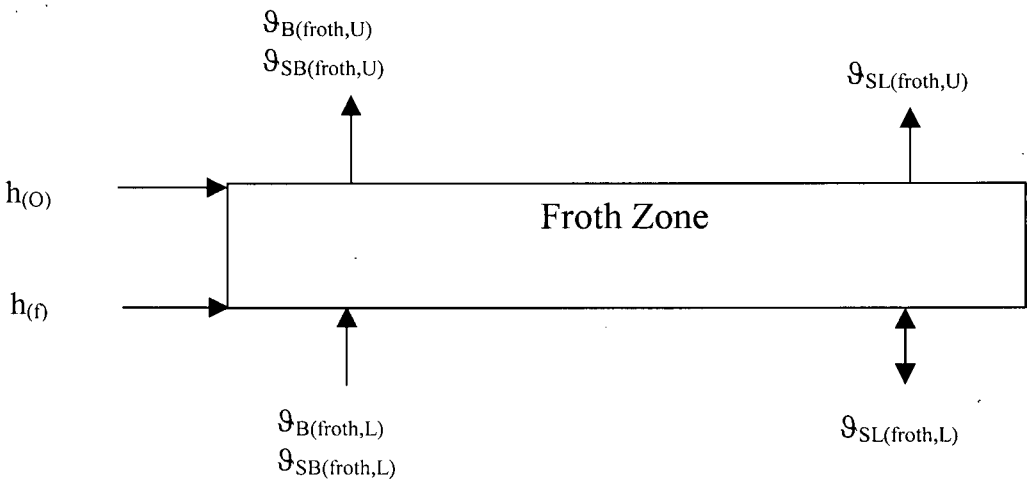


**Figure 48: Froth-zone superficial surface-area flows**

### 5.4.3.2 Flows

A bubble surface rate passes into the froth zone through the lower boundary ($\vartheta_{B(froth,L)}$ [$s^{-1}$]), and out the upper boundary ($\vartheta_{B(froth,U)}$ [$s^{-1}$]), where $|\vartheta_{B(froth,L)}| \geq |\vartheta_{B(froth,U)}|$ due to bubble coalescence.

The overflow bubble surface rate is calculated knowing the average overflow bubble size and volumetric gas flow rate using Equation 116. The lower boundary bubble surface rate is calculated in the recollection-zone model.

A superficial suspended-solids surface-area rate ($\vartheta_{SL(froth,L)}$ [$s^{-1}$]) may also be flowing into the froth zone (negative bias) or from the froth zone (positive bias). In the case of a negative bias, a superficial suspended-solids surface-area rate will enter the overflow product ($\vartheta_{SL(froth,U)}$ [$s^{-1}$]).

A superficial attached-solids surface-area rate ($\vartheta_{SB(froth,L)}$ [$s^{-1}$]) is associated with the input superficial bubble-surface-area flux ($\vartheta_{B(froth,L)}$ [$s^{-1}$]) passing the lower boundary. The attached solids cannot exceed a specific maximum loading: $\phi_{BS}=\vartheta_{BS}/\vartheta_{B}$ (using the bubble size at the appropriate boundary). Solids surface carried into the overflow may be a smaller value than that which entered the froth lower boundary; "L", if coalescence of bubbles occurs. Equation 125 is used to define the overflow attached solids.

If $|\vartheta_{B(froth,U)}\phi_{SB}| < |\vartheta_{SB(froth,L)}|$ then $\vartheta_{SB(froth,U)} = \vartheta_{B(froth,U)}\,\phi_{SB}$ Equation 125
Else $\vartheta_{SB(froth,U)} = \vartheta_{SB(froth,L)}$

In this relationship, "$\vartheta_{SB(froth,U)}$" [$s^{-1}$] is the sum of all individual mineral and particle size-class surface-areas and "$\phi_{SB}$" [dimensionless] is the maximum loading (solids surface divided by bubble surface). If calculated loading is greater than the maximum load, the calculated load is scaled to equal the maximum load using the assumption that all minerals; "m", and size-classes; "n", are scaled equally (Equation 126). Excess solids are returned to the liquid stream and are added to the solids that are already present. The direction of solids outflow within the liquid stream depends on the bias conditions.

$$\vartheta^{*}_{SB(froth,U)(m,n)} = \vartheta_{SB(froth,U)(m,n)}\frac{\phi_{SB,\max}}{\phi_{SB}} \qquad \text{Equation 126}$$

The liquid flow in the froth zone (Figure 49) depends on the difference between the wash-water and overflow water volumetric flow rates according to Equation 127.

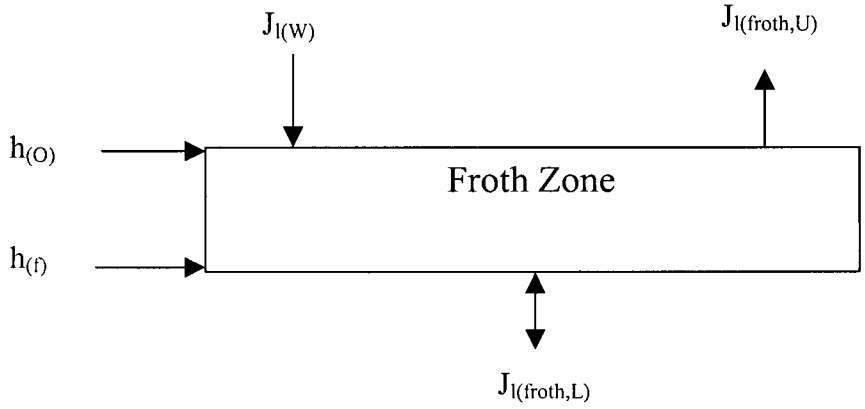


**Figure 49: Froth-zone liquid balance**

$$J_{l(froth,L)} = J_{l(W)} - J_{l(froth,U)} \qquad \text{Equation 127}$$

In Equation 127, "$J_{l(froth,L)}$" [cm $s^{-1}$] is the superficial water velocity at the froth-pulp interface or that passing the froth-zone lower boundary; "$J_{l(W)}$" [cm $s^{-1}$] is the superficial wash-water rate entering the upper boundary and "$J_{l(froth,U)}$" [cm $s^{-1}$] is the superficial water rate in the overflow or that passing the froth-zone upper boundary.

### 5.4.3.3 Positive Bias

A positive bias is defined as a downward particle settling-velocity in the column. This model maintains a simple relationship wherein the liquid rate plus the particle settling-velocity, within that fluid, is the solids bias. In most positive bias environments flow is downward through the froth zone with the initial solids concentration in the water set at to zero (0). Thus, water flowing downward through the lower boundary, out of the froth zone, will have a superficial attached-solids surface-area as indicated in Equation 128.

$$\vartheta_{SL(froth,L)} = |\vartheta_{SB(froth,U)} - \vartheta_{SB(froth,L)}| \qquad \text{Equation 128}$$

In Equation 128, "$\vartheta_{SL(froth,L)}$" [$s^{-1}$] is the superficial suspended-solids surface-area flux passing downward through the lower boundary (positive with positive bias), "$\vartheta_{SB(froth,L)}$" [$s^{-1}$] is the superficial attached-solids surface-area flux passing upward through the lower boundary and "$\vartheta_{SB(froth,U)}$" [$s^{-1}$] is the overflow superficial attached-solids surface-area flux.

Under small negative liquid bias, the solids bias may be positive. This bias occurs whenever the particle settling velocity is downward with respect to column elevation ($u_p + J_{sl} > 0$).

#### 5.4.3.4 Negative Bias

Water flow is upward through the lower-zone boundary under negative bias conditions. The solids carried by this stream pass through the froth lower boundary ($\vartheta_{SL(froth,L)}$ [$s^{-1}$]), flow through the zone and out the upper boundary with the water ($J_{l(froth,U)}$ [cm $s^{-1}$]), along with the solids "dropped off" the bubbles through coalescence as determine by Equation 129.

$$\vartheta_{SL(froth,U)} = \vartheta_{SB(froth,L)} - \vartheta_{SB(froth,U)} + \vartheta_{SL(froth,L)} \qquad \text{Equation 129}$$

In Equation 129 "$\vartheta_{SL(froth,U)}$" [$s^{-1}$] is the superficial suspended-solids surface-area flux passing the upper boundary; "$\vartheta_{SB(froth,L)}$" [$s^{-1}$] is the superficial attached-solids surface-area flux upward through the bottom boundary and "$\vartheta_{SB(froth,U)}$" [$s^{-1}$] is the superficial attached-solids surface-area flux through the froth-zone upper boundary.

The model assumes that there is no transfer of solids surface from the liquid stream to the bubble stream within the froth zone. No turbulence is modeled in the froth zone although turbulence and a bias distribution do occur. There may be areas within the cross-section of a large column wherein a bias of the opposite sign to the average exist. Thus, in a slightly positive bias environment the model will underestimate entrainment.

The implications of this model is that carrying capacity does not vary directly with bias. The ultimate carrying capacity is a measure of the packing factors, induction time and bubble residence time. However, bias may affect bubble coalescence within the froth zone; and thus, may impact operational carrying capacity.

## 5.4.4 **Pulp Zone**

### 5.4.4.1 Introduction

In this model, the pulp zone consists of two zones: the collection and recollection zones. This model describes the collection and recollection zone according to the flow regime and holdups found within those zones. All equations necessary for this model are contained within the Background the Theory section (2) or are derived in this section. Figure 49 shows a solids and liquid balance around the pulp zones.

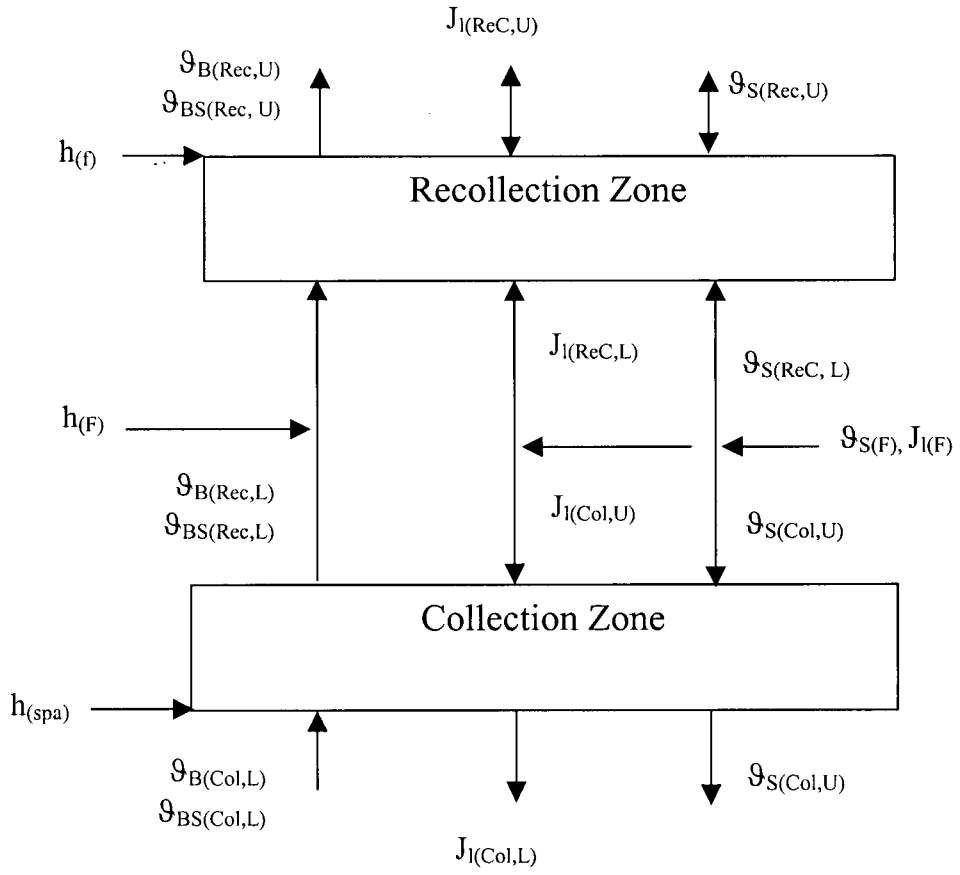


**Figure 50: Pulp-zone superficial surface-area rate balance**

In Figure 50, "h" [cm] is an elevation; "$\vartheta$" [$s^{-1}$] is a superficial surface-area rate; "J" [cm $s^{-1}$] is a superficial velocity; "f" is the pulp-froth interface; "F" is the feed elevation; "Spa" is the sparger elevation; "ReC" is the recollection zone; "Col" if the collection zone; "froth" is the froth zone; "U" is an upper boundary and "L" is a lower boundary.

### 5.4.4.2 Bubble Flow

The gas flow enters at the sparger elevation ($h_{(spa)}$ [cm]) which by definition is the collection zone lower boundary ($h_{(Col,L)}$ [cm]). The superficial bubble-surface-area flux at this location ($\vartheta_{B(Col,L)}$ [$s^{-1}$]) is calculated using Equation 130 (Equation 116).

$$\vartheta_{B(x)} = 6\frac{J_{g(x)}}{d_{b(x)}} \qquad \text{Equation 130}$$

The initial gas flow rate ($J_{g(atm)}$ [cm $s^{-1}$]) is measured or converted to standard temperature and pressure. In Equation 130, "$J_{g(x)}$" [cm $s^{-1}$] is the superficial gas rate at standard temperature and pressure at elevation "x" as determined by Equation 131.

$$J_{g(x)} = J_{g(atm)}\frac{P_{(atm)}}{P_{(x)}} \qquad \text{Equation 131}$$

This model assumes that the average bubble size at the sparger elevation is known. This value is dependent upon the sparger characteristics and reagent concentrations.

Assuming that no gas is dissolved, evolved, or reacted, the surface-area at any elevation in the column can be calculated by modifying the bubble size; "$d_{bx}$" [cm], using the pressure at that elevation; "$P_x$" [g $cm^{-1}s^{-2}$] using Equation 132.

$$\frac{d_{b(x)}}{d_{b(Col,L)}} = \sqrt[3]{\frac{P_{Col,L}}{P_{(x)}}} \qquad \text{Equation 132}$$

In Equation 132, "$d_{b(x)}$" [cm] is the bubble size at any location and "$P_{(x)}$" [g $cm^{-1}s^{-2}$] is the pressure at that location. The initial bubble size ($d_{b(spa)}$ [cm]) is calculated at the sparger elevation.

### 5.4.4.3 Pressure

The pressure at the overflow is assumed to be ambient atmospheric pressure ($P_{(atm)}$ [g $cm^{-1}s^{-2}$]). The pressure at the bottom of the froth zone; "$P_{(Froth,L)}$" can be found using Equation 133.

$$P_{(Froth,L)} = P_{(atm)} + g\rho_{(Froth)}\left(h_{(Froth,U)} - h_{(Froth,L)}\right) \qquad \text{Equation 133}$$

In Equation 133, "g" [cm $s^{-2}$] is the gravitational acceleration and "$\rho_{(Froth)}$" [g $cm^{-3}$] is the froth bulk density. "U" [cm] is the elevation at the zone upper boundary elevation (U=0) and "L" is the elevation at the lower boundary elevation.

Pressure at the collection-zone upper boundary; "$P_{(ReC,U)}$" [g $cm^{-1}s^{-2}$] is the pressure at the froth-zone lower elevation; "$P_{(Froth,L)}$" [g $cm^{-1}s^{-2}$]. The pressure at the bottom of the recollection zone can be found using Equation 134.

$$P_{(ReC,L)} = P_{(ReC,U)} + g\rho_{(ReC)}\left(h_{(ReC,U)} - h_{(Rec,L)}\right) \qquad \text{Equation 134}$$

In Equation 134, "$\rho_{ReC}$" [g $cm^{-3}$] is the recollection-zone overall density. "$P_{(ReC,L)}$" equals the pressure at the collection-zone upper boundary ($P_{(Col,U)}$). The pressure at the bottom of the collection zone is found using Equation 135

$$P_{(Col,L)} = P_{(Col,U)} + g\rho_{(Col)}\left(h_{(Col,U)} - h_{(Col,L)}\right) \qquad \text{Equation 135}$$

In Equation 135 "$\rho_{(Col)}$" [g $cm^{-3}$] is the collection-zone average density. The overall zone densities can be found using Equation 137 (where "z" is the zone).

$$\rho_z = \frac{m_{SB(z)} + m_{SL(z)} + m_{L(z)}}{V_z}$$ Equation 136

In Equation 136 "$m_{(z)}$" [g] is the mass in a zone (z) for the solids attached to the bubbles (B), the solids suspended in the liquid (SL) and the liquid (L). "$V_z$" [$cm^3$] is the total zone volume.

The average mass of solids attached to the bubbles within a zone; "$m_{SB}$" [g] can be calculated using Equation 137.

$$\frac{m_{SB(z)}}{V_z} = \frac{d_p}{12}\left[\frac{\vartheta_{SB(z,U)}\rho_{SB(z,U)}\varepsilon_{B(z,U)}}{J_{g(z,U)}} + \frac{\vartheta_{SB(z,L)}\rho_{SB(z,L)}\varepsilon_{B(z,L)}}{J_{g(z,L)}}\right]$$ Equation 137

In Equation 137 "$d_p$" [cm] is the particle diameter; "$\rho_s$" [g $cm^{-3}$] is the average density of particles, "$\vartheta_{SB}$" is the superficial attached-solids surface-area flux [$s^{-1}$]; "$\varepsilon_B$" is the bubble phase fractional holdup which includes both gas and attached solids and "$J_g$" [cm $s^{-1}$] is the superficial gas flow rate. Also in Equation 137 "U" indicates that this variable is taken at the upper boundary elevation while "L" is the lower boundary elevation.

Equation 137 is derived from the solids-surface-area attached to the bubbles within the zone (Equation 138) and surface-area and volume relationships.

$$\frac{S_{(z)}}{V_z} = \frac{1}{2}\left[\frac{\vartheta_{SB(z,U)}\varepsilon_{B(z,U)}}{J_{g(z,U)}} + \frac{\vartheta_{SB(z,L)}\varepsilon_{B(z,L)}}{J_{g(z,L)}}\right]$$ Equation 138

The mass of solids suspended in the liquid ($m_{SL}$ [g]) is determined using Equation 139.

$$\frac{m_{SL(z)}}{V_z} = \frac{d_p}{12}\left[\varepsilon_{L(z,U)}C_{p(z,U)}\rho_{s(z,U)} + \varepsilon_{L(z,L)}C_{p(z,L)}\rho_{s(z,L)}\right]$$ Equation 139

In Equation 139 "$\varepsilon_L$" is the liquid phase fractional volumetric holdup which itself is composed of a liquid fraction ($\varepsilon_{LL}$) and a solids fraction ($\varepsilon_{SL}$). The solids fraction is found by dividing Equation 139 by the solids density. Thus, assuming that all liquid in the zone is in the "liquid" phase, the average mass of liquid in the zone can be calculated using Equation 140.

$$\frac{m_L}{V_z} = \rho_w \varepsilon_{L(z)} \left[ 1 - \frac{d_p}{12} \left( C_{p(z,U)} + C_{p(z,L)} \right) \right] \qquad \text{Equation 140}$$

In Equation 140 "$\rho_w$" is the density of water.

### 5.4.4.4 Liquid Flow – Liquid Phase

The liquid phase flows within the column are illustrated in Figure 51. This figure also shows the mathematical relationships between the flows.

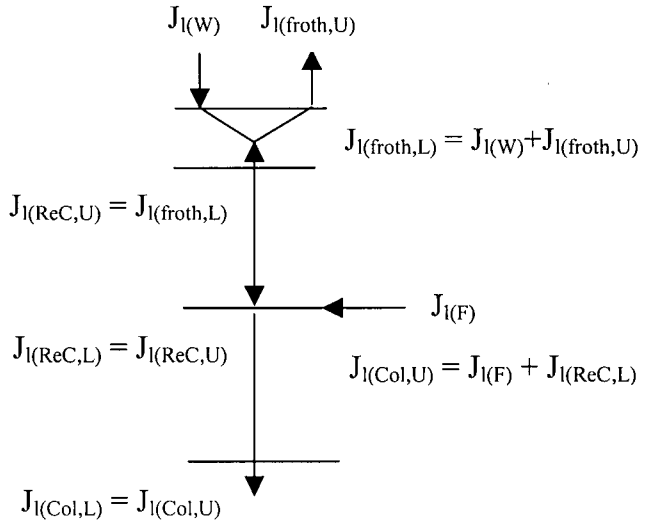


**Figure 51: Column liquid flow schematic**

In Figure 51 "$J_l$" [cm $s^{-1}$] is the superficial liquid rate; "W" is the wash-water; "U" is the upper boundary elevation; "L" is the lower boundary elevation; "froth" is the froth zone, "ReC" is the recollection zone and "Col" is the collection zone.

### 5.4.4.5 Liquid Flow – Solids Phase

Solids bias is the sum of liquid flow and particle settling-velocity. This bias may have the same or the opposite sign as the liquid flow.

#### 5.4.4.5.1 Froth Zone

Under positive bias conditions, when the sum of the superficial liquid velocity and the particle settling-velocity are greater then zero (0), Equation 141 and Equation 142 characterize the solids flow in the liquid phase (originally presented as Equation 128).

$$\vartheta_{SL(froth,L)} + \vartheta_{SB(froth,L)} - \vartheta_{SB(froth,U)} = 0 \qquad \text{Equation 141}$$

$$\vartheta_{SL(froth,U)} = 0 \qquad \text{Equation 142}$$

In Equation 141 the superficial suspended-solids surface-area rate in the liquid phase that passes the lower boundary ($\vartheta_{SL(froth,L)}$ [$s^{-1}$]) is the difference between the solids attached to the bubbles that enter and leave the froth zone. Water flows from the upper boundary, in the positive bias environment, initially contains no solids (Equation 142).

When the solids bias is negative, or the sum of the superficial liquid velocity and the particle settling-velocity is less then zero, the solids flow in the liquid phase is characterized by Equation 143 and Equation 144.

$$\vartheta_{SL(froth,U)} = \vartheta_{SB(froth,L)} - \vartheta_{SB(froth,U)} + \vartheta_{SL(froth,L)} \qquad \text{Equation 143}$$

$$\vartheta_{SL(froth,L)} = \vartheta_{SL(\mathrm{Re}C,U)} \qquad \text{Equation 144}$$

The solids flux in entering the froth zone is the same as the flux exiting the recollection-zone upper boundary (Equation 144). The solids flux passing the froth-zone upper boundary, in the liquid phase, is the flux entering plus the solids "dropped-off" the bubbles (Equation 143).

As bubbles pass through the froth-zone coalescence may occur which reduces the total bubble-surface-area. The bubble-surface-area flux entering the froth zone ($\vartheta_{B(froth,L)}$ [$s^{-1}$]) is determined hydrostatically from the sparger bubble size and pressures (Equation 130 and Equation 132). The final overflow bubble-surface-area flux ($\vartheta_{B(froth,U)}$ [$s^{-1}$]) is determined using the estimated overflow bubble size (Equation 145).

$$\vartheta_{B(froth,U)} = 6\frac{J_{g(atm)}}{d_{b(froth,U)}} \qquad \text{Equation 145}$$

The amount of solids loaded on the bubble (found using Equation 146) is limited to a maximum as determined by Equation 147.

$$\vartheta_{SB(froth,U)} = \vartheta_{SB(\mathrm{Re}C,L)} \qquad \text{Equation 146}$$

$$\vartheta_{SB(froth,U)} \leq \phi_{SB(\max)}\vartheta_{B(froth,U)} \qquad \text{Equation 147}$$

In Equation 147 "$\phi_{SB}$" [dimensionless] is the maximum solids loading on the bubble.

#### 5.4.4.5.2 Feed Distribution

The suspended-solids surface-area rate passing the feed elevation into the recollection zone depends on the bias. Under positive bias conditions the solids flow upward through the recollection-zone lower boundary. Feed to the vessel is split between the collection and recollection zones under negative bias conditions. All particles with a settling velocity greater than the liquid bias move toward the collection zone. Particles accumulate in a zone when the particle settling-velocity and liquid bias are opposite and equal. Turbulence, changing slurry density and other factors prevents this accumulation from occurring in the "real" system.

5.4.4.5.3 Recollection Zone – Negative Bias

The solids in-flow to the recollection zone depends on the solids superficial bias. Under negative bias conditions, wherein there is an upward flow of solids from the feed elevation, the in-flow is across the lower boundary elevation ($\vartheta_{SL(ReC,L)}$ [$s^{-1}$]) is found using Equation 148.

$$\vartheta_{SL(ReC,L)} = \left(J_{l(Rec,L)} + u_{p(Rec,L)}\right) C_{p(F)} \qquad \text{Equation 148}$$

In Equation 148 "$J_{l(ReC,L)}$" [cm $s^{-1}$] is the superficial liquid velocity; "$u_{p(ReC,L)}$" [cm $s^{-1}$] is the particle settling-velocity and "$C_{p(F)}$" [$cm^{-1}$] is the feed specific surface.

The solids flow upward through the recollection zone. Some of these particles will collide and attach to bubbles and the remainder will pass through the zone upper boundary. The superficial attached-solids surface-area rate exiting the upper boundary elevation ($\vartheta_{SB(ReC,U)}$ [$s^{-1}$]) can be calculated from Equation 149 with the maximum limited by Equation 150.

$$\vartheta_{SB(ReC,U)} = \vartheta_{SB(ReC,L)} + f\left(k_f, t_{p(ReC)}, Pe_{ReC}\right)\vartheta_{SL(ReC,L)} \qquad \text{Equation 149}$$

$$\vartheta_{SB(ReC,U)} \leq \phi_{SB(max)}\vartheta_{B(ReC,U)} \qquad \text{Equation 150}$$

The resulting outflow of solids surface remaining in suspension is found in Equation 151

$$\vartheta_{SL(ReC,U)} = \vartheta_{SL(ReC,L)} - \vartheta_{SB(ReC,U)} + \vartheta_{SB(ReC,L)} \qquad \text{Equation 151}$$

5.4.4.5.4 Recollection Zone – Positive Bias

Under positive bias conditions, wherein there is an downward flow of solids from the pulp-froth interface elevation, the in-flow is across the upper boundary ($\vartheta_{SL(ReC,U)}$ [$s^{-1}$]) and is found using Equation 152.

$$\vartheta_{SL(ReC,U)} = \left(J_{l(Rec,U)} + u_{p(Rec,U)}\right) C_{p(froth,L)} \qquad \text{Equation 152}$$

In Equation 152 "$J_{l(ReC,U)}$" [cm $s^{-1}$] is the superficial liquid velocity; "$u_{p(ReC,U)}$" [cm $s^{-1}$] is the particle settling-velocity and "$C_{p(froth,L)}$" [$cm^{-1}$] is the specific solids surface found at that elevation.

The solids flow downward through the recollection zone. Some of these particles will collide and attach to bubbles while the remainder will pass out the zone lower boundary. The superficial attached-solids surface-area rate exiting the upper boundary elevation ($\vartheta_{SB(ReC,U)}$ [$s^{-1}$]) can be calculated from Equation 153 limited by Equation 154.

$$\vartheta_{SB(ReC,U)} = \vartheta_{SB(ReC,L)} + f\left(k_f, t_{p(ReC)}, Pe_{ReC}\right)\vartheta_{SL(ReC,U)} \qquad \text{Equation 153}$$

$$\vartheta_{SB(ReC,U)} \leq \phi_{SB(max)}\vartheta_{B(ReC,U)} \qquad \text{Equation 154}$$

The resulting outflow of solids surface remaining in suspension is found in Equation 155

$$\vartheta_{SL(ReC,L)} = \vartheta_{SL(ReC,U)} - \vartheta_{SB(ReC,U)} + \vartheta_{SB(ReC,L)} \qquad \text{Equation 155}$$

### 5.4.4.6 Collection-Zone Flows

The collection-zone axial boundaries are the feed elevation ($h_F = h_{(Col,U)}$) and the sparger elevation ($h_{Spa} = h_{(Col,L)}$) as shown in Figure 50. The model accounts for collection of particles onto bubble within this zone.

Bubbles generated at the spargers enter the collection-zone lower boundary ($h_{spa}$ [cm]). Rising bubbles result in an upward flow ("-") of bubble-surface-area ($\vartheta_B$ [$s^{-1}$]) without any solids loading ($\vartheta_{SB} = 0$) as illustrated in Figure 50. Upward flow of bubbles will occur as long as "$\rho_b$" < "$\rho_{sl}$".

The solids entering the collection zone in the liquid phase ($\vartheta_{SL(Col,U)}$ [$s^{-1}$]) can be calculated using Equation 156 wherein the in-flow of solids equals the feed plus or minus the bias ($\vartheta_{SL(ReC,L)}$ [$s^{-1}$]).

$$\vartheta_{SL(Col,U)} = \vartheta_{SL(ReC,L)} + \vartheta_{SL(Feed)} \qquad \text{Equation 156}$$

The superficial attached-solids surface-area rate is calculated using Equation 157 limited by the carrying capacity as shown in Equation 158.

$$\vartheta_{SB(Col,U)} = f\left(k_f, t_{p(Col)}, Pe_{(Col)}\right)\vartheta_{SL(Col,U)} \qquad \text{Equation 157}$$

$$\vartheta_{SB(Col,U)} \le \phi_{SB}\vartheta_{B(Col,U)} \qquad \text{Equation 158}$$

The superficial suspended-solids surface-area rate phase passing the collection-zone lower boundary elevation ($\vartheta_{SL(Col,L)}$ [$s^{-1}$]) can be calculated using Equation 159.

$$\vartheta_{SL(Col,L)} = \vartheta_{SL(Col,U)} + \vartheta_{SB(Col,U)} \qquad \text{Equation 159}$$

### 5.4.4.7 Surface Loading Function

The transfer of solids-surface-area from the liquid- to bubble-phase is calculated using the Wehner and Wilhelm (1956) axial dispersion relationship (Equation 59 presented here as Equation 160) as applied by Dobby (1984), Yoon et. al. (1991) and Yoon (1993). "a" is a function of rate constant, residence-time and Peclet number as shown in Equation 161.

$$f(k,t,Pe) = 1 - \frac{4ae^{\frac{Pe_s}{2}}}{(1+a)^2 e^{\frac{aPe_s}{2}} - (1-a)^2 e^{\frac{-aPe_s}{2}}} \qquad \text{Equation 160}$$

$$a^2 = 1 + \frac{4k_f t_{p(z)}}{Pe_{s(z)}} \qquad \text{Equation 161}$$

In Equation 161, "$k_f$" [$s^{-1}$] is the kinetic rate constant determined in the batch test model; "$t_{p(z)}$" [s] is the particle residence-time in the zone and "$Pe_{(x)}$" is the Peclet number. The Peclet number used in both Equation 160 and Equation 161 is the empirical relationship determined by Xu and Finch's (1992) usage of Levenspiel's (1972) equation originally presented in Equation 52. This equation is combined with Shah et. al.'s (1982) equation, originally presented as Equation 49, as Equation 162.

$$Pe_{s(z)} = \frac{(\left|J_{l(z)} + u_{p(z)}\right|)h_{(z)}}{\alpha d_c J_{g(z)}^{0.23}} \qquad \text{Equation 162}$$

In Equation 162 "$J_l$" [cm $s^{-1}$] is the superficial liquid-phase velocity within the zone; "$u_p$" [cm $s^{-1}$] is the average particle settling-velocity of a mineral – size fraction and "$h_{(z)}$" [cm] is the zone height. The dispersion number "Di" [$cm^2 s^{-1}$] is the denominator of this equation. The symbol "$d_c$" [cm] is the column diameter, "$J_g$" [cm $s^{-1}$] is the gas superficial flow rate average within the zone and $\alpha$ is a proportionality constant. Alternative equations can be used to calculate the solids Peclet number as shown in the mixing section (2.8).

The superficial liquid velocity ($J_l$ [cm $s^{-1}$]) is the average velocity within the zone. The particle settling-velocity ($u_p$ [cm $s^{-1}$]) is the velocity of a particular mineral and particle size.

The absolute value of these two velocities is used in the calculation. The particle settling-velocity ($u_p$ [cm $s^{-1}$]) is calculated using Masliyah's (1979) relationship (Equation 163) initially presented as Equation 41.

$$u_{p(x)} = \frac{g d_p^2 \phi_{l(x)}^{2.7} \left(\rho_{p(x)} - \rho_{sl(x)}\right)\left(1 - \varepsilon_{g(x)}\right)}{18\mu_l \left(1 + 0.15 \mathrm{Re}_{p(x)}^{0.687}\right)} \qquad \text{Equation 163}$$

In Equation 163 "$\phi_l$" is the average liquid fraction in the zone; "$d_p$" [cm] is the particle diameter of a mineral, size-class fraction; "$\rho_p$" [g $cm^{-3}$] is the particle density; "$\rho_{sl}$" [g $cm^{-3}$] is the average slurry density (defined as the total mass of solids and liquid divided by the solid and liquid volume); "$\varepsilon_g$" is the average gas holdup and "$\mu_l$" [g $cm^{-1}s^{-1}$] is the fluid viscosity which is assumed to be 0.01. The particle Reynolds' number is calculated using the relationship presented in Equation 164 (originally presented in Equation 42). Equation 163 calculates the particle settling-velocity ($u_p$ [cm $s^{-1}$]) at a location "x".

$$\mathrm{Re}_{p(x)} = d_p u_{p(x)} \varepsilon_{l(x)} \frac{\rho_p - \rho_{sl(x)}}{\mu_l} \qquad \text{Equation 164}$$

In Equation 164 "$\varepsilon_l$" is the fractional liquid holdup. If the particle is not spherical, Equation 44 may be used to calculate settling velocity.

Referring to Equation 161, "$t_{p(x)}$" [s] is the particle residence-time (Equation 165).

$$t_{p(z)} = h_{(z)} \frac{1 - \varepsilon_{g(z)}}{\left(J_{l(z)} + u_{p(z)}\right)} \qquad \text{Equation 165}$$

In Equation 165, "z" refers to an average value within a zone; "h" [cm] is the total zone height, "$\varepsilon_g$" is the gas holdup, "$J_l$" [cm $s^{-1}$] is the superficial liquid velocity and "$u_p$" [cm $s^{-1}$] is the particle settling-velocity.

### 5.4.4.8 Bubble Phase Holdup

The bubble phase holdup ($\varepsilon_B$) is the gas holdup ($\varepsilon_g$) plus the holdup of solids attached to the bubbles ($\varepsilon_{SB}$). The gas holdup ($\varepsilon_g$) can be estimated using Equation 166. In Equation 166 "x" indicates an elevation; "$\varepsilon_{g(x)}$" is the fractional gas-holdup, "$J_l$" [cm $s^{-1}$] is the liquid phase superficial velocity; "$J_g$" [cm $s^{-1}$] is the superficial gas velocity and "$u_b$" [cm $s^{-1}$] is the bubble rise-velocity.

$$\varepsilon_{g(x)} = \frac{J_{l(x)} + J_{g(x)}}{u_{b(x)}} \qquad \text{Equation 166}$$

The bubble rise-velocity ($u_b$ [cm $s^{-1}$]) can be calculated using Yianatos et. al.'s (1988) modification of the Masliyah's (1979) hindered settling relationship (Equation 29 from Finch and Dobby; 1990) presented again here as Equation 167.

$$u_{b(x)} = \frac{g d_{b(x)}^2 \left(\rho_{sl(x)} - \rho_{b(x)}\right)\left(1 - \varepsilon_{g(x)}\right)^{m-1}}{0.18\left(1 + 0.15\,\mathrm{Re}_{b(x)}^{0.687}\right)} \qquad \text{Equation 167}$$

In Equation 167 "x" is an elevation; "$d_b$" [cm] is calculated using Equation 132; "g" [cm $s^{-2}$] is the gravitational acceleration; "$\rho_{sl}$" [g $cm^{-3}$] is the slurry density; "$\rho_b$" [g $cm^{-3}$] is the bubble density; "$\varepsilon_g$" is the fractional gas-holdup; "$Re_b$" is the bubble Reynolds number and "m" is a function of Reynolds number.

The bubble density ($\rho_b$ [g $cm^{-3}$]) can be estimated using Equation 168. This equation is also presented in terms of superficial surface-area rates in Equation 169

$$\rho_b = \frac{\rho_{s(O)} \phi_{SB} d_p}{\phi_{SB} d_p + d_b} \qquad \text{Equation 168}$$

$$\rho_b = \frac{\vartheta_{SB} d_p \rho_p}{\vartheta_{SB} d_p + \vartheta_B d_b} \qquad \text{Equation 169}$$

The slurry density is calculated in a fashion similar to Equation 169 as shown in Equation 170.

$$\rho_{sl} = \frac{\vartheta_{SL} d_p \rho_{SL}}{\vartheta_{SL} d_p + J_L} \qquad \text{Equation 170}$$

The value of "m" used in Equation 167 is calculated using Equation 31 presented here as Equation 171.

$$m = 4.45\,\mathrm{Re}_{b(x)}^{-0.1} \qquad \text{Equation 171}$$

The bubble Reynolds' number ($Re_b$) is calculated using the method found Equation 32 using the Dobby and Finch three-phase configuration (shown here as Equation 172).

$$\mathrm{Re}_{b(x)} = \frac{u_{b(x)} d_{b(x)} \left(\rho_l - \rho_{b(x)}\right)\left(1 - \varepsilon_{g(x)}\right)}{\mu_l} \qquad \text{Equation 172}$$

In Equation 172, "$\mu_l$" [g $cm^{-1}s^{-1}$] is the fluid viscosity that is assumed to be 0.01. This assumption may not be valid under all conditions.

### 5.4.4.9 Solids Specific Surface

The feed specific solids surface ($C_{p(F)}$ [$cm^{-1}$]) value is assigned to the average zone specific solid surface's; "$C_{p(z,0)}$" [$cm^{-1}$]. This value is then adjusted by the superficial solids-surface-area flux with time until and equilibrium is reached using Equation 173.

$$C_{p(i+1)} = C_{p(i)} + \frac{t_{(i)}}{h_{(z)}}\left[\vartheta_{SL(z,U)} - \vartheta_{SL(z,L)} + \vartheta_{SB(z,L)} - \vartheta_{SB(z,U)}\right] \qquad \text{Equation 173}$$

### 5.4.5 Application of the Continuous Model

There are five parts to the kinetic continuous flotation model each of which is composed of a number of steps.

Part 1: Physical Inputs - Enter the following:

1. Effective Column diameter ($d_c$ [cm])
2. Heights:
    a. Sparger ($h_{(spa)}$ [cm]),
    b. Feed port ($h_{(F)}$ [cm]),
    c. Pulp/froth interface ($h_{(f)}$ [cm]),
    d. Column lip elevations ($h_{(O)}$ [cm]) and
    e. Vessel elevation ($h_{(v)}$ [cm]) – assumed equal to column lip elevation.

Part 2: Operational inputs - Enter the following:

1. Superficial gas rate ($J_g$ [cm $s^{-1}$])
2. Average bubble size ($d_b$ [cm])
3. Superficial mass rate of mineral (m,n); ($m_{p(m,n)}t^{-1}A^{-1}$ [g $cm^{-2}s^{-1}$]) (Where "m" is the mineral and "n" is the size-class and "A" [$cm^2$] is the column area)
4. Average particle size ($d_{p(m,n)}$ [cm])
5. Superficial feed liquid flow rate ($J_{l(F)}$ [cm $s^{-1}$])
6. Superficial wash-water rate; ($J_{l(W)}$ [cm $s^{-1}$])
7. Superficial overflow water rate ($J_{l(O)}$ [cm $s^{-1}$])

Part 3: Flotation parameter values as determined through test work and the batch model:

1. Maximum surface-area loading ($\phi_{SB}$ [dimensionless])
2. Maximum recovery ($R_\infty$ [dimensionless] array of m,n size)
3. Flotation rate constant ($k_f$ [$s^{-1}$] array of m,n size)

Part 4: Model initial variable values

1. Assume, initially, that superficial solids-surface-area concentration within each zone ($C_{p(m,n)}$ [$cm^{-1}$]) is the feed value.
2. Assume a gas holdup ($\varepsilon_g$)

Part 5: Calculations

All the following are calculated at the upper and lower boundaries of each zone and for the average of each pulp zone (collection and recollection zone).

1. Density of liquid phase ($\rho_{sl(z)}$ [g $cm^{-3}$]) using Equation 169,
2. Density of zone contents ($\rho_{(z)}$ [g $cm^{-3}$]) using Equation 136,
3. Pressure ($P_{(x)}$ [g $cm^{-1}s^{-2}$]) for zone upper and lower boundaries using Equation 133, Equation 134 and Equation 135.
4. Bubble size ($d_{b(x)}$ [cm]) for zone upper and lower boundaries and zone average using Equation 132.
5. Bubble density ($\rho_{b(x)}$ [g $cm^{-3}$]) for zone average using Equation 169.
6. Bubble rise-velocity ($u_{b(x)}$ [cm $s^{-1}$]) for zone average using Equation 167.
7. Gas holdup ($\varepsilon_{g(x)}$ [dimensionless]) for zone average using Equation 166.
8. Iterate on part 5 step 1 (density of liquid phase) to specific tolerance
9. Particle settling-velocity ($u_{p(m,n)(x)}$ [cm $s^{-1}$]) for zone upper and lower boundaries and zone average using Equation 163.
10. Zone Single Particle residence-time ($t_{p(m,n)(z)}$ [s]) zone averages using Equation 165.
11. Zone Peclet number ($Pe_{(m,n)(z)}$ [dimensionless]) using Equation 162.
12. Solids transfer to gas phase ($R_{p(m,n)(x)}$ [dimensionless]) using Equation 160.
13. Recollection-zone solids transfer between zones by bubble movement ($\vartheta_{SB(x)}$ [$s^{-1}$]): negative bias using Equation 149 -- positive bias using Equation 153.
14. Recollection-zone solids transfer between zones by liquid movement ($\vartheta_{SL(x)}$ [$s^{-1}$]): negative bias using Equation 148 -- positive bias using Equation 152.

15. Recollection-zone carrying capacity limitations: negative bias using Equation 150 -- positive bias using Equation 154.
16. Collection-zone solids transfer between zones by bubble movement ($\vartheta_{SB(x)}$ [$s^{-1}$]) using Equation 157.
17. Collection-zone solids transfer between zones by liquid movement ($\vartheta_{SL(x)}$ [$s^{-1}$]) using Equation 156.
18. Collection-zone carrying capacity limitations: negative bias using Equation 150 – positive bias using Equation 158.
19. Superficial solids-surface-area concentrations ($C_{p(m,n)(x)}$ [$cm^{-1}$]) for zone upper and lower boundaries and zone averages using Equation 173.
20. Iterate on part 5 step 1 (density of liquid phase) to specific tolerance
21. Overflow superficial bubble-surface-area flux ($\vartheta_{B(froth,U)}$ [$s^{-1}$]) using Equation 145.
22. Overflow superficial attached-solids surface-area flux ($\vartheta_{SB(froth,U)}$ [$s^{-1}$]) using "$\vartheta_{SB(froth,L)}$" and "$\phi_{SB}$" (Equation 147).
23. Overflow superficial suspended-solids surface-area flux ($\vartheta_{SL(froth,x)}$ [$s^{-1}$]) where "x" is "U" for negative bias and "U" for positive bias (Equation 143).
24. Iterate on part 5 step 1 (density of liquid phase) to specific tolerance

The iterations of part 5: steps 8, 20 and 24, calculate the difference in density (calculated by square root) between one iteration, "i", and the next, "i+1", and compare that difference; "$\Delta\rho$", to an input number or tolerance. The iteration is terminated when the difference is less than the tolerance.

### 5.4.6 Model Validation

This model is a significant modification of previous continuous column models. As such, it must be tested to verify prediction accuracy. Ideal tests would involve a comparison between actual plant performance and the predictions of this model based on the parameters generated in the previous batch model and laboratory-scale tests. Material for these tests should highlight wide ranges in each model parameter: rate constants, maximum recovery, entrainment and carrying capacity. In addition, the effect of operational variables should also be investigated such as volume fraction of solids, particle size distribution, bubble size distribution, feed rate, gas rate and froth residence-time. Column design will also play a significant role that will impact on the Peclet number used in the model as well as the boundaries between the model zones.

INCO matte and Quinto graphite ore were used because they provided variation in particle size and shape, feed grade, and continuous column scales as shown in Table 23.

**Table 23 Summary of Differences between Quinto and INCO tests.**

| Parameter | Quinto Mines | INCO |
|---|---|---|
| Particle size | < 10 μm | ~ 44 μm |
| Particle shape | Plate like | Approximately cubic |
| Feed Grade | ~ 2% | ~80% |
| Continuous Column | Pilot Scale | Plant Scale |

## 5.5 Comparison of Applications

### 5.5.1 **INCO Industrial-Scale Column**

A comparison was made using the continuous column model response with parameters generated from the batch mechanical-cell, with or without entrainment, and with parameters generated using the batch column. These were compared to performance data from the INCO Coppercliff matte separation plant #2 column. The INCO column is controlled to produce specific products. As such, air rate, froth level, and reagents are continually being modified. These changes are not accounted for in this comparison. The model used a constant froth-zone level. Sparger bubble size, overflow bubble size and air rate are varied by the model to produce a grade-recovery response.

The results presented here must be interpreted in light of error that could be present. No size fraction data was available for the INCO #2 column, thus, the rates and maximum recoveries used in the continuous column model were weighted averages of those values determined in the batch tests. While the feed used in the tests was the feed to the #2 column, it was not taken during the time that the #2 column data was available. Thus, there may be differences in composition. The controlled nature of the matte used at INCO means that these differences are probably minor. However, the size-class distribution and mineral grades may be different along with the composition of the minerals themselves. The batch test feed was 88.3% whereas the #2 column feed ranged from 80 to 85% chalcocite.

Accuracy of the model response under loaded flotation conditions is limited since bubble size was estimated visually during batch tests and pilot tests were conducted using collection zone drift flux analysis (INCO) or estimated through sparger performance characteristics. If hindered flotation is to be modeled more accurate determinations of overflow bubble size are required along with a good overflow particle size characterization.

Figure 52 compares the INCO #2 column performance and the responses of the continuous kinetic model. Plant-scale performance shows column production when feed grade was approximately 85% chalcocite. Batch tests were conducted with a feed grade of 88.5% chalcocite. Both column and mechanical-cell generated parameters were used in the model assuming a feed grade of 85% chalcocite.

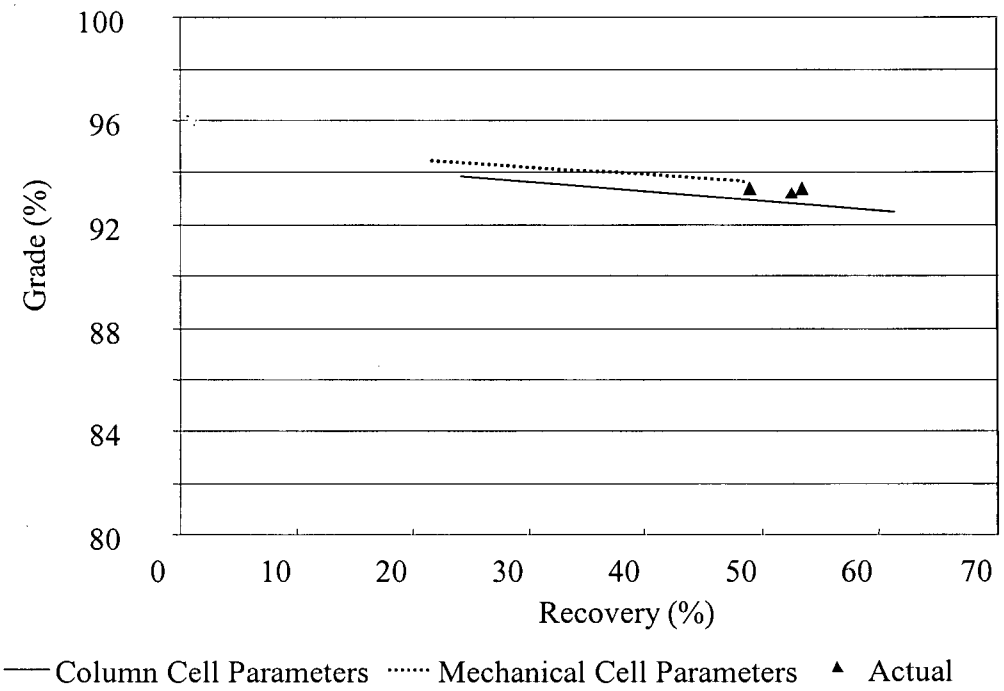


**Figure 52: Comparison between model results using parameters generated by the batch mechanical-cell and the batch column along with actual INCO column performance on approximately the same feed. Feed grade was approximately 85% chalcocite.**

At the feed grades shown in Figure 52 there is similarity between model responses and the plant-scale performance. Plant-scale production data lies between the responses of the model using parameters generated by the batch column and mechanical-cell parameters. The response line of the model when using mechanical cell data ends at approximately 50% recovery -- recoveries high than this value require a negative bias or a longer residence time than the plant column.

Figure 53 compares the INCO #2 column performance and the continuous kinetic model responses. Plant-scale performance shows column production when feed grade was approximately 83% chalcocite. Batch tests were conducted with a feed grade of 88.5% chalcocite. Both column and mechanical-cell generated parameters were used in the model assuming a feed grade of 83% chalcocite.

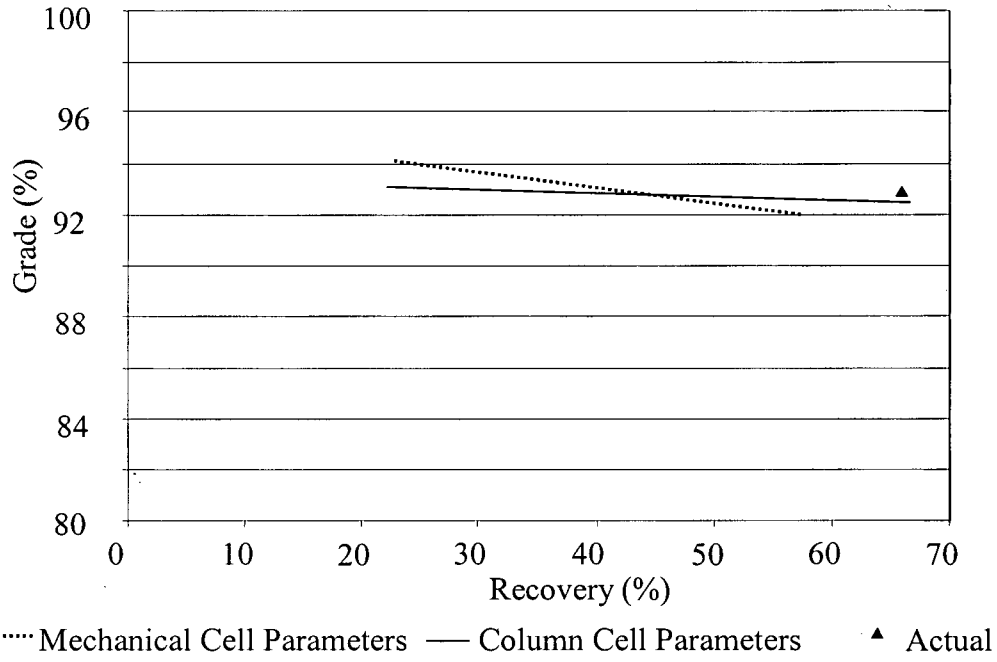


**Figure 53: Comparison between model results using parameters generated by the batch mechanical-cell and the batch column along with INCO #2 copper cleaner column performance on approximately the same feed. Feed grade was approximately 83% chalcocite.**

The 83% grade chalcocite comparison (Figure 53) shows that the production column performance is similar to the continuous kinetic model responses when used with parameters generated using column data. The model response when using parameters derived from mechanical-cell data appears much less accurate.

Figure 54 compares the INCO #2 column performance and the continuous kinetic model responses. Plant-scale performance shows column production when feed grade was approximately 80% chalcocite. Batch tests were conducted with a feed grade of 88.5%

chalcocite. Both column and mechanical-cell generated parameters were used in the model assuming a feed grade of 83% chalcocite. Also shown in Figure 54 is the continuous kinetic model response when used with parameters generated by the batch model that assumed no entrainment.

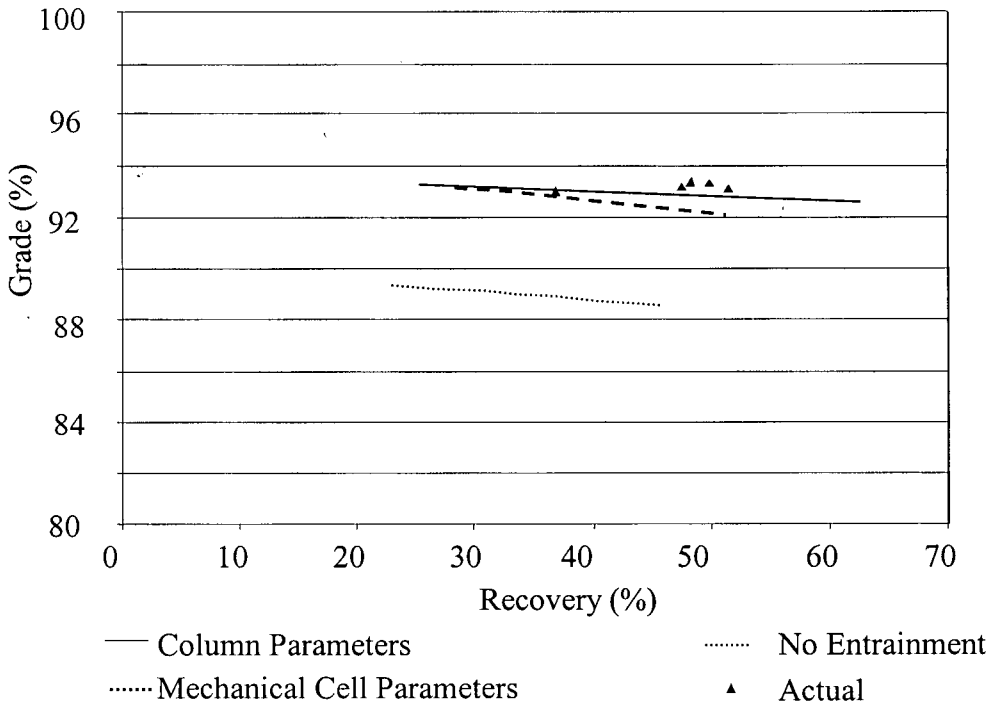


**Figure 54: Comparison between model response using parameters generated by the batch mechanical-cell and the batch column along with actual INCO column performance on approximately the same feed. Feed grade was approximately 80% chalcocite.**

The model response based on batch column parameters generated without entrainment (Figure 54) compare very poorly to the full-scale column performance. This poor comparison is a good indication that the "traditional" rates generated through batch mechanical flotation cells should not be used to size flotation columns without incurring considerable risk.

In these tests the mechanical-cell generated parameters produced a response from continuous model similar the plant performance but with larger error then when modeled using batch

column generated parameters. The mechanical-cell results must be interpreted in light of the different mechanisms of collision, attachment and detachment that occur in comparison to a column. The mechanical-cell is a highly turbulent vessel where significant energy is present to collide small particles with the rising bubbles. This turbulence is not present in the quiescent column where particles may have little momentum independent of the water stream. Cavitation may occur immediately behind the agitator impeller in the mechanical-cell that could result in the growth of micro bubbles on the particle surface. The presence of air bubbles on the solids surface could accelerate the attachment process.

The same energy that allows good collection of fines in the mechanical-cell is also responsible for increased detachment of particles from the bubble at large particle sizes in comparison to columns. Thus, the column should be a better collector of large particles given equivalent residence-times. However, large particles in plant-scale columns have significantly shorter residence-times than the smaller particles.

## 5.5.2 Quinto Graphite Continuous Column Comparison

Figure 55 compares the Quinto pilot-scale column performance and the continuous kinetic model responses using both column and mechanical-cell batch data. The model parameters were generated using approximately the same feed grades as the pilot-scale column.

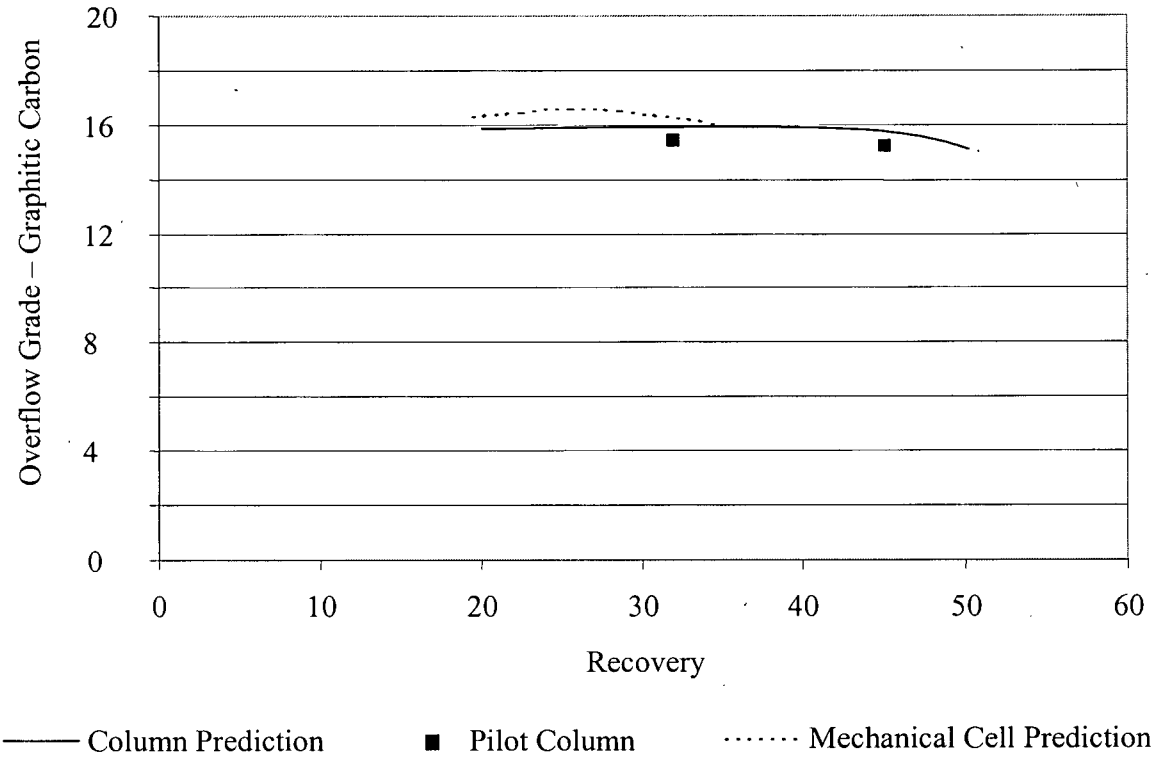


**Figure 55: Comparison between model results using parameters generated by the batch mechanical-cell and the batch column along with actual Quinto pilot-scale column performance on approximately the same feed. Feed grade was approximately 1.4% graphite.**

In Figure 55 the continuous column model responses using parameters generated by the batch column approximate the pilot-scale column performance over the limited number of samples available. The mechanical-cell however, uses a maximum recovery lower than the pilot-scale column recovery. Thus, the mechanical-cell generated parameters disclude recoveries over 48.8% without a negative bias.

## 5.5.3 Model Sensitivity

### 5.5.3.1 Introduction

Variations in surface area, both of the bubbles and particles, along with the three flotation parameters: kinetic rate constants, maximum recovery and maximum bubble loading affect the model response. Thus, errors in these inputs or parameters will cause errors in the response. These inputs were varied to investigate the sensitivity of the model. The model grade – recovery response was generated by varying the air rate from low values to maximum rates (dependant upon the bubble and slurry velocities).

### 5.5.3.2 Particle Size – Particle Surface Area

Error is possible in the determination of particle size which is used to calculate the surface area. Thus, it is important to know the response of the model to different particle size measurements. The model response was tested for particles with an average diameter equal to 0.5, 1.0, 1.5 and 2 times the measured Quinto particle size using the mechanical cell parameters. These responses are shown in Figure 56.

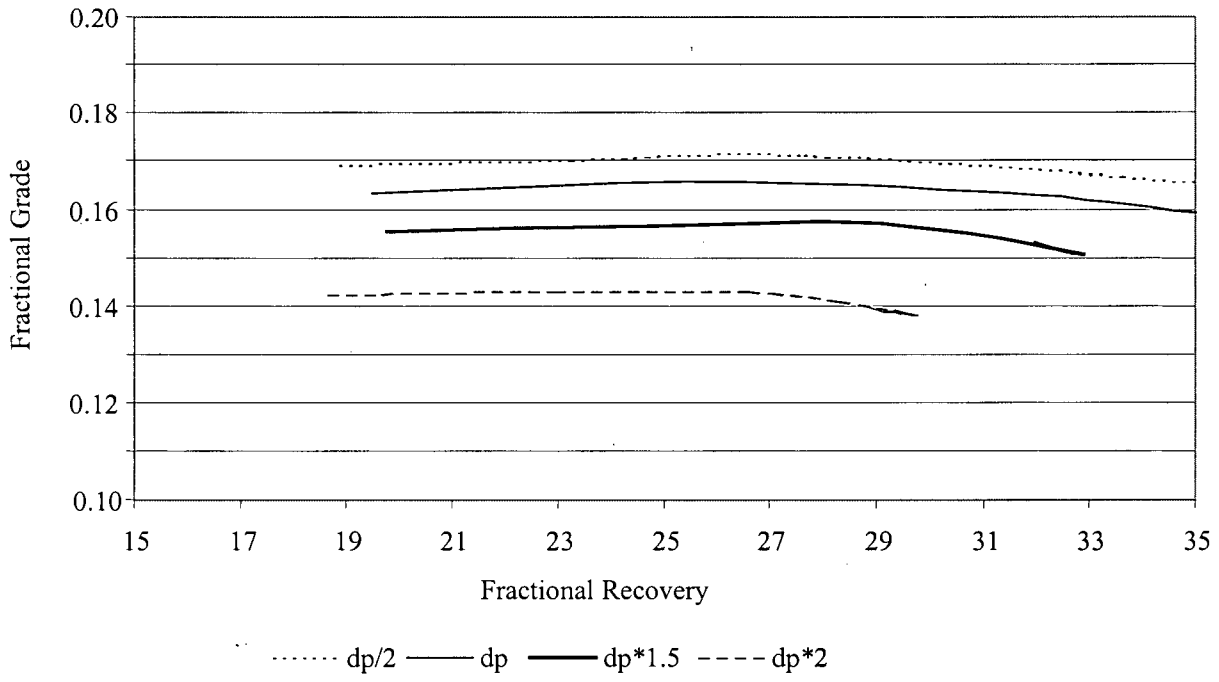


**Figure 56: Sensitivity of model response to particle size variations, Quinto graphite flotation using mechanical cell parameters.**

In Figure 56 the grade - recovery response for alternative particle sizes is shown along with the particle size used. When particles are smaller, more air is required for transport, thus carrying capacity limitation are more of a consideration. However, when carrying capacity is not limiting, these particles have a larger residence time, thus a higher recovery. With larger particles, residence time in the column becomes a consideration. Within the range tested, the response produces larger changes from the determined particle size response when particle size is increased rather than decreased. Variations in grade may be the result of increased graphite flotation without a corresponding large increase in "other" recovery to the overflow.

Certain error is expected due to particle size since the average particle size value depends on the method of calculation. For the Quinto graphite tests, the difference between geometric and Sauter mean diameters is on the order of 1% meaning that little difference in response is expected. However, a difference of approximately 10% is experienced between these two averages in the INCO data. Model response is also dependant upon the "$d_{max}$" [cm] (maximum particle size) and "$d_{min}$" [cm] (minimum particle size) values used in the largest and smallest size fractions.

#### 5.5.3.3 Bubble Size – Bubble Surface Area

Bubble surface area is estimated using a single bubble size rather than a distribution of sizes. This means that the bubble surface area flux is subject to considerable error. The exact amount of this error is unknown. Bubble surface area errors affect the magnitude of the bubble loading parameter but not overall flotation kinetics. The effect of these errors is shown in Table 24.

**Table 24: Surface Area Error Effect on Bubble Load**

| Estimate | Bubble Load | Comments |
|---|---|---|
| $\vartheta_{B,pred} < \vartheta_{B,actual}$ | $\phi_{pred} > \phi_{actual}$ | More surface area of solids may be floated then predicted (under estimation of capacity). |
| $\vartheta_{B,pred} > \vartheta_{B,actual}$ | $\phi_{pred} < \phi_{actual}$ | Less surface area of solids may be floated then predicted (over estimation of capacity). |
| $\vartheta_{S,pred} > \vartheta_{S,actual}$ | $\phi_{pred} > \phi_{actual}$ | Less surface area of solids may be floated then predicted (over estimation of capacity). |
| $\vartheta_{S,pred} < \vartheta_{S,actual}$ | $\phi_{pred} < \phi_{actual}$ | More surface area of solids may be floated then predicted (under estimation of capacity). |

If excess bubble surface area is available then lowering the bubble sizes may reduce recovery due to kinetic considerations since a change in bubble size affects gas holdup, thus, also particle residence time. This effect is illustrated by the model response shown in Figure 57. This figure uses the Quinto batch mechanical cell parameters with varying bubble size.

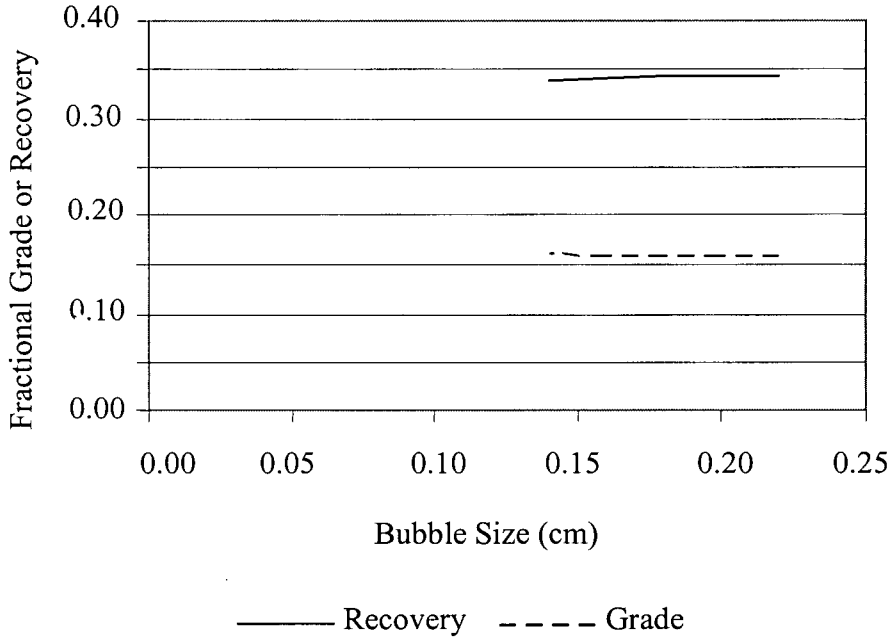


**Figure 57: Grade – recovery model response with changing bubble size under non-loaded conditions.**

In Figure 57 recovery increases slightly with an increase in bubble size since the larger bubbles result in low gas holdup, therefore, larger particle residence times. The grade in Figure 57 remains essentially constant.

A different response is generated by altering bubble size under highly loaded conditions. This effect is shown in Figure 58 wherein the bubbles become fully loaded at approximately 0.12 cm. In this figure little change in recovery occurs as bubble size is increased to approximately 0.12 cm. Increases in bubble size, past 0.12 cm, result in a decrease in recovery as there is insufficient bubble surface to remove the solids area.

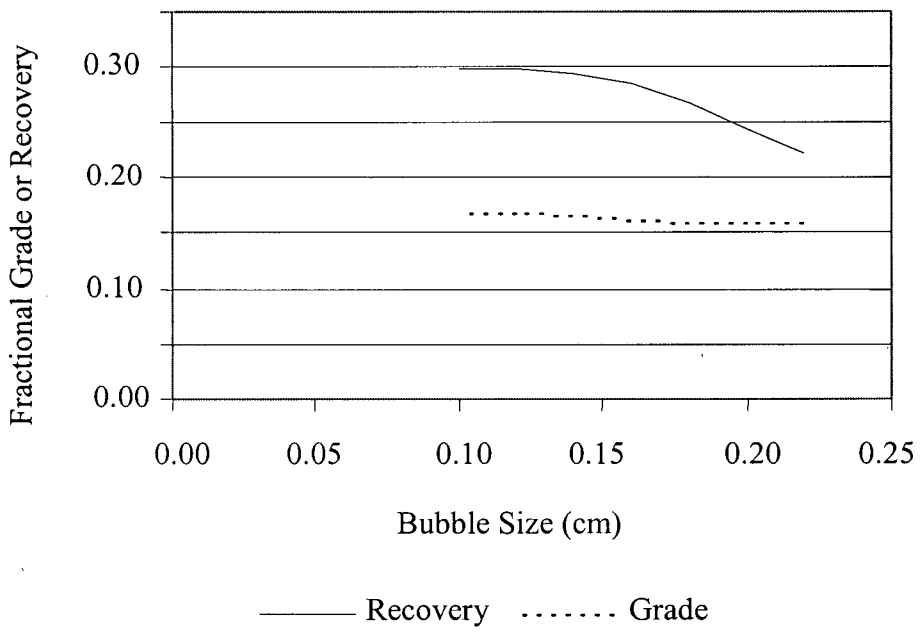


**Figure 58 Grade – recovery model response with changing bubble size under loaded conditions.**

The response of the model will not be affected by errors in bubble surface area unless the area produces hindered flotation conditions as illustrated by the change in recovery in Figure 58 at the bubble size larger than approximately 0.12 cm.

### 5.5.3.4 Flotation Rate Constant

Variations in the flotation rate constant do affect the model response. This effect is illustrated in Figure 59. The rate constant determined for the graphitic carbon in the Quinto tests was 0.008 [$s^{-1}$]. Figure 59 shows the change in grade with recovery for rates of 0.012, 0.010, 0.006 and 0.004 [$s^{-1}$].

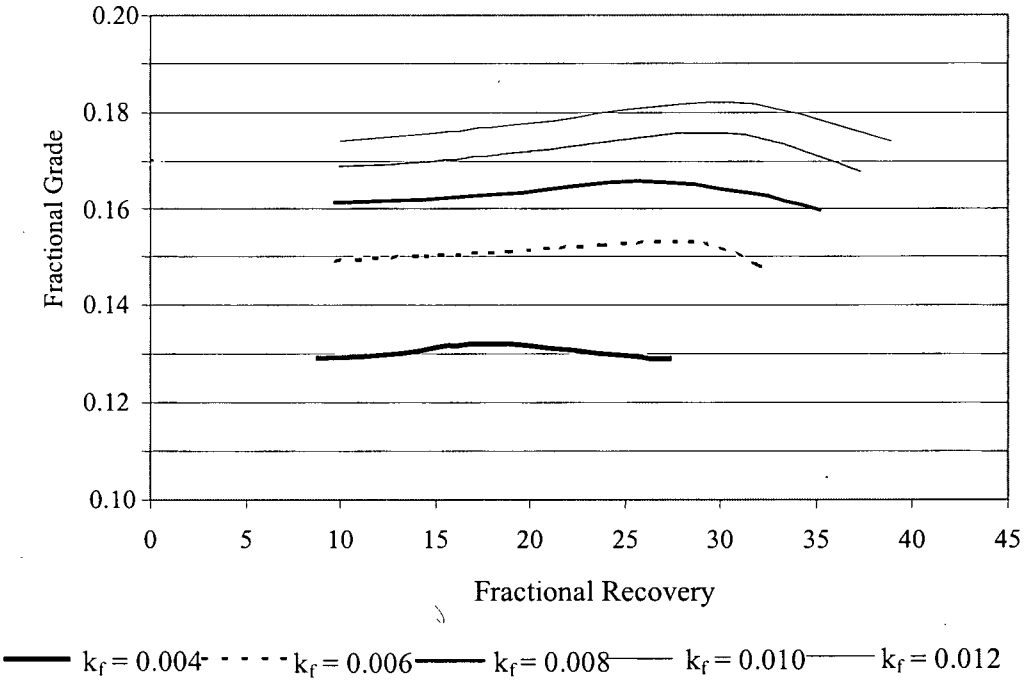


**Figure 59: Model sensitivity to changes in rate constant; "$k_f$" [$s^{-1}$]**

The higher rate constants result in higher grade and recovery. Grade is increased because more graphite floats relative to the gangue minerals. Recovery is increased since the residence time remains the same, but the rate of flotation has increased.

Model response is very sensitive to changes in rate constant. Thus, steps should be taken to ensure the error contained in "$k_f$" is minimized.

### 5.5.3.5 Maximum Recovery

Variations in the maximum recovery affect the model response. This effect is illustrated in Figure 60. The maximum recovery is adjusted from 100% of the mechanical cell generated parameter (48.8%) to 90, 80 and 70% of this value to illustrate the effect this parameter has on model response.

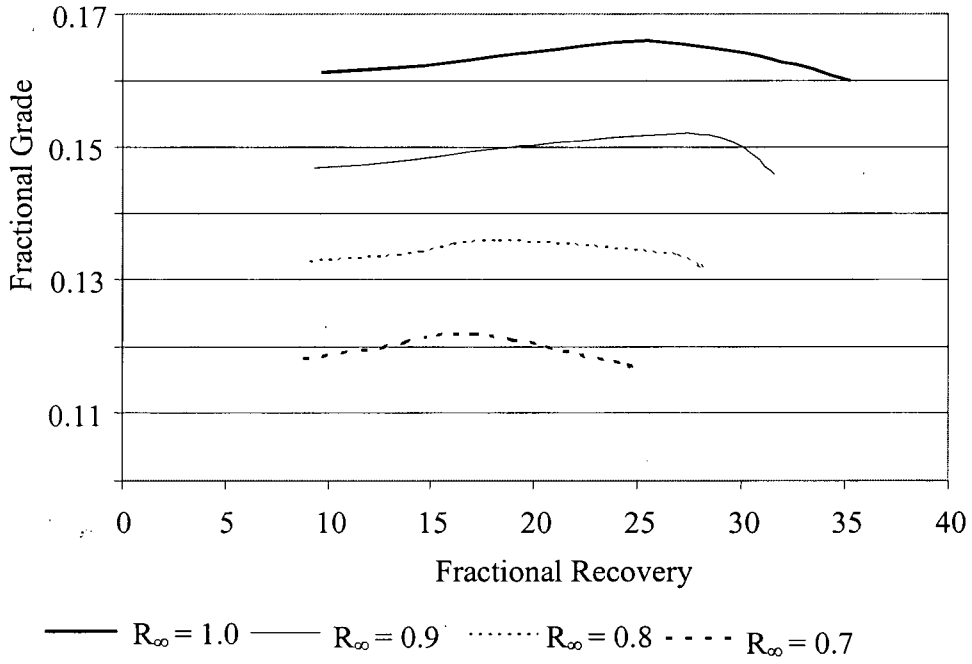


**Figure 60: Model sensitivity to changes in maximum recovery; "$R_\infty$"**

### 5.5.3.6 Entrainment

The entrainment parameter generated in the batch model is used to separate the effects of entrainment from flotation, but this parameter is not used in the continuous model. Froth mixing, which accounts for a distribution of bias flow across the froth, is assumed to be plug flow in the model. Thus, there is no change in the grade recovery relationship with changes in positive bias (Figure 61). When bias is negative a fraction of the liquid phase within the froth zone passes into the overflow. This results in reduced overflow grades.

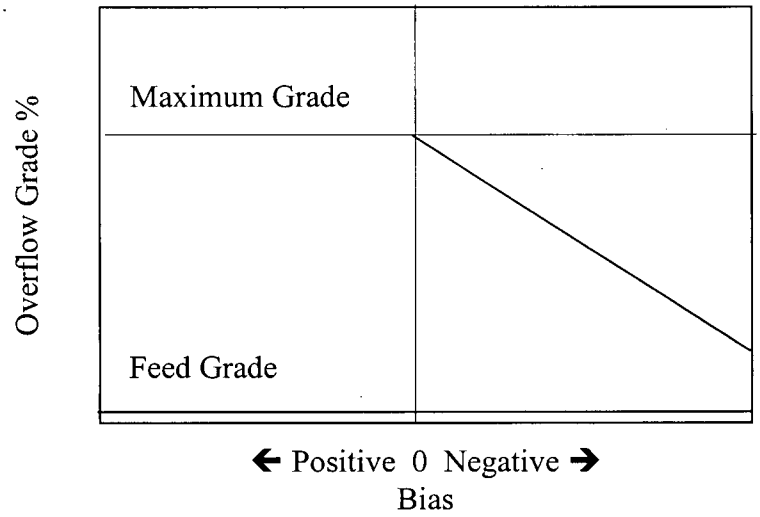


**Figure 61: The generalized effect of negative bias on overflow grade**

### 5.5.3.7 Maximum Bubble Load

Variations in the maximum bubble load have a small affect the model response. This effect is illustrated in Figure 62. The maximum load is adjusted from 100% of the mechanical cell generated parameter (0.64) to 80, 60 and 40% of this value to illustrate the effect this parameter has on model response.

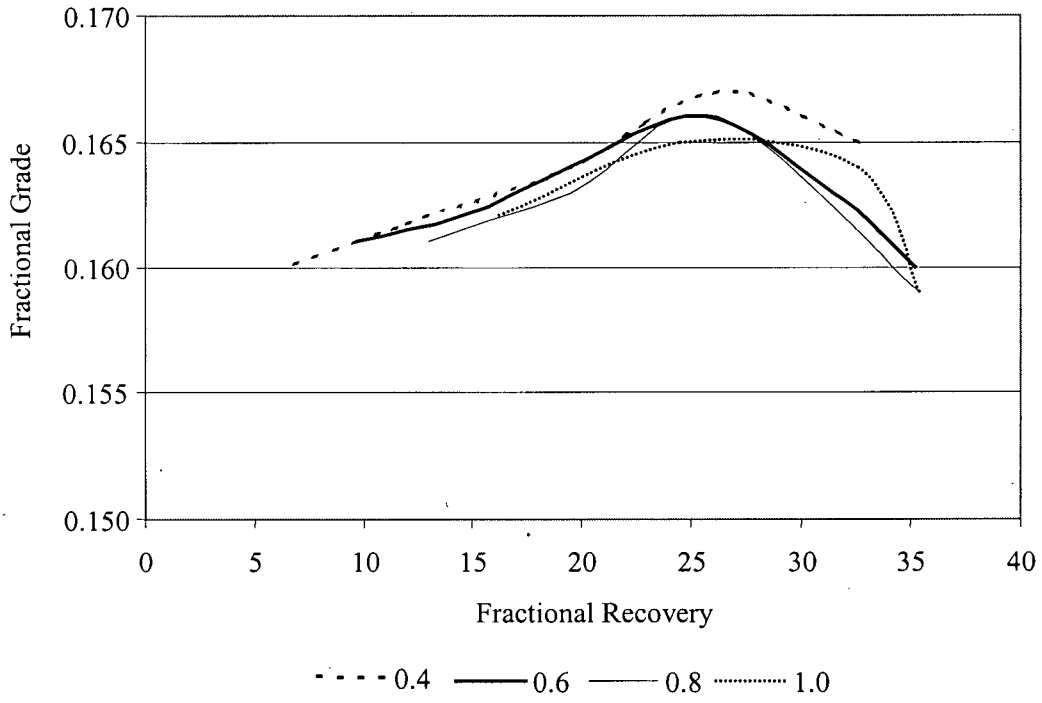


**Figure 62: Model sensitivity to changes in maximum bubble load; "$\phi_{SB}$"**

The recovery response of the model is affected by the bubble load only when fully loaded conditions are experienced. This is shown in Figure 62 as the maximum recovery for the 100, 80 and 60 percent of maximum load result in essentially no maximum recovery change. However, the 40% curve has a much lower maximum recovery as the maximum air rate limit solids surface area removal. Loading has minor effects on grade as the slower floating minerals are not able to collect on the bubble surface after it is significantly loaded.

## 5.6 Mechanistic Bubble Loading "Model Framework"

### 5.6.1 Introduction

The goal of this "model" is the characterization of bubble-loading and solids-removal rates. This "model" could be expanded to two stages by including the froth and entrainment relationships, presented in the continuous kinetic model if mixing is also incorporated. The "model" determines:

1. The induction time ($t_i$): this parameter can be determined when the bubble is loaded ($\theta_l$ [radians]) at angles greater than the angle of streamline departure ($\theta_m$ [radians]) as measured from the forward stagnation point. These are minimal load conditions as shown in Figure 63.

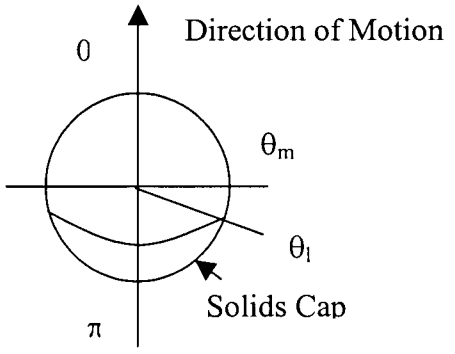


**Figure 63: Loading conditions for induction time determination: $\theta_l > \theta_m$**

2. The solids packing factor ($\Gamma$): this parameter can be estimated when bubble loading ($\theta_l$ [radians]), approximately equals the minimum angular distance needed for attachment ($\theta_i$ [radians]). These maximal load conditions as shown in Figure 64.

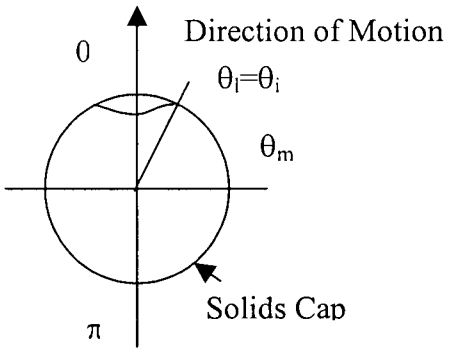


**Figure 64: Loading conditions for solids packing determination: $\theta_l << \theta_m$**

A series of tests should be run using the batch column at different slurry velocities to determine if the predictions of bubble loading with bubble residence-time are correct. This velocities will give a range of bubble residence-times independent of bubble size. Both induction time and maximum loading should be independent of solids concentration and solids residence-time.

This "model" has not been validated. A batch version may be validated by estimating the induction and loading under one set of conditions and using these to predict the value under another set of conditions such as varying air rate, vessel size, mineral concentrations or residence-times. A continuous model must be derived to model industrial-scale continuous operation.

A bubble that has no residence-time cannot carry particles since no collisions will have occurred. Bubble load increases with bubble residence-time as more particles collide and attach. The average bubble residence-time within a batch mechanical-cell pulp zone is on the order of one second. The actual residence-time depends on slurry conditions, vessel dimensions and bubble size. This short residence-time means that bubbles may not be fully loaded as they pass into the froth zone, or as they pass into the overflow. Thus, a "carrying capacity" limit, or maximum, determined in these cells may actually be a bubble residence-time limitation. Carrying capacity, or bubble loading, determined in batch mechanical-cell tests, or in column tests, may be lower than the full-scale units unless bubble residence-times are equal or a method is devised to compensate for the residence-time differences.

## 5.6.2 "Model" Assumptions

The following assumptions are made concerning factors that affect flotation:

1. Batch tests are performed using discrete timed samples. Continuous column operation would be modeled using small element volumes that are composed of the entire vessel cross-section and a specific axial distance.

2. The packing factor; $\Gamma$ [dimensionless] in batch operation may vary with time as the vessel solids composition changes. In continuous operation, the packing factor ($\Gamma$) may vary with axial location as the vessel solids composition changes. In both cases, "$\Gamma$" is assumed to remain constant within the sample interval or within a small element volume. If insufficient data is available "$\Gamma$" is assumed constant.

3. The floatable solids-surface-area concentration ($C_p$ [$cm^{-1}$]) in batch operation is assumed to be constant with axial location, but not with time. In continuous operation the concentration is assumed to be constant with time but not axial location. The average "$C_p$" [$cm^{-1}$] of a timed sample, or within a control volume, is used to represent the entire interval and there is a "$C_p$" for each mineral and size-class.

4. A fraction of the particles within each population, represented by a maximum recovery, is assumed to have a specific induction time with no variations. Other particles, within the same population, are assumed not to float.

5. All bubbles are assumed to be the average size within a timed sample (batch) or a control volume (continuous). Bubble size will vary between elemental volumes, using in the continuous model, because hydrostatic forces decrease with axial distance. Surfactants concentration may decrease with time in the batch unit.

6. The system kinetics is determined by the induction time needed for particle attachment.

7. All angles on the bubble are measured from the front stagnation point. Thus, the lead point on the bubble has a zero angle and the back of the bubble has an angle of $\pi$ radians (Figure 65). All angular measurements are made in radians.

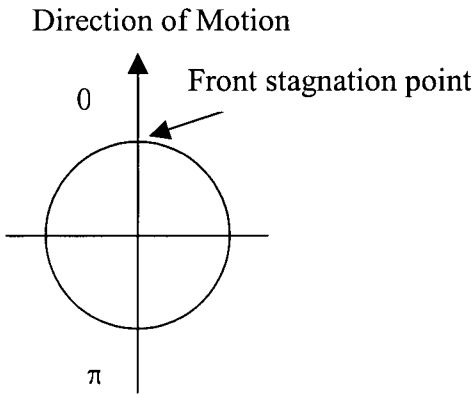


**Figure 65: Angle measurements used in the "model" are based from the forward stagnation point**

8. Mixing is not taken into consideration.
9. Particle detachment is not considered.

## 5.6.3 Batch Collection "Model"

### 5.6.3.1 Collision

Particle collision with a bubble is a function of flow conditions and relative locations. Particles that collide with the bubble exist within a specific starting radius of the bubble centerline. This radius is dependent upon the streamline pattern around the bubble. The area swept out by the bubble is the bubble cross-sectional area ($A_{xb}$ [$cm^2$]) and the effective area of collision is that area multiplied by the collision efficiency ($A_{xb}E_c$ [$cm^2$]) as shown in Figure 66.

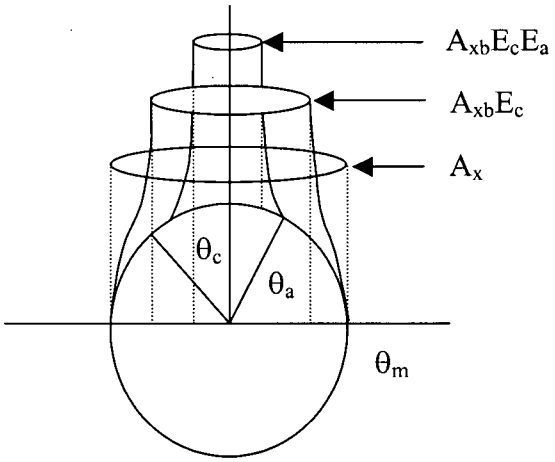


**Figure 66: Active Area of Attachment**

The collision efficiency ($E_c$) can be estimated using the models of Plate and Schulze's (1991) or of Dobby and Finch (1986a) (Equation 67). In the Dobby and Finch model, the collision efficiency at low Stokes' number is further broken into interceptional ($E_{ci}$) (Equation 68) and gravitational efficiencies ($E_{cg}$) (Equation 69). The low Stokes' number collision efficiency is modified to give higher Stokes' number efficiencies (Equation 71).

Particles within the collision area ($A_{xb}E_c$) move with the water streamlines and collide with the bubble between forward stagnation point and the angle of departure ($\theta_m$ [radians]). Particles are assumed to move away from the bubble surface after the point of maximum streamline compression ($\theta_m$).

### 5.6.3.2 Attachment

The attachment efficiency ($E_a$) is a measure of the probability of a particle, within "$A_{xb}E_cE_a$", attaching to the bubble. For attachment to occur, the time of particle contact with the bubble, or contact time ($t_c$), must be greater than the induction time ($t_i$). Induction time is a composite of the time required for the film of water separating bubble and particle to thin, rupture, and for a stable three-phase contact to form. Induction time is a function of mineral surface characteristics, including modifications by reagents or oxidation and surface roughness. The contact time is a function of particle sliding velocity and travel length over the bubble surface.

In Figure 66 "$\theta_a$" [radians] is the maximum angle at which a particle collides with the bubble that actually attaches to the bubble. The particle must be within the area characterized by "$A_{xb}E_cE_a$" (Figure 66) to attach to a bubble. The attachment efficiency ($E_a$) is the ratio of projected bubble cross-sections using "$\theta_a$" and "$\theta_m$" (Equation 174).

$$E_{a(m,n)} = \frac{\sin^2 \theta_{a(m,n)}}{\sin^2 \theta_m}$$

Equation 174

Using Equation 174, the attachment efficiency ($E_a$) value will remain constant, and independent of loading, until the angle from the forward stagnation point to the accumulated solids-surface-area cap is less then the angle of streamline departure ($\theta_m$). After this point loading attachment efficiency ($E_a$) becomes a function of loading.

### 5.6.3.3 Minimum Induction Angle

A particle must be in contact with the bubble for more than the induction time ($t_i$ [s]) for attachment to occur. Particles travel over the bubble surface with a velocity ($v_\theta$ [cm $s^{-1}$]) that may be estimated, at specific angles, by the empirical correlations presented as Equation 76. Thus, the required travel distance ($v_\theta t_i$ [cm]) can be determined. The total bubble circumference is "$\pi d$", thus, radial distance required for attachment is the travel distance divided by the bubble diameter (Equation 175).

$$\theta_{i(m,n)} = \frac{2t_{i(m,n)}v_{\theta(m,n)}}{d_{p(n)} + d_b} \qquad \text{Equation 175}$$

In Equation 175, "$\theta_i$" is the minimum angular distance required for induction; "$t_i$" [s] is the induction time; "$v_\theta$" [cm $s^{-1}$] is the particle velocity along the bubble surface; "$d_p$" [cm] is the particle diameter and "$d_b$" [cm] is the bubble diameter.

### 5.6.3.4 Attachment Angle

The largest angle that a particle can initially contact the bubble that will still become attached ($\theta_a$ [radians]) can be calculated using Equation 176.

$$\theta_{a(m,n)} = \theta_e - \frac{2t_{i(m,n)}v_{\theta(m,n)}}{d_{p(n)} + d_b} \qquad \text{Equation 176}$$

In Equation 176, "$\theta_e$" is the smaller of the angle of streamline departure ($\theta_m$ [radians]) or the angle of accumulated solids surface ($\theta_l$ [radians]). The assumption is made that attached particles are swept to the rear of the bubble. As particles accumulate they form a "cap" which progressively increases in size. The angular bubble coverage by this "cap" extends from "$\theta_l$" to $\pi$ radians.

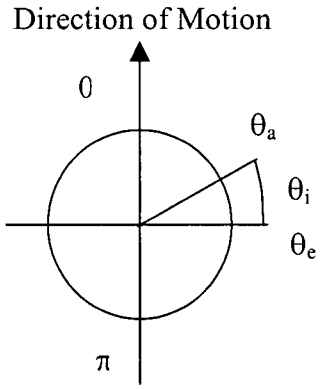


**Figure 67: Maximum angle of collision that leads to attachment ($\theta_a$) is the final travel angle ($\theta_e$) minus the angle of travel needed for attachment ($\theta_i$)**

### 5.6.3.5 Instantaneous Surface Loading

The instantaneous rate of solids-surface-area loading ($\Lambda$ [$cm^2s^{-1}$]) on a bubble can be determined using Equation 177. The superficial attached-solids surface-area flux ($\vartheta_{SB}$ [$s^{-1}$]) equivalent to Equation 177 is found in Equation 178 (where "$t_b$" [s] is the bubble residence-time).

$$\Lambda = \frac{\pi d_b^2}{4} \sum_{j=1}^{m} \sum_{k=1}^{n} E_{c(j,k)} E_{a(j,k)} \left(u_b + u_{p(j,k)}\right) C_{p(j,k)} \qquad \text{Equation 177}$$

$$\vartheta_{SB} = \frac{\vartheta_B t_b}{4} \sum_{j=1}^{m} \sum_{k=1}^{n} E_{c(j,k)} E_{a(j,k)} C_{p(j,k)} \left(u_b + u_{p(m,n)}\right) \qquad \text{Equation 178}$$

The premise of Equation 177 is that all particles that pass through ($[u_p+u_b]C_p$) the active bubble cross-sectional surface-area ($A_{xb}E_cE_a$) will be attached. Equation 177 assumes that the bubble area, covered by a particle, is represented by particle cross-sectional area. The instantaneous loading ($\Lambda$) is constant when $\theta_l < \theta_m$. The solids specific surface ($C_p$ [$cm^{-1}$]) changes with height (continuous column) or with time (batch vessel). Only attachment efficiency ($E_a$) is dependent on bubble loading.

Equation 178 is derived from Equation 177 since the bubble-surface-area is $\pi d_b^2$ [$s^{-1}$] and the bubble loading occurs over the bubble residence-time.

### 5.6.3.6 Solids Loading

The particle-surface-area on a bubble is "$\Lambda t_b$" [$cm^2$]) where "$t_b$" [s] is the bubble residence-time. Equation 179 may be used to calculate the bubble area covered with particles ($S_{CB}$).

$$S_{CB} = \Lambda t_{(i)} \Gamma \qquad \text{Equation 179}$$

In Equation 179 "$t_{(i)}$" [s] is a time interval. The packing factor is a function of the entire population of floatable minerals and may change with time (batch-mode) or with axial distance (continuous-mode).

### 5.6.3.7 Loading Angle

Assuming a single bubble with a specific solids-surface-area attached, the maximum angle of that surface "cap" is determined by Equation 180.

$$\theta_l = \pi - \arccos\left(1 - \frac{2S_{CB}}{\pi d_b^2}\right) \qquad \text{Equation 180}$$

Where the loading angle ($\theta_l$ [radians]) is measured from front stagnation point.

Proof of Equation 180:

If "C" is the upper half of a circle $x^2+y^2=r^2$, then the surface may be calculated by revolving "C" about the x-axis. The parametric equations for "C" are x = rcos(t) and y = rsin(t) where "t" lies between 0 and $\pi$. The bubble-surface-area ($S_B$ [$cm^2$]) can be calculated using Equation 181.

$$S_{CB} = \int_{(\pi-0)}^{(\pi-\theta_l)} 2\pi y \sqrt{\left(\frac{dx}{dt}\right)^2 + \left(\frac{dy}{dt}\right)^2}\, dt \qquad \text{Equation 181}$$

Using the identity $\sin^2 t+\cos^2 t=1$ with Equation 181 results in Equation 182 which can then be solved for Equation 183 and Equation 184.

$$S_{CB} = \int_{(\pi-0)}^{(\pi-\theta_l)} 2\pi r_b \sin t \sqrt{r_b^2 \sin^2 t + r_b^2 \cos^2 t}\, dt \qquad \text{Equation 182}$$

$$S_{CB} = 2\pi r_b^2 \int_{(\pi-0)}^{(\pi-\theta_l)} \sin t\, dt \qquad \text{Equation 183}$$

$$S_{CB} = 2\pi r_b^2 \left[\cos t\right]_{(\pi-0)}^{(\pi-\theta_l)} \qquad \text{Equation 184}$$

Isolating for the maximum angle of surface coverage ($\phi_l$) using bubble diameter ($d_b$) rather than the radius ($r_b$) results in Equation 180.

Assuming that "i" is an interval and that the solids "cap" on the bubble advances in that interval from "$\theta_{l(i)}$" to "$\theta_{l(i+1)}$" then the change in bubble-surface-area can be calculated using Equation 185.

$$\Delta S_{CB} = 2\pi r_b^2 \left[\cos t\right]_{\left(\pi-\theta_{l(i)}\right)}^{\left(\pi-\theta_{l(i+1)}\right)} \qquad \text{Equation 185}$$

Isolating for the angle of loading at the end of the sample ($\phi_{l(i+1)}$ [radians]) (Equation 186, Equation 187 and Equation 188) results in Equation 189.

$$\Delta S_{CB} = 2\pi r_b^2 \left[ \cos\left(\pi - \theta_{l(i+1)}\right) - \cos\left(\pi - \theta_{l(i)}\right) \right] \qquad \text{Equation 186}$$

$$\frac{\Delta S_{CB}}{2\pi r_b^2} + \cos\left(\pi - \theta_{l(i)}\right) = \cos\left(\pi - \theta_{l(i+1)}\right) \qquad \text{Equation 187}$$

$$\pi - \theta_{l(i+1)} = \arccos\left[ \frac{\Delta S_{CB}}{2\pi r_b^2} + \cos\left(\pi - \theta_{l(i)}\right) \right] \qquad \text{Equation 188}$$

$$\theta_{l(i+1)} = \pi - \arccos\left[ \frac{\Delta S_{CB} - 2\pi r_b^2 \cos\left(\pi - \theta_{l(i)}\right)}{2\pi r_b^2} \right] \qquad \text{Equation 189}$$

Equation 190 results when Equation 179 is substituted into Equation 189. Further substitution using Equation 177 gives Equation 191.

$$\theta_{l(i+1)} = \pi - \arccos\left[ \frac{2\Lambda t_{(i)} \Gamma}{\pi d_b^2} - \cos\left(\pi - \theta_{l(i)}\right) \right] \qquad \text{Equation 190}$$

$$\theta_{l(i+1)} = \pi - \arccos\left[ \frac{t_{(i)}\Gamma}{2} \sum_{j=1}^{m} \sum_{k=1}^{n} E_{c(j,k)} E_{a(j,k)} \left(u_b + u_{p(j,k)}\right) C_{p(j,k)} - \cos\left(\pi - \theta_{l(i)}\right) \right] \qquad \text{Equation 191}$$

Substitution of Equation 174 (assuming "$\theta_m = \pi/2$") into Equation 191 results in Equation 192.

$$\theta_{l(i+1)} = \pi - \arccos\left[ \frac{t_{(i)}\Gamma}{2} \sum_{j=1}^{m} \sum_{k=1}^{n} E_{c(j,k)} \sin^2 \theta_{a(j,k)} \left(u_b + u_{p(j,k)}\right) C_{p(j,k)} - \cos\left(\pi - \theta_{l(i)}\right) \right] \qquad \text{Equation 192}$$

Using Equation 175, Equation 192 can be expanded to Equation 193.

$$\theta_{l(i+1)} = \pi - \arccos\left[\frac{t_{(i)}\Gamma}{2}\sum_{j=1}^{m}\sum_{k=1}^{n} E_{c(j,k)}\sin^2\left(\theta_e - \frac{2t_{i(j,k)}v_{\theta(j,k)}}{d_{p(k)}+d_b}\right)\left(u_b + u_{p(j,k)}\right)C_{p(j,k)} - \cos\left(\pi - \theta_{l(i)}\right)\right] \quad \text{Equation 193}$$

Collection efficiency ($E_c$), interval time ($t_i$), particle velocity on the bubble surface ($v_\theta$), particle diameter ($d_p$) and solids specific surface ($C_p$) are dependent on particle composition (j) and size (k). The total surface coverage change is the sum of all individual size fraction and minerals.

A single attachment efficiency value can be used in the instantaneous surface loading calculation (Equation 177) if the time increment ($t_{(i)}$) results in $\theta_l > \theta_m$, otherwise, the surface loading, attached solids, cap angle must be determined using smaller time increments that are summed to a final load.

### 5.6.3.8 Particle Concentration

The particle concentration within a batch vessel is assumed to change with time. The initial concentration is the total surface-area of that mineral size-class fraction divided by the vessel liquid phase volume. The concentration is reduced by the removal rate of solids with time.

### 5.6.3.9 Superficial Attached-Solids Surface-Area Flux

The expansion of Equation 178 to give superficial attached-solids surface-area flux ($\vartheta_{SB}$" [$s^{-1}$]) in terms of induction time ($t_i$ [s]) is presented in Equation 194.

$$\Delta\vartheta_{SB(m,n)} = \frac{\vartheta_B E_{c(m,n)}}{4} \frac{\sin^2\left(\theta_e - \frac{2t_{i(m,n)}v_{\theta(m,n)}}{d_{p(n)}+d_b}\right)}{\sin^2\theta_m} t_b\left(u_b + u_{p(m,n)}\right)C_{p(m,n)} \qquad \text{Equation 194}$$

In Equation 194 the change in the superficial attached-solids surface-area rate is determined. In this equation, "$\vartheta_B$" [$s^{-1}$] is the superficial bubble-surface-area flux; "$C_p$" [$cm^{-1}$] is the specific surface or particle-surface-area concentration; "$t_b$" [s] is the bubble residence-time; "$u_b$" [cm $s^{-1}$] is the bubble rise-velocity; "$u_p$" [cm $s^{-1}$] is the particle settling-velocity; "$\theta_e$" [radians] is the maximum angle prior to particle departure from the bubble; "$t_i$" [s] is the particle induction time; "$v_\theta$" [cm $s^{-1}$] is the particle velocity on the bubble surface; "$d_b$" [cm] is the bubble diameter, and "$d_p$" [cm] is the particle diameter.

When using Equation 194, the change in particle-surface-area depends upon the load when the load angle ($\theta_l$ [radians]) is less than departure angle ($\theta_m$ [radians]). Thus, as long as "$\theta_l$" > "$\theta_m$" one increment can be used. When solids load forms an angle less then "$\theta_m$" the change in particle-surface-area flux over a small axial distance is taken.

### 5.6.4 "Model" use for Flotation Characterization

The equations presented in this "model" can be used to characterize flotation. Under the current configuration this "model" assumes (1) that a mineral size-class fraction has a single induction time and (2) that the total population of particles attaches to the bubble surface with a specific packing. Using the first assumption, and also assuming both that initial solids content on a bubble is zero and that the solids surface "cap" on the bubble has an angle of greater than the angle of particle departure ($\theta_m$ [radians]), Equation 194 can be rearranged to find that induction time ($t_i$ [s]) as shown in Equation 201 (Equation 195 through Equation 200).

$$\frac{4\Delta\vartheta_{SB(m,n)}}{\vartheta_{B(m,n)}C_{p(m,n)}t_b\left(u_b+u_{p(m,n)}\right)E_{c(m,n)}}\sin^2\theta_m=\sin^2\left(\theta_e-\frac{2t_{i(m,n)}v_{\theta(m,n)}}{d_{p(n)}+d_b}\right) \quad \text{Equation 195}$$

$$a_{(m,n)}=\frac{4\Delta\vartheta_{SB(m,n)}}{\vartheta_B C_{p(m,n)}t_b\left(u_b+u_{p(m,n)}\right)E_{c(m,n)}} \quad \text{Equation 196}$$

$$a_{(m,n)}\left(\sin\theta_m\right)^2=\left(\sin\left(\theta_e-\frac{2t_{i(m,n)}v_{\theta(m,n)}}{d_{p(n)}+d_b}\right)\right)^2 \quad \text{Equation 197}$$

$$\arccos\left(a_{m,n}^{0.5}\sin\theta_m\right)=\theta_e-\frac{2t_{i(m,n)}v_{\theta(m,n)}}{d_{p(n)}+d_b} \quad \text{Equation 198}$$

$$\frac{2t_{i(m,n)}v_{\theta(m,n)}}{d_{p(n)}+d_b}=\theta_e-\arccos\left(a_{m,n}^{0.5}\sin\theta_m\right) \quad \text{Equation 199}$$

$$t_{i(m,n)}=\frac{\left(d_{p(n)}+d_b\right)\left[\theta_e-\arccos\left(a_{(m,n)}^{0.5}\sin\theta_m\right)\right]}{2v_{\theta(m,n)}} \quad \text{Equation 200}$$

$$t_{i(m,n)} = \frac{\left(d_{p(n)} + d_b\right)\left[\theta_e - \arccos\left(\left[\frac{4\Delta\vartheta_{SB(m,n)}}{\vartheta_B C_{p(m,n)} t_b \left(u_b + u_{p(m,n)}\right) E_{c(m,n)}}\right]^{0.5} \sin\theta_m\right)\right]}{2v_{\theta(m,n)}}$$

Equation 201

The induction time ($t_i$ [s]) may be determined by tests with a short bubble residence-time where the attached solids "cap" is small.

The surface-area not covered on the bubble ($S_{NCB}$ [$cm^2$] - Equation 202) can be determined from Equation 186.

$$S_{NCB} = \frac{\pi d_b^2}{2}\left[\cos(0) - \cos(\theta_l)\right]$$

Equation 202

The bubble surface covered by solids ($S_{CB}$ [$cm^2$]) is found using Equation 203 since the total bubble surface is $\pi d_b^2$ and cos(0) = 1.

$$S_{CB} = \pi d_b^2 - \frac{\pi}{2} d_b^2 \left[1 - \cos(\theta_l)\right]$$

Equation 203

Equation 204 is a simplified version of Equation 203.

$$S_{CB} = \frac{\pi}{2} d_b^2 \left[1 - \cos(\theta_l)\right]$$

Equation 204

The ratio of covered bubble-surface-area flux to total bubble-surface-area flux is equal to the ratio of covered individual bubble-surface-area to total individual bubble-surface-area assuming that coverage of all bubbles is equal. This relationship is found in Equation 205.

$$\frac{\vartheta_{CB}}{\vartheta_B} = \frac{S_{CB}}{S_B}$$

Equation 205

Using Equation 203 and Equation 205 along with the "$S_B$" = $\pi d_b^2$. Equation 206 can be determined.

$$\vartheta_{CB} = \vartheta_B \frac{1-\cos(\theta_l)}{2} \qquad \text{Equation 206}$$

Substituting "$\Gamma\vartheta_{SB}=\vartheta_{CB}$" (from Equation 179) into Equation 206 results in Equation 207.

$$\Gamma = \frac{\vartheta_B (1-\cos\theta_l)}{2\vartheta_{SB}} \qquad \text{Equation 207}$$

The definition of bubble loading ($\phi_{SB}$ [dimensionless]) is the ratio of particle- to bubble-surface-area superficial fluxes. Equation 208 results from this definition and Equation 207. The maximum bubble loading ($\phi_{SB,max}$ [dimensionless]) can be estimated by substituting "$\theta_i$" for "$\theta_l$" in Equation 208.

$$\phi_{SB} = \frac{1-\cos\theta_l}{2\Gamma} \qquad \text{Equation 208}$$

"$\theta_e$" can replace "$\theta_l$" assuming that the loading angle is greater than the critical angle ($\theta_l > \theta_m$). Equation 212 results when "$\theta_e$" is isolated from Equation 194 (using steps Equation 209 through Equation 211)

$$\frac{4\Delta\vartheta_{SB(m,n)}}{\vartheta_B} \frac{\sin^2\theta_m}{C_{p(m,n)} t_b \left(u_b + u_{p(m,n)}\right) E_{c(m,n)}} = \sin^2\left(\theta_e - \frac{2t_{i(m,n)} v_{\theta(m,n)}}{d_{p(n)} + d_b}\right) \qquad \text{Equation 209}$$

$$\left[\frac{4\Delta\vartheta_{SB(m,n)}}{\vartheta_B} \frac{\sin^2\theta_m}{C_{p(m,n)} t_b \left(u_b + u_{p(m,n)}\right) E_{c(m,n)}}\right]^{0.5} = \sin\left(\theta_e - \frac{2t_{i(m,n)} v_{\theta(m,n)}}{d_{p(n)} + d_b}\right) \qquad \text{Equation 210}$$

$$\arccos\left(\left[\frac{4\Delta\vartheta_{SB(m,n)}}{\vartheta_B}\frac{\sin^2\theta_m}{C_{p(m,n)}t_b\left(u_b+u_{p(m,n)}\right)E_{c(m,n)}}\right]^{0.5}\right)=\theta_e-\frac{2t_{i(m,n)}v_{\theta(m,n)}}{d_{p(n)}+d_b}$$

Equation 211

$$\theta_e=\arccos\left(\left[\frac{4\Delta\vartheta_{SB(m,n)}}{\vartheta_B}\frac{\sin^2\theta_m}{C_{p(m,n)}t_b\left(u_b+u_{p(m,n)}\right)E_{c(m,n)}}\right]^{0.5}\right)+\frac{2t_{i(m,n)}v_{\theta(m,n)}}{d_{p(n)}+d_b}$$

Equation 212

The bubble residence time needed to load a bubble to the critical angle, or the angle at which further loading reduces the attachment efficiency, can be determined. If the assumptions are made that initial bubble loading is zero and increment time is the bubble residence time then Equation 190 simplifies to Equation 213.

$$\theta_l=\pi-\arccos\left[\frac{2\Lambda t_b\Gamma}{\pi d_b^2}-1\right]$$

Equation 213

When Equation 177 is substituted for the instantaneous loading ($\Lambda$) and simplified, Equation 214 results.

$$\theta_l=\pi-\arccos\left[t_b\Gamma\frac{\sum_{j=1}^{m}\sum_{k=1}^{n}E_{c(j,k)}E_{a(j,k)}\left(u_b+u_{p(j,k)}\right)C_{p(j,k)}}{2}-1\right]$$

Equation 214

Note: this equation assumes that the specific surface ($C_p$ [$cm^{-1}$]) and other variables remain constant along the vessel axial dimension. This does hold true in batch devices or well mixed vessels. The bubble residence time required to load to the critical angle can be determined by rearranging Equation 214 resulting in Equation 215.

$$t_b=\frac{2}{\Gamma}\frac{\left[\cos(\pi-\theta_l)+1\right]}{\sum_{j=1}^{m}\sum_{k=1}^{n}E_{c(j,k)}E_{a(j,k)}\left(u_b+u_{p(j,k)}\right)C_{p(j,k)}}$$

Equation 215

### 5.6.5 Future Development

A working, continuous model must also be developed in order to use the parameters generated. One such possibility is a cylindrical coordinate finite element model that accounts for liquid and bubble flow in three dimensions. The calculations presented in this model "framework" could be used to predict surface transfer from the suspended to the attached state within each element.

### 5.6.6 Tests for "Model" Validation

This "model" is an application of mechanistic flotation theory that could be used to estimate carrying capacity (loading) and the removal of solids-surface-area by bubble transport. To this end, a comparison should be made between actual flotation in various sized vessels and "model" predictions. Material for these tests should highlight wide ranges in each "model" parameter: induction time, maximum recovery, entrainment and particle size and shape (packing). In addition, the effect of operating variables should be investigated including volume fraction of solids, bubble size distribution, feed rate, and gas rate.

### 5.6.7 Mechanistic Bubble Loading "Model" Steps

There are three parts to the proposed mechanistic "model" for flotation parameter estimations: determination of (1) induction times [(m,n) array] [s], (2) packing factor [dimensionless], and (3) the critical loading angle; "$\theta_m$".

Part 1: Determination of induction times

A batch test should be run wherein the bubbles are loaded with solids to angles greater than critical ($\theta_l > \theta_m$ where both angles are measured from the bubble forward stagnation point). This condition can be achieved by using small bubble residence-times within the flotation vessel. A series of tests can be done with varying bubble residence-times. These tests should result in a constant induction time until loading exceeds the critical angle ($\theta_l < \theta_m$ when assuming that $\theta_e = \theta_m$) using Equation 201. Thus, induction time can be calculated without knowing the packing factor. Equation 201 is presented here again as Equation 216.

$$t_{i(m,n)} = \frac{\left(d_{p(n)} + d_b\right)\left[\theta_e - \arccos\left(\left[\frac{4\Delta\vartheta_{SB(m,n)}}{\vartheta_B C_{p(m,n)} t_b \left(u_b + u_{p(m,n)}\right) E_{c(m,n)}}\right]^{0.5} \sin\theta_m\right)\right]}{2v_{\theta(m,n)}} \quad \text{Equation 216}$$

In Equation 216 the following variables and parameters are used:

- "$d_{p(n)}$" [cm] and "$d_b$" [cm] are the particle and bubble diameters. These are input variables, thus are known.
- "$\theta_e$" [radians] is the maximum sliding angle and is assumed equal to the point of streamline departure from the bubble ($\theta_m$ [radians]). The critical angle and can be calculated using Equation 74.
- "$\Delta\vartheta_{SB(m,n)}$" [$s^{-1}$] is the floated (overflow) solids-surface-area flux of a mineral and size-class fraction assuming an initial value of zero (0).

- "$\vartheta_B$" [$s^{-1}$] is the bubble-surface-area flux as calculated by Equation 130.
- "$C_p$" [$cm^{-1}$] is the solids specific surface as calculated using Equation 173.
- "$t_b$" [s] is the bubble residence-time as determined by dividing the total zone height ($h_{(z)}$ [cm]) by the bubble rise-velocity ($u_b$ [cm $s^{-1}$]).
- "$u_b$" [cm $s^{-1}$] is the bubble rise-velocity as estimated by Equation 167.
- "$u_p$" [cm $s^{-1}$] is the particle settling-velocity as estimated by Equation 163.
- "$E_c$" [dimensionless] is the collision efficiency as determined by Equation 67.
- "$v_\theta$" [cm $s^{-1}$] the particle velocity over the bubble surface as determined by Equation 76. Note: this value varies with position on the bubble.

Part 2: Determination of packing factor

The actual bubble solid-cap loading-angle is unknown. Floatable solids will load a bubble to "$\theta_i$", at infinite residence-time, meaning that Equation 207 (Equation 217) can be used to predict the loading factor. To determine the packing factor a series of tests must be performed at progressively longer bubble residence-times and the packing calculated assuming loading to "$\theta_a$". (Longer bubble residence times can be achieved either by increasing column length or by decreasing the bubble rise velocity with respect to the column.) The test results will plot as an asymptotic curve of packing factor verses bubble residence-time. The asymptote of this curve will be the actual packing factor.

$$\Gamma = \frac{\vartheta_B (1 - \cos\theta_i)}{2\vartheta_{SB}} \qquad \text{Equation 217}$$

In this equation,

- "$\Delta\vartheta_{SB}$" [$s^{-1}$] is the floated solids-surface-area flux to the overflow since the initial "$\vartheta_{SB}$" [$s^{-1}$] is zero.
- "$\vartheta_B$" [$s^{-1}$] is the bubble-surface-area flux as calculated by Equation 130.
- "$\theta_i$" [radians] is the minimum angle needed for attachment, which is calculated using Equation 175.

Part 3: Estimation of critical loading angle.

The fastest flotation will occur when bubbles are loaded less than the critical angle. Using the series of tests from stage 1 and stage 2, the values of induction time ($t_i$) are calculated assuming "$\theta_l > \theta_m$". A change in the induction time (as estimated by Equation 201) versus bubble residence-time slope will indicate that "$\theta_l = \theta_m$". Since this change will be gradual the exact value of "$\theta_m$" may remain unknown. These values can be calculated directly by isolating for "$\theta_e$" in Equation 194 as shown in Equation 212.

The superficial attached-solids surface-area flux can be calculated using Equation 194.

# 6 Conclusions

## 6.1 Batch Column Tests

The batch column test developed is an effective means of gathering kinetic data to be used in the batch kinetic model. The tests have the following benefits and advantages when compared to batch mechanical cell tests or pilot-scale continuous column tests:

1. Approximately equal residence time for all particle sizes, unlike continuous column where the residence time depends on the collection zone length, gas holdup and individual particle settling velocities.
2. Variable bubble residence times that allows characterization of bubble loading with time.
3. Small volume of feed material that allows the test to be used on drill core or grab samples compared to the larger samples (on the order of hundred's of kilograms) needed for continuous column testing.
4. Testing time for a single test is about half-an-hour, not including sample preparation, meaning that the test can be used to check circuit performance or in circuit tuning.
5. The test vessel design promotes an even distribution of wash-water similar to well designed pilot- or plant-scale columns.
6. The batch column's movable feed elevation means that the recollection-zone dimensions can be adjusted to maximize performance or to characterize the recollection zone.

The batch column test allows the simulation of continuous column performance with respect to bubble loading, kinetics, bias conditions, and maximum loading.

## 6.2 Batch Kinetic Model

The batch kinetic model has been designed to accept data from either bench-scale batch mechanical-cell or column tests. The flotation parameters generated in this model: rate constants (Equation 110, as summarized in Table 25), entrainment constants (Equation 103), maximum recoveries (ratio of floating surface are to total surface area for a mineral and size class fraction) and carrying capacity (Equation 119) are determined by a simplex method of non-linear regression using an objective function (Equation 93). The model also requires a calculation of the "dead" or inactive volume of the column (Equation 97) and of particle residence time (Equation 98).

**Table 25: Summary of Batch Column Test Parameters**

| | |
|---|---|
| $\vartheta_{SB(i)}t_{(i)} = \frac{S_{SB(i)}}{A} = \left( C_{pf(i)}h_{(z)} - \vartheta_{SLF(O,i)}\frac{t_{(i)}}{2} \right)\left(1 - e^{-k_{f(i)}t_{(i)}}\right)$ | Equation 110 |
| $\vartheta_{SL(O,i)} = k_e J_{l(O,i)}\left(\frac{C_{p(i)} + C_{p(i+1)}}{2}\right)$ | Equation 103 |
| $\phi_{SB(i)} = \frac{\vartheta_{SB(i)}}{\vartheta_{B(i)}}$ | Equation 119 |
| $\varepsilon_{m,n} = \sum_{i=1}^{L}\sqrt{\left(\vartheta_{S(O,i)(m,n)}t_{(i)} - \vartheta^{*}_{S(O,i)(m,n)}t_{(i)}\right)^2}$ | Equation 93 |
| $V_d = \frac{\pi}{12}h_{(spa,L)}d^2_{c(spa,L)}$ | Equation 97 |
| $\frac{t}{t_{(i)}} = \frac{\left[\frac{\left(h_{(v)} - h_{(f)} - h_{(spa)}\right)\left(1-\varepsilon_g\right)}{J_l + u_p}\right]_1}{\left[\frac{\left(h_{(z)} - h_{(f)} - h_{(spa)}\right)\left(1-\varepsilon_g\right)}{J_l + u_p}\right]_1 + \left[\frac{h_{(r)}}{J_r - u_p}\right]_2 + \left[\frac{V_d}{A_c J_l}\right]_3}$ | Equation 98 |

This model has the following characteristics:

1. The model uses either mechanical-cell or column generated data. When possible column generated data should be used as this will limit the error incorporated into the model by entrainment estimations. Column rate constants and maximum recoveries will be different than mechanical cells since the two cells have different turbulences.

2. Solids are classified as being associated with either the bubble- or liquid-phase. Flotation is the transfer from the liquid-phase to the bubble-phase. "Drop-back" in the froth zone is transfer from the bubble-phase to the liquid-phase.

3. Entrainment is treated as solids bulk transport by the liquid-phase. Thus, entrainment is suspended solids carried to the overflow by feed water. The assumption of plug flow in the froth zone may not be accurate depending on column size and wash water addition design. The parameter is only used to characterize non-floating solids recovered to the overflow. Calculation of entrainment, flotation rates and maximum recovery are done using the recovery within a size class, thus, errors in the determination of the average size within a size class do not affect these parameters.

4. The model uses specific surfaces and superficial surface-area rates calculated using geometric means. Alternative means, such as the Sauter mean diameter, do exist. The specific and superficial surface areas reflect the surface nature of flotation, as compared to mass flows. This description allows the detection of flotation delays and hindered settling conditions, or allows the prediction of these conditions. The model response depends on the surface area input; thus, the type of average particle size used and the maximum and minimum particle sizes. Also, response error depends upon the surface area measurement error.

5. The flotation rate constant is used to characterize floating solids to the overflow. It is determined by minimization of error along with maximum recovery and entrainment. Errors in test data may result in these three parameters also being in error. It is also

possible that the simplex error minimization routine will set these parameters at a local, rather than global minimum. The rate constant error due to surface area measurement error is minimial since it is determined by a ratio of surface areas both of which are subject to the same error.

6. The effective residence-time of a batch column is calculated.

7. The maximum recycle rate, or column downward liquid-phase flow can be calculated.

8. Bubble loading (carrying capacity) is defined as the ratio between attached particle and bubble, surface-areas. Under hindered flotation conditions the solids removal rate becomes a function of bubble-surface-area rate and maximal loading. The maximum bubble loading determined in the batch tests may not be the ultimate bubble loading if insufficient bubble residence time was used. This is usually the case in batch mechanical cell tests and may be the case for column batch tests. Bubble loading is sensitive to both errors in particle and bubble size determinations.

9. The model does not account for locking. As a result, non floating minerals may float with rates similar to floating minerals with their maximum recovery being an indication of the percentage of the material that is locked.

10. Use of the batch column model with test data generated from batch column tests and mechanical cell tests (INCO and Quinto Mines) show that, for the tested material, the predictions of the model give a good approximation test data when entrainment is taken into account.

11. Average particle size is calculated using the geometric mean. Other methods of calculating mean may be used that will result in a different value for the particle size, thus, a different model response.

The batch model uses the procedure outlined in section 5.3.13 found on page 149.

## 6.3 Continuous Kinetic Model

The continuous kinetic model, within the range of ores tested, adequately predicts continuous column performance. This model incorporates many changes from earlier work.

1. The continuous flotation model uses the rate constant, maximum recovery and bubble loading parameters determined from the batch kinetic model with input data from either batch mechanical-cell or batch column tests. Kinetic rate and maximum recoveries determined using the batch model in conjunction with batch mechanical-cell test data have limited use in predicting plant-scale column performance unless entrainment constrains are taken into consideration. This is supported by INCO #2 column feed ($2^{nd}$ copper cleaner) and Quinto graphite flotation tests. The validity should be confirmed by testing ores with other particle size distributions and floatability. Batch column generated parameters are preferred in order to minimize error because entrainment is then not a consideration and vessel turbulence is approximately the same in both vessels.

2. The carrying capacity of the batch column and the INCO #2 column were both approximately 0.67. The equal value between modes indicate that batch column tests may be performed to estimate carrying capacity. Mechanical-cell tests indicated a carrying capacity of 0.47, thus, should not be used to determine column carrying capacities. Carrying capacity depends on both bubble and particle surface area calculations.

3. The model uses specific surfaces and superficial surface-area rates that reflect the surface nature of flotation. The solids surface-area is associated with either the liquid- or bubble-phase, each of which are tracked separately. These rates are sensitive to errors in particle size.

4. Transfer of solids from suspension (liquid-phase) to attached state (bubble-phase) occurs by first-order kinetics using the axial dispersion model.

5. The effective solids residence-time of the continuous column is calculated using liquid- and bubble-phase fractional holdups, liquid-phase superficial velocity and particle settling velocity.

6. The froth zone is modeled using loss of bubble surface-area. Loss of area transfers attached solids to the liquid-phase if maximal loading is exceeded.

7. Positive bias is the downward flow of solids by bulk transport, whereas, negative bias is the upwards flow. Solids transferred to the liquid-phase in the froth zone are returned to the recollection zone under positive bias conditions. The solids specific surface transported with the liquid-phase, that enters the froth, and solids that are transferred into the liquid within the froth zone, join the overflow stream under negative bias conditions.

8. The collection and recollection zones are modeled separately to account for the possible differences in solids concentration, flow rates and mixing conditions.

9. Model parameters must be used that were generated using similar sized particles. Errors in particle diameter calculations will result in model response errors.

10. Errors in maximum bubble load only affect model response if maximum loading is encountered at the maximum gas rate. In addition, the bubble residence-time in the mechanical-cell is much shorter than in the batch column although both are shorter than the industrial continuous columns. Thus, the carrying capacity predicted by the mechanical-cell will be further from the industrial column value than the batch column.

11. Errors in the flotation rate and maximum recovery parameters significantly affect model response. However, these errors can be minimized by using batch column tests, similar batch and continuous column size classes and by using several initial conditions while repeating the simplex error minimization routine. The rate constants determined in a continuous column depend on an accurate calculation of particle settling-velocity and mixing characteristics thus should not be used without careful consideration.

12. Entrainment is not considered in positive bias columns. However error may be present when mixing occurs in the froth zone.

13. The froth-zone model operates in parallel with the pulp zone and includes the following:

    a) Bias calculation
    b) Carrying capacity limitations
    c) Overflow attached-solids ($\vartheta_{SB(O)}$" $[s^{-1}]$)
    d) Overflow suspended-solids ($J_{SL(O)}$ or $J_{SL(L,froth)}$ $[s^{-1}]$) -- depends on bias.

## 6.4 Mechanistic Bubble Loading Model

### 6.4.1 Mixing

The mechanistic model framework does not incorporate mixing. A plug-flow model could be developed by incorporating the mechanistic bubble loading model framework into models similar to the kinetic flotation models presented in this thesis. A finite element analysis that incorporates this framework could be used to model other mixing regimes.

### 6.4.2 Parameter Comparison with Kinetic Models

There are three stages to this proposed mechanistic "model" for flotation parameter estimations: determination of (1) induction, (2) packing factor and (3) the critical loading angle ($\theta_m$).

The rate of solids loading on the bubbles is determined in the kinetic models by the kinetic rate constant. In the mechanistic model it is determined by both the induction time and the particle travel time on the bubble surface and may not be constant.

In both the kinetic and mechanistic models entrainment is determined by an entrainment parameter and the flow of feed water into the overflow stream.

Carrying capacity in the kinetic models is determined by the maximum bubble load which is an empirical number. In the mechanistic model carrying capacity is determined by a packing factor and is dependant upon the bubble residence time.

### 6.4.3 Determination of Induction Times

This model determines induction time (Equation 218, previously presented as Equation 201) rather than rate constants. To determine induction times, a batch test should be run wherein the bubbles are loaded with solids to angles greater than critical (small loads). This condition can be achieved using short bubble residence-times. The induction times determined in these tests should be constant with time until loading exceeds the critical angle ($\theta_l < \theta_m$) using Equation 218.

$$t_{i(m,n)} = \frac{\left(d_{p(n)} + d_b\right)\left[\theta_e - \arccos\left(\left[\frac{4\Delta\vartheta_{SB(m,n)}}{\vartheta_B C_{p(m,n)} t_b \left(u_b + u_{p(m,n)}\right) E_{c(m,n)}}\right]^{0.5} \sin\theta_m\right)\right]}{2v_{\theta(m,n)}} \quad \text{Equation 218}$$

### 6.4.4 Determination of Packing Factor

The "model" uses a solids packing factor (Equation 219, originally presented as Equation 207) rather than carrying capacity or bubble loads. At infinite residence-time floatable solids will load a bubble to the minimum angle needed for attachment ($\theta_i$). Thus, Equation 207 (Equation 219) can be used to determine the loading factor. A series of tests must be performed at progressively longer bubble residence-times, and the packing calculated assuming that the load angle equals the minimum angle for attachment ($\theta_l = \theta_i$). The test results will plot as an asymptotic curve of packing factor verses bubble residence-time. The asymptote of this curve will be the packing factor estimate.

$$\Gamma = \frac{\vartheta_B\left(1 - \cos\theta_l\right)}{2\vartheta_{SB}} \quad \text{Equation 219}$$

### 6.4.5 Relationship Between Packing Factor and Bubble Load

The packing factor of this model can be related to the bubble loads of the kinetic models as shown in Equation 220 (originally presented as Equation 208).

$$\phi_{SB} = \frac{1-\cos\theta_l}{2\Gamma} \qquad \text{Equation 220}$$

### 6.4.6 Estimated Critical Angle

Using the relationship described in "Stage 1", a change in the induction time (as estimated by Equation 201) will occur at a bubble residence-time. The loading at this point is such that "$\theta_l = \theta_m$". Since this change will be gradual the exact value of "$\theta_m$" may remain unknown.

### 6.4.7 Bubble Residence Time at Critical Angle

The bubble residence time needed to load the bubble to the critical angle can be determined using Equation 215 presented here as Equation 221.

$$t_b = \frac{2}{\Gamma}\frac{\left[\cos(\pi-\theta_l)+1\right]}{\sum_{j=1}^{m}\sum_{k=1}^{n} E_{c(j,k)}E_{a(j,k)}\left(u_b+u_{p(j,k)}\right)C_{p(j,k)}} \qquad \text{Equation 221}$$

At bubble residence times in excess of the value determined in Equation 221 the bubble loading rate will be reduced.

The superficial attached-solids surface-area flux can be calculated using Equation 194.

The equations presented as the mechanistic bubble loading framework may be used as a batch flotation model when they are combined with an entrainment and froth model as presented in the kinetic models. It may be possible to use these equations in a continuous model that accounts for axial and radial flows.

# 7 Recommendations

## 7.1 Testing

The models and tests presented in this thesis explore the differences between mechanical-cell and columns in order to use mechanical-cell data for column sizing purposes. However, more tests need to be done, on a wide range of particle sizes, densities, hydrophobicities and concentrations, in order to provide extra confidence in these procedures. The differences between the collection mechanisms of the two types of cells must also be explored in more detail in order to compile a more mechanistic flotation model. It may be possible to model industrial-scale mechanical-cells using the same techniques if a suitable model is developed for these cells.

The tests done for this thesis are limited due to the small number of large-scale columns accessible. For more accurate modeling of industrial units more tests must be performed where comparisons can be made between the model responses using batch test data and "real" industrial-scale performance.

Further test work needs to be accessed in order to test the continuous column model developed. Only positive bias condition data were available for the industrial columns, thus, this model has not been tested for the prediction of negative bias performance. Also, the model response has not been tested using columns that are operating under fully loaded conditions, or very large particle sizes.

Improved bubble size measurement equipment and techniques must be used to reduce the error associated with the bubble size.

Future tests should be conducted using a more detailed particle size analysis in order to minimize solids surface area errors.

## 7.2 Batch Model

The batch model is an empirical representation, and can only be used to represent flotation conditions that have been tested. The model, in its' current configuration, does not adequately incorporate delay in flotation, adjustments for deep froths, change in interface with time, or loading variability with bubble residence-time. These elements could be added, or expanded, to the model in order to make it more flexible.

## 7.3 Continuous Model

The continuous model should be modified to account for water and solids entrained within bubble wakes, the sparger and feed zones should be treated separately due to their mixing characteristics, and both froth zone drainage and mixing need to be addressed. Additional pulp-zone mixing models, such as the Gaussian-Convective and Sedimentation-Convective models, need to be explored. Inclusion of a bubble size distribution term or possible bubble size-classes should be investigated. The current model has two conditions that it cannot model: (1) when the sum of the particle settling velocity and liquid velocity are zero, and (2) when the bubbles have a zero rise velocity. These two conditions must be addressed to make a robust model.

## 7.4 Bubble Loading or Mechanistic Model

The bubble-loading "model" is preliminary and must be considered only as a framework for further study. It characterizes induction time and particle packing, but it has neither been tested nor has a working model been developed. Tests must be conducted on bubble loading with bubble residence-time and packing factors along with the surface-area flux predictions in order to check the relationships described. The batch column can be used to characterize bubble residence-time considerations since bubble residence-time is a function of the recycle rate in the batch column. The model could also be expanded by considering bubble size classes. A mathematical model relating the kinetic rate constant with induction time could be formulated. In order to use the model in batch it must be expanded to incorporate entrainment and froth behaviors. To use the model in continuous mixing issues must be addressed. The particle velocity over the bubble surface needs to be determined as a function that can easily be used to calculate particle contact time between any two angles on the bubble surface.

## 7.5 Batch Column

The physical size of the batch column should be reduced so that 500 or 1000 g samples can be tested.

A base sparging system should be designed and tested that eliminates the dead volume below the sparger.

# 8 Nomenclature

## 8.1 Variables, Parameters and Constants

| Symbol | Units | Definition |
|---|---|---|
| A | $s^{-1}$ | Mass transfer rate - pulp to froth |
| A | | Exponential constant |
| $a_{Pe}$ | | Function of k, t, and Pe |
| B | | Proportionality constants<br>Mass transfer rate from froth to pulp |
| $A_x$ | $cm^2$ | Cross-sectional area |
| C | | Concentration by mass, volume, or number of particles |
| $C_p$ | $cm^{-1}$ | Specific surface. |
| Ca | $g\ cm^{-2}s^{-1}$ | Area carrying capacity |
| $C_D$ | --- | Drag coefficient |
| $C_L$ | $g\ cm^{-1}s^{-1}$ | Lip loading capacity |
| d | cm | Diameter: c – column, ce – effective column diameter |
| $d_{80}$ | cm | Size at which 80% (w/w) of the material is smaller |
| Di | $cm^2s^{-1}$ | Dispersion coefficient |
| E | --- | Efficiency<br>a – attachment<br>c – collision<br>d – detachment<br>cg – gravitational collision<br>ci – interceptional collision<br>k – collection |
| f() | | Function |
| F | --- | True flotation recovery intercept |
| $F_{(Sch)}$ | ---- | Schuhmann's froth factor |
| g | $cm\ s^{-2}$ | Gravitational acceleration |

| Symbol | Units | Definition |
|---|---|---|
| h | cm | Height |
| J | $cm\ s^{-1}$ | Superficial velocity<br>g* - compensated gas |
| $k_e$ | --- | Entrainment proportionality constant |
| $k_f$ | $s^{-1}$ | Mineral rate constant<br>f – fast floating<br>s – slow floating |
| L | cm | Length |
| m | | Exponential function |
| m | g | Mass |
| $N_x$ | --- | Number of |
| $N_s$ | $cm\ s^{-1}$ | Peripheral impeller velocity |
| Nb | --- | Number of baffles |
| Np | --- | Dispersion number or inverse Peclet number |
| P | --- | Probability |
| $P_x$ | $g\ cm^{-1}s^{-2}$ | Pressure |
| Pe | --- | Peclet number |
| $Q_{(Sch)}$ | | Schuhmann's specific rate of flotation |
| Q | $cm^3\ s^{-1}$ | Volumetric flow rate |
| r | cm | Radius |
| R<br>$R_{(m,n)}$ | --- | Recovery |
| R | | Radius<br>c = critical radius |
| $R_w(t)$ | --- | Water recovery |
| Re | --- | Reynolds' number:<br>c - column, |
| $R_f$ | --- | Froth recovery |
| $R_\infty$ | --- | Maximum recovery at infinite time |

| Symbol | Units | Definition |
|---|---|---|
| $S_x$ | $cm^2 s^{-1}$ | Superficial surface-area flux |
| Sk | --- | Stokes' number |
| t | s | Retention time or time interval<br>c – contact<br>f – water thin film thinning time<br>i – induction<br>(i) - interval<br>l – liquid retention time<br>r – rupture of thin film time<br>s – sliding time<br>tcp – time for formation of three-phase contact |
| T | | Temperature |
| $u_b$ | $cm\ s^{-1}$ | Bubble swarm rise-velocity |
| $u_i$ | $cm\ s^{-1}$ | Characteristic velocity |
| $u_l$ | $cm\ s^{-1}$ | Interstitial liquid flow rate |
| $u_p$ | $cm\ s^{-1}$ | Hindered particle settling-velocity |
| $u_T$ | $cm\ s^{-1}$ | Terminal bubble rise-velocity |
| V | $cm^3$ | Volume |
| $v_\theta$ | $cm\ s^{-1}$ | Particle settling-velocity on the bubble surface |
| $x_i$ | cm or μm | Particle size x-axis dimension |
| X() | | Transfer function |
| $y_i$ | cm or μm | Particle size y-axis dimension |
| Y() | | Transfer function |
| $z_i$ | cm or μm | Particle size z-axis dimension |
| Z | --- | Normalized axial distance |

| Symbol | Units | Definition |
|---|---|---|
| $\alpha$ | radians | Misalignment |
| $\beta_{(m,n)}(t)$ | --- | Entrainment proportionality |
| $\varepsilon$ | --- | Error term |
| $\varepsilon_x$ | --- | Fractional holdup |
| $\phi$ | --- | Fast flotating fraction |
| $\phi_{SB}$ | --- | Bubble loading: solids to bubble-surface-area ratio |
| $\phi_{SB,Max}$ | --- | Maximal bubble loading |
| $\Gamma$ | --- | Solids-surface-area packing |
| $\vartheta$ | $s^{-1}$ | Superficial surface-area flux |
| $\Lambda$ | $cm^2 s^{-1}$ | Instantaneous solids-surface-area loading rate |
| $\mu$ | $g\ cm^{-1} s^{-1}$ | Viscosity |
| $\theta$ | radians | Particle angle<br>a – greatest angle of collision that leads to attachment<br>c – critical angle, angle of departure, compression angle or collision angle<br>cone – base angle of the column<br>cvr – maximum angle for attachment<br>e – minimum of "m" or "l"<br>(i) - dimensionless time at interval I<br>i – angular distance needed to attach a particle<br>l – maximum angle of solids cap<br>m – maximum angle equivalent to "c"<br>o – collision angle = $\theta_t$<br>t – collision or contact angle |
| $\rho$ | $g\ cm^{-3}$ | Density |
| $\xi$ | | Vorticity |

## 8.2 Subscripts

| Symbol | Units | Subscript Description |
|---|---|---|
| b | | Bubble |
| B | | Bubble phase |
| c | | Column |
| CB | | Surface area on a bubble covered |
| d | | Dead volume |
| e | | By entrainment |
| F,f | | By flotation |
| G | | Gas |
| L | | Liquid |
| L | | Liquid phase |
| N,n | | Non-floating |
| NCB | | Surface area on a bubble not covered |
| Np | | Number of particles |
| r | | Recycle |
| P | | Individual mineral – size-class particle |
| S,s | | Bulk solids |
| Sl | | Slurry (liquid-phase) |
| W | | Wash-water |
| x | | Direction |
| xb | | Bubble cross-sectional area |
| y | | Direction |
| z | | Direction |

| Symbol | Units | Subscript Description |
|---|---|---|
| (atm) | | atmospheric |
| (Col) | | Collection zone |
| (D) | | Drop-back or downward between froth and pulp |
| (f) | | Froth – pulp interface |
| (F) | | Feed |
| (froth) | | Froth zone |
| (i) | | Timed interval |
| (z,L) | | Lower boundary |
| (m) | | Mineral |
| (n) | | Size Fraction |
| (O) | | Overflow |
| (r) | | Recycle |
| (ReC) | | Recollection zone |
| (spa) | | Sparger |
| (U) | | Underflow |
| (z,U) | | Upper boundary |
| (v) | | Vessel |
| (W) | | Wash-water |
| (x) | | At an axial elevation |
| (z) | | Average value within a zone |

Note: this table does not include variables that are used once, or are of limited scope. These definitions are given with the equation descriptions.

# 9 References

**Abouzeid, A.Z.M., 1989**. Transport of particulates in mineral processing systems – tumbling units. Power Handling Process., 1(3):255-262.

**Adel, G.T., Mankosa, M.J., Luttrel, G.H., and Yoon, R.H.,1991**. Full-scale testing of microbubble column flotation. Column '91. Ed's Agar, Huls and Hyma. 1:263-274.

**Akita, K., and Yoshida, F., 1973.** Gas holdup and volumetric mass transfer coefficient in bubble columns. Ind. Engng. Chem. Proc. Des. Dev., 12(1):76

**Alford, R.A., 1992**. Modelling of single flotation column stages and column circuits. Int. J. Miner. Process., 36:155-174.

**Amelunxen, R.L., 1990.** Column flotation: new carrying capacity considerations for scale-up. Expomineria '90. Santiago Chile, May 14.

**Anfruns, J.P., and Kitchener, J.A., 1976**. The absolute rate of capture of single particles by single bubbles. In: M.C. Fuerstenau (ed.), *Flotation. A.M. Gaudin Memorial Volume*, AIME pp 625-637.

**Arbiter, N., 1951**. Flotation rates and flotation efficiency, AIME Trans, 190:791-796.

**Arbiter, N., and Harris, C.C., 1961.** Power requirements and scale-up in flotation. Nature, 191:268-270.

**Arbiter, N., and Harris, C.C., 1976.** Flotation kinetics, in *Froth Flotation: 50$^{th}$ Anniversary Volume*, NY, AIME

**Argo, W.B., and Cova, D.R., 1965.** Longitudinal mixing in sparged tubular reactors. Ind. Eng. Chem. Process. Des. Dev., 4:352-359

**Barnea, E., and Mizrahi, J., 1973**. A generalized approach to the fluid dynamics of particulate systems, 1. General correlation for fluidization and sedimentation in solid multiparticulate systems. Chem. Eng. J., 5:171-189.

**Bischoff, K.B., and Levenspiel, O., 1962a**. Fluid dispersed - generalization and comparison of mathematical models - 1: Generation of mathematical models. Chem. Eng. Sci., 17:245-255

**Bischoff, K.B., and Levenspiel, O., 1962b**. Fluid dispersed - generalization and comparison of mathematical models - II: Comparison of models. Chem. Eng. Sci., 17:257-264

**Bisshop, J.P., and White, M.E., 1976.** Study of particle entrainment in flotation froths. Trans. Inst. Min. Metall., 85:C191-194

**Blau, G.E., Klimpel, R.R., and Steiner, E.C., 1972.** Equilibrium constant estimation and model distinguishability. Ind. Eng. Chem. Fundam., 11(3):324-332.

**Boutin, P., and Wheeler, D.A., 1967.** Column flotation development. Can Mining J., March.

**Box, G.E.P., Hunter, W.G., and Hunter, J.S., 1978.** *Statistics for Experimenters.* John Wiley and Sons.

**Box, G.E.P., and Draper, N.R., 1987.** *Empirical Model-Building and Response Surfaces.* John Wiley and Sons.

**Bradshaw, D.J., and O'Connor, C.T., 1996.** Measurements of the sub-processes of bubble loading in flotation. Miner. Engng., 2:443-448.

**Brown, D.J.A., 1965.** A photographic study of froth flotation. Fuel Soc. J., 16:22-34

**Bushell, C.H.G., 1962.** Kinetics of flotation, SME Transactions, C-129: p 266-278.

**Castillo, D., 1988.** Column flotation simulator. Private Communications.

**CESL (Cominco Engineering Services Ltd), 1998.** Personal communications, test and sparger performance data.

**Chander, S., 1985.** Oxidation/reduction effects in depression of sulphide minerals. A review. Minerals and Metallurgical Processing., Feb.

**Christiansen, E.B., and Barker, D.H., 1965.** The effect of shape and density on the free settling rate of particles at high Reynolds' numbers. AIChE J., 11(1):145-151.

**Ciensky, T., and Coffin, V.I., 1981.** Column flotation operation at Mines Gaspe molybdenum circuit. Presented at the 13th annual meeting of Canadian Mineral Processors, Ottawa, Jan. 1981.

**Clift, R., Grace, J.R., and Weber, M.E., 1978.** *Bubble, Drops, and Particles.* Academic Press, NY NY Chpt 12:321-347.

**Clingan, B.V., and McGregor, D.R., 1987.** Column flotation experience at Magma Copper Co., Minerals and Metallurgical Processing., 3(3):121-125.

**Coffin V.I. and Misczak, 1982.** Column flotation at Mines Gaspe, XIV IMPC, Toronto, paper IV-21

**Colborn, R.P., 1969.** The study of a distributive rate constant model in predicting the performance of a phosphate flotation system. Ph.D. Thesis, University of Natal.

**Concha, F., and Almendra, E.R., 1979a.** Settling velocities of particulate systems.,1: Settling velocities of suspensions of individual spherical particles. Int. J. Miner. Process. 5:349-367

**Concha, F., and Almendra, E.R., 1979b.** Settling velocities of particulate systems, 2: Settling velocities of suspensions of spherical particles. Int. J. Miner. Process., 6:31-41.

**Concha, F., and Barrientos, A., 1986a.** Settling velocities of particulate systems, 4: Settling of non-spherical isometric particles. Int. J. Miner. Process.,18:297-308.

**Concha, F., et. al., 1986b** Settling velocities of particulate systems, 5: Settling velocities of suspensions of particles of arbitrary shape. Int. J. Miner. Process., 18:309-322.

**Cova, D.R., 1966.** Catalyst suspension in gas-agitated tubular reactors. Ind. Eng. Chem. Process. Des. Dev., 5:20. Reference .

**Crawford, R., and Ralston, J., 1988.** The influence of particle size and contact angle in mineral flotation. Int. J. Miner. Process., 23:1-24

**Cutting, G.W., Barber, S.P., and Newton, S., 1986.** Effects of froth structure and mobility on the performance and simulation of continuously operated flotation cells. Int. J. Miner. Process., 16:43-61.

**Deckwer, W., Bruckhart, R., and Zoll, E., 1974**. Mixing and mass transfer in tall bubble columns. Chem. Engng. Sci., 29:2177

**Derjaguin, B.V., and Dukhin, S.S., 1960-61.** Theory of flotation of small and medium sized particles. Trans. Inst. Min. Metall., 70:221-245

**Derjaguin, B.V., Dukhin, S.S., Rulev, N.N., 1986.** *Microflotation.* Nauka Publishers, Moscow. As referred to by Rubinstein (1995).

**Derjaguin, B.V., and Kussakov, M., 1939.** Acta Physiocochim, 10 p25

**Dobby, G.S., 1984**. A fundamental flotation model and flotation column scale-up. Ph.D. Thesis, McGill University, Montreal Quebec.

**Dobby, G.S., and Finch, J.A., 1985a.** Mixing characteristics of industrial flotation columns. Chem. Engng. Sci., 40(7):1061-1068.

**Dobby, G.S., and Finch, J.A., 1985b.** Flotation column scale-up and simulation. Pres. At the 17th annual CMP meeting, Ottawa, Jan 22-24.

**Dobby, G.S., and Finch J.A., 1986a.** Flotation column scale-up and modeling. CIM Bulletin 79:89-96

**Dobby, G.S., and Finch J.A., 1986b**. Particle collection in columns - gas rate and bubble size effects. Can. Metal. Q., 25(1):9-13.

**Dobby, G.S., and Finch J.A., 1986c**. A model of particle sliding time for flotation size bubbles. Particle collection in columns - gas rate and bubble size effects. Can. Metal. Q., 25(1):9-13.

**Dobby, G.S., and Finch J.A., 1986d**. A model of particle sliding time for flotation size bubbles. J. Colloid and Interface Sci., 109(2):493-498.

**Dobby, G.S., and Finch, J.A., 1987.** Particle size dependence in flotation derived from a fundamental model of the capture process. Int. J. Miner. Process., 21:241-260.

**Dobby, G.S., Kosick, G.A., and Matwijenko, O., 1990.** Pilot plant testing for column flotation circuit design. CMP Conference, Ottawa Canada, Jan.

**Dowling, E.C. Jr., Klimpel, R.R., and Aplan, F.F., 1985**. Model discrimination in the flotation of base metal sulfide ores – circuitry and reagent variations. Minerals and Metallurgical Proc., 87-101., also in *Design and Installation of Concentration and Dewatering Circuits*, A.L. Mular and M.A. Anderson (eds) SME-AIME (1986).

**Dowling, E.C. Jr., Klimpel, R.R., And Aplan, F.F., 1986.** Use of kinetic models to analyze industrial flotation circuits. In: D.R. Gaaskell, J.P. Hager, J.E. Hoffmann and P.J. Mackey (eds) Proceedings of the Reinhardt Schumann Int. Symposium Innovative Technology and Reactor Design in Extraction Metallurgy. TMS-AIME, Warrendale, PA pp 553-552.

**Eigeles, M.A., 1939**. Kinetics of the attachment of mineral particle to air bubble (in Russian) as referred to by Nguyen, VA., et. al., 1998. Dokl. Akad. Nauk. SSSR 24(4):342-346.

**Eigeles, M.A., 1964.** The basis of the flotation of non-sulfide minerals (2nd ed. In Russian). Nedra, Moscow. As referred to by Nguyen et. al. 1998.

**Espinosa-Gomez R., Finch, J.A. and Yianatos, J.B., 1988.** Column carrying capacity: particle size and density effects. Miner. Engng., 1(1):77-79.

**Espinosa-Gomez R., Yianatos, J., and Finch, J.A., 1988.** Carrying capacity limitations in flotation columns. In: K.V.S. Sastry (ed) *Column Flotation '88*, Int. Symp. on Column Flotation, AIME Phoenix. Chap 15 p 143-148.

**Espinosa-Gomez, R., Johnson, N.W., Pease, J.D., Munro, P.D., 1989**. The commissioning of the first flotation columns at Mount Isa Mines Ltd., In: G.S. Dobby and S.R. Rao (eds) *Processing of Complex Ores*, No. 1, pp 293-302.

**Falutsu, M., and Dobby, G.S., 1989a.** Direct measurement of froth drop back and collection zone recovery in a laboratory column. Miner. Engng., 2:377.

**Falutsu, M., and Dobby, G.S., 1989b.** Direct measurement of froth performance in a laboratory column. *Processing Of Complex Ores.*, (Dobby, G.S., Rao, S.R., eds) CIM Halifax, Canada. 335.

**Farkas, E.J., and Leblond, P.F., 1969.** Solids concentration profile in the bubble column slurry reactor Can. J. Chem. Eng., 47:215.

**Fichera, M.A., and Chudacek, M.W., 1991.** Batch cell flotation models – A review. Miner. Engng 5(1):41-55.

**Finch, J.A., and Dobby, G.S., 1990.** *Column Flotation.* Pergamon Press.

**Finch, J.A., and Dobby, G.S., 1991.** Column flotation: A selected review. Part I. Int. J. Miner. Process., 33:343-354.

**Flint, I.M., 1989.** Bubble Generation in Flotation Columns. M.A.Sc. Thesis, Dept. of Metallurgy, University of Toronto.

**Flint, L.R., 1974.** A Mechanistic Approach to Flotation Kinetics. Trans. Inst. Min. Metall., 83:C90-C95

**Flint, L.R., and Howarth, W.J., 1971.** The collision efficiency of small particles with spherical air bubbles. Chem. Eng. Sci., 26: 1155-1168.

**Flynn, S.A., and Woodburn, E.T., 1987.** Development of a froth model for fine-particle beneficiation by flotation. Trans. IMM 96:C191-198.

**Frew, J.A., and Davey, K.J., 1988.** Effect of feed grade on industrial zinc rougher flotation. Int. J. Miner. Process., 23:181-204.

**Froment, G.E., and Bischoff, K.B., 1979.** *Chemical reactor analysis and design.* Wiley, NY NY Capt 12, pp 592-659.

**Garsia-Zuniga, H., 1935.** Flotation recovery is an exponential function of time. Bol. Min. Soc. Nac. Min., Santiago, 47:83-86, as referred to by Varbanov R. et. al. 1993.

**Gaudin, A.M., 1932.** *Flotation* pp 86-119 McGraw-Hill Book Company Reference 1

**Gaudin, A.M., 1957.** *Flotation*, 2nd Ed., McGraw-Hill NY NY.

**Glembotsky, V.A., 1953.** The time of attachment of air bubbles to mineral particles in flotation and its measurement (in Russian). As referred to by Nguyen, VA., 1998. Izv. Akad. Nauk. SSSR (OTN) 11:1524-1531

**Goodall, C.M., and O'Connor, C.T., 1991a.** Residence-time distribution studies in a flotation column. Part I: The modeling of RTD's in a laboratory column flotation cell. Int. J. Miner. Process., 31:97-113.

**Goodall, C.M., and O'Connor, C.T., 1991b.** Residence-time distribution studies in a flotation column. Part II: The relationship between solids residence-time distribution and metallurgical performance. Int. J. Miner. Process., 36:219-228.

**Gorain, B.K., Franzidis, J.-P., and Manlapig, E.V., 1996**. The effect of gas distribution properties on the kinetics of flotation; in Column '96: Proceedings of the 35th Annual Conference of Metallurgists CIM, Montreal, Canada, 299-313, 26-28 August.

**Gorain, B.K., Franzidis, J.-P., and Manlapig, E.V., 1999**. The empirical prediction of bubble surface area flux in mechanical flotation cells from cell design and operating data. Minerals Engng., 12(3):309-322.

**Gorain, B.K., Napier-Munn, T.J., Franzidis, J.-P., and Manlapig, E.V., 1998.** Studies on impeller type, impeller speed and air flow rate in an industrial-scale flotation cell. Part 5: Validation of k-Sb relationship and effect of froth depth. Minerals Engng., 11(7):615-626.

**Gy, P., 1979.** *Sampling of Particulate Materials: Theory and Practice.* Elsevier Scientific Publishing Company.

**Hanumanth, G.S., and Williams, D.J.A., 1992**. A three-phase model of froth flotation. Int. J. Miner. Process., 34:261-273.

**Happel, J., and Brenner, H., 1964**. *Low Reynold's Number Hydrodynamics*. Prentice Hall, Englewoods Cliff, NJ

**Harris, C.C., 1978.** Multiphase models of flotation machine behavior. Int. J. Miner. Process., 5:107-129.

**Harris, C.C., and Chakravarti, A., 1970.** Semi-batch froth flotation kinetics: Species distribution analysis. Trans. Am. Inst. Min. Eng., 247:162-172.

**Harris, C.C., Jowett, A., and Ghosh, S.K., 1963.** Analysis of data from continuous flotation testing. Trans. Am. Inst. Min. Engng., 226:444-447.

**Harris, C.C., and Raja, A., 1966.** A modified laboratory flotation cell. Trans. Am. Inst. Min. Engng., 235:150-156.

**Harris, C.C. and Rimmer, H.W., 1966.** Study of two-Phase model of the flotation process, Trans. Instn. Min. Metall., 75,C153-162.

**Hewitt, D., Fornasiero, D., and Ralston, J., 1994.** Bubble particle attachment efficiency. Minerals Engineering, 7(5/6):657-665.

**Horst, W.E., 1958.** Scale-up relationships in spodumene flotation. Min. Engng., 10:1182-1185.

**Huber-Panu, I., Ene-Danalache, E., and Cojocaariu, D.G., 1976.** Mathematical models of batch and continuous flotation. *Flotation, A.M. Gaudin Memorial Volume.* M.C. Fuerstanau, ed. Vol 2

**Hukki, R.T., 1953.** Discussion on paper "Measurement and Evaluation of the Rate of Flotation as a Function of Particle Size" by T.M. Morris, AIME Trans 196:1122-1124.

**Imafuku, K., Wang, T.-Y., Koide, K., and Kubota. H.,1968.** The behavior of solid particles in the bubble column. J. Chem. Engng. Jpn. 1:153.

**Imaizumi, T., and Inoue, T. 1965.** Kinetic considerations of froth flotation. Proc. 6th Int. Miner. Process. Congress, 581-593.

**Ityokumbul, M.T., 1992.** A new modeling approach to flotation column design. Miners. Engng., 5(6):685-693.

**Ityokumbul, M.T., 1994**. A non-parametric method for particle settling velocity determination in a slurry bubble column. Chem. Eng. J., 54:1-6.

**Ityokumbul, M.T., Kosaric, N., and Bulani, W., 1988.** Parameter estimation with simplified boundary conditions. Chem. Eng. Sci., 43(9):2457-2462.

**Ityokumbul, M.T., and Trubelja, M.P., 1998**. Carrying capacity in a pilot flotation column. Mineral and Metallurgical Processing 15(2):41-46.

**Jacoby, S.L., and Kowalik, J.S., 1980**. *Mathematical Modeling with Computers.* Prentice-Hall.

**Jameson, G.J., Nam, S., and Moo Young, M., 1977.** Physical factors affecting recovery rates in flotation. Min. Sci. Eng., 9(3):103-118

**Jowett, A., 1966**. Gangue mineral contamination of froth. British Chem. Eng., Vol. 2, No. 5, pp 330-333.

**Jowett, A., 1980.** Formation and disruption of particle-bubble aggregates in flotation. In: P Somasundran (Ed), *Fine Particle Processing.* Vol. 1., AIME pp 720-754

**Jowett, A., and Safvi, S.M.M., 1960.** Refinements in methods of determining flotation rates. AIME Transactions v 217, p 351-357

**Kapur, P., and Mehrotra, S., 1973.** Phenomenological model for flotation kinetics. Trans. I.M.M., 82C:229-224.

**Kasiredy, V.K., and Al Taweel, 1989**. Column flotation of ultra fine coal. In: *Advances in Mineral and Coal Processing using Flotation*. Eng. Found. Conf. Series, SME Palm Coast, 1989 pp 356-366.

**Kato, Y., Nishiqaki, A., Fukuda, T., and Tanaka, A., 1972.** The behavior of suspended solid particles and liquid in bubble columns. J. Chem. Engng., Japan., 5:112-117

**Kelly, E.G., and Carlson, C.E., 1991.** Technical Note: Two flotation models: resolution of a conflict. Miners. Engng., 4(12):1333-1338.

**Kelly, E. G., Spottiswood, D. J., 1982.** *Introduction to mineral processing*, J. Wiley & Sons, New York.

**Kelsall, D.F., 1961.** Application of probability in assessment of flotation systems. Bulletin of the Inst of Mining and Met., 70:191

**Kho, C.J., and Sohn, H.J., 1989.** Column flotation of talc. Int. J. Miner. Process., 27:157-167.

**King, R.P., 1974.** The simulation of flotation plants. Trans. SME/AIME 258-286.

**Kirjavainen, V.M., 1989**. Application of a probability model for the entrainment of hydrophilic particles in froth flotation. Int. J. Miner. Process., Vol. 27, pp 63-74.

**Kirjavainen, V.M., 1992**. Mathematical model of the entrainment of hydrophilic particles in froth flotation. Int. J. Miner. Process., Vol. 35, pp 1-11.

**Kirjavainen, V.M., and Laapas, H.R., 1988**. A study of entrainment mechanism in flotation. In: 14th Int. Miner. Process. Cong., Stockhold, Sweden, June 5-10. Part B, Forssberg, K.S.E. (ed). 665-677. Elsevier.

**Klassen, V.I., and Mokrousov, V.A., 1963.** *An Introduction to the Theory of Flotation.* Butterworths, London p 493

**Klimpel, R.R., Hansen, R.D., and Meyer, W.C., 1979.** Laboratory characterization of the influence of reagent changes on coal flotation, AIME Annual Meeting, New Orleans, LA Preprint 79-11

**Klimpel, R.R., 1980**. Selection of chemical reagents for flotation. Mineral Processing Plant Design, 2nd ed.

**Kojima, H., Iguchi, A., and Asano, K., 1984.** Solid holdup in bubble columns with suspended solid particles under continuous operation. Can. J. Chem. Eng., 62:346.

**Kojovic, T., 1988**. Automated model building. Ph.D. Thesis, University of Queensland, 355 p., as referred to by Alford, R.A., 1992.

**Kumar, S., Degaleesan, T.E., Laddha, G.S., and Hoelscher, H.E., 1976.** Bubble swarm characteristics in bubble columns. Can. J. Chem. Eng., 54:503-508.

**Laplante, A.R., Yianatos, J.B., and Finch, J.A., 1988**. On the mixing characteristics of the collection zone in flotation columns. In: K.V.S. Sastry (ed), *Column Flotation '88*. SME, pp 69-79.

**Laskowski, J.S., 1986.** The relationship between floatability and hydrophobicity, In: *Advances in Mineral Processing* (P. Somasundaran, ed.) AIME, p 189-208.

**Leja, J., 1982.** *Surface Chemistry of Froth Flotation* Plenum Press NY

**Levenspiel, O., 1972** *Chemical Reaction Engineering* Wiley, N.Y., Chapter 9.

**Levenspiel, O., and Fitzgerald, T.J., 1983**. A warning on the misuse of the dispersion model. Chem. Eng. Sci., 38(3): 489-491.

**Levich, V., 1962**. *Physiochemical Hydrodynamics*. Prentice Hall. Englewood Cliffs, NJ 213-219.

**Lockett, M.J., and Kirkpatrick, R.D., 1975**. Ideal bubbly flow and actual flow in bubble columns. Trans. Instn. Chem. Engrs., 53:267-273.

**Luttrel, G.H., 1986.** Hydrodynamic studies and mathematical modeling of fine coal flotation. Ph.D. Thesis, Virginia Polytechnic Institute and State University.

**Luttrell, G.H., Adel, G.T., Yoon, R.H., and Weber, A.T., 1988.** Microbubble flotation of fine coal. In: K.V.S. Sastry (ed), *Column Flotation '88*, SME Annual Meeting.

**Lynch, A.J., Johnson, N.W., McKee, D.J., and Thorne, G.C., 1974**. The Behavior of minerals in sulphide flotation process with reference to simulation and control. J.S.A. IMM, 74:349-360.

**Lynch, A.J., Johnson, N.W., Manlapig, E.V., and Thorne, G.C., 1981.** *Mineral and coal flotation circuits: Their simulation and control.* Elsevier Scientific Publ.

**Maachar, A., and Dobby, G.S., 1992**. Measurement of feed water recovery and entrainment solids recovery in flotation columns. Can. Metall. Q., 31(3):167-172.

**Magnussen, P., and Schumacher, V., 1978.** 5th Int. Chem. Reaction Engng. Symp., Houston, p337-347.

**Mankosa, M.J., Adel, G.T., Luttrell, G.T., and Yoon, R.H., 1990.** Modeling of column flotation with a view toward scale-up and control. In: R.K. Rajamani and J.A. Herbst (Eds.) *Control '90*, 119th Annual SME Meeting, Salt Lake City Utah, Feb. 26 – March 1, 1990. SME Littleton Co., p 35-42.

**Mankosa, M.J., Luttrell, G.H., Adel, G.T., and Yoon, R.H., 1992.** A study of axial mixing in column flotation. Int. J. Miner. Process.,35:51-64.

**Marti, M.C., Roeckel, M., Aspe, E., and Novoa, M., 1994.** Fat removal from process waters of the fish meal industry. A survey of three flotation methods. Env. Tech., 15:29-39.

**Masliyah, J.H., 1979.** Hindered settling in a multi-species particle system. Chem. Eng. Sci., 34:1166-1168.

**Mavros, P., 1992.** Technical Note: Validity and limitations of the closed-vessel analytical solution to the axial dispersion model. Miner. Eng., Vol. 5, No. 9, pp 1053-1060.

**Mavros, P., 1993a.** Mixing in flotation columns. Part I: Axial dispersion modeling. Miner. Engng., 6(5):465-478.

**Mavros, P., 1993b.** Mixing in flotation columns. Part III: Internal Circulation. Minerals Engng., 6(11):1167-1182.

**Mavros, P., and Daniilidou, A., 1993a.** Mixing in flotation columns. Part II: Liquid-phase residence-time distributions studies. Minerals Engng., 6(7):707-719

**Mavros, P., Lazaridis, N.K., and Matis, K.A., 1989.** A study and modeling of liquid phase mixing in a flotation column. Int. J. Miner. Process., 26:1-16.

**Mehrotra, S.P., and Podmanabhan, N.P.H., 1990.** Analysis of flotation kinetics of Malanjkhand copper ore, India, in terms of distributed flotation rate constant. Trans. Inst. Miner. Metall. C99:32-42.

**Mezhov, EH., Samatov, A.V., and Troyanovskiy, L.V., 1992.** Extraction of trivalentactinides and lanthanides from nitric acid solutions by ion flotation. Sep. Sci. Tech., 27(5):599-611.

**Mica, T., and Fuerstanau, D., 1968**. A microscopic model of glotation process. In: O. Begdanov (ed), Proc. VIIIth IMPC, Leningrad, Vol. 2: 246-269.

**Mills, P.J.T., and O'Connor, C.T., 1990.** The modeling of liquid and solids mixing in a flotation column. Miner. Engng., 3(6):567-576.

**Mills, P.J.T., and O'Connor, C.T., 1992a**. Technical Note: The use of the axial dispersion model to describe mixing in a flotation column. Miner. Eng., Vol. 5., No. 8, pp 939-944.

**Mills, P.J.T., and O'Connor, C.T., 1992b**. The mixing characteristics of solid and liquid phases in a flotation column. Miner. Eng. Vol. 5, Nos 10-12, pp 1195-1205.

**Mori, S., Okamoto, H., Hara, T and Aso, K., 1986**. Kinetics studies of fluorite flotation. Proc. 15th Int. Min. Process. Cong., Cannes, 3:155-162.

**Morris, T.M., 1952.** Measurement and evaluation of the rate of flotation as a function of particle size. Trans. AIMME 193:794-798

**Moys, M.H., 1978**. A study of a plug-flow model for flotation froth behavior. Int. J. Miner. Process., 5:21-38.

**Moys, M.H., 1984**. Residence-time distributions and mass transport in the froth phase of the flotation process. Int. J. Miner. Process., 13:117-142.

**Moys, M.H., and Finch, J .A., 1991**. The use of temperature measurements in the analysis and control of flotation columns. Can. Metall. Q., 30(3):131-137.

**Mular, A.L., and Musara, W.T., 1991**. Batch column flotation: rate data measurement. Column 91.

**Muroyama, K., and Fan, L.S., 1985.** Fundamentals of gas-liquid-solid fluidization. AIChE J., 31(1):1-34.

**Murray, P., and Fan, L.-S., 1989.** Axial solid distribution in slurry bubble columns. Ind. Eng. Chem. Res., 28:1697-1703

**Nelder, J.A., and Mead, R., 1965**. A stepwise non-derivative hill-climbing algorithm. Computer Journal, 7:308-313.

**Newall, A., Gray, D., and Alford, R., 1989**. The application of flotation columns to gold recovery at Paddington Gold Mine, W.A., In: B Harris (ed), *Precious Metals 1989*, Proc. 13th Int. Precious Metals Institute (IMPI) Conf., Montreal Que. pp 287-289.

**Nguyen Van, A., 1993.** On the sliding time in flotation. Int. J. Miner. Process., 37:1-25.

**Nguyen Van, A., Ralston, J., Schulze, H.J., 1998.** On modeling of bubble-particle attachment probability in flotation. Int. J. Miner. Process., 53:225-249.

**Nguyen Van, A., and Kmet, S., 1992.** Collision efficiency for fine mineral particles with single bubble in a countercurrent flow regime. Int. J. Miner. Process., 35:205-223

**Nguyen Van, A., and Kmet, S., 1994.** Probability of collision between particles and bubbles in flotation: the theoretical inertialess model involving a swarm of bubbles in pulp phase. Int. J. Miner. Process., 40:155-169.

**Nguyen Van, A., Schulze, H.J., Ralston, J., 1997.** Elementary steps in particle-bubble attachment. Int. J. Miner. Process., 51:183-195

**Nguyen A.V., 1998.** Particle-bubble encounter probability with mobile bubble surfaces. Int. J. Miner. Process., 55:73-86.

**O'Connor, C.T., and Goodall, C.M., 1991**. Residence-time distribution studies in a flotation column Part 1: The modeling of residence-time distributions in a laboratory column flotation cell. Int. J. Miner. Process., 31:97.

**Ohki, Y., and Inoue, H., 1970.** Longitudinal mixing of the liquid phase in bubble columns. Chem. Eng. Sci., 25:1

**Ostergaard, K., and Michelsen, M.L., 1969**. On the use of the imperfect tracer pulse method for determination of holdup and axial mixing. (Tripartitie Conference 1968) Can. J. Chem. Engng., 47(4):107-112.

**Pal, R., and Masliyah, J.H., 1990**. Flow characteristics of a flotation column. Can. Metall. Q., 29(2):97-103.

**Petri, B., and Dobby, G.S., 1993.** De-inking wastepaper in a flotation column. Presented at the 2nd Research Forum on Recycling, Ste-Adele, Quebec, Oct. 6, 1993.

**Pettyjohn, E.S., and Christiansen, E.B., 1948.** Effect of particle shape on free settling velocity of isometric particles. Chem. Eng. Progr., 44(2):157-172.

**Plate, H., and Schulze, H., 1991.** Modeling of the overall process based on physico-chemical microprocesses - technique and application. In 17th Int. Mineral Processing Cong. Dresden, 23-28.09.1991, 2:365-377

**Rasemann, W., 1988.** On the attachment probability of bubble/particle contacts in solid/liquid suspensions. Int. J. Miner. Process., 24:247-267

**Reay, D., and Ratcliff, G.A., 1973.** Removal of fine particles form water by dispersed air flotation: effects of bubble size and particle size on flotation efficiency. Can. J. Chem. Eng., 51: 178-185.

**Reith, T., Renken, S., and Isreal, B.A., 1968**. Gas holdup and axial mixing in the fluid phase of bubble columns. Chem. Eng. Sci., 23:619.

**Reuter, M.A. and van Deventer, J.S.J., 1992.** The simulation and identification of flotation processes by use of a knowledge based model. Int. J. Miner. Process., 35:13-49.

**Rice, R.G., and Littlefield, M.A., 1987**. Dispersion Coefficients for Ideal Bubbly Flow in Truly Vertical Bubble Columns. 42(8):2045-2053.

**Rice, R.G., Oliver, A.D., Newman, J.P., and Wiles, R.J., 1974.** Reduced dispersion using baffles in column flotation. Powder Tech. 10:201-210.

**Richardson, J.F., and Zaki, W.N., 1954.** Sedimentation and fluidization: Part I. Trans. Instn. Chem. Engrs., 32:35-53.

**Roberson, J.A., and Crowe, C.T., (1980).** *Engineering Fluid Mechanics* 2nd Ed., Houghton Mifflin Company, London.

**Ross, V.E., 1990b.** Flotation and entrainment of particles during batch flotation tests. Minerals Engng., 3(3):245-256.

**Ross, V.E., 1990c.** A study of the froth phase in large-scale pyrite flotation cells. Int. J. Miner. Process., 30:143-157.

**Ross, V.E., 1991a.** Comparison of methods for evaluation of true flotation. Trans IMM C121-126

**Ross, V.E., 1991b.** An investigation of sub-processes in equilibrium froths. II. The effect of operating conditions. Int. J. Miner. Process., 31:51-71.

**Rubinstein, J.B., 1995.** *Column Flotation: Process, Designs and Practice*, Gordon and Breach Science Publishers.

**Sadler III, L.Y., 1973.** Dynamic response of the continuous mechanical froth flotation cell. Trans. Am. Inst. Min. Eng., 254:336-343.

**Sastry, K.V.S., 1990.** Principles and methodology of mineral process modeling. In: *Control '90*, Chpt 1.

**Sastry, K.V.S., 1996.** Carrying capacity in flotation columns. Minerals Engineering 9:465-468.

**Sastry. K.V.S., and Fuerstenau, D.W., 1970.** Theoretical analysis of a countercurrent flotation column. Trans. AIME 247:46-52.

**Schiller, L., and Neumann, A., 1933.** Z. Ver. Dtsch. Ing., 77:318, (in German) as referred to by Xu et. al., 1991.

**Schubert, H., and Bischofberger, C., 1978.** On the hydrodynamics of flotation machines. Int. J. Miner. Process., 5:131-142

**Schuhmann, R. Jr., 1942.** Flotation kinetics, 1. Methods for steady-state study of flotation problems. J. Phys. Chem., 46:891-902.

**Schulze, H.J., 1977a**. New theoretical and experimental investigations on stability of bubble/particle aggregates in flotation: The theory of the upper particle size of floatability. Int. J. Miner. Process., 4:241-259

**Schulze, H.J., 1977b.** New theoretical and experimental investigations on the upper particle size of flotability in flotation machines. Int. J. Miner. Process., 9:321-328.

**Schulze, H.J., 1982.** Dimensionless number and approximate calculation of the upper particle size of flotabiltiy in flotation machines. Int. J. Miner. Process., 9:321-328.

**Schulze, H.J., 1984**. Physico-chemical elementary processes in flotation, in: *Developments in Mineral Processing* Vol. 4, Elsevier, Amsterdam.

**Schulze, H.J., 1989.** Hydrodynamics of bubble-mineral particle collision. Miner. Process. Extr. Metall. Rev., 5:43-76

**Schulze, H.J., 1992.** Probability of particle attachment on gas bubbles by sliding. Adv. in Colloid Interface Sci., 40:283-305

**Schulze, H.J., and Gottschhalk, G., 1981.** Experimentelle untersuchung der hydrodynamischen wechselwirkung von partikeln mit einer gasblase (original title) given in English in the Proceedings 13th Annual Int. Mineral Processing Congress, Warsaw, June 1979, Laskowski J., (Ed.), Elsevier, NY Part A, p 63-84.

**Schulze, H.J., Radoev, B., Geidel, Th., Stechemesser, H., and Topper, E., 1989**. Investigations of the collision process between particles and gas bubbles in flotation - A theoretical analysis. Int. J. Miner. Process., 27:263-278

**Seeley, L.E., Hummel, R.L., and Smith, J.W., 1975.** Experimental velocity profiles in laminar flow around spheres at intermediate Reynolds' numbers. J. Fluid Mechanics, 68(3):591-608

**Shah, Y.T., Stiegel, G.J., and Sharma, M.M., 1978.** Backmixing in gas-liquid reactors A.I.Ch.E. J., 24(3):369-401

**Shah, Y.T., Kelkar, B.G., Godbole, S.P., and Deckwer, W.D., 1982.** Design parameters estimation for bubble column reactors, AIChE J, 28:353-357.

**Shinji Nagata, 1975**. *Mixing: Principles and Applications*. Wiley, NY NY, Chap 5 pp 215-247.

**Sinkankas, J., 1964**. *Mineralogy*. Van Nostrand Reinhold Co., Toronto.

**Sivamohan, R., 1990.** The problem of recovering very fine particles in mineral processing - A review. Int. J. Miner. Process., 28:247-288.

**Slattery, J.C., 1972**. *Momentum, Energy and Mass Transfer in Continua*. McGraw - Hill, NY NY

**Smith, D.N., Ruether, J.A., 1985**. Dispersed solid dynamics in a slurry bubble column. Chem. Eng. Sci., 40(5):741-754.

**Smith, D.N., Ruether, J.A., Shah, Y.T., and Badgujar, M.N., 1986.** Modified sedimentation-dispersion model for solids in a three-phase slurry column. AIChE J., 32:426.

**Stechemesser, H., Geidel, T., and Weber, K., 1980.** Expansions of three-phase contact line after rupture of thin non-symmetrical liquid films: 1. Relationships between rate of expansion and radius of three-phase contact. Colloid Polymer Sci., 258(1):109-110.

**Subrahmanyam, T.V., and Forssberg, E., 1988**. Froth characteristics and grade-recovery relationships in the flotation of lead-zinc and copper ores. Minerals Engng., 1(1):41-52.

**Subrahmanyam, T.V., Prestidge, C.A., and Ralston, J., 1996.** Contact angle and surface analysis studies of sphalerite particles. Minerals Engineering, 9(7):727-741.

**Suganuma, T., and Yamanishi, T., 1966.** Behavior of solid particles in bubble columns. Kagaku Kogaku 30:1136.

**Sutherland, K.L., 1948**. Kinetics of the flotation process. J. Proc. Eng., 52:394-425.

**Suttill, K.R., 1989**. Larger sizes still dominate flotation cell applications. E&MJ Flotation Cell Survey, E&MJ Jan., 98-103.

**Sven-Nilsson, J., 1934.** Einfluss der Beruhrungszeit zwischen Mineral und Luftblase bei der Flotation. Kolloidzeitschrift, 69:230-232 (In German) as referred to by Nguyen (1998)

**Swanson, V.F., 1967.** The development of a formula for direct determination of free settling velocity of any size particle. Trans. SME/AIME, 238:160-166.

**Swanson, V.F., 1978.** Proceedings of Int. Powder and Bulk Solid Handling and Proc. Cong. Rosemount, Ill., p82

**Szatkowski, M., 1987.** Some comments on flotation kinetics. Chem. Engng. Sci., 42(10):2475-2478.

**Szatkowski, M., and Freyberger, W.L., 1985a**. Kinetics of flotation with fine bubbles. Trans IMM (section C) 84:61-70.

**Szatkowski, M., and Freyberger, W.L., 1985b.** Model describing mechanism of the flotation process. Trans IMM 94:C129-135.

**Szekely, J., Evans, J.W., and Brimacombe, J.K., 1987.** *The Mathematical Modeling of Primary Metals Processing Operations.* Wiley.

**Tinge, J.T. and Drinkenburg, A.A.H., 1986.** The influence of slight departures from vertical alignment on liquid dispersion and gas holdup in a bubble column. Chem. Engng. Sci., 41(1):165-169

**Tomlinson, H.S., and Flemming, M.G., 1963, 1965**. Flotation rate studies. In A. Roberts (Ed.), *Mineral Processing*. Cong.. of Miner. Process., Cannes, (1963) Pergamon press 1965.

**Torobin, L.B., and Gauvin, W.H., 1959**. Fundamental aspects of solid - gas flow. Part 2. Can. J. Chem. Engng., 37:167-176.

**Trahar, W.J., 1981.** A rational interpretation of the role of particle size in flotation. Int. J. Miner. Process., 8:289-327.

**Trahar, W.J., and Warren, L.J., 1976.** The floatability of very fine particles - A review. Int. J. Miner. Process., 3:103-131.

**Uribe-Salas, A., Gomez, C.O., and Finch, J.A., 1990**. Bias rate and entrainment. McGill University. Personal Communications. Similar to Uribe-Salas et. al. 1991.

**Uribe-Salas, A., Leroux, M., Gomez, C.O., Finch, J.A., and Huls, B.J., 1991**. A conductivity technique for level detection in flotation cells. "Copper '91" Aug. 18-21, Ottawa Ont., CIM.

**Villeneuve, J., Guillaneau, J.-C., and Durance, M.-V., 1995.** Flotation modeling: A wide range of solutions for solving industrial problems. Miners. Engng., 8(4/5):409-420.

**Wadell, J., 1932.** Volume, shape and roundness of rock particles. J. Geol. 15:443-451.

**Wadell, J., 1934.** The coefficient of resistance as a function of Reynolds' number for solids of various shapes. J. Franklin Inst., 217:459-490.

**Walkowiak, W., 1991.** Mechanism of selective ion flotation. 1. Selective flotation of transition metal cations. Sep. Sci. and Tech., 26(4):559-568.

**Wallis, G.B., 1962**. A simplified one-dimensional representation of two-component vertical flow and its application to batch sedimentation. IIIrd Congr. Euro. Fed. Chem. Engrs., London, June

**Wallis, G.B., 1969**. *One Dimensional Two-phase Flow*. McGraw-Hill, NY NY Chpt. 9:243-279.

**Warren, L.J., 1985.** Determination of the contributions of true flotation and entrainment in batch flotation tests. Int. J. Miner. Process., Vol. 14, pp 33-44.

**Weber, M.E., 1981.** Collision Efficiencies for small particles with a spherical collector at intermediate Reynolds' numbers. J. Sep. Proc. Tech., 2(1):29-33

**Weber, M.E., and Paddock, D., 1983.** Interceptional and gravitational collision efficiencies for single collectors at intermediate Reynolds numbers. J. of Colloid and interface Science, 94(2):328-335

**Wehner, J.F., and Wilhelm, R.H., 1956**. Boundary conditions of flow reactor. Chem. Eng. Sci., 6:89.

**Wilson, S.W., 1990.** Flotation column scale-up at INCO's matte separation plant. M.A.Sc. Thesis, University of Toronto, Dept. of Metallurgy and Materials Sci.

**Wills, B.A., 1992**. *Mineral Processing Technology*, 5th ed., Pergamon Press, Oxford.

**Woo, S.W., 1971.** Simultaneous free and forced convection around submerged cylinders and spheres. Ph.D. Thesis, McMaster University, Hamilton Ontario.

**Woodburn, E.T., 1970**. Mathematical modeling of flotation processes. Miner. Sci. Engng., 2:3-17.

**Woodburn, E.T., Kropholler, H.W., Greene, J.C.A., and Cramer, L.A., 1976.** The utility and limitations of mathematical modeling in the prediction of the properties of flotation networks. In: M.C. Fuerstenau (ed), *Flotation, A.M. Gaudin Memorial Volume, 2.* AIME, NY NY pp 638-674.

**Woodburn, E.T., Loveday, B.K., 1965.** The effect of variable residence-time on the performance of a flotation system. J.S.Afr. Inst. Min. Metall. 65:612-623.

**Woods, R., 1976**. Electrochemistry of sulphide flotation. In: *Flotation, A.M. Gaudin Memorial* Volume 1, Chapter 10.

**Woods, R., 1984**. Electrochemistry of sulphide flotation, In: M.H. Jones and J.T. Woodcock (eds) *Principles of Flotation*, AusIMM.

**Xu, M., 1987**. Sparger study in flotation columns. Ph.D. Thesis, McGill University, Dept of Mining and Metallurgical Engineering.

**Xu, M., and Finch, J.A., 1991a.** Estimating vessel dispersion number in flotation columns. In G.E. Agr, B.J. Huls, and D.B. Hyma (eds) *Column '91*, CIM Sudbury Ontario, 437.

**Xu, M., and Finch, J.A., 1991b.** The axial dispersion model in flotation column studies. Miner. Engng., 4: 553-562.

**Xu, M., and Finch, J.A., 1992.** Solids mixing in the collection zone of flotation columns. Miner. Engng.,5(9):1029-1039.

**Xu, M., Finch, J.A., and Uribe-Salas, A., 1991.** Maximum gas and bubble surface rates in flotation columns. Int. J. Miner. Process., 32:233-250.

**Xu, M., Uribe-Salasm A., Finch, J.A., and Gomez, C.O., 1989.** Gas rate limitation in column flotation. In: G.S. Dobby and S.R. Rao (Eds.), *Processing of Complex Ores.* Pergamon Press, Oxford, pp 397-407.

**Yalcin, T., 1992**. Determination of flotation rate constants from semi-batch flotation data. Minerals Engineering, 5(6):695-706.

**Ye, Y., and Miller, J.D., 1989.** The significance of bubble/particle contact time during collision in the analysis of flotation phenomena. Int. J. Miner. Process., 25:199-219.

**Yianatos, J.B., and Bergh, L.G., 1991.** RTD Studies in an industrial flotation column: use of radioactive tracer technique: In: *Column '91.* Ed. Agar, Huls, and Hyma. CIM 1:221-234. Also in Int. J. Mineral Process., 36(1992):81-91.

**Yianatos, J.B., and Finch, J.A., 1990.** Gas holdup versus gas rate in bubbly regime. Int. J. Miner. Process., 29:141-146

**Yianatos, J.B., Finch, J.A., Dobby, G.S., and Xu, M.**, 1988. Bubble size estimation in a bubble swarm. J. of Colloid and Interface Sci., Vol. 126, No. 1, pp 37-44.

**Yoon, R.-H., 1993**. Microbubble flotation. Miner. Engng., 6(6):619-630.

**Yoon, R.-H. and Luttrell, (1989).** The effect of bubble size on fine particle flotation. In: Laskowski, J.S. (ed.) *Mineral Processing and Extraction Metallurgy Review, Vol. 5, Frothing in Flotation: The Jan Leja Volume.* Gordon and Breach, New York pp 101-122

**Yoon, R.H., Mankosa, M.J., and Luttrell, G.H., 1993.** Design and scale-up criteria for column flotation. AusIMM – XVIII Int. Mineral Processing Congress, Sydney Australia, 785.

**Yoon, R.H., Mankosa, M.J., Luttrell, G.H., and Adel, G.T., 1991**. Full-scale testing of microbubble column flotation. *Column '91*, Sudbury Canada, CIM (Agar, G.E., Juls, B.J., Hyma, D.B. eds), Vol 1: 263.

**Yoon, R.-H., and Yordon, J.L., 1991**. The critical rupture thickness of thin water films on hydrophobic surfaces. J. Colloid Interface Sci., 146:565-572.

**Yordon, J.L., and Yoon, R.-H., 1986.** Induction time measurements for the quartz-amine flotation system. Presented at the 115$^{th}$ SME Annual meeting, New Orleans, LA., SME, Littleton CO (Pre-print 86-105, 10 pp)

**Yuan, X.-M., Palsson, B.I., and Forssberg, K.S.E., 1996**. Statistical interpretation of flotation kinetics for a complex sulphide ore. Minerals Engineering, 9(4):429-442.

**Zuber, N., 1964**. On the dispersed two-phase flow in laminar flow regime. Chem. Eng. Sci., 19:897-917.

**Zuber, N., and Hench, J., 1962**. Rept. No. 62GL100, General Electric Company, Schenectady, NY., as referred to by Xu et. al., (1989) and Pal and Masliyah (1989)

# 10 Data Appendix

## 10.2 Introduction

Actual weights of samples and products are given, when possible, rather than percentages in order to preserve the original data. Times are all given in seconds, lengths in centimeters, and mass in grams. Particle size is given in micrometers.

## 10.2 INCO Data

### 10.2.1 **Batch Mechanical-Cell**

Feed grade to all batch tests was 70.7% copper or 88.3% chalcocite. In all tests the copper mineral is assumed to be chalcocite ($Cu_2S$) with a density of 5.6 and a copper content of 80%. The nickel mineral is assumed to be heazelwoodite ($Ni_3S_2$) with a nickel content of 73.55%. The remaining mass or residuals is termed "other" and is assumed to be composed of silicates with a density of 2.67. The size-classes used in this test where –44, -74/+44 and +74 micrometers.

The results of the four batch mechanical-cell tests are given in the following tables. The first batch test is presented in Table 26, Table 27 and Table 28. Table 26 shows the total interval mass recoveries for test #1 for each size class along with water recovery and the estimated overflow bubble size. Figure 68 plots the overflow solids mass rate [g $s^{-1}$] for all size fractions of test #1. Figure 69 plots the same data as Figure 68 on a log-normal scale. Figure 70 plots the bubble size as a function of time. Table 27 and Table 28 show the copper and nickel assays, respectively, from test #1.

The second batch test results are found in Table 29, Table 30 and Table 31. The third batch test results are found in Table 32, Table 33, and Table 34 while the fourth batch test results are found in Table 35, Table 36 and Table 37.

**Table 26: Batch mechanical-cell test #1, total masses**

| Time | Weight | | | Bubble | Water |
|---|---|---|---|---|---|
| [s] | -44 | -74/44 | +74 | $d_b$ [cm] | $v_{w(O)}$ |
| 30 | 127.4 | 57.2 | 8.0 | 0.22 | 199.8 |
| 60 | 71.0 | 23.4 | 5.4 | 0.22 | 103.6 |
| 120 | 59.6 | 19.3 | 2.9 | 0.24 | 39.7 |
| 240 | 68.9 | 12.3 | 3.0 | 0.26 | 24.7 |
| 480 | 69.5 | 18.9 | 1.8 | 0.30 | 35.5 |
| 960 | 25.6 | 2.9 | 0.3 | 0.30 | 46.6 |
| Under | 74.5 | 90.0 | 48.6 | | |

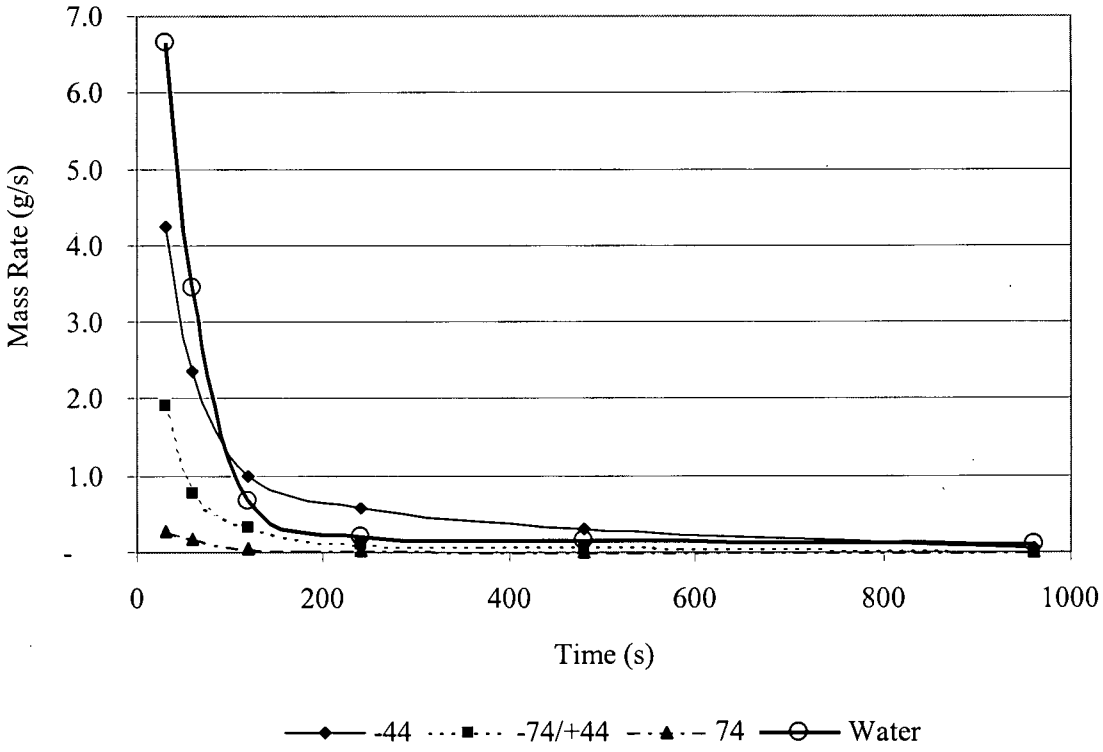


**Figure 68: Mass rate versus time for batch mechanical-cell test #1, total masses.**

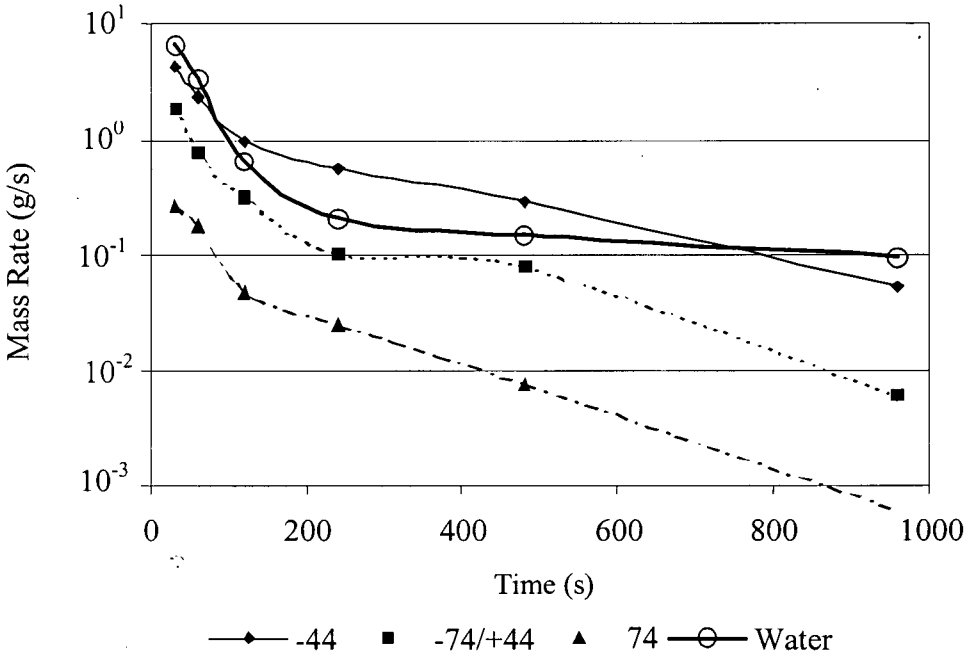


**Figure 69: Mass rate versus time for batch mechanical-cell test #1, total masses-log normal scale.**

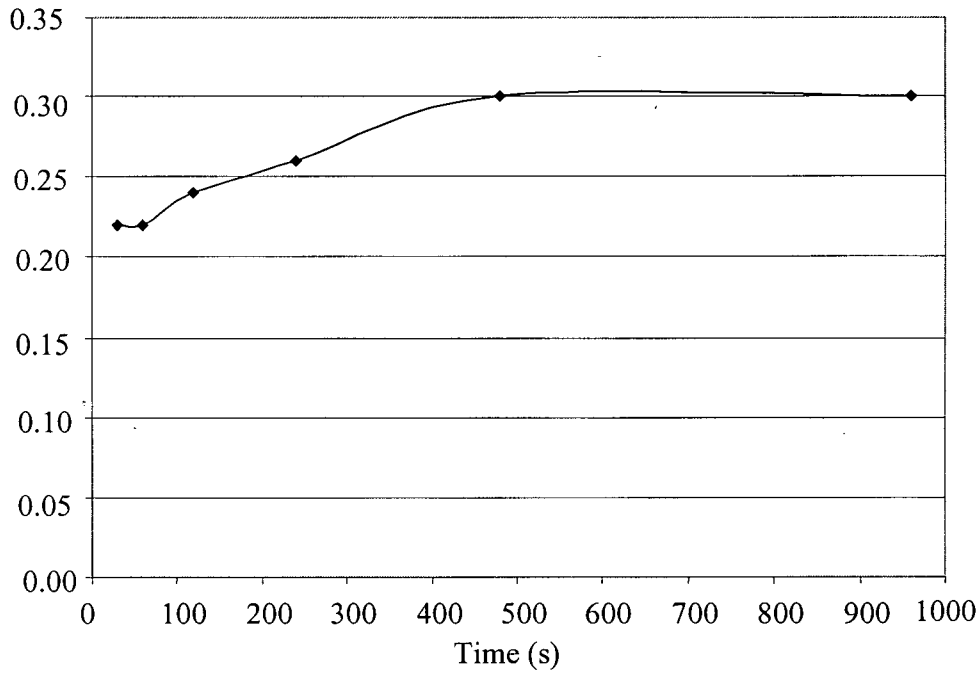


**Figure 70: Bubble diameter versus time for batch mechanical-cell test #1**

**Table 27: Batch mechanical-cell test #1, copper assays**

| Time [s] | Copper -44 | -74/44 | +74 |
|---|---|---|---|
| 30 | 76.8% | 77.1% | 77.9% |
| 60 | 78.3% | 78.4% | 77.4% |
| 120 | 78.3% | 77.3% | 77.5% |
| 240 | 76.0% | 76.8% | 76.4% |
| 480 | 75.5% | 76.8% | 77.3% |
| 960 | 74.8% | 70.5% | 76.0% |
| Under | 59.3% | 66.1% | 69.6% |

**Table 28: Batch mechanical-cell test #1, nickel assays**

| Time [s] | Nickel -44 | -74/44 | +74 |
|---|---|---|---|
| 30 | 1.9% | 1.8% | 2.0% |
| 60 | 1.6% | 1.7% | 2.3% |
| 120 | 1.6% | 1.9% | 2.2% |
| 240 | 1.8% | 2.0% | 2.3% |
| 480 | 2.9% | 2.6% | 2.8% |
| 960 | 3.4% | 2.6% | 2.9% |
| Under | 16.1% | 11.4% | 10.6% |

**Table 29: Batch mechanical-cell test #2, total masses**

| Time | Weight | | | Bubble | Water |
|---|---|---|---|---|---|
| | -44 | -74/44 | +74 | $d_b$ [cm] | $v_{w(O)}$ |
| 30 | 128.1 | 56.8 | 8.0 | 0.23 | 195.8 |
| 60 | 71.9 | 25.2 | 5.2 | 0.23 | 105.4 |
| 120 | 59.2 | 18.8 | 2.9 | 0.23 | 39.8 |
| 240 | 67.8 | 15.2 | 3.0 | 0.24 | 24.7 |
| 480 | 69.5 | 18.8 | 2.2 | 0.24 | 35.7 |
| 960 | 33.1 | 9.1 | 1.8 | 0.26 | 6.6 |
| Under | 75.9 | 88.9 | 47.8 | | |

**Table 30: Batch mechanical-cell test #2, copper assays**

| Time | Copper | | |
|---|---|---|---|
| [s] | -44 | -74/44 | +74 |
| 30 | 76.4% | 77.1% | 77.7% |
| 60 | 78.0% | 78.2% | 77.1% |
| 120 | 78.1% | 77.3% | 77.7% |
| 240 | 76.2% | 77.0% | 76.3% |
| 480 | 75.4% | 77.0% | 77.5% |
| 960 | 75.0% | 70.5% | 76.2% |
| Under | 59.1% | 66.0% | 69.7% |

**Table 31: Batch mechanical-cell test #2, nickel assays**

| Time | Nickel | | |
|---|---|---|---|
| [s] | -44 | -74/44 | +74 |
| 30 | 2.0% | 1.8% | 2.1% |
| 60 | 1.5% | 1.8% | 2.3% |
| 120 | 1.6% | 1.8% | 2.3% |
| 240 | 1.7% | 1.9% | 2.4% |
| 480 | 2.8% | 2.7% | 3.1% |
| 960 | 4.1% | 3.2% | 3.6% |
| Under | 16.5% | 11.3% | 11.0% |

**Table 32: Batch mechanical-cell test #3, total masses**

| Time [s] | Weight -44 | -74/44 | +74 | Bubble $d_b$ [cm] | Water |
|---|---|---|---|---|---|
| 30 | 126.1 | 56.5 | 8.1 | 0.22 | 163.6 |
| 60 | 72.5 | 23.8 | 4.9 | 0.23 | 117.3 |
| 120 | 60.0 | 19.5 | 2.9 | 0.24 | 42.9 |
| 240 | 70.3 | 12.3 | 2.7 | 0.24 | 24.7 |
| 480 | 70.1 | 18.7 | 2.4 | 0.25 | 32.6 |
| 960 | 32.5 | 6.2 | 2.7 | 0.25 | 36.7 |
| Under | 73.8 | 92.1 | 49.5 | | |

**Table 33: Batch mechanical-cell test #3, copper assays**

| Time [s] | Copper -44 | -74/44 | +74 |
|---|---|---|---|
| 30 | 77.1% | 77.5% | 78.2% |
| 60 | 78.3% | 78.3% | 77.7% |
| 120 | 78.0% | 77.5% | 77.5% |
| 240 | 75.6% | 77.0% | 76.2% |
| 480 | 75.4% | 77.0% | 77.0% |
| 960 | 75.0% | 70.4% | 75.8% |
| Under | 59.2% | 66.0% | 69.7% |

**Table 34: Batch mechanical-cell test #3, nickel assays**

| Time [s] | Nickel -44 | -74/44 | +74 |
|---|---|---|---|
| 30 | 2.0% | 1.8% | 2.0% |
| 60 | 1.6% | 1.8% | 2.4% |
| 120 | 1.6% | 1.9% | 2.2% |
| 240 | 1.8% | 2.1% | 2.3% |
| 480 | 2.8% | 2.6% | 2.9% |
| 960 | 4.2% | 4.7% | 3.4% |
| Under | 16.0% | 11.3% | 10.1% |

**Table 35: Batch mechanical-cell test #4, total masses**

| Time | Weight | | | Bubble | Water |
|---|---|---|---|---|---|
| [s] | -44 | -74/44 | +74 | $d_b$ [cm] | $v_{w(O)}$ |
| 30 | 126.1 | 58.1 | 8.2 | 0.20 | 197.4 |
| 60 | 71.0 | 23.6 | 5.3 | 0.20 | 109.1 |
| 120 | 60.5 | 19.0 | 2.8 | 0.21 | 38.8 |
| 240 | 72.1 | 13.1 | 3.0 | 0.23 | 34.4 |
| 480 | 59.7 | 18.8 | 2.6 | 0.24 | 25.8 |
| 960 | 33.1 | 12.8 | 2.4 | 0.24 | 6.6 |
| Under | 75.2 | 88.7 | 48.4 | | |

**Table 36: Batch mechanical-cell test #4, copper assays**

| Time | Copper | | |
|---|---|---|---|
| [s] | -44 | -74/44 | +74 |
| 30 | 77.1% | 77.5% | 77.5% |
| 60 | 78.1% | 77.9% | 77.7% |
| 120 | 78.0% | 77.5% | 77.5% |
| 240 | 75.6% | 77.3% | 76.2% |
| 480 | 75.4% | 77.0% | 76.1% |
| 960 | 71.8% | 70.4% | 75.8% |
| Under | 59.2% | 66.0% | 68.8% |

**Table 37: Batch mechanical-cell test #4, nickel assays**

| Time | Nickel | | |
|---|---|---|---|
| [s] | -44 | -74/44 | +74 |
| 30 | 2.0% | 1.8% | 2.1% |
| 60 | 1.6% | 1.8% | 2.1% |
| 120 | 1.6% | 1.9% | 2.2% |
| 240 | 1.8% | 2.4% | 2.3% |
| 480 | 2.2% | 2.6% | 2.9% |
| 960 | 5.6% | 4.7% | 3.4% |
| Under | 15.6% | 11.3% | 10.1% |

## 10.2.2 Batch Mechanical-Cell Performance

Figure 37 shows the –44 μm chalcocite test data and batch model response on a log-normal curve. This data is presented in Figure 71 on a linear scale. The comparison between the batch model response and test data for the chalcocite –74/+44 micrometer fraction is shown in Figure 72 while the +74 micrometer fraction is shown in Figure 73.

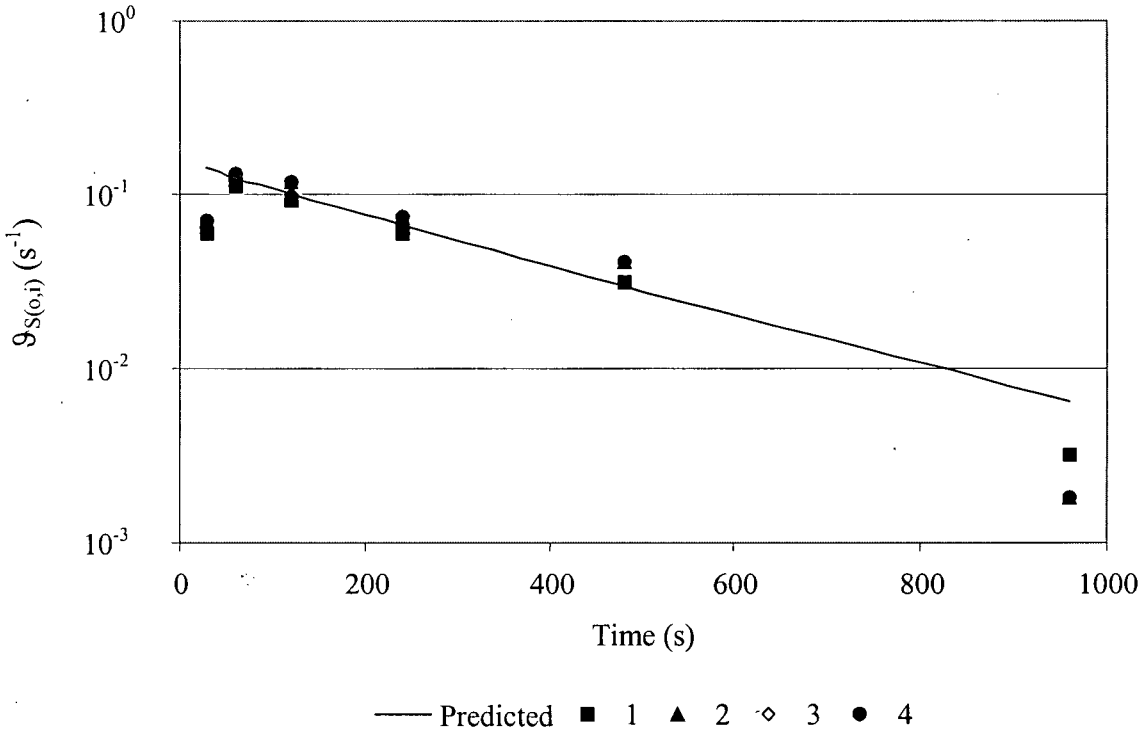


**Figure 71: Model performance on –44 μm chalcocite showing all four tests and the predicted surface area flux on a linear plot. X-axis is time in seconds while Y-axis is overflow superficial total-solids surface-area rate ($s^{-1}$).**

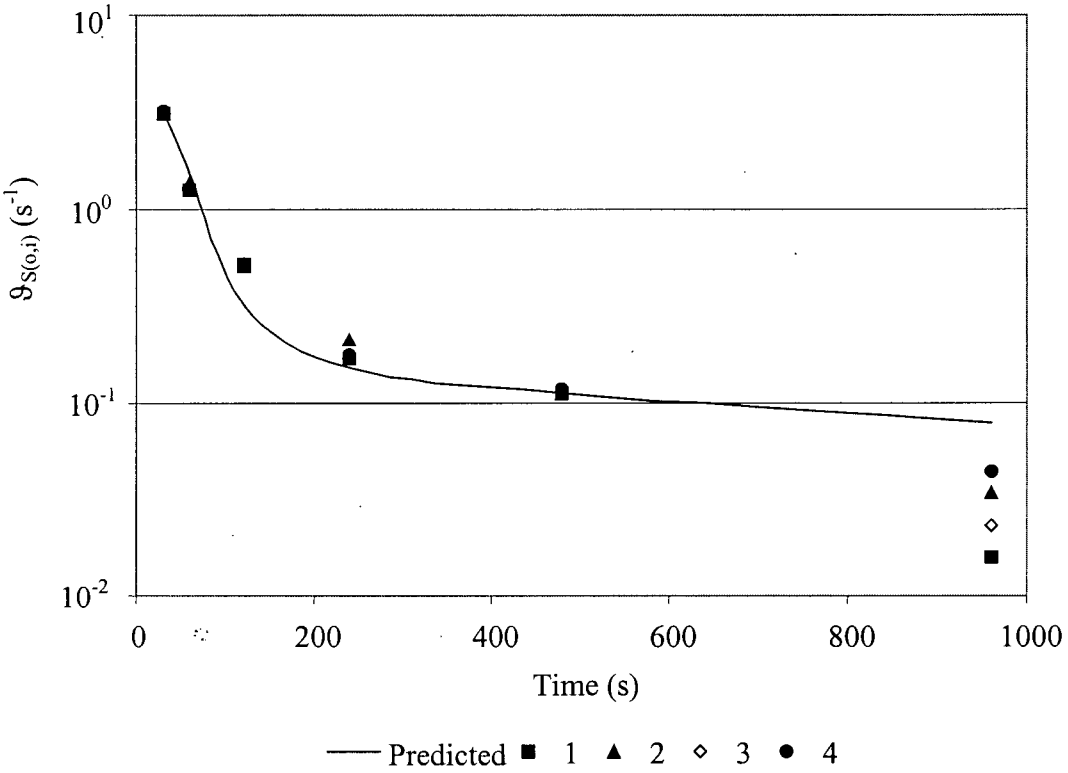


**Figure 72: Model performance on –74/+44 μm chalcocite showing all four tests and the predicted surface-area flux on a semi-log plot. X-axis is time in seconds while Y-axis is overflow superficial total-solids surface-area rate ($s^{-1}$).**

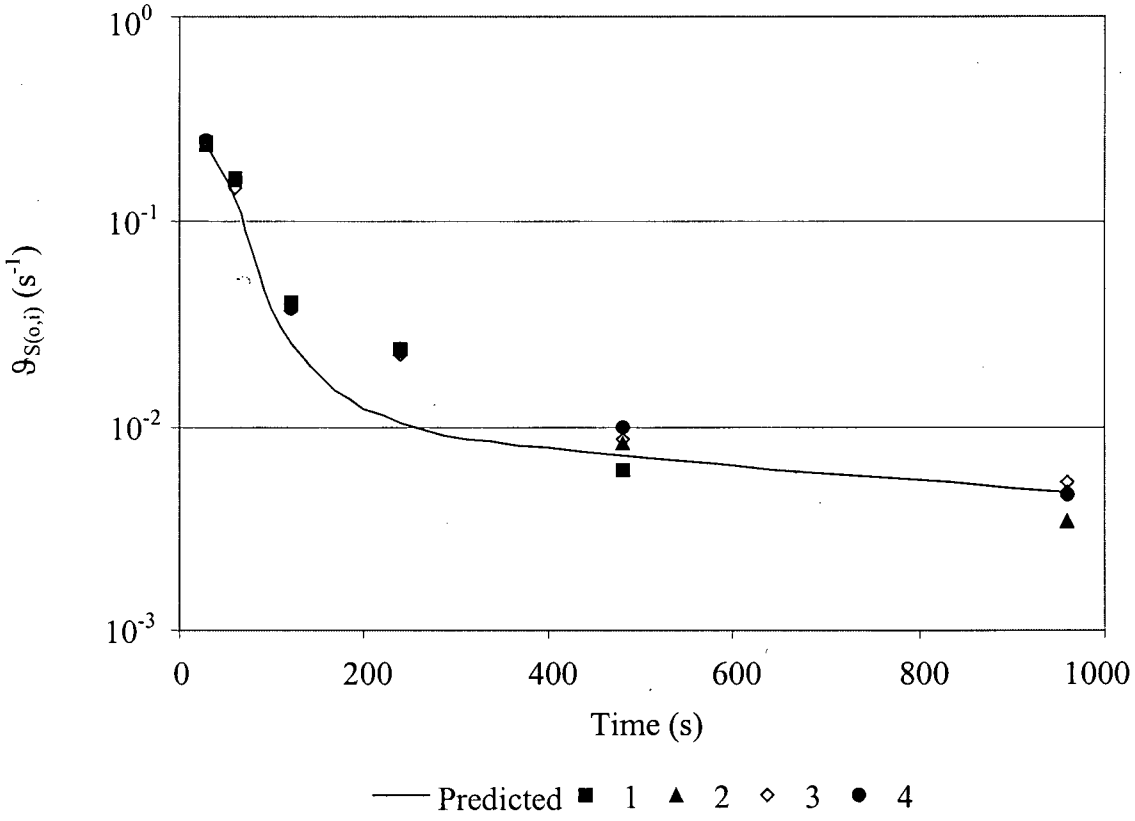


**Figure 73: Model performance on +74 μm chalcocite showing all four tests and the predicted surface-area flux on a semi-log plot. X-axis is time in seconds while Y-axis is overflow superficial total-solids surface-area rate ($s^{-1}$).**

Figure 74 shows the –44 μm heazelwoodite test data and batch model response on a log-normal curve. The comparison between the batch model response and test data for the heazelwoodite –74/+44 micrometer fraction is shown in Figure 75 while the +74 micrometer fraction is shown in.

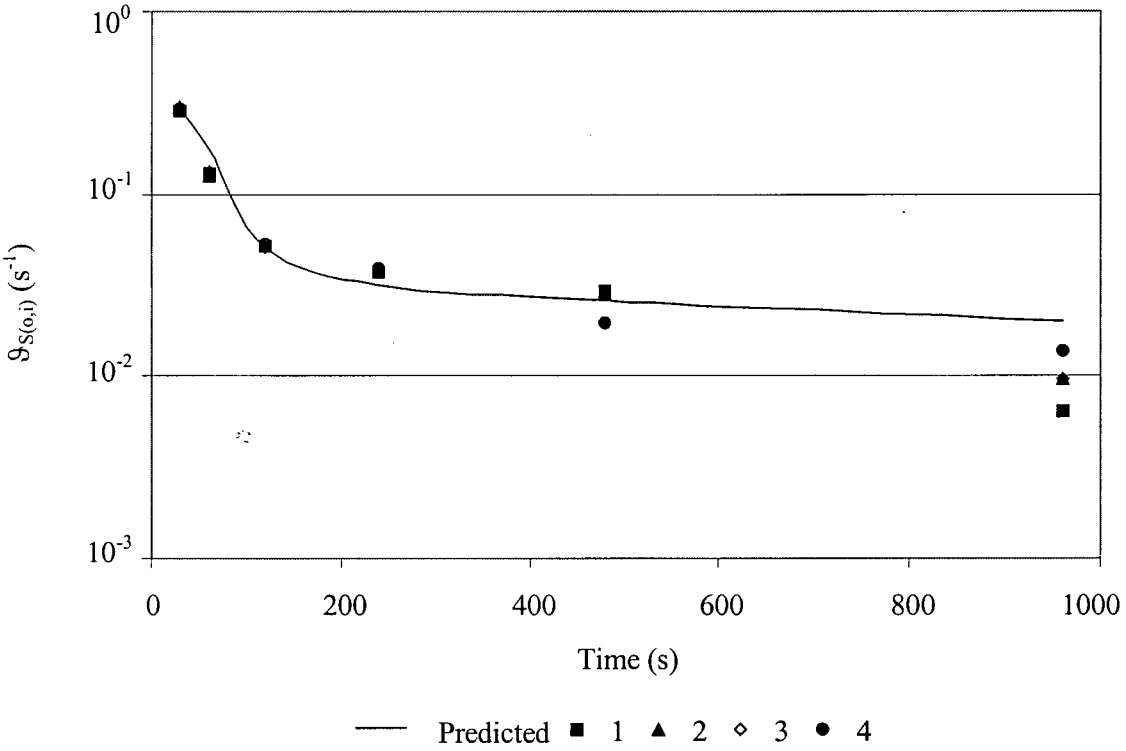


**Figure 74: Model performance on –44 μm heazelwoodite showing all four tests and the predicted surface-area flux on a semi-log plot. X-axis is time in seconds while Y-axis is overflow superficial total-solids surface-area overflow rate ($s^{-1}$).**

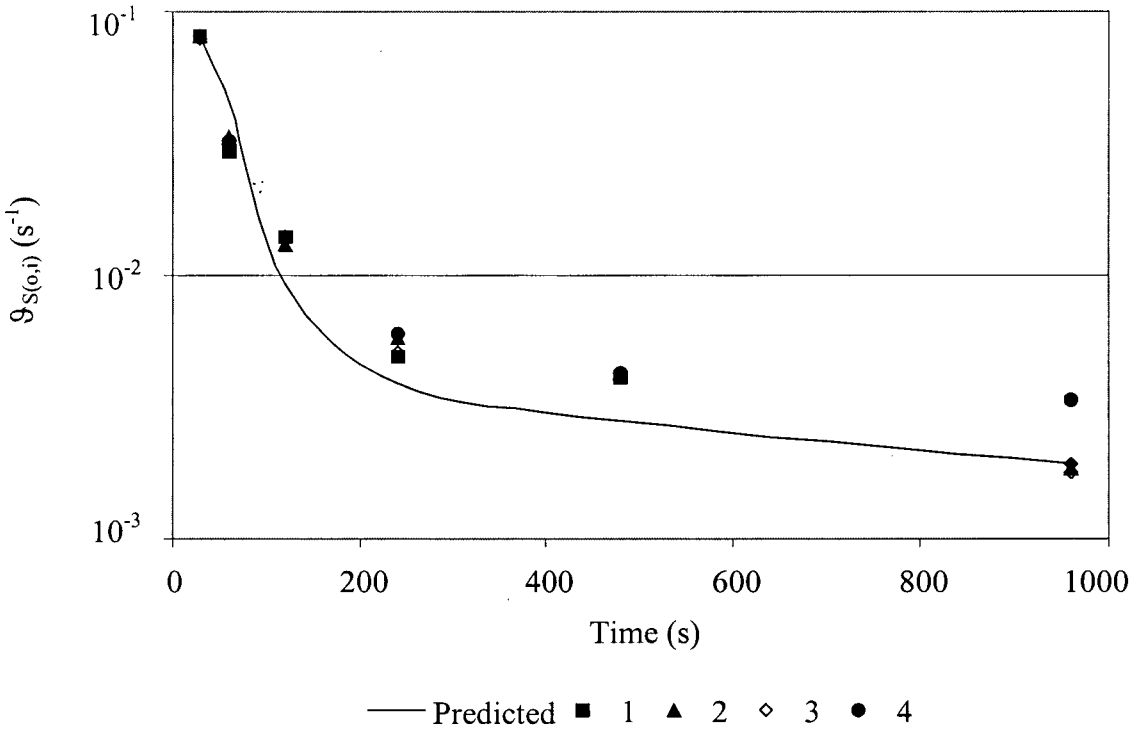


**Figure 75: Model performance on –74/+44 μm heazelwoodite showing all four tests and the predicted surface-area flux on a semi-log plot. X-axis is time in seconds while Y-axis is overflow superficial total-solids surface-area rate ($s^{-1}$).**

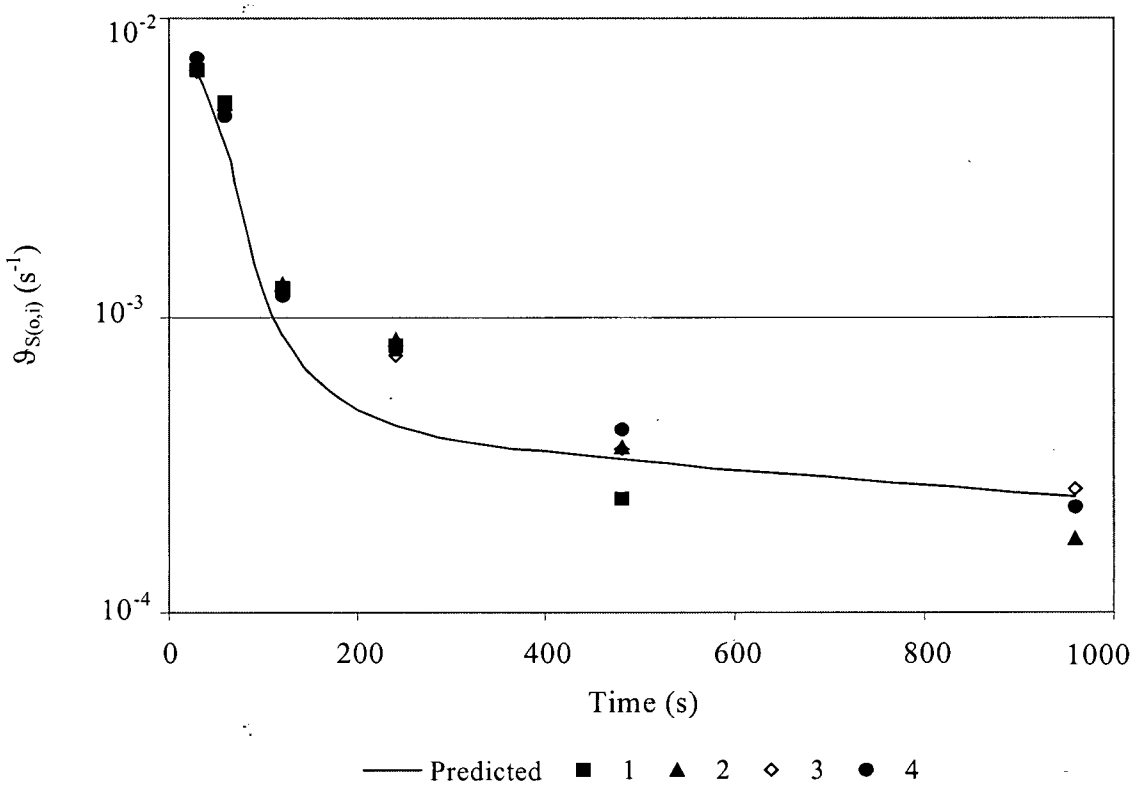


**Figure 76: Model performance on +74 μm heazelwoodite showing all four tests and the predicted surface-area flux on a semi-log plot. X-axis is time in seconds while Y-axis is overflow superficial total-solids surface-area overflow ($s^{-1}$).**

Figure 77 shows the –44 μm "other" test data and batch model response on a log-normal curve. The comparison between the batch model response and test data for the "other" –74/+44 micrometer fraction is shown in Figure 78. No plot is given for the +74 micrometer fraction since essentially none of this size fraction was present.

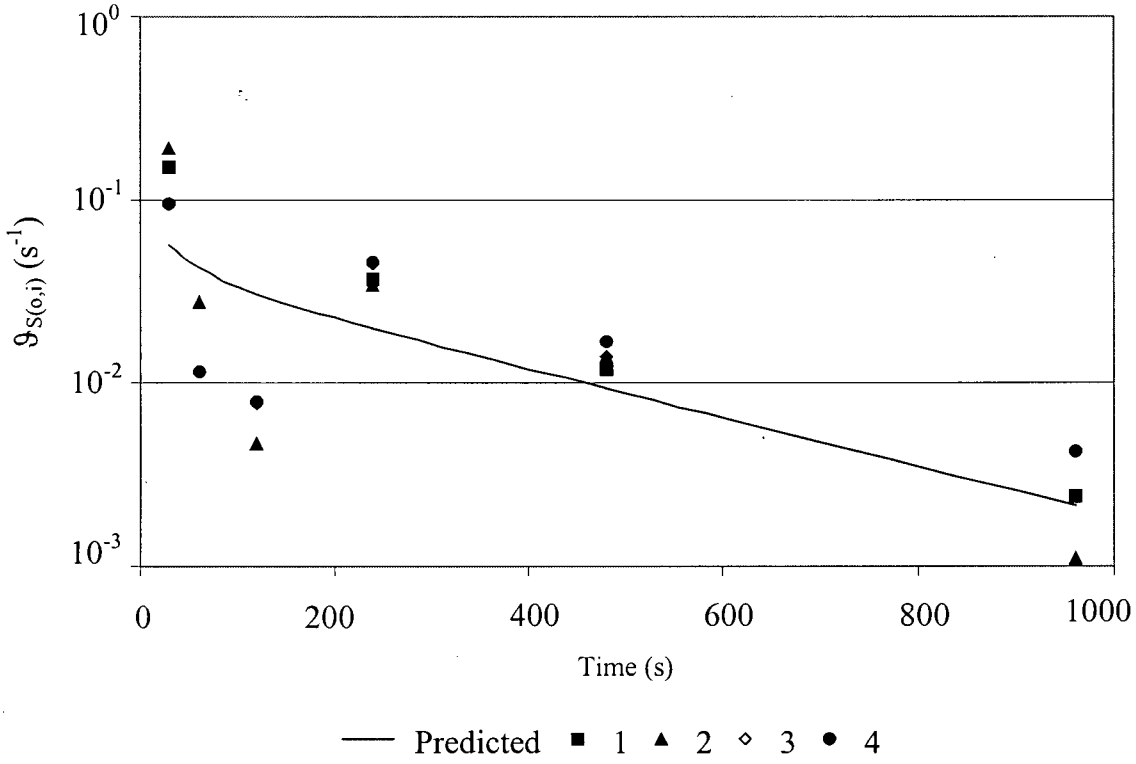


**Figure 77: Model performance on –44 μm "other" or residual material showing all four tests and the predicted surface-area flux on a semi-log plot. X-axis is time in seconds while Y-axis is overflow superficial total-solids surface-area rate ($s^{-1}$).**

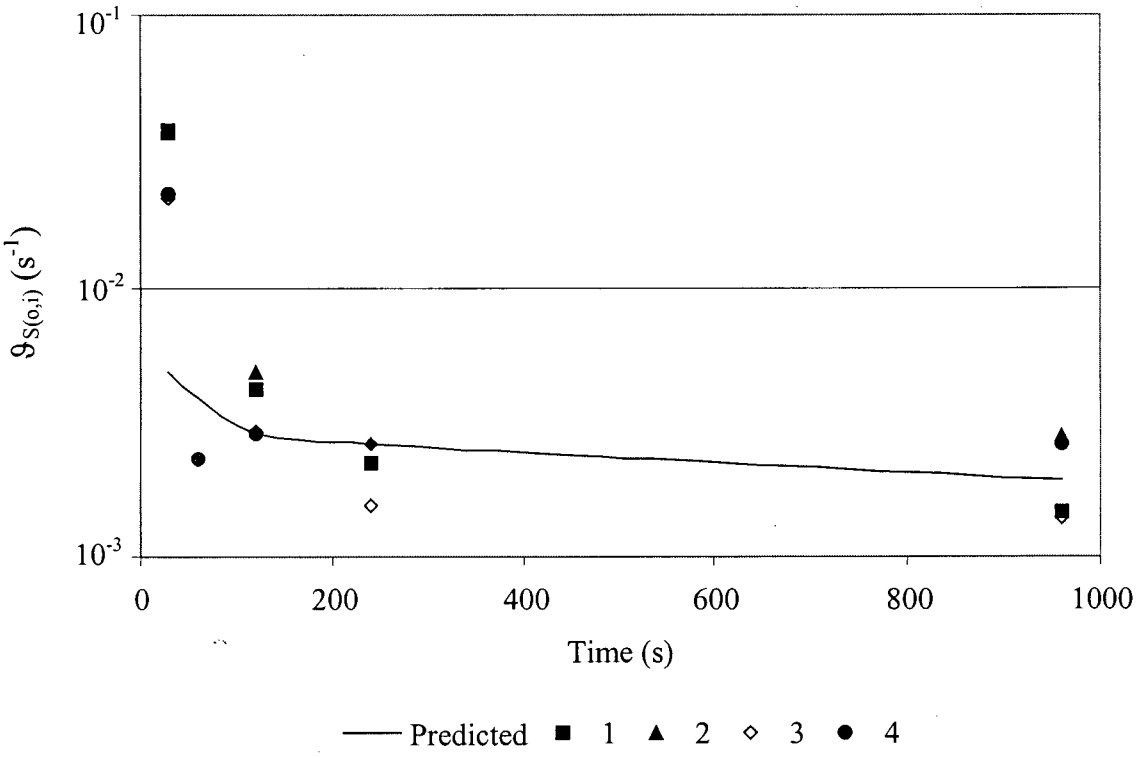


**Figure 78: Model performance on –74/+44 μm "other" or residual material showing all four tests and the predicted surface-area flux on a semi-log plot. X-axis is time in seconds while Y-axis is overflow superficial total-solids surface-area rate ($s^{-1}$).**

### 10.2.3 No Entrainment Accounting

The batch model becomes similar to the models that are typically used by industry to configure, size, and optimize flotation circuits when the entrainment parameter is set to a null value. This simplified version of the model is included here in order to illustrate the need for a good entrainment "module" within the flotation model.

The kinetic rate constant and maximum recovery values obtained by assuming a zero entrainment and discounting carrying capacity are found in Table 38.

**Table 38: Mechanical-cell test parameters to minimize error without entrainment**

| | -44 μm | -74/+44 μm | +74 μm |
|---|---|---|---|
| **Chalcocite** | | | |
| Kinetic rate, "$k_f$" | 0.0086 $s^{-1}$ | 0.015 $s^{-1}$ | 0.016 $s^{-1}$ |
| Maximum recovery, "$R_\infty$" | 84% | 59% | 32% |
| Entrainment factor, "$k_e$" | Set to zero | Set to zero | Set to zero |
| **Heazelwoodite** | | | |
| Kinetic rate, "$k_f$" | 0.0061$s^{-1}$ | 0.015 $s^{-1}$ | 0.01 $s^{-1}$ |
| Maximum recovery, "$R_\infty$" | 41% | 19% | 8.8% |
| Entrainment factor, "$k_e$" | Set to zero | Set to zero | Set to zero |
| **Other** | | | |
| Kinetic rate, "$k_f$" | 0.0053 $s^{-1}$ | 0.0019 $s^{-1}$ | * |
| Maximum recovery, "$R_\infty$" | 69% | 31% | * |
| Entrainment factor, "$k_e$" | Set to zero | Set to zero | * |

In Table 38 no values for the +74 micrometer "other" size fraction are shown since only a few grams of material were present in this fraction.

A comparison between the model responses under the "no entrainment" restriction and the test data is shown in Figure 79 and Figure 80. Figure 79 shows the superficial total-solids surface-area rate ("$\vartheta_s$" [$s^{-1}$]) using a log scale, plotted against time. The predicted flotation response on the log-normal plot shows as a straight line (Figure 79) that does not seem to represent the data well.

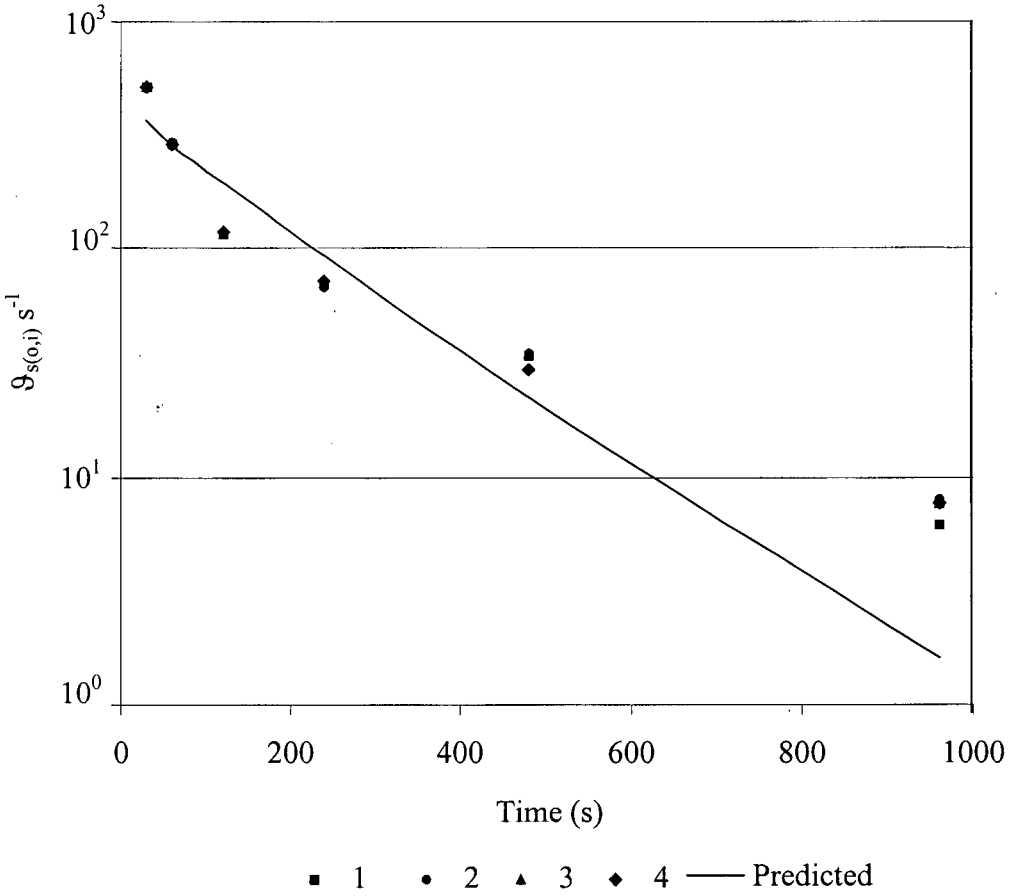


**Figure 79: Model performance without entrainment for the -44 μm chalcocite fraction showing all four tests and the predicted surface-area flux on a semi-log plot. X-axis is time in seconds while Y-axis is overflow superficial total-solids surface-area rate ($s^{-1}$). (Used to illustrate the importance of entrainment.)**

Figure 80 shows the same data as shown in Figure 79 using linear scales. This type of plot "seems" to indicate a good fit between the test data and model response.

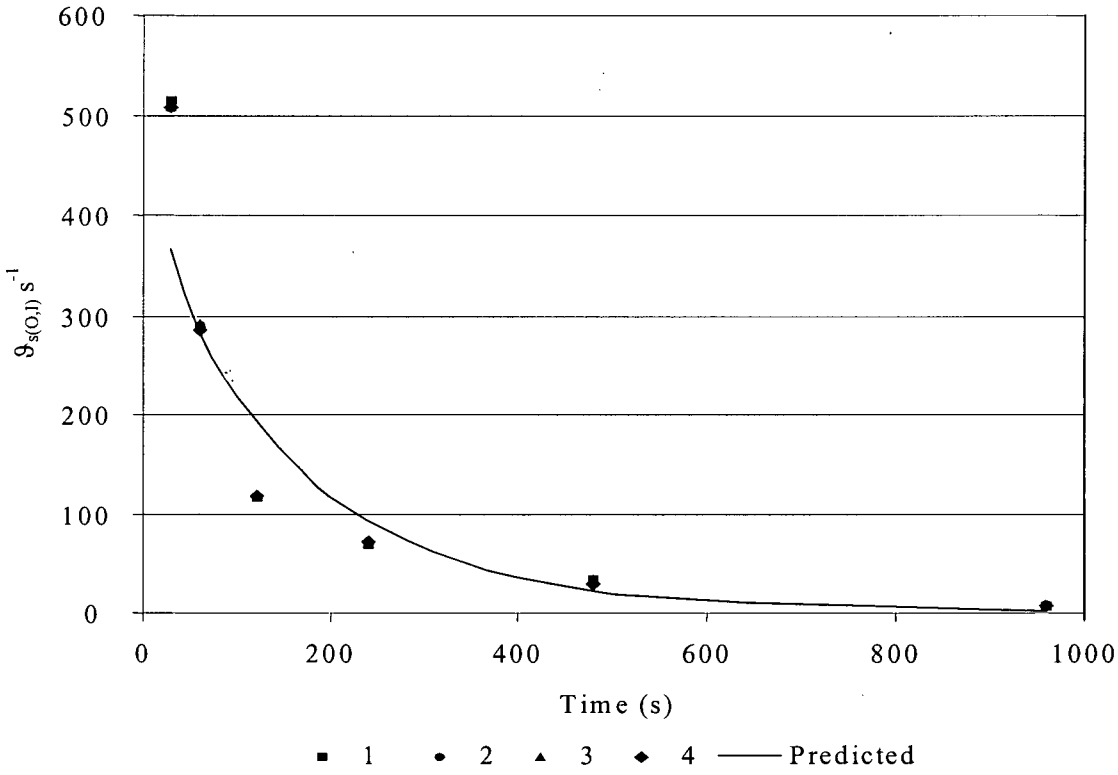


**Figure 80: Model performance without entrainment for the -44 μm Chalcocite fraction showing all four tests and the predicted surface-area flux. X-axis is time in seconds while Y-axis is overflow superficial total-solids surface-area rate ($s^{-1}$).**

The longer retention time float sample, which has a smaller superficial solids surface-area-flux, is better shown on the log-normal plot when large flows exist early in the test. Figure 81 shows a more traditional cumulative recovery response with time. This figure also shows that the model response using batch mechanical-cell data, when entrainment is not considered, results in a poor fit with the actual test data.

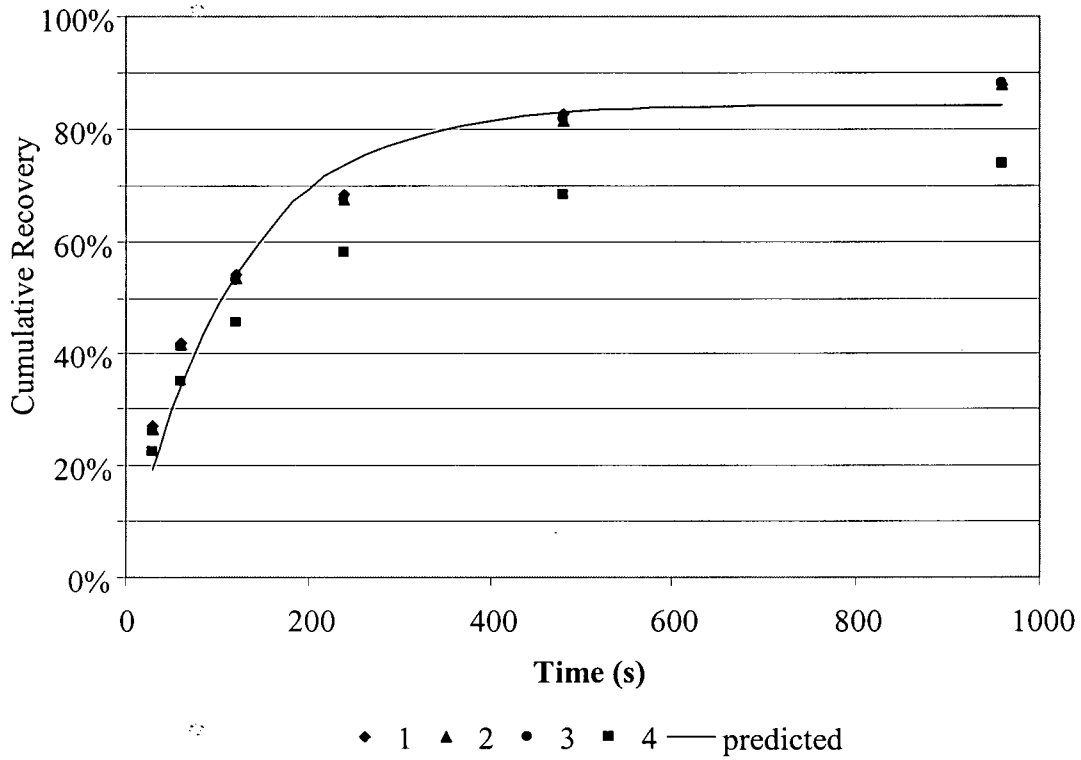


**Figure 81: Model performance without entrainment for the -44 μm chalcocite fraction showing all four tests and the cumulative recovery with time.**

### 10.2.4 Batch Column

The results of both batch column tests are found in the following tables. The first batch test is presented in Table 26, Table 27 and Table 28. The second batch test results are found in Table 29, Table 30 and Table 31.

**Table 39: Batch column test #1, total masses**

| Time [s] | Weight -44 | -74/44 | +74 | Bubble $d_b$ [cm] | Water $v_{w(O)}$ |
|---|---|---|---|---|---|
| 30 | 298.5 | 76.4 | 28.6 | 0.24 | 226.8 |
| 60 | 275.9 | 70.1 | 24.0 | 0.24 | 244.0 |
| 120 | 464.0 | 102.7 | 30.3 | 0.24 | 519.9 |
| 240 | 619.2 | 131.7 | 38.3 | 0.25 | 767.8 |
| 480 | 565.5 | 102.5 | 34.6 | 0.26 | 633.5 |
| 960 | 155.6 | 30.6 | 5.4 | 0.28 | 218.3 |
| Under | 779.3 | 119.8 | 35.1 | | |

**Table 40: Batch column test #1, copper assays**

| Time [s] | Copper -44 | -74/44 | +74 |
|---|---|---|---|
| 30 | 76.4% | 77.0% | 77.4% |
| 60 | 76.4% | 76.5% | 77.1% |
| 120 | 75.3% | 76.0% | 76.4% |
| 240 | 75.1% | 75.1% | 76.3% |
| 480 | 73.8% | 72.5% | 72.8% |
| 960 | 73.6% | 71.6% | 73.0% |
| Under | 55.6% | 59.9% | 62.7% |

**Table 41: Batch column test #1, nickel assays**

| Time [s] | Copper -44 | -74/44 | +74 |
|---|---|---|---|
| 30 | 2.2% | 2.2 % | 2.2% |
| 60 | 2.3% | 2.1% | 2.4% |
| 120 | 2.4% | 2.4% | 2.8% |
| 240 | 2.9% | 3.2% | 3.6% |
| 480 | 3.4% | 5.1% | 5.2% |
| 960 | 4.2% | 6.5% | 5.8% |
| Under | 19.4% | 17.5% | 14.5% |

**Table 42: Batch column test #2, total masses**

| Time [s] | Weight -44 | -74/44 | +74 | Bubble $d_b$ [cm] | Water $v_{w(O)}$ |
|---|---|---|---|---|---|
| 30 | 293.2 | 62.9 | 23.9 | 0.22 | 242.4 |
| 60 | 277.8 | 81.2 | 28.6 | 0.20 | 241.7 |
| 120 | 483.8 | 102.6 | 30.3 | 0.23 | 513.7 |
| 240 | 620.2 | 131.1 | 34.2 | 0.24 | 763.1 |
| 480 | 568.3 | 102.4 | 38.3 | 0.26 | 632.6 |
| 960 | 145.3 | 15.7 | 15.2 | 0.26 | 215.7 |
| Under | 776.3 | 119.5 | 45.0 | | |

**Table 43: Batch column test #2, copper assays**

| Time [s] | Copper -44 | -74/44 | +74 |
|---|---|---|---|
| 30 | 76.2% | 77.0% | 77.4% |
| 60 | 76.2% | 76.2% | 76.8% |
| 120 | 75.3% | 75.7% | 76.1% |
| 240 | 75.1% | 74.9% | 76.0% |
| 480 | 73.6% | 72.2% | 72.6% |
| 960 | 73.4% | 71.6% | 73.0% |
| Under | 55.3% | 59.7% | 62.6% |

**Table 44: Batch column test #2, nickel assays**

| Time [s] | Copper -44 | -74/44 | +74 |
|---|---|---|---|
| 30 | 2.1% | 2.2% | 2.1% |
| 60 | 2.2% | 2.0% | 2.3% |
| 120 | 2.4% | 2.3% | 2.8% |
| 240 | 2.8% | 3.1% | 3.5% |
| 480 | 4.1% | 4.9% | 5.1% |
| 960 | 4.1% | 6.4% | 5.8% |
| Under | 18.6% | 17.5% | 14.4% |

The rotameter readings, interface level and calculated bias rates are found in Table 45 (Test #1) Table 46 (Test #2) and Table 47 (Test #3).

**Table 45:** INCO batch column test wash-water and bias rates (Test #1)

| Time (min.) | Rotameter Setting | Interface Level | Calculated Bias |
|---|---|---|---|
| 0.5 | 10 $cm^3 s^{-1}$ | 19.0 cm | 0.035 cm $s^{-1}$ |
| 1.0 | 10 $cm^3 s^{-1}$ | 18.0 cm | 0.032 cm $s^{-1}$ |
| 2.0 | 10 $cm^3 s^{-1}$ | 16.5 cm | 0.025 cm $s^{-1}$ |
| 4.0 | 8 $cm^3 s^{-1}$ | 13.6 cm | 0.024 cm $s^{-1}$ |
| 8.0 | 4 $cm^3 s^{-1}$ | 9.3 cm | 0.018 cm $s^{-1}$ |
| 16.0 | 2 $cm^3 s^{-1}$ | 0.2 cm | 0.019 cm $s^{-1}$ |

**Table 46: INCO batch column test wash-water and bias rates (Test #2)**

| Time (min.) | Rotameter Setting | Interface Level | Calculated Bias |
|---|---|---|---|
| 0.5 | 10 $cm^3 s^{-1}$ | 19.0 cm | 0.035 cm $s^{-1}$ |
| 1.0 | 10 $cm^3 s^{-1}$ | 18.0 cm | 0.032 cm $s^{-1}$ |
| 2.0 | 10 $cm^3 s^{-1}$ | 16.2 cm | 0.030 cm $s^{-1}$ |
| 4.0 | 8 $cm^3 s^{-1}$ | 13.3 cm | 0.024 cm $s^{-1}$ |
| 8.0 | 4 $cm^3 s^{-1}$ | 8.5 cm | 0.020 cm $s^{-1}$ |
| 16.0 | 2 $cm^3 s^{-1}$ | 1.3 cm | 0.015 cm $s^{-1}$ |

**Table 47: INCO batch column test wash-water and bias rates (Test #3)**

| Time (min.) | Rotameter Setting | Interface Level | Calculated Bias |
|---|---|---|---|
| 0.5 | 10 $cm^3 s^{-1}$ | 18.9 cm | 0.038 cm $s^{-1}$ |
| 1.0 | 10 $cm^3 s^{-1}$ | 17.8 cm | 0.033 cm $s^{-1}$ |
| 2.0 | 10 $cm^3 s^{-1}$ | 16.2 cm | 0.028 cm $s^{-1}$ |
| 4.0 | 8 $cm^3 s^{-1}$ | 13.3 cm | 0.024 cm $s^{-1}$ |
| 8.0 | 4 $cm^3 s^{-1}$ | 9.0 cm | 0.018 cm $s^{-1}$ |
| 16.0 | 2 $cm^3 s^{-1}$ | 0.4 cm | 0.018 cm $s^{-1}$ |

The plot of model response versus test data for both column tests, -74/+44 micrometer fraction chalcocite is found in Figure 82 plotted on a log-normal scale using surface area rates. The same data and model is plotted as a time – recovery curve in Figure 83. Figure 84 shows the +74 micrometer chalcocite fraction using rates while Figure 85 is the equivalent time-recovery curve.

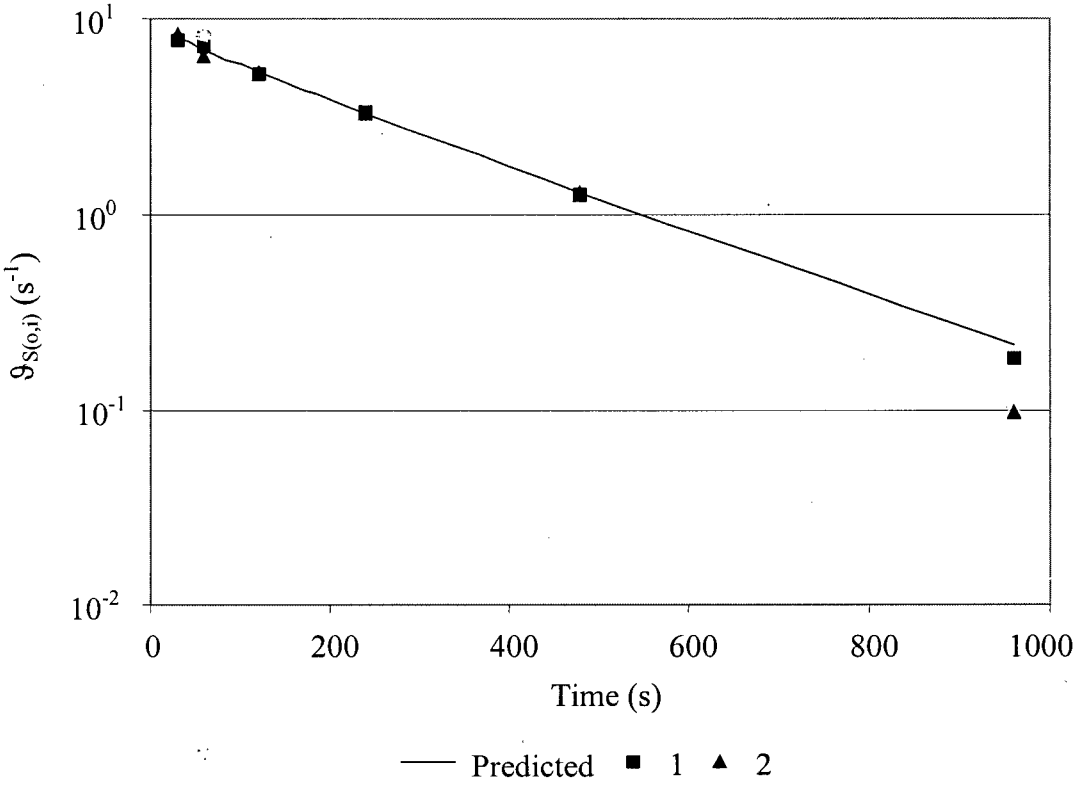


**Figure 82: Model performance on –74/+44 μm chalcocite, batch column, showing both tests and the predicted surface-area flux on a semi-log plot. X-axis is time in seconds while Y-axis is overflow superficial total-solids surface-area rate ($s^{-1}$).**

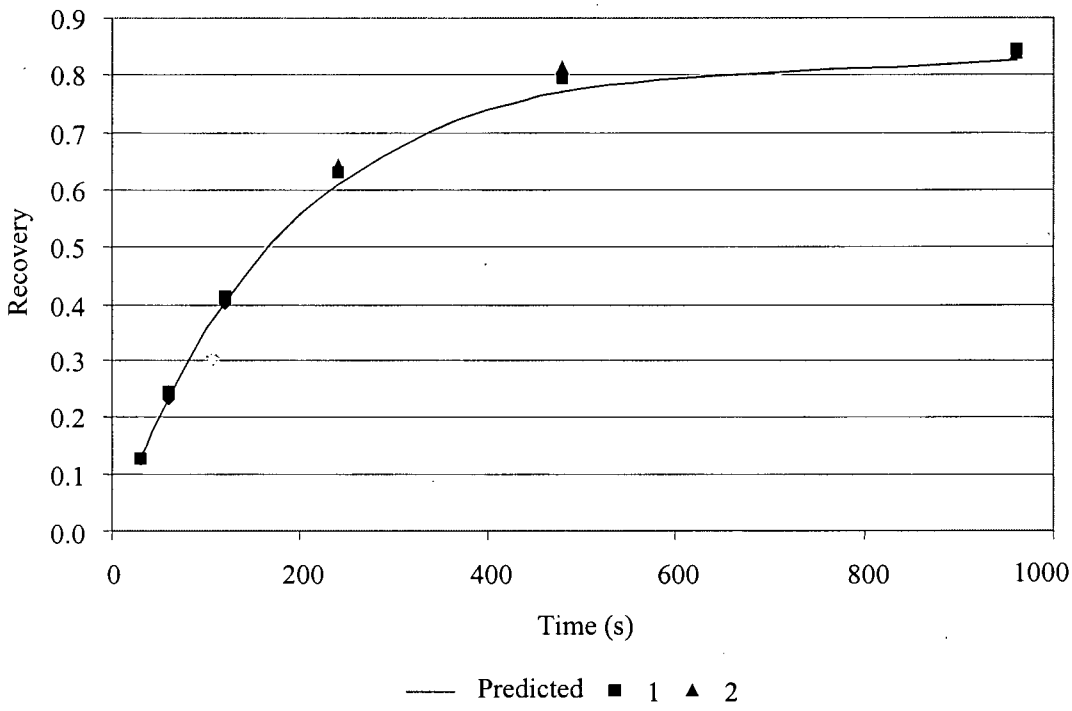


**Figure 83: Model performance on –74/+44 μm chalcocite, batch column, showing cumulative recovery with time.**

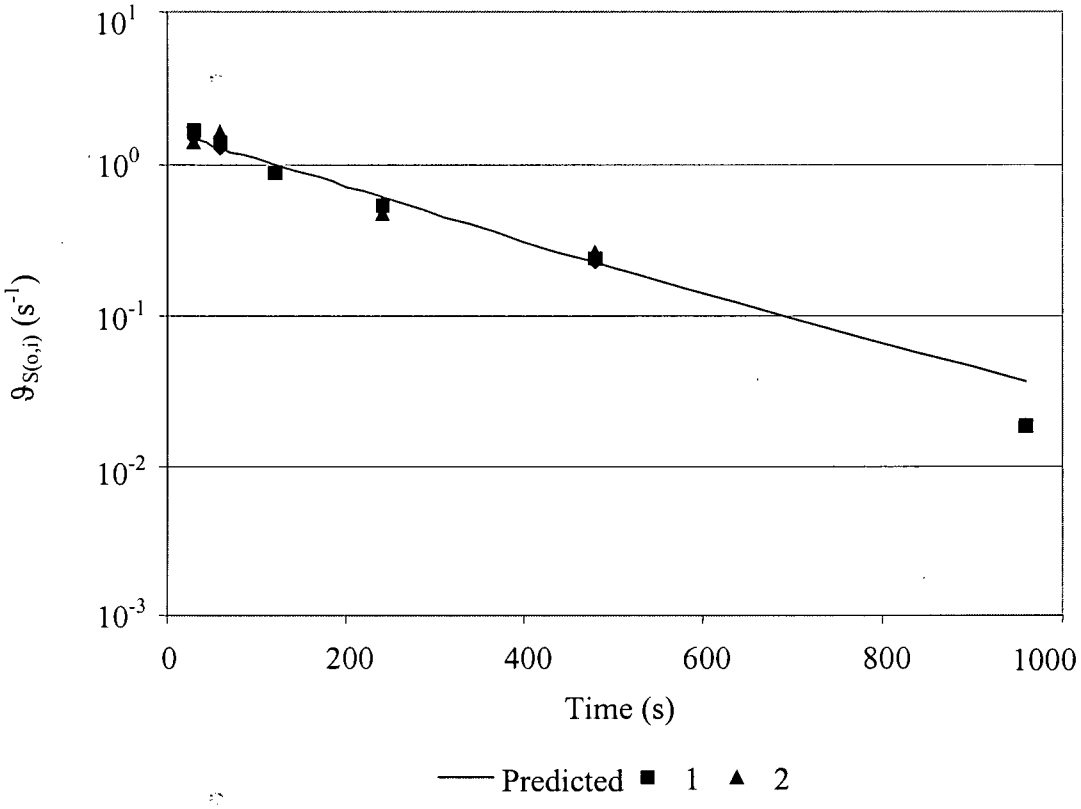


**Figure 84: Model performance on +74 μm chalcocite, "batch' column, showing both tests and the predicted surface-area flux on a semi-log plot. X-axis is time in seconds while Y-axis is overflow superficial total-solids surface-area rate ($s^{-1}$).**

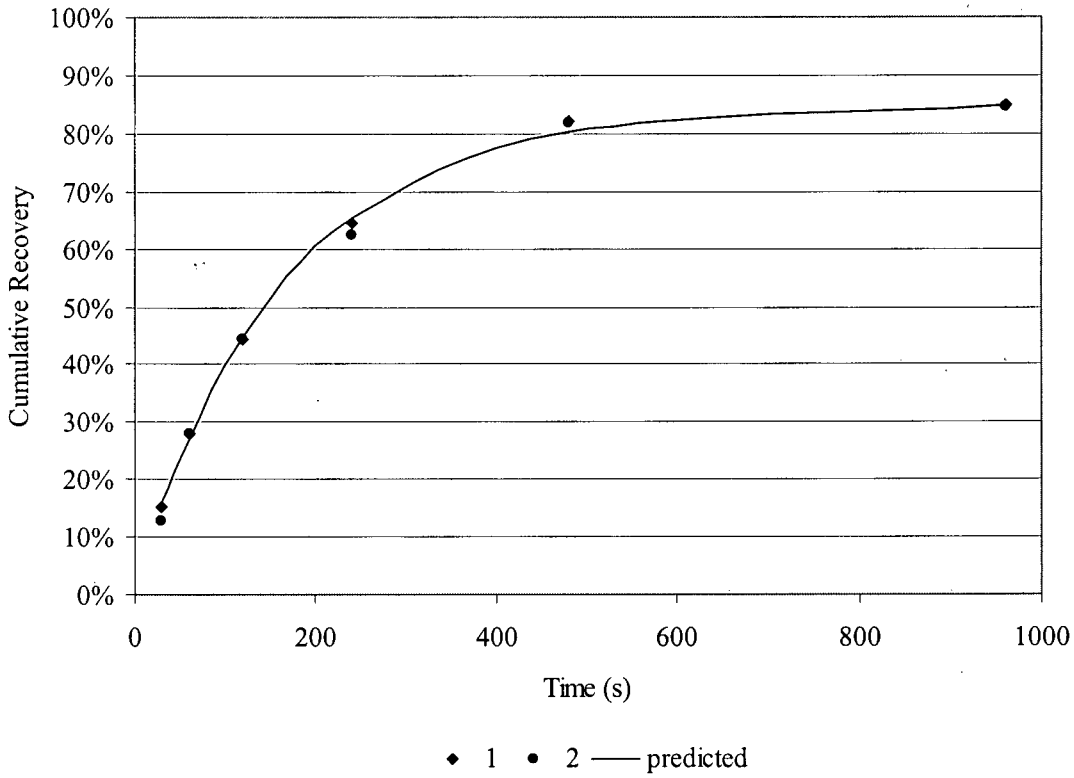


**Figure 85: Model performance on +74 μm chalcocite, "batch' column, showing cumulative recovery with time.**

The plot of model response versus test data, as rates, for both column, -44 micrometer fraction, haezelwoodite, is found in Figure 86. The equivalent time – recovery plot for the –44 haezelwoodite fraction is found in Figure 87. The –74/+44 haezelwoodite fractions are plotted in Figure 88 (rates) and Figure 89 (time-recovery). The +74 haezelwoodite fractions are plotted in Figure 90 (rates) and Figure 91 (time-recovery).

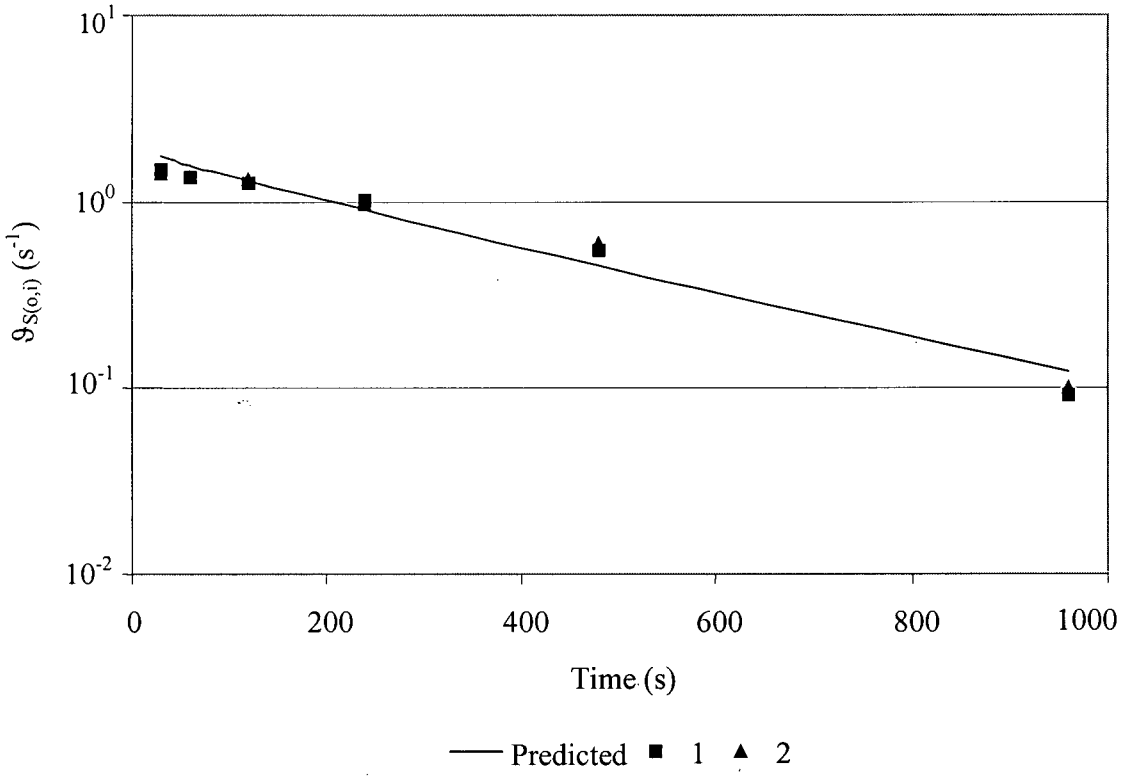


**Figure 86: Model performance on -44 μm heazelwoodite, batch column showing both tests and the predicted surface-area flux on a semi-log plot. X-axis is time in seconds while Y-axis is overflow superficial total-solids surface-area rate ($s^{-1}$).**

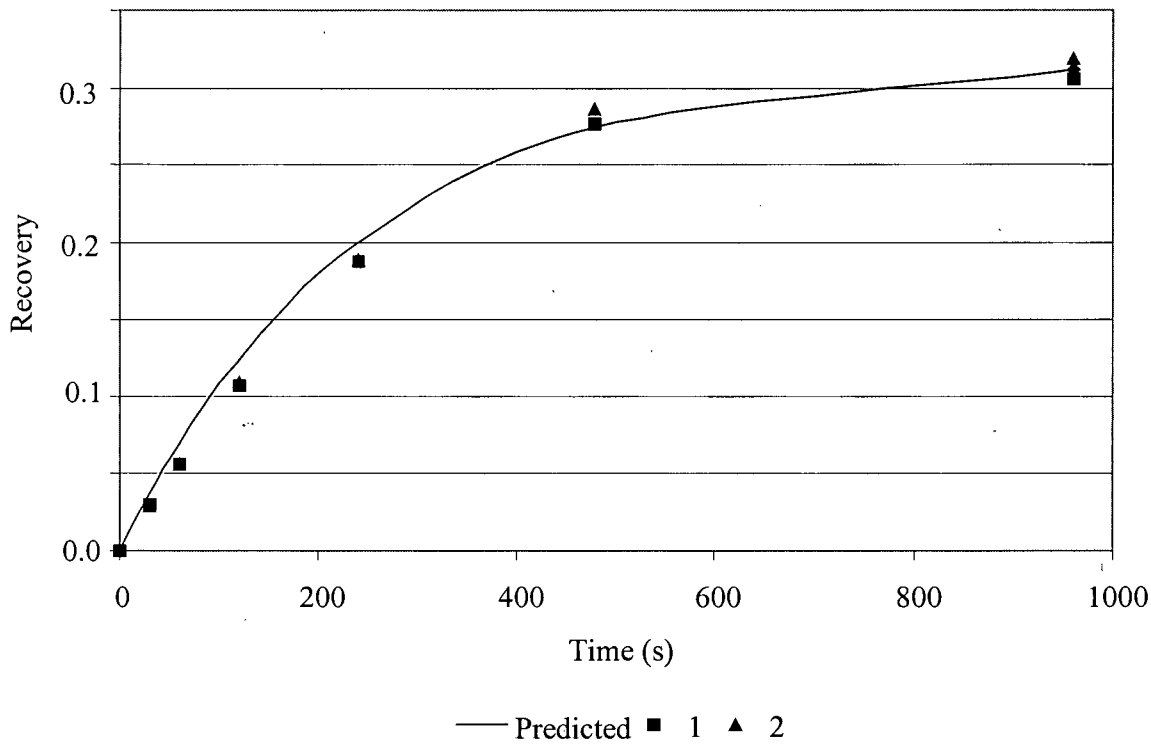


**Figure 87: Model performance on -44 μm heazelwoodite, batch column, showing cumulative recovery with time.**

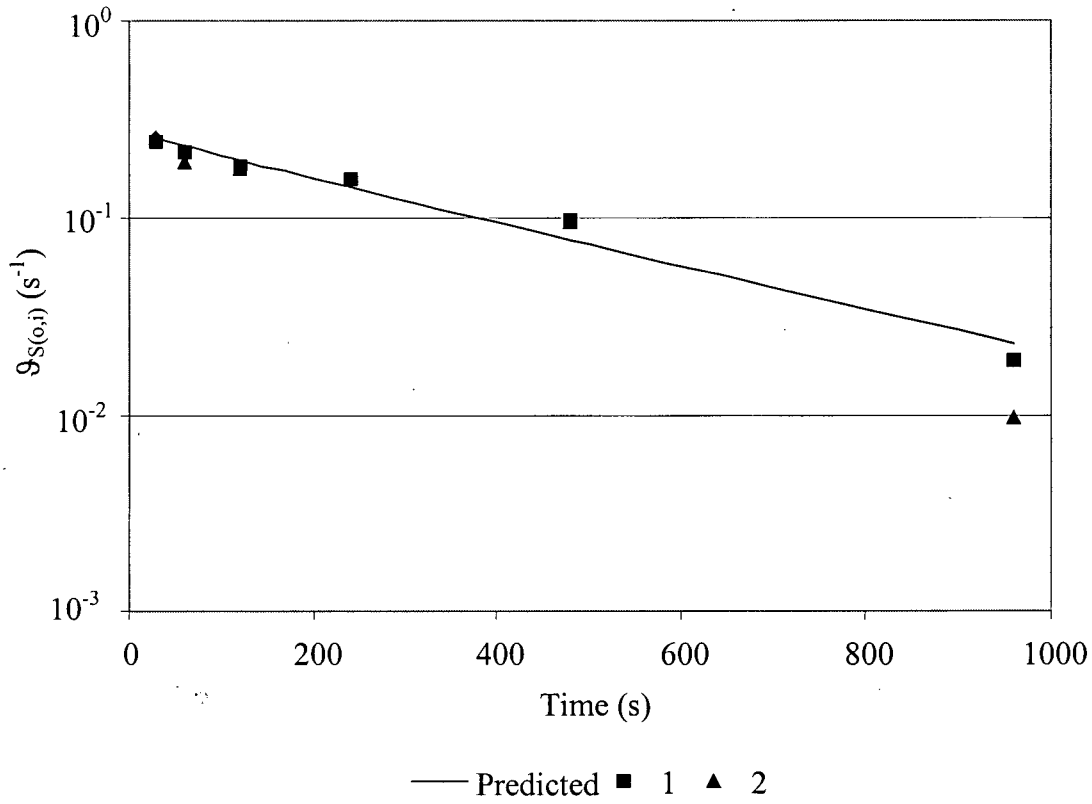


**Figure 88: Model performance on –74/44 μm heazelwoodite, batch column showing both tests and the predicted surface-area flux on a semi-log plot. X-axis is time in seconds while Y-axis is overflow superficial total-solids surface-area rate ($s^{-1}$).**

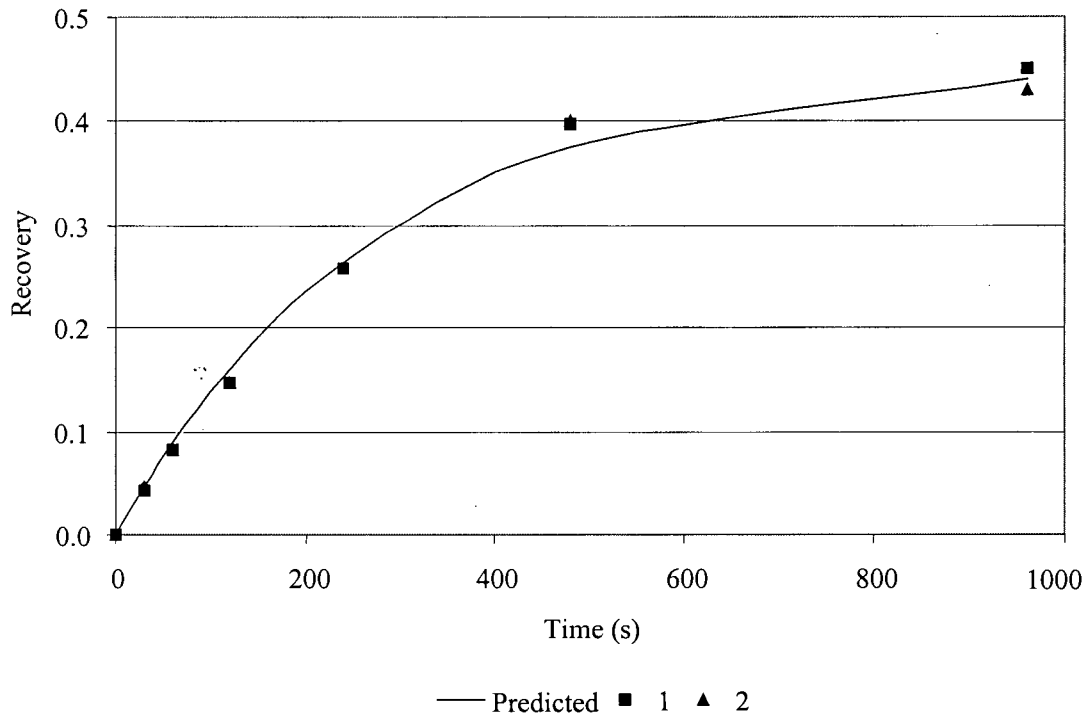


**Figure 89: Model performance on –74/+44 μm heazelwoodite, batch column, showing cumulative recovery with time.**

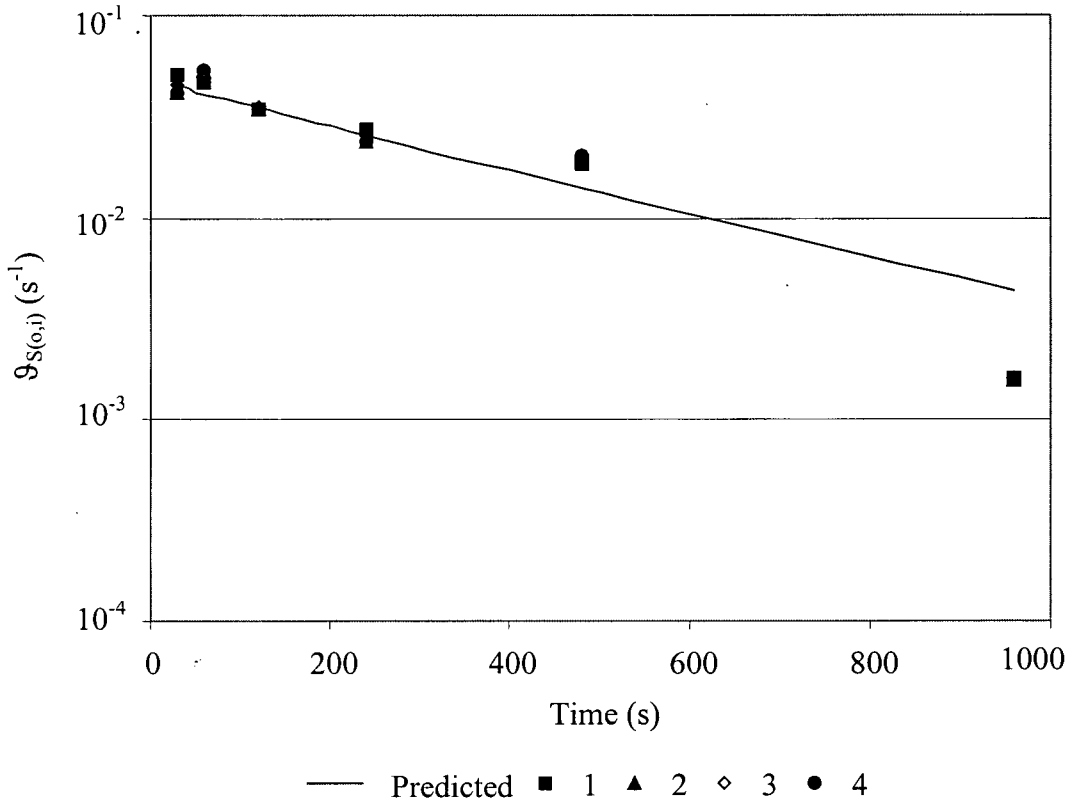


**Figure 90: Model performance on +74 μm heazelwoodite, batch column showing both tests and the predicted surface-area flux on a semi-log plot. X-axis is time in seconds while Y-axis is overflow superficial total-solids surface-area rate ($s^{-1}$).**

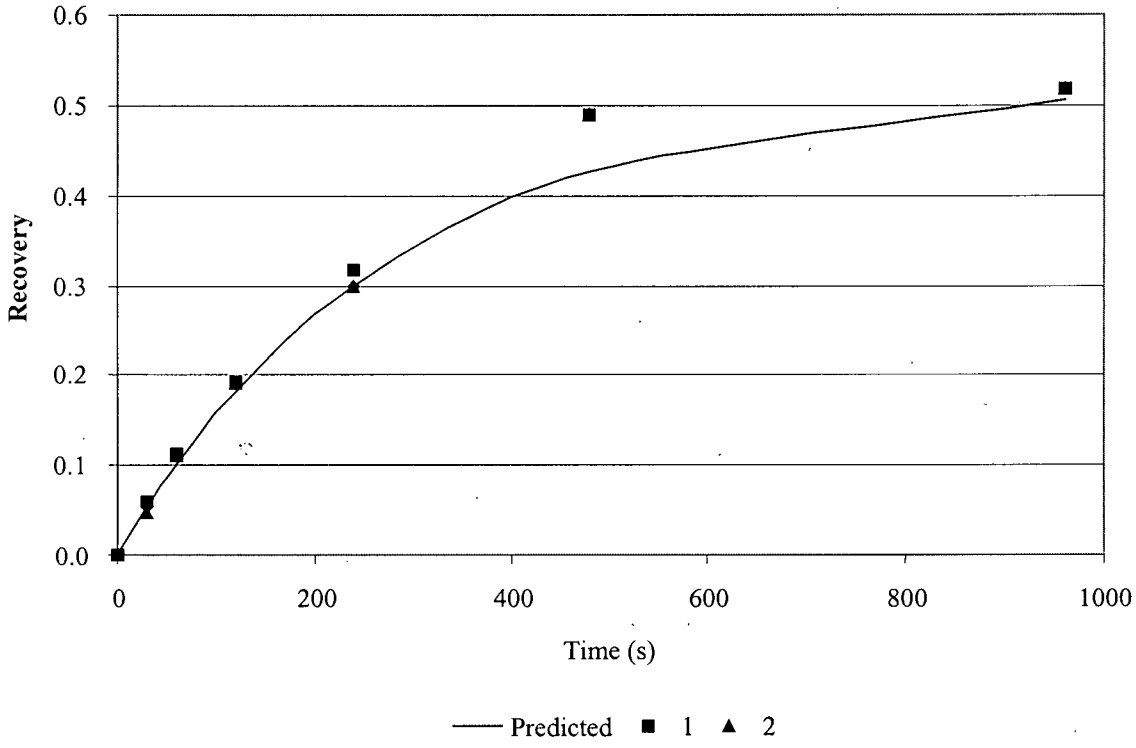


**Figure 91: Model performance on +74 μm heazelwoodite, batch column, showing cumulative recovery with time.**

The plot of model response versus test data, as rates, for both column, -44 micrometer fraction, "other", is found in Figure 92. The –74/+44 "other" fractions are plotted in Figure 93. There is no +74 "other" are plots since on a few grams of this size fraction was found.

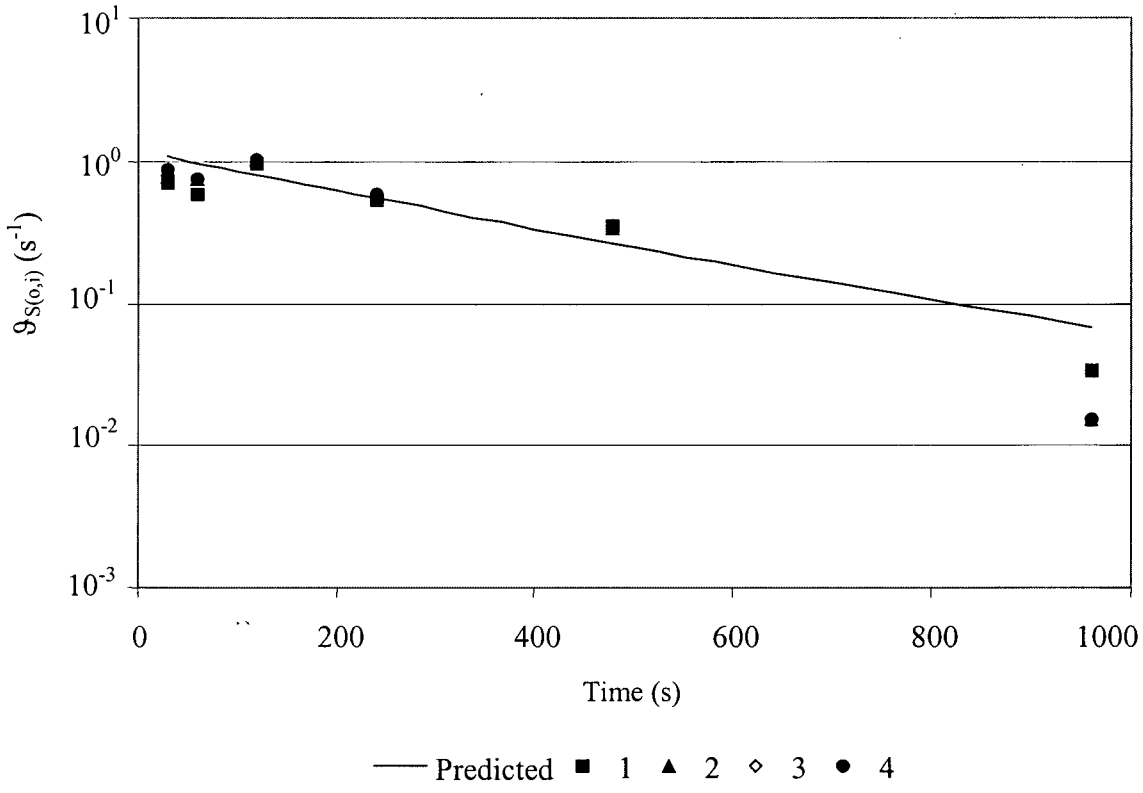


**Figure 92: Model performance on -44 μm "other", batch column showing both tests and the predicted surface-area flux on a semi-log plot. X-axis is time in seconds while Y-axis is overflow superficial total-solids surface-area rate ($s^{-1}$).**

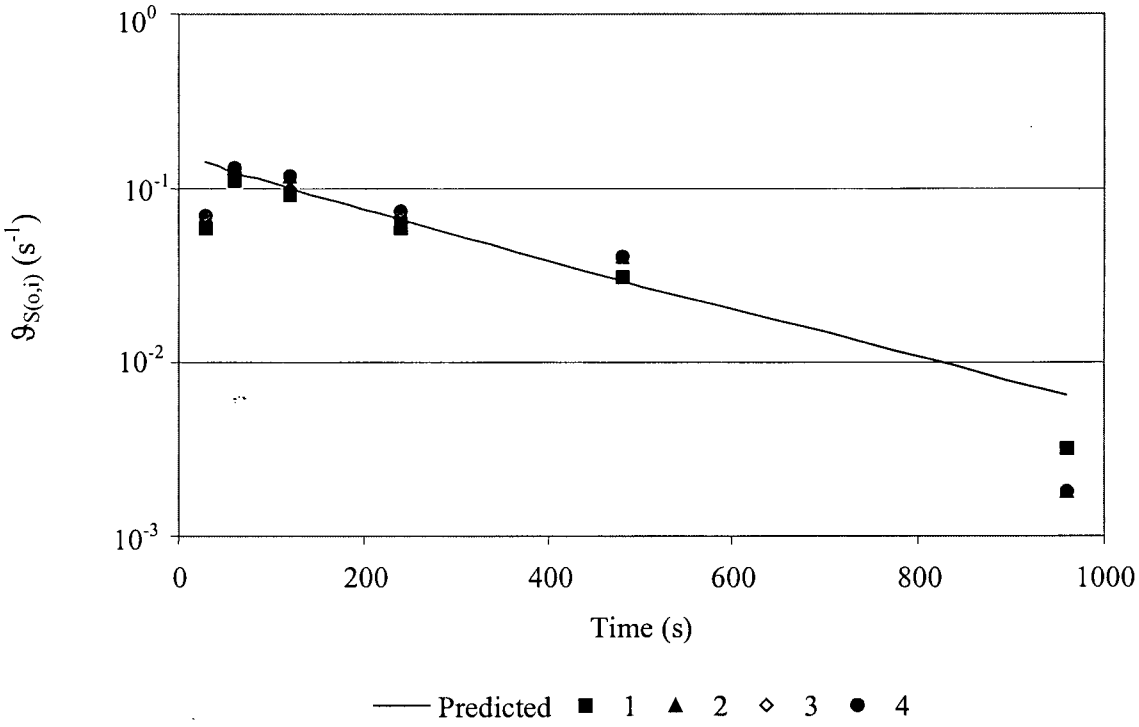


**Figure 93: Model performance on –74/+44 μm "other", batch column showing both tests and the predicted surface-area flux on a semi-log plot. X-axis is time in seconds while Y-axis is overflow superficial total-solids surface-area rate ($s^{-1}$).**

## 10.3 Quinto Data

### 10.3.1 Batch Mechanical-Cell

The overflow mass of each test is shown in Table 48, Figure 94 (linear) and Figure 95 (log-linear) as overflow mass transfer rates. The bubble diameters of each test, with time, are shown in Table 49 (Figure 96). Water overflow (Table 50) is plotted as an overflow volume transfer rate in Figure 97. The graphic carbon assays for each overflow steam and the remainders in the cell are shown in Table 52 and plotted in Figure 98.

**Table 48: Batch mechanical-cell test #1, total masses**

| Time | $M_{sO}$ [g] | | | |
|---|---|---|---|---|
| [s] | Test 1 | Test 2 | Test 3 | Test 4 |
| 60 | 250.4 | 228.6 | 222.3 | 244.1 |
| 120 | 193.0 | 163.1 | 112.7 | 171.0 |
| 240 | 248.0 | 273.3 | 286.9 | 262.3 |
| 480 | 299.4 | 209.3 | 225.9 | 235.4 |
| 960 | 453.7 | 515.4 | 484.4 | 469.7 |
| 1500 | 451.9 | 552.0 | 594.8 | 525.6 |
| Under | 8,589.2 | 8,560.4 | 8,567.8 | 8,575.0 |
| Feed | 10,485.6 | 10,502.1 | 10,494.8 | 10,483.1 |

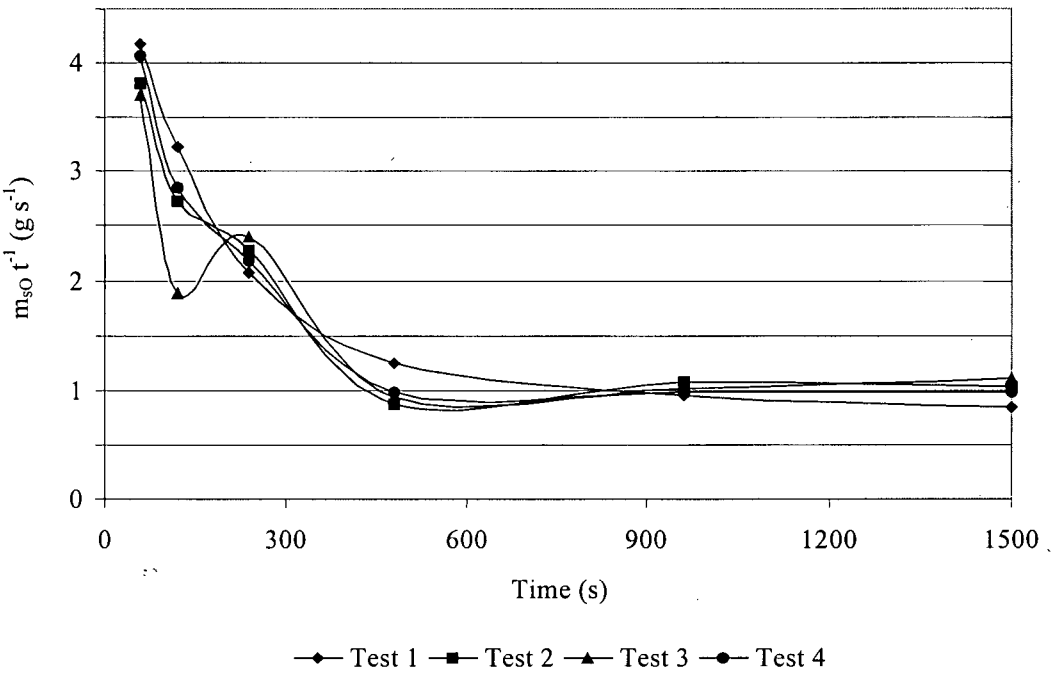


**Figure 94: Mass rate versus time for batch mechanical-cell.**

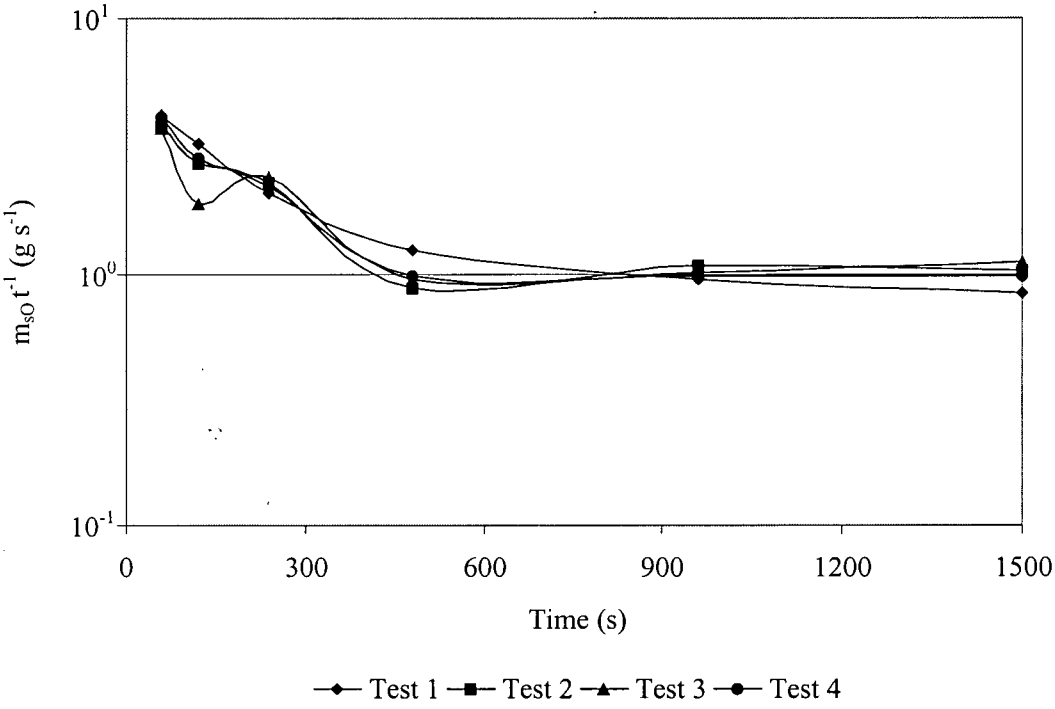


**Figure 95: Mass rate versus time for batch mechanical-cell on a log-normal scale.**

**Table 49: Batch mechanical-cell bubble diameter**

| Time | $d_b$ [cm] | | | |
|---|---|---|---|---|
| [s] | Test 1 | Test 2 | Test 3 | Test 4 |
| 60 | 0.22 | 0.20 | 0.23 | 0.22 |
| 120 | 0.22 | 0.22 | 0.23 | 0.22 |
| 240 | 0.24 | 0.24 | 0.24 | 0.24 |
| 480 | 0.26 | 0.28 | 0.27 | 0.26 |
| 960 | 0.30 | 0.28 | 0.30 | 0.30 |
| 1500 | 0.30 | 0.28 | 0.32 | 0.30 |

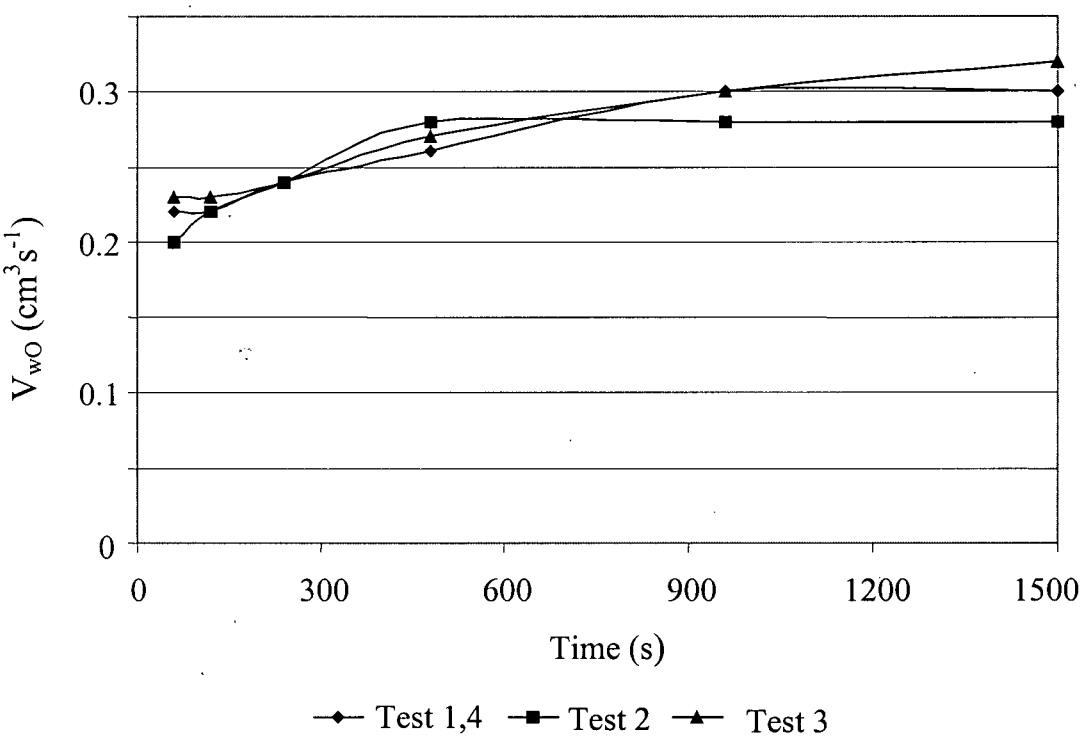


**Figure 96: Bubble diameter versus time for batch mechanical-cell.**

**Table 50: Batch mechanical-cell overflow water rate**

| Time | $V_{wO}$ [$cm^3s^{-1}$] | | | |
|---|---|---|---|---|
| [s] | Test 1 | Test 2 | Test 3 | Test 4 |
| 60 | 243.3 | 236.0 | 229.5 | 241.3 |
| 120 | 202.4 | 214.9 | 214.5 | 210.6 |
| 240 | 249.4 | 252.4 | 260.0 | 255.4 |
| 480 | 291.8 | 291.4 | 298.7 | 287.6 |
| 960 | 343.0 | 355.2 | 333.8 | 345.7 |
| 1500 | 564.2 | 556.2 | 599.6 | 582.4 |

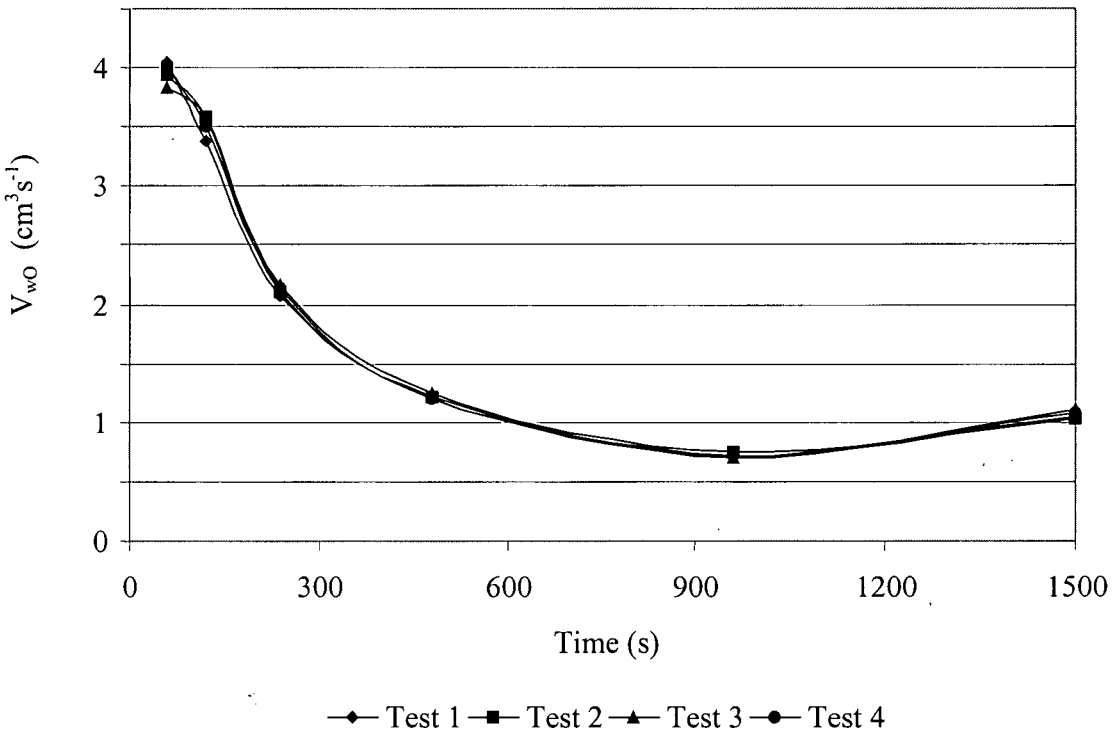


**Figure 97: Water volume transfer rate across the mechanical-cell overflow**

**Table 51: Batch mechanical-cell graphitic carbon assays (cG)**

| Time | cG % | | | |
|---|---|---|---|---|
| [s] | Test 1 | Test 2 | Test 3 | Test 4 |
| 60 | 7.3 | 7.6 | 7.3 | 7.5 |
| 120 | 8.1 | 8.1 | 8.2 | 9.3 |
| 240 | 5.2 | 5.2 | 5.4 | 5.3 |
| 480 | 3.6 | 3.6 | 3.4 | 3.5 |
| 960 | 1.9 | 1.9 | 2.1 | 2.0 |
| 1500 | 1.7 | 1.7 | 1.9 | 1.8 |
| Under | 0.9 | 0.9 | 0.8 | 0.9 |
| Feed | 1.4 | 1.4 | 1.3 | 1.4 |

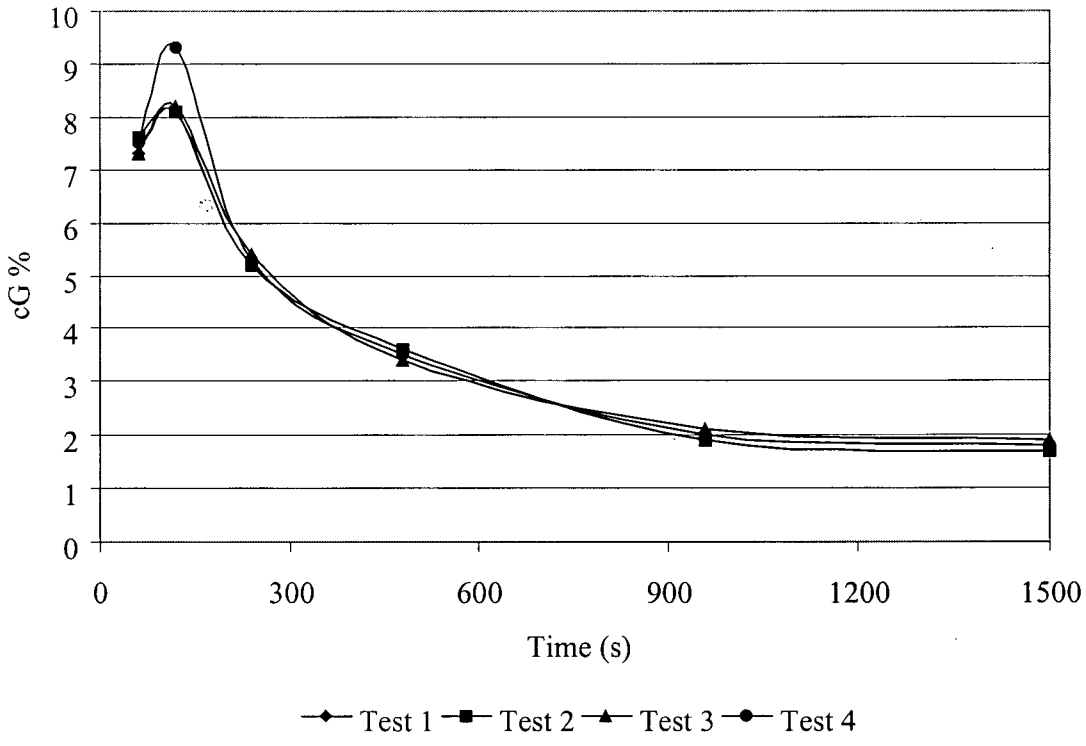


**Figure 98: Graphitic carbon (cG) versus time for the Quinto batch mechanical-cell tests.**

### 10.3.2 Batch Mechanical-Cell Performance

The performance of the batch model, on the graphite, when using the Quinto mechanical-cell, is shown by comparing the actual superficial solids-surface-area flux of graphite across the overflow ($\vartheta_{s(O,i)}$ [$s^{-1}$]) versus the response values of the model. These values are found in Table 52 and plotted in Figure 99 (normal) and Figure 100 (log-normal).

**Table 52: Quinto superficial graphite-surface-area flux to the overflow, mechanical-cell tests**

| Time | $\vartheta_{s(O,I)}$ ($s^{-1}$) | | | | |
|---|---|---|---|---|---|
| | Test #1 | Test #2 | Test #3 | Test #4 | Predicted |
| 60 | 0.99 | 0.94 | 0.88 | 0.99 | 0.93 |
| 120 | 0.86 | 0.71 | 0.50 | 0.77 | 0.80 |
| 240 | 0.36 | 0.38 | 0.42 | 0.38 | 0.55 |
| 480 | 0.14 | 0.10 | 0.10 | 0.11 | 0.37 |
| 960 | 0.06 | 0.07 | 0.07 | 0.06 | 0.26 |
| 1500 | 0.05 | 0.06 | 0.07 | 0.06 | 0.22 |

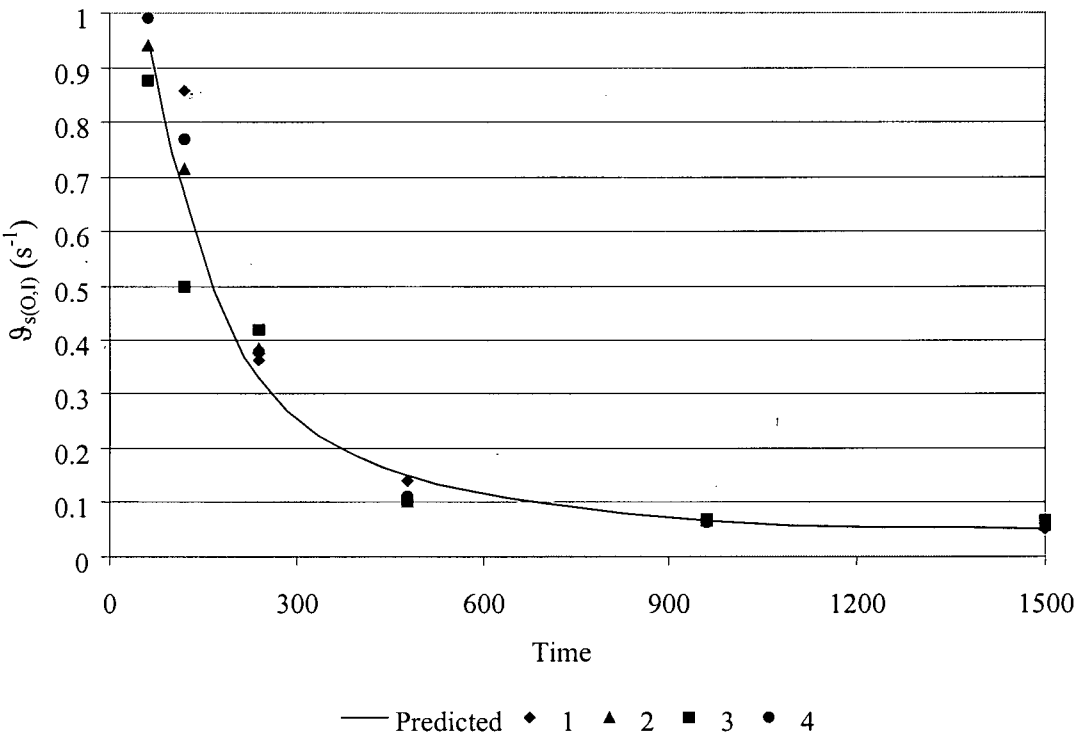


**Figure 99: Model performance on graphite showing all four tests and the predicted solids-surface-area flux on a linear plot. X-axis is time in seconds while Y-axis is superficial surface overflow rate ($s^{-1}$).**

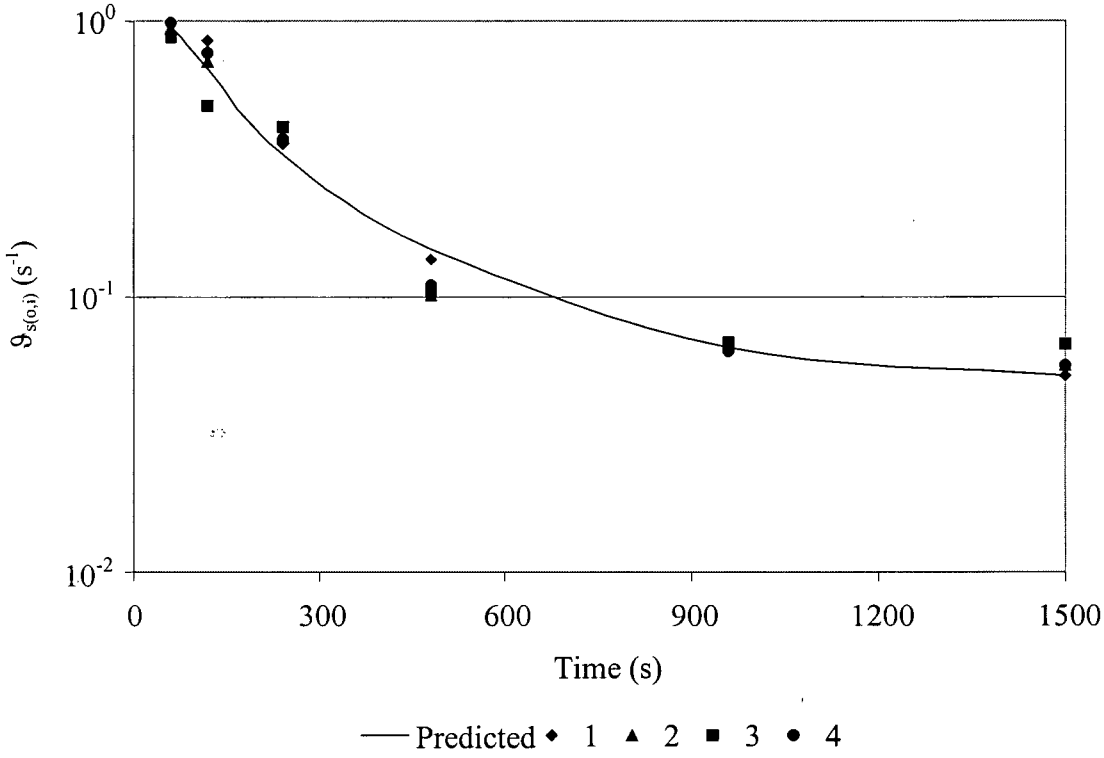


**Figure 100: Model performance graphite showing all four mechanical-cell tests and the predicted surface-area flux on a semi-log plot. X-axis is time in seconds while Y-axis is overflow superficial solids-surface-area rate ($s^{-1}$).**

### 10.3.3 **Batch Column**

Table 53 shows the mass the graphite assays for each sample, including 60, 120, 240, 480, 960 and 1,500 second intervals and the underflow or remainder sample. Feed values were determined from a sample of the comminution circuit feeding both column and pilot plant. The mass data is plotted in Figure 101 using a linear scale and in Figure 102 using log-normal scales. The graphite assays are plotted versus time in Figure 103. Table 54 shows the overflow water rates and bubble diameters of the various interval samples. The overflow water rate, with respect to time, is plotted in Figure 104 while the bubble size is plotted versus time in Figure 105.

**Table 53: Batch column total masses and graphite assays**

| Time | Test 1 | | Test 2 | |
|---|---|---|---|---|
| [s] | $m_{s,O(i)}$ [g] | cG [%] | $m_{s,O(i)}$ [g] | cG [%] |
| 60 | 16.2 | 12.6 | 15.7 | 10.3 |
| 120 | 15.2 | 11.8 | 15.0 | 9.4 |
| 240 | 27.0 | 11.6 | 25.9 | 9.1 |
| 480 | 44.0 | 10.6 | 41.9 | 8.7 |
| 960 | 66.8 | 9.8 | 68.1 | 7.6 |
| 1500 | 56.3 | 6.4 | 62.5 | 5.6 |
| Under | 3,346.9 | 1.1 | 2,788.2 | 0.9 |
| Feed | | 1.65 | | 1.45 |

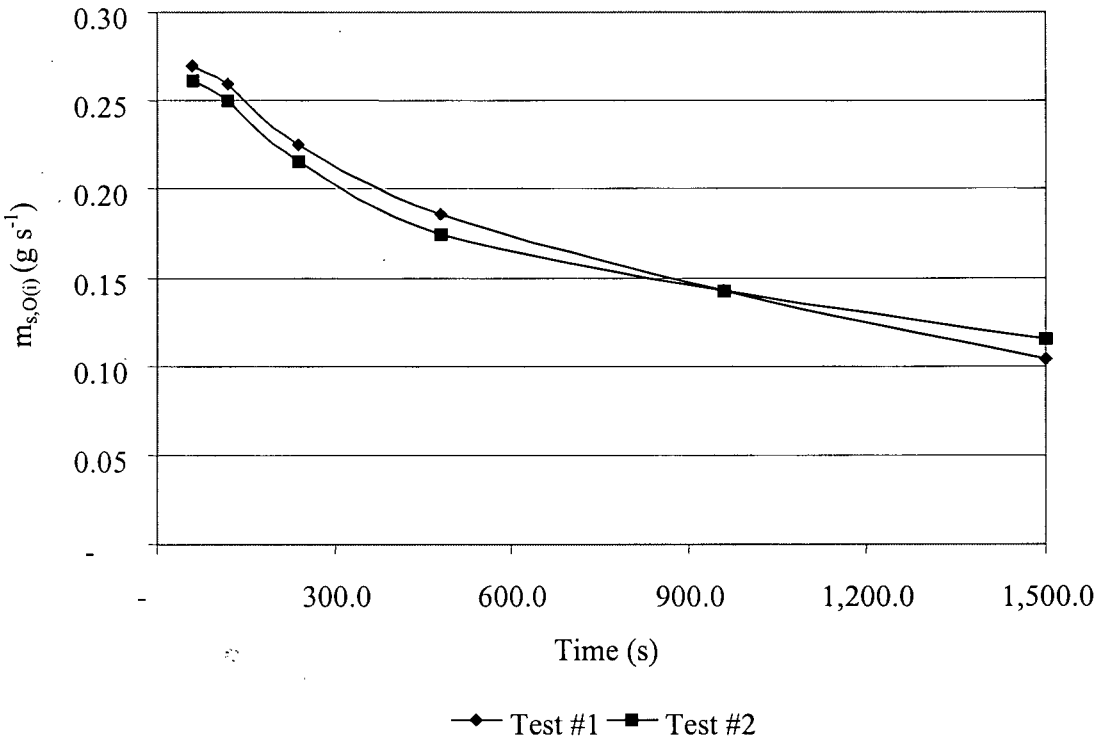


**Figure 101: Mass rate versus time for batch column cell: total masses.**

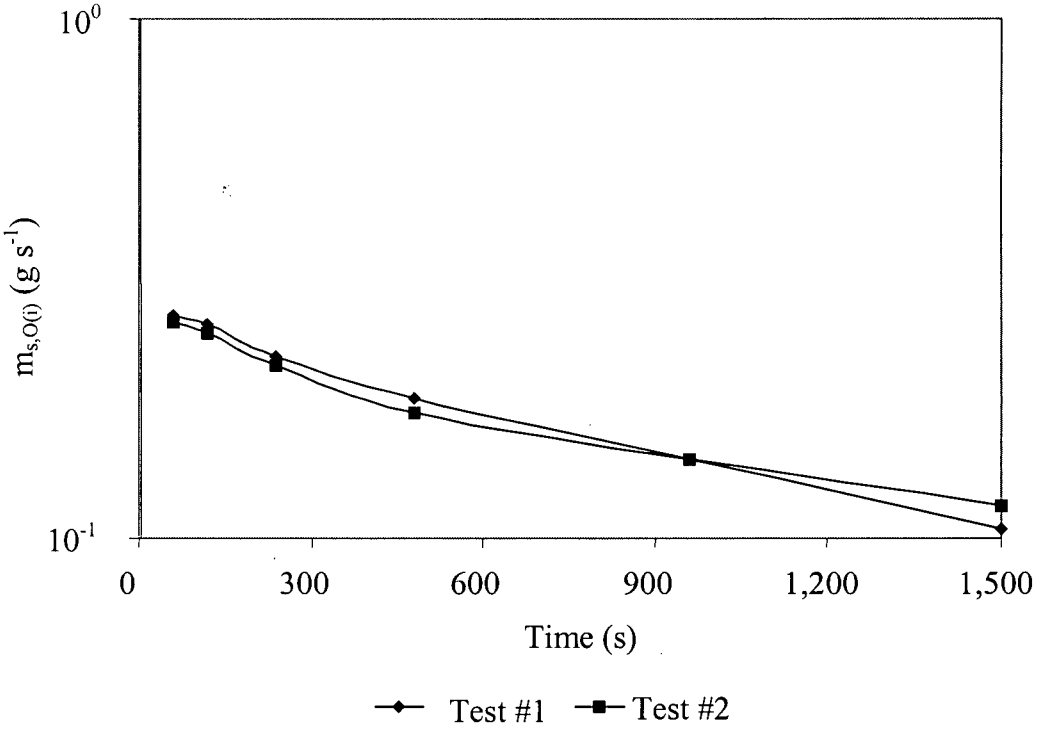


**Figure 102: Mass rate versus time for batch column, total masses, log-normal scale.**

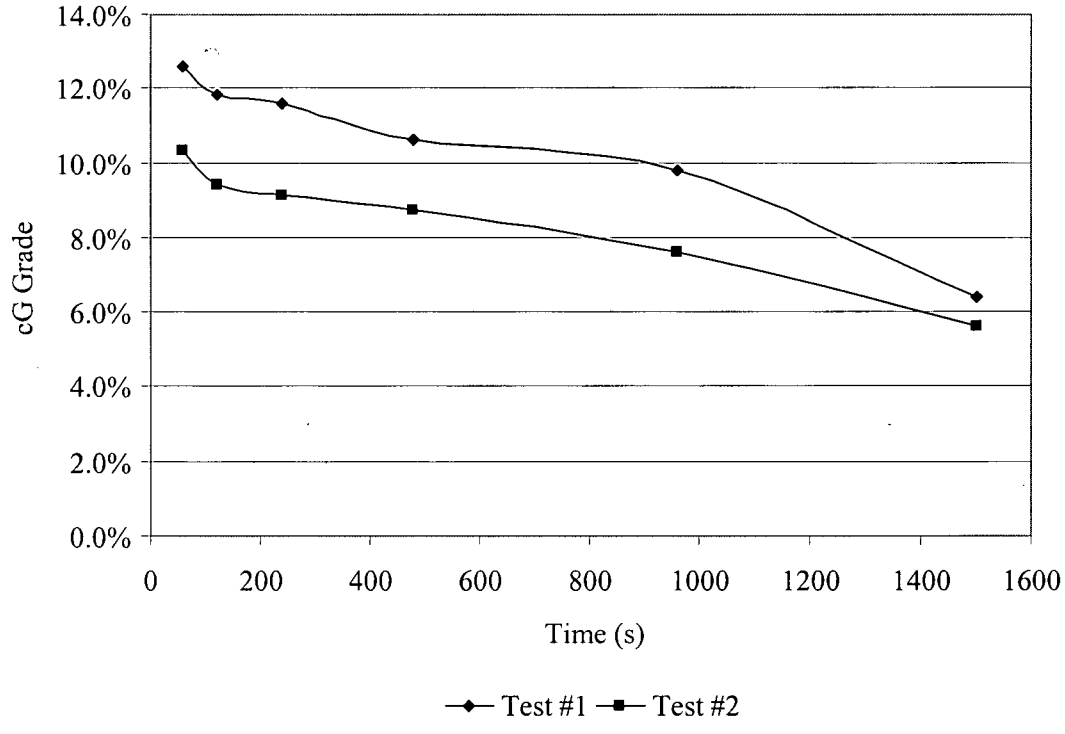


**Figure 103: Graphitic carbon (cG) versus time for the Quinto batch column tests**

**Table 54: Batch column – overflow water volume and bubble diameter**

| Time | Test 1 | | Test 2 | |
|---|---|---|---|---|
| [s] | $V_{w,O(i)\,s}$[cm$^3$] | $d_b$ [cm] | $V_{w,O(i)}$ [cm$^3$] | $d_b$ [cm] |
| 60 | 235.3 | 0.26 | 246.7 | 0.24 |
| 120 | 242.6 | 0.26 | 236.8 | 0.24 |
| 240 | 375.7 | 0.26 | 360.1 | 0.26 |
| 480 | 572.5 | 0.28 | 552.2 | 0.28 |
| 960 | 753.6 | 0.30 | 800.2 | 0.30 |
| 1500 | 625.4 | 0.32 | 636.5 | 0.30 |

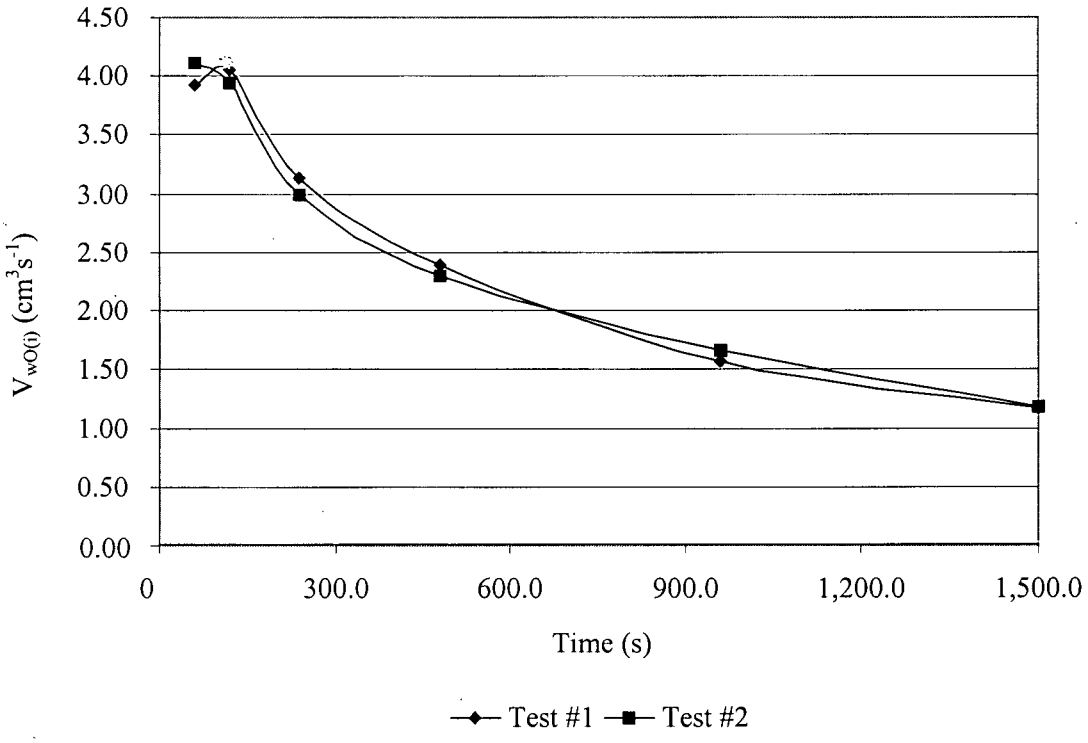


**Figure 104: Overflow water rate versus time for batch column**

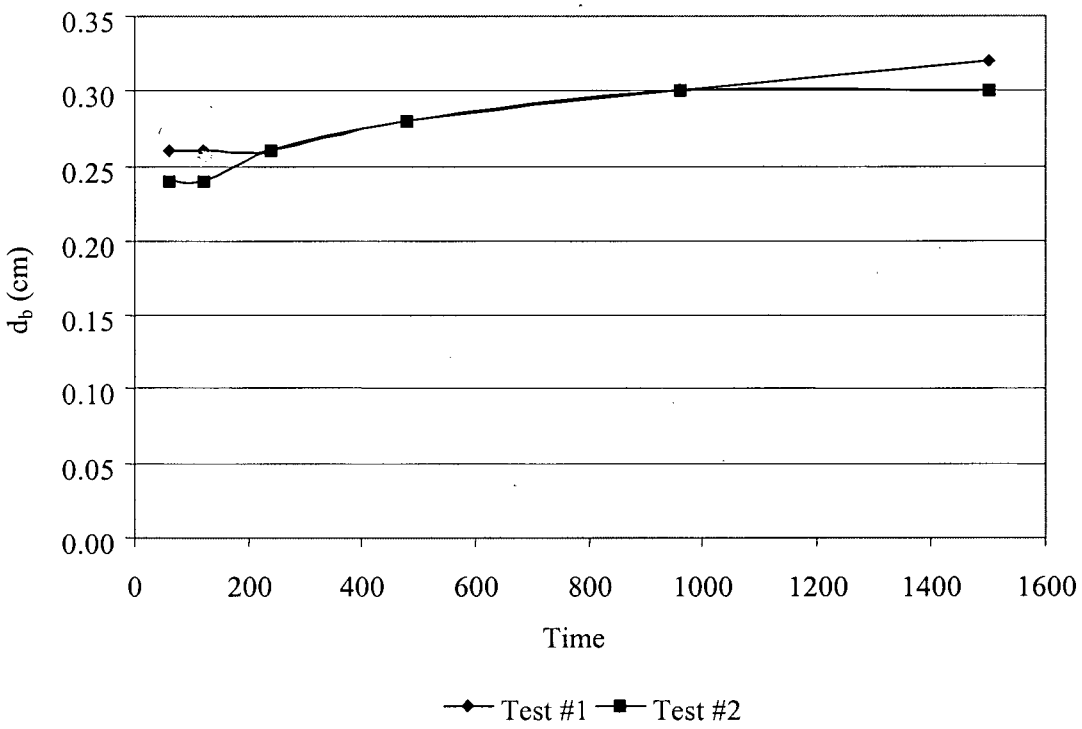


**Figure 105: Bubble size versus time for the Quinto batch column tests.**

### 10.3.4 Batch Column Performance

Table 55 shows the Quinto test data and the batch model response for both graphite and "other" fractions. This data is presented graphically in Figure 106 (originally presented as Figure 44). The comparison between the batch model response and test data for the Quinto "other" is shown in Figure 107 (originally presented as Figure 45).

**Table 55: Quinto superficial graphite-surface-area flux to the overflow, column tests**

| Time | $\vartheta_{s,O(i)}$ [$s^{-1}$] cG | | | $\vartheta_{s,O(i)}$ [$s^{-1}$] "other" | | |
|---|---|---|---|---|---|---|
| 0 | Test #1 | Test #2 | Predicted | Test #1 | Test #2 | Predicted |
| 60 | 1.97 | 1.56 | 1.71 | 1.09 | 1.09 | 1.03 |
| 120 | 1.78 | 1.36 | 1.68 | 1.06 | 1.05 | 0.99 |
| 240 | 1.51 | 1.14 | 1.37 | 0.92 | 0.91 | 0.93 |
| 480 | 1.14 | 0.88 | 0.97 | 0.77 | 0.74 | 0.82 |
| 960 | 0.81 | 0.63 | 0.57 | 0.59 | 0.61 | 0.65 |
| 1500 | 0.39 | 0.38 | 0.47 | 0.45 | 0.51 | 0.47 |

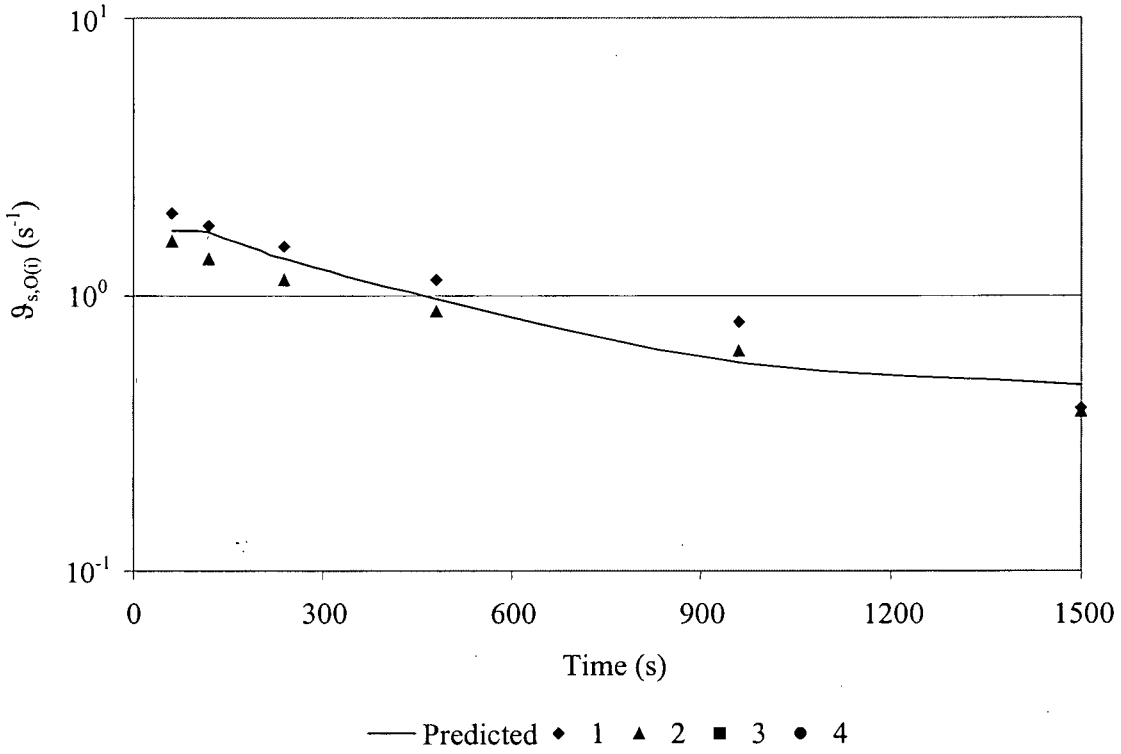


**Figure 106: Model performance on graphite showing both tests and the predicted surface-area flux on a log-linear plot. X-axis is time in seconds while Y-axis is superficial surface overflow rate ($s^{-1}$).**

There is a significant difference between the solids content of test #1 and test #2. As such, the objective function minimization will determine an average between these to solids contents.

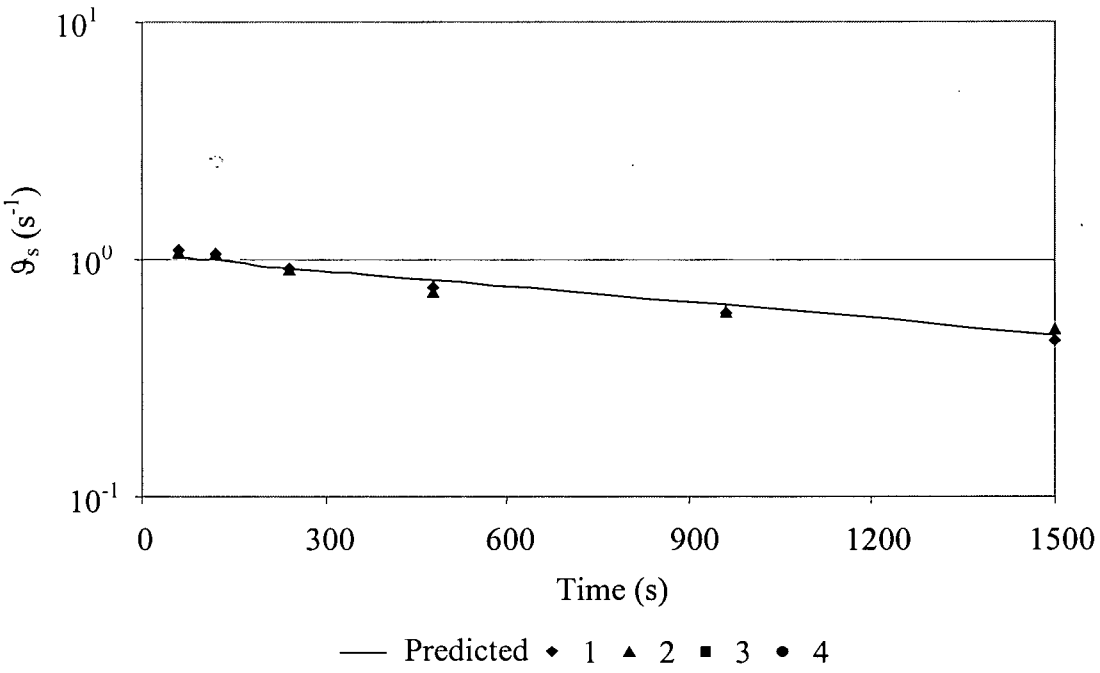


**Figure 107: Model performance "other" showing both tests and the predicted surface-area flux on a semi-log plot. X axis is time in seconds while Y axis is superficial surface overflow rate ($s^{-1}$).**

# 11 Continuous Column Tests

## 11.1 INCO Second Copper Cleaner

A 1.8 m diameter column has been used as the 2nd copper cleaner within this process. The high copper product of this cleaner is called the MK product. Reagents used in this separation are DPG (diphenylguanidine) and lime. All industrial column results are readings from the Outokumpu Courier 300 OSA system. Typical feed to this column is given in Table 56. The overflow from this industrial column, as determined by the OSA system, is shown in Table 57. The amount of overflow solids was estimated from the Wilson (1990) data (± 2% error) using the copper and nickel recoveries and the overall density of the overflow product. Underflow results are not given by Wilson (1990) but were calculated from bias and recovery data. These calculated mineral and element values, plus flow conditions are shown in Table 58.

Table 56: Feed Characteristics, 2nd Copper Cleaner, 1.8 m column (Wilson 1990)

| Test | Solids g/s | Feed % sol | Water cm/s | Copper % | Nickel % | Chalcocite % | Hazelwood % | Other % |
|---|---|---|---|---|---|---|---|---|
| 1 | 5,866 | 35.7 | 0.83 | 67.98 | 10.07 | 84.30 | 13.70 | 1.98 |
| 2 | 7,303 | 49.5 | 0.59 | 66.61 | 11.18 | 82.60 | 15.20 | 2.23 |
| 3 | 7,608 | 49.5 | 0.61 | 66.85 | 10.96 | 82.90 | 14.90 | 2.23 |
| 4 | 7,303 | 49.5 | 0.59 | 67.34 | 10.51 | 83.50 | 14.30 | 2.17 |
| 5 | 7,425 | 49.5 | 0.60 | 68.15 | 9.85 | 84.50 | 13.40 | 2.07 |
| 6 | 6,416 | 49.5 | 0.51 | 68.71 | 9.34 | 85.20 | 12.70 | 2.04 |
| 7 | 7,060 | 49.5 | 0.57 | 68.79 | 9.34 | 85.30 | 12.70 | 1.99 |
| 8 | 7,822 | 49.5 | 0.63 | 68.63 | 9.49 | 85.10 | 12.90 | 1.96 |
| 9 | 6,416 | 30.5 | 1.15 | 65.89 | 11.91 | 81.70 | 16.20 | 2.13 |
| 10 | 6,295 | 31.4 | 1.08 | 65.73 | 12.06 | 81.50 | 16.40 | 2.15 |
| 11 | 6,905 | 33.2 | 1.09 | 65.65 | 12.13 | 81.40 | 16.50 | 2.12 |
| 12 | 7,000 | 34.4 | 1.05 | 65.32 | 12.50 | 81.00 | 17.00 | 2.05 |
| 13 | 6,875 | 35.0 | 1.00 | 64.35 | 13.31 | 79.80 | 18.10 | 2.13 |
| 14 | 7,578 | 36.5 | 1.04 | 64.84 | 12.87 | 80.40 | 17.50 | 2.15 |
| 15 | 7,547 | 36.7 | 1.02 | 65.16 | 12.50 | 80.80 | 17.00 | 2.13 |
| 16 | 7,112 | 36.9 | 0.96 | 65.24 | 12.50 | 80.90 | 17.00 | 2.12 |
| 17 | 7,028 | 37.0 | 0.94 | 65.08 | 12.65 | 80.70 | 17.20 | 2.14 |
| 18 | 7,303 | 36.9 | 0.98 | 64.84 | 12.87 | 80.40 | 17.50 | 2.13 |
| 19 | 8,678 | 36.8 | 1.17 | 66.53 | 11.40 | 82.50 | 15.50 | 1.98 |
| 20 | 8,495 | 37.1 | 1.13 | 65.56 | 12.21 | 81.30 | 16.60 | 2.02 |
| 21 | 8,770 | 37.8 | 1.13 | 65.08 | 12.72 | 80.70 | 17.30 | 2.04 |
| 22 | 8,953 | 38.6 | 1.12 | 65.48 | 12.35 | 81.20 | 16.80 | 2.03 |
| 23 | 8,647 | 39.0 | 1.06 | 65.89 | 11.99 | 81.70 | 16.30 | 1.98 |
| 24 | 8,617 | 39.1 | 1.05 | 65.81 | 12.13 | 81.60 | 16.50 | 1.94 |
| 25 | 8,709 | 39.2 | 1.06 | 65.56 | 12.35 | 81.30 | 16.80 | 1.93 |
| 26 | 9,014 | 39.4 | 1.09 | 65.56 | 12.35 | 81.30 | 16.80 | 1.92 |
| 27 | 9,228 | 39.6 | 1.11 | 65.56 | 12.35 | 81.30 | 16.80 | 1.94 |

Table 57: Overflow Results of the 2nd copper cleaner 1.8 m column (Wilson 1990)

| Test | Solids g/s | Conc % Sol | Water cm/s | Copper % | Nickel % | Chalcocite % | Hazelwood % | Other % |
|---|---|---|---|---|---|---|---|---|
| 1 | 2,524 | 31.60 | 0.43 | 75.65 | 3.16 | 93.80 | 4.30 | 1.90 |
| 2 | 2,945 | 45.10 | 0.28 | 75.16 | 3.38 | 93.20 | 4.60 | 2.20 |
| 3 | 3,115 | 46.80 | 0.28 | 75.08 | 3.46 | 93.10 | 4.70 | 2.20 |
| 4 | 3,113 | 44.80 | 0.30 | 75.16 | 3.46 | 93.20 | 4.70 | 2.10 |
| 5 | 3,454 | 45.40 | 0.33 | 75.16 | 3.46 | 93.20 | 4.70 | 2.10 |
| 6 | 3,087 | 40.60 | 0.35 | 75.16 | 3.46 | 93.20 | 4.70 | 2.10 |
| 7 | 3,316 | 50.90 | 0.25 | 75.32 | 3.38 | 93.40 | 4.60 | 2.00 |
| 8 | 3,608 | 61.40 | 0.18 | 75.40 | 3.31 | 93.50 | 4.50 | 2.00 |
| 9 | 2,659 | 31.00 | 0.47 | 75.48 | 3.31 | 93.60 | 4.50 | 1.90 |
| 10 | 2,628 | 28.70 | 0.51 | 75.40 | 3.38 | 93.50 | 4.60 | 1.90 |
| 11 | 3,016 | 28.90 | 0.58 | 75.32 | 3.53 | 93.40 | 4.80 | 1.80 |
| 12 | 3,138 | 29.00 | 0.60 | 75.16 | 3.68 | 93.20 | 5.00 | 1.80 |
| 13 | 2,904 | 27.40 | 0.60 | 75.00 | 3.75 | 93.00 | 5.10 | 1.90 |
| 14 | 3,381 | 28.70 | 0.66 | 75.08 | 3.75 | 93.10 | 5.10 | 1.80 |
| 15 | 3,342 | 28.10 | 0.67 | 75.24 | 3.53 | 93.30 | 4.80 | 1.90 |
| 16 | 3,027 | 27.70 | 0.62 | 75.32 | 3.53 | 93.40 | 4.80 | 1.80 |
| 17 | 2,863 | 28.00 | 0.58 | 75.24 | 3.60 | 93.30 | 4.90 | 1.80 |
| 18 | 2,887 | 29.00 | 0.56 | 75.16 | 3.68 | 93.20 | 5.00 | 1.80 |
| 19 | 2,884 | 25.70 | 0.66 | 75.16 | 3.60 | 93.20 | 4.90 | 1.90 |
| 20 | 2,596 | 24.50 | 0.63 | 75.00 | 3.68 | 93.00 | 5.00 | 2.00 |
| 21 | 2,617 | 24.90 | 0.62 | 75.00 | 3.75 | 93.00 | 5.10 | 1.90 |
| 22 | 2,947 | 26.50 | 0.64 | 75.24 | 3.60 | 93.30 | 4.90 | 1.80 |
| 23 | 2,831 | 25.00 | 0.67 | 75.32 | 3.46 | 93.40 | 4.70 | 1.90 |
| 24 | 2,726 | 25.00 | 0.64 | 75.24 | 3.53 | 93.30 | 4.80 | 1.90 |
| 25 | 2,684 | 25.40 | 0.62 | 75.08 | 3.60 | 93.10 | 4.90 | 2.00 |
| 26 | 2,744 | 26.20 | 0.61 | 75.08 | 3.68 | 93.10 | 5.00 | 1.90 |
| 27 | 2,705 | 26.20 | 0.60 | 75.24 | 3.60 | 93.30 | 4.90 | 1.80 |

Table 58: Underflow Results of the 2nd copper cleaner 1.8 m column, calculated from Wilson (1990).

| Test | Solids g/s | Tails %sol | Water cm/s | Copper % | Nickel % | Chalcocite % | Hazelwood % | Other % |
|---|---|---|---|---|---|---|---|---|
| 1 | 3,343 | 22.6 | 0.90 | 63.0 | 15.3 | 78.1 | 20.8 | 1.1 |
| 2 | 4,358 | 30.9 | 0.77 | 61.9 | 16.4 | 76.8 | 22.4 | 0.9 |
| 3 | 4,494 | 30.9 | 0.79 | 62.0 | 16.1 | 76.9 | 22.0 | 1.2 |
| 4 | 4,190 | 30.4 | 0.76 | 61.9 | 15.8 | 76.7 | 21.4 | 1.8 |
| 5 | 3,972 | 29.2 | 0.76 | 62.1 | 15.4 | 77.0 | 21.0 | 2.0 |
| 6 | 3,330 | 28.6 | 0.65 | 61.8 | 14.8 | 76.6 | 20.1 | 3.3 |
| 7 | 3,742 | 28.3 | 0.75 | 62.6 | 14.6 | 77.6 | 19.9 | 2.6 |
| 8 | 4,215 | 28.3 | 0.84 | 63.2 | 14.8 | 78.4 | 20.1 | 1.5 |
| 9 | 3,758 | 19.9 | 1.19 | 59.4 | 18.0 | 73.6 | 24.5 | 1.9 |
| 10 | 3,667 | 20.7 | 1.10 | 58.8 | 18.3 | 73.0 | 24.8 | 2.2 |
| 11 | 3,890 | 12.7 | 2.09 | 58.6 | 18.8 | 72.7 | 25.6 | 1.8 |
| 12 | 3,859 | 22.6 | 1.04 | 57.9 | 19.7 | 71.8 | 26.7 | 1.5 |
| 13 | 3,971 | 23.5 | 1.01 | 57.3 | 20.3 | 71.1 | 27.6 | 1.3 |
| 14 | 4,197 | 2.0 | 1.05 | 56.6 | 20.2 | 70.2 | 27.5 | 2.3 |
| 15 | 4,206 | 24.1 | 1.04 | 57.5 | 19.7 | 71.3 | 26.7 | 2.0 |
| 16 | 4,093 | 24.4 | 1.00 | 58.0 | 19.1 | 71.9 | 26.0 | 2.1 |
| 17 | 4,165 | 24.7 | 1.00 | 57.8 | 18.9 | 71.7 | 25.6 | 2.6 |
| 18 | 4,416 | 24.8 | 1.05 | 57.7 | 18.9 | 71.5 | 25.7 | 2.8 |
| 19 | 5,794 | 27.5 | 1.20 | 62.4 | 15.3 | 77.4 | 20.8 | 1.8 |
| 20 | 5,899 | 28.3 | 1.17 | 62.0 | 16.0 | 76.9 | 21.7 | 1.4 |
| 21 | 6,153 | 29.0 | 1.18 | 60.4 | 16.5 | 74.9 | 22.5 | 2.6 |
| 22 | 6,007 | 28.9 | 1.16 | 60.3 | 16.6 | 74.8 | 22.6 | 2.6 |
| 23 | 5,816 | 29.3 | 1.10 | 61.3 | 16.1 | 76.1 | 21.9 | 2.0 |
| 24 | 5,891 | 29.5 | 1.10 | 61.5 | 16.0 | 76.2 | 21.8 | 2.0 |
| 25 | 6,025 | 29.9 | 1.11 | 61.4 | 16.1 | 76.1 | 21.9 | 2.0 |
| 26 | 6,270 | 30.0 | 1.15 | 61.4 | 16.1 | 76.2 | 21.9 | 2.0 |
| 27 | 6,523 | 30.5 | 1.17 | 61.7 | 15.8 | 76.6 | 21.5 | 20 |

## 11.2 Quinto Pilot Column

Performance of the Quinto pilot column operating in closed circuit with a scavenger floating graphite is shown in Table 59. Graphite assays were determined using the Leco furnace. Feed solids were assumed to be equal to the batch column feed which was taken as a thief stream of the pilot column feed. Overflow and underflow solids content where calculated using the graphite assays.

**Table 59: Quinto Continuous Pilot Column Performance – Solids Balance**

| Test | Feed | | Overflow | | Underflow | | |
|---|---|---|---|---|---|---|---|
| | Solids | Grade | Solids | Grade | Solids | Grade | Recovery |
| | $g\ s^{-1}$ | % | $g\ s^{-1}$ | % | $g\ s^{-1}$ | % | % |
| Test #1 | 517 | 1.4 | 15 | 15.5 | 502 | 0.1 | 32 |
| Test #2 | 610 | 1.4 | 25 | 15.4 | 585 | 0.08 | 45 |

The liquid balance (Table 60) around the Quinto pilot column was calculated using the liquid contents of the samples and calculated solids balance.

**Table 60 Quinto Continuous Pilot Column Performance – Liquid Balance**

| Test | Feed | Overflow | Underflow | Bias | Wash |
|---|---|---|---|---|---|
| | $cm^3\ s^{-1}$ | $cm^3\ s^{-1}$ | $cm^3\ s^{-1}$ | $cm^3\ s^{-1}$ | $cm^3\ s^{-1}$ |
| Test #1 | 1119 | 53.3 | 1151.4 | 32.4 | 85.7 |
| Test #2 | 1089 | 78.5 | 1098.2 | 9.1 | 87.6 |

A partial schematic drawing of the Quinto pilot scale column is shown in Figure 108.

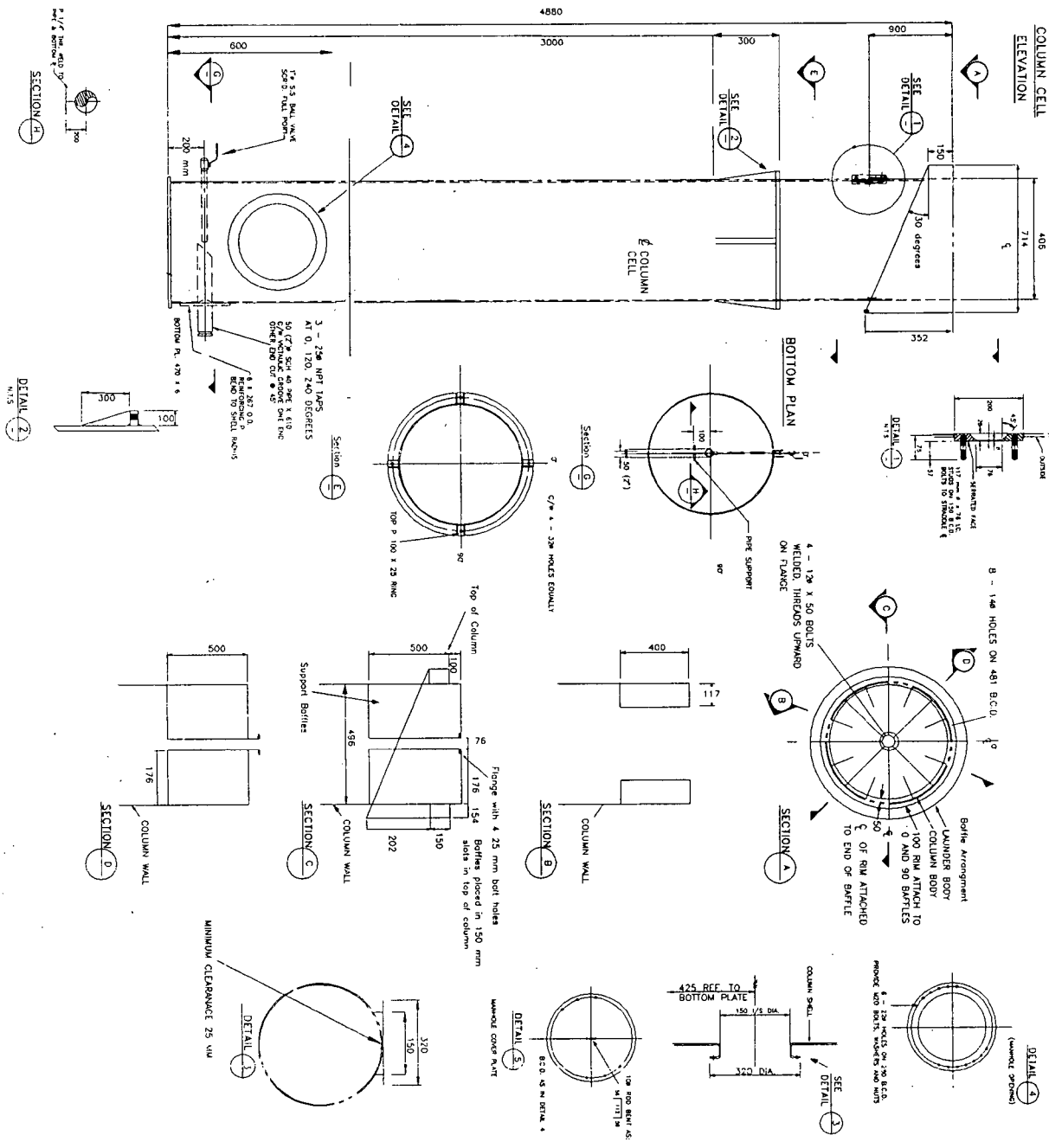


**Figure 108: Partial construction drawings of the Quinto pilot-scale column cell**

# 12 Particle Size Analysis

## 12.1 Particle Distribution

### 12.1.1 Introduction

There are many ways in which a particle size distribution may be characterized mathematically. Two possible ways are the Gate-Gaudin-Schuhmann (Equation 222) and Rosin-Rammler (Equation 223) distributions.

$$\bar{y}_i = \left(\frac{x_i}{\bar{x}_i}\right)^n \qquad \text{Equation 222}$$

$$\bar{y}_i = 1 - e^{-\left(\frac{x_i}{\bar{x}_i}\right)^\beta} \qquad \text{Equation 223}$$

In Equation 80, "$\bar{x}_i$" is a measure of the average particle size and is known as the size modulus and "β" is a measure of the spread of sizes and is known as the distribution modulus. The Gates-Gaudin-Schuhmann model uses the empirical exponential "n".

### 12.1.2 Quinto Overflow

#### 12.1.2.1 Introduction

The Quinto overflow stream particle size data was examined using both non-linear regression and linear regression after transforming the data using both the Rosin-Rammler and Gates-Gaudin-Schuhmann models of particle size.

#### 12.1.2.2 Rosin-Rammler Non-Linear Method

The Quinto overflow was tested in a Malvern particle size analyzer. This information is presented (Table 61) as a particles size; "$x_i$" [micrometers] and the volume of solids, as a fraction, that lie within the band bounded by that size and the size smaller.

**Table 61: Quinto Overflow Size Class Data and Rosin-Rammler Predicted Values**

| Particle Size $x_i$ | Volume Within Band | Cumulative Measured $y_i$ | Cumulative Predicted $\hat{y}_i$ | Unweighted Residuals $y_i - \hat{y}_i$ | Weighted Residuals $\hat{y}_i(y_i - \hat{y}_i)$ |
|---|---|---|---|---|---|
| 77.5 | 0 | 1.00 | 1.00 | 0.00 | 0.00 |
| 66.9 | 0.001 | 1.00 | 1.00 | 0.00 | 0.00 |
| 57.7 | 0.001 | 1.00 | 1.00 | 0.00 | 0.00 |
| 49.8 | 0.003 | 1.00 | 1.00 | 0.00 | 0.00 |
| 42.9 | 0.006 | 0.99 | 1.00 | -0.01 | -0.01 |
| 37.1 | 0.010 | 0.98 | 1.00 | -0.02 | -0.02 |
| 32 | 0.011 | 0.97 | 0.99 | -0.02 | -0.02 |
| 27.6 | 0.022 | 0.95 | 0.97 | -0.02 | -0.02 |
| 23.9 | 0.035 | 0.91 | 0.94 | -0.03 | -0.02 |
| 20.5 | 0.044 | 0.87 | 0.89 | -0.02 | -0.02 |
| 17.7 | 0.059 | 0.81 | 0.83 | -0.02 | -0.02 |
| 15.3 | 0.065 | 0.74 | 0.76 | -0.01 | -0.01 |
| 13.2 | 0.069 | 0.67 | 0.68 | -0.00 | -0.00 |
| 11.4 | 0.067 | 0.61 | 0.60 | 0.01 | 0.01 |
| 9.8 | 0.060 | 0.55 | 0.51 | 0.03 | 0.02 |
| 8.5 | 0.066 | 0.48 | 0.44 | 0.04 | 0.02 |
| 7.3 | 0.074 | 0.41 | 0.37 | 0.04 | 0.01 |
| 6.3 | 0.077 | 0.33 | 0.31 | 0.02 | 0.01 |
| 5.4 | 0.069 | 0.26 | 0.26 | 0.01 | 0.00 |
| 4.7 | 0.056 | 0.21 | 0.21 | -0.01 | -0.00 |
| 4.1 | 0.051 | 0.15 | 0.18 | -0.02 | -0.00 |
| 3.5 | 0.043 | 0.11 | 0.14 | -0.03 | -0.00 |
| 3 | 0.031 | 0.08 | 0.11 | -0.03 | -0.00 |
| 2.6 | 0.024 | 0.06 | 0.09 | -0.04 | -0.00 |
| 2.2 | 0.019 | 0.04 | 0.07 | -0.04 | -0.00 |
| 1.9 | 0.017 | 0.02 | 0.06 | -0.04 | -0.00 |

The cumulative fraction passing the size "$x_i$", as measured, is "$y_i$". These values of "$x_i$" and "$y_i$" where fit using the simplex method of non-linear regression to Equation 80 – the Weibull or Rosin – Rammler function. The response of this function is the predicted fraction passing; "$\hat{y}_i$", at size "i".

The difference between the measured values and those predicted by the Rosin-Rammler model; $(y_i - \hat{y}_i)$, are the un-weighted residuals. The sum of these un-weighted residuals is minimized by the simplex method. These values, for the Quinto overflow size class data,

along with weighted residuals are found in Table 61. Both the measured and predicted fraction finer are plotted against particle size in Figure 109. In this non-linear regression, "$\bar{x}_i$" = 12.181 and $\beta = 1.503$ and an $\eta^2$ or eta squared value of 0.997.

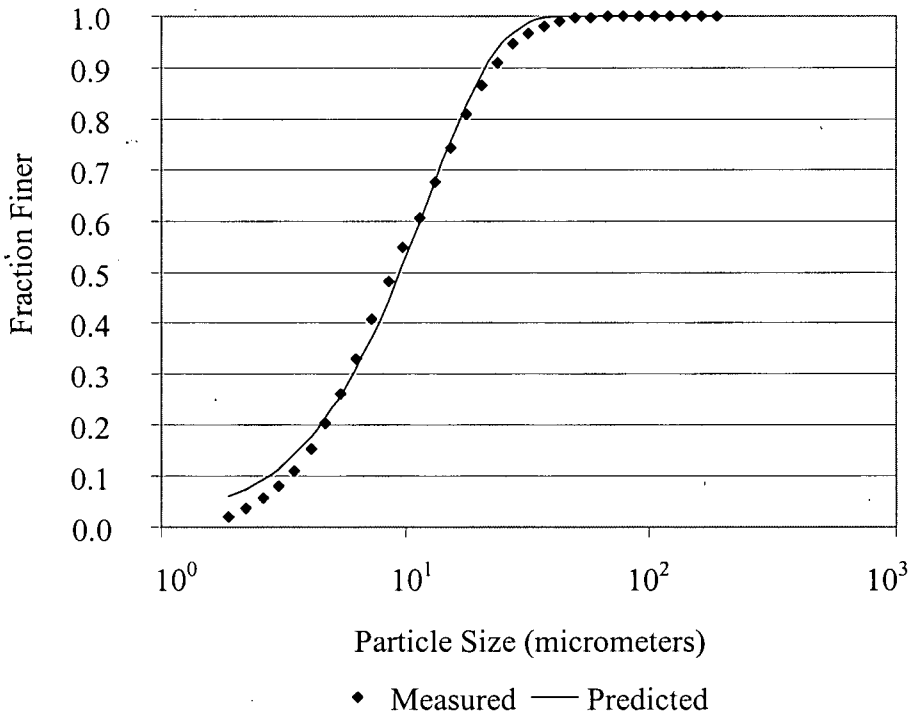


**Figure 109: Quinto overflow size class data and Weibull distribution predicted size distribution**

The residuals produced by the difference between measured and predicted fraction finer are shown in Figure 110. This figure shows that the residuals are not randomly distributed, however, the Weibull distrubtion is still an accurate predictor of the particle size distribution.

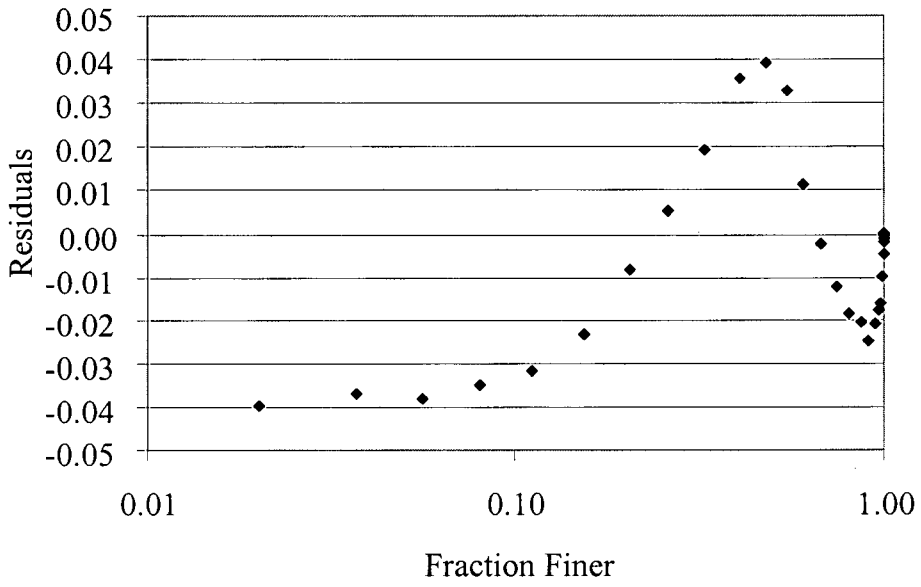


**Figure 110: Quinto overflow size class data Wiebull distribution un-weighted residuals**

This residual data may also be presented as weighted residuals, as shown in Figure 111, however, this presentation shows similar results to the un-weighted residuals in this case.

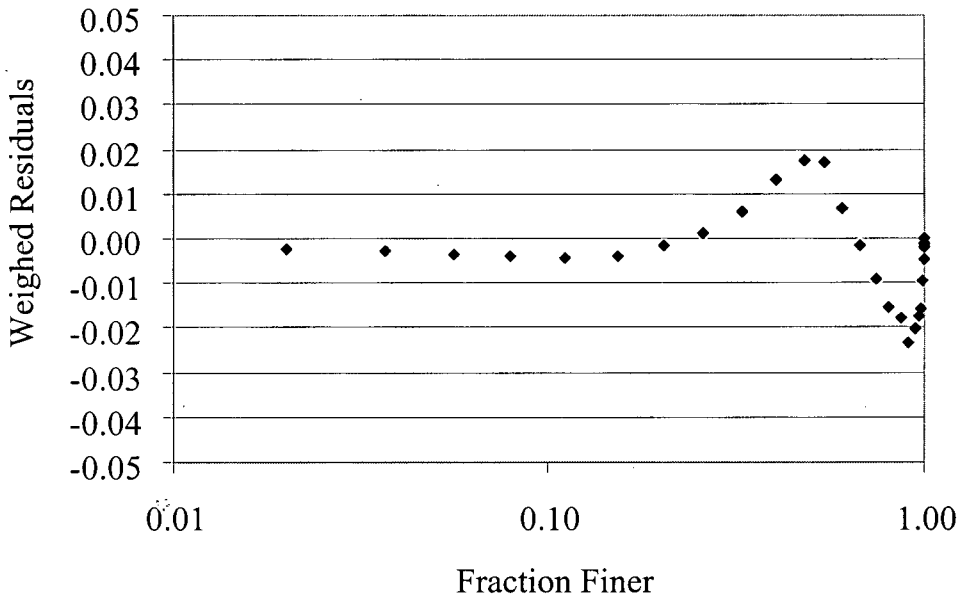


**Figure 111: Quinto overflow size class data Wiebull distribution weighted residuals**

The non-linear correlation coefficient; "$\eta^2$", can be determined from this information by use of Equation 224 where "$\bar{y}_i$" is the average fraction passing. "$\eta^2$" will be equal to $r^2$ when the relationship is linear. If the relationship is not linear then "$\eta^2$" will be larger than $r^2$.

$$\eta^2 = 1 - \frac{\sum (y_i - \hat{y}_i)^2}{\sum (y_i - \bar{y}_i)^2} \qquad \text{Equation 224}$$

In the Quinto overflow example the "$\eta^2$" values of 0.997 means that there is a very strong correlation between the measured and predicted values.

### 12.1.2.3 Rosin-Rammler Linear Method

These statistics may also be determined by linearizing the Weibull function by using logs (ln). This linearization is found in Equation 225.

$$\ln\left(-\ln\left[1 - \bar{y}_i\right]\right) = \beta \ln x_i - \beta \ln \eta \qquad \text{Equation 225}$$

This equation is analogous to the linear equation defined in Equation 226 where "y" is the left side of Equation 225, "ax" is equivalent to "$\beta \mathbf{ln} x_i$" and b is equivalent to "$\beta \ln \bar{x}$".

$$y = ax + b \qquad \text{Equation 226}$$

The slope of Equation 226; "a" may be calculated using Equation 227 where "n" is the number of samples and both "x" and "y" are those of Equation 226.

$$a = \beta = \frac{n\sum_{i=1}^{n} x_i y_i - \sum_{i=1}^{n} x_i \sum_{i=1}^{n} y_i}{n\sum_{i=1}^{n} x_i^2 - \left(\sum_{i=1}^{n} x_i\right)^2} \qquad \text{Equation 227}$$

The intercept of Equation 226; "b" may be calculated using Equation 228.

$$b = -\beta \ln \eta = \frac{\sum_{i=1}^{n} y_i - a\sum_{i=1}^{n} x_i}{n} \qquad \text{Equation 228}$$

Using Quinto overflow as an example:

Table 62 shows the size; "$X_i$" and the fraction finer; "$Y_i$" converted to natural log equivalents "$x_i$" and "$y_i$" where "$x_i$" is the natural log of "Xi" and "yi" is found using the left side of Equation 225.

**Table 62: Linearization of Quinto Data and Statistical Calculations: "X" and "Y" are non-linear data while "x" and "y" are linearlized data.**

| $X_i$ | $Y_i$ | $x_i$ | $y_i$ | $x_i^2$ | $y_i^2$ | xy |
|---|---|---|---|---|---|---|
| 42.9 | 0.99 | 3.759 | 1.527 | 14.129 | 2.332 | 5.740 |
| 37.1 | 0.98 | 3.614 | 1.364 | 13.058 | 1.861 | 4.929 |
| 32 | 0.97 | 3.466 | 1.255 | 12.011 | 1.574 | 4.348 |
| 27.6 | 0.95 | 3.318 | 1.097 | 11.008 | 1.204 | 3.640 |
| 23.9 | 0.91 | 3.174 | 0.879 | 10.074 | 0.772 | 2.789 |
| 20.5 | 0.87 | 3.020 | 0.713 | 9.123 | 0.508 | 2.154 |
| 17.7 | 0.81 | 2.874 | 0.507 | 8.257 | 0.257 | 1.458 |
| 15.3 | 0.74 | 2.728 | 0.298 | 7.441 | 0.089 | 0.813 |
| 13.2 | 0.67 | 2.580 | 0.103 | 6.658 | 0.011 | 0.266 |
| 11.4 | 0.61 | 2.434 | -0.060 | 5.922 | 0.004 | -0.146 |
| 9.8 | 0.55 | 2.282 | -0.225 | 5.209 | 0.051 | -0.514 |
| 8.5 | 0.48 | 2.140 | -0.425 | 4.580 | 0.180 | -0.909 |
| 7.3 | 0.41 | 1.988 | -0.639 | 3.952 | 0.409 | -1.271 |
| 6.3 | 0.33 | 1.841 | -0.915 | 3.388 | 0.837 | -1.684 |
| 5.4 | 0.26 | 1.686 | -1.200 | 2.844 | 1.441 | -2.024 |
| 4.7 | 0.21 | 1.548 | -1.445 | 2.395 | 2.088 | -2.236 |
| 4.1 | 0.15 | 1.411 | -1.817 | 1.991 | 3.301 | -2.564 |
| 3.5 | 0.11 | 1.253 | -2.150 | 1.569 | 4.621 | -2.693 |
| 3 | 0.08 | 1.099 | -2.484 | 1.207 | 6.172 | -2.729 |
| 2.6 | 0.06 | 0.956 | -2.783 | 0.913 | 7.743 | -2.659 |
| 2.2 | 0.04 | 0.789 | -3.199 | 0.622 | 10.230 | -2.522 |
| 1.9 | 0.02 | 0.642 | -3.902 | 0.412 | 15.225 | -2.504 |
| sum | | 48.599 | -13.501 | 126.763 | 60.911 | 1.682 |

Using Equation 227 and the data from Table 62 the value of $\beta$ is determined to be 1.623353 and the value of $-\beta \ln\eta$ is determined to be –4.19969 resulting in a $\eta$ or $\bar{x}_i$ value of 13.29 (Equation 80). To assess the fit of this curve, the correlation coefficient may be calculated using Equation 229. This results in a r value of 0.9858 or an $r^2$ value of 0.9718.

$$r = \frac{n\sum_{i=1}^{n} x_i y_i - \sum_{i=1}^{n} x_i \sum_{i=1}^{n} y_i}{\sqrt{\left[n\sum_{i=1}^{n} x_i^2 - \left(\sum_{i=1}^{n} x_i\right)^2\right]\left[n\sum_{i=1}^{n} y_i^2 - \left(\sum_{i=1}^{n} y_i\right)^2\right]}}$$

Equation 229

Since the correlation coefficient, $r^2$ is smaller than the non-linear $\eta^2$ the non-linear approach is probably a more accurate determination of the relationship although both show strong correlation.

The plot of $\mathbf{ln}(-\mathbf{ln}(1-y_i))$ vs $\mathbf{ln}(x_i)$, the result of the linearization, should produce a straight line if true linearization has been performed. This plot is shown in Figure 112.

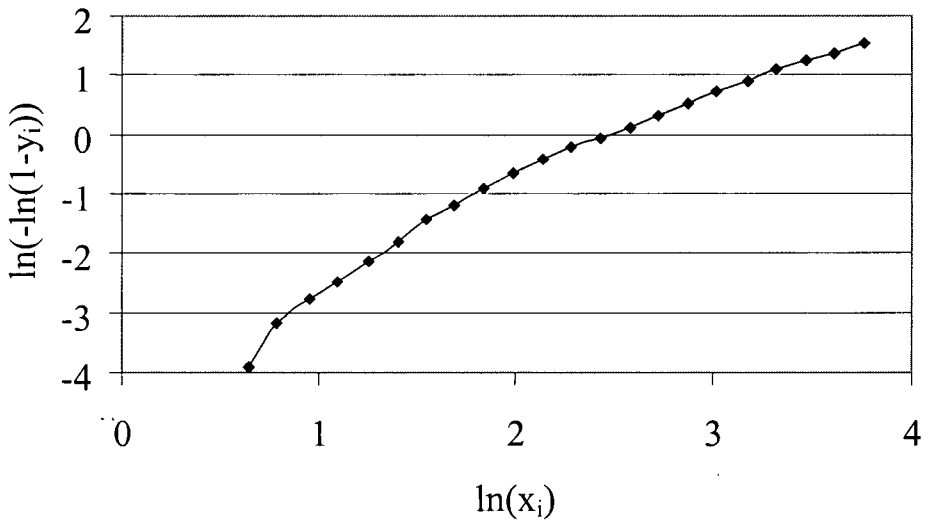


**Figure 112: Linearized plot of Quinto data according to Equation 225.**

Figure 112 is replotted in Figure 113 as a Rosin – Rammler plot of the Quinto overflow material particle size distribution.

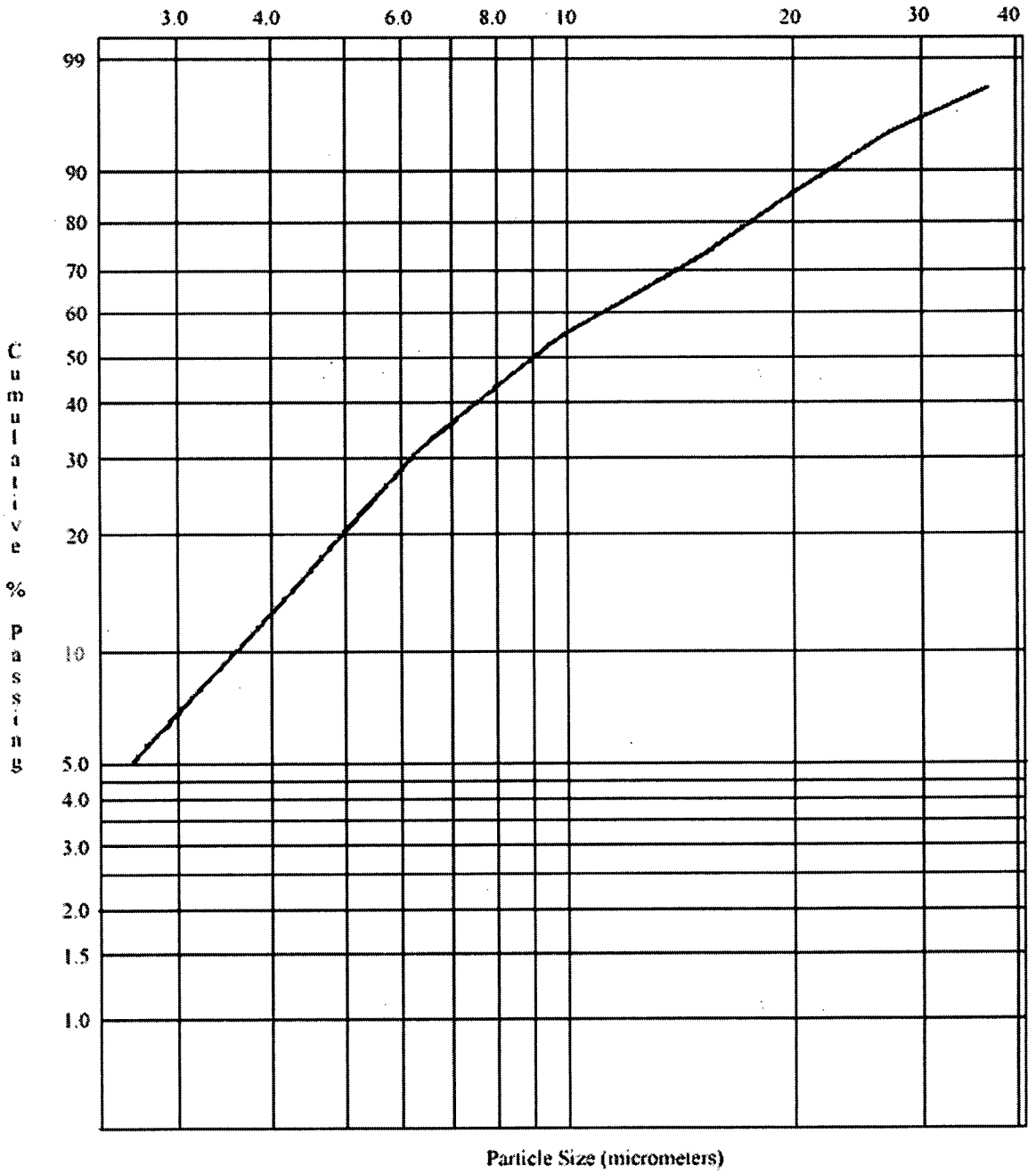


**Figure 113: Rosin-Rammler plot of Quinto overflow particle size distribution**

### 12.1.2.4 Gates-Gaudin-Schuhmann Non-Linear Method

The Gate-Gaudin-Schuhmann model may also be used to characterize the particle size distribution. When a simplex non-linear regression is performed using the Gates-Gaudin-Schuhmann model, "x" and "n" are found to be 48 and 0.469 respectively. Using the eta

squared formula, the non-linear "correlation coefficient" was determined to be 0.977. Since this was less than that of the Rosin-Rammler model and the $r^2$ value is always equal to or smaller and $\eta^2$, the linear method was not followed. The results of the Gate-Gaudin-Schuhmann model are presented in Table 63.

**Table 63 Quinto Overflow Size Class Data and Gates-Gaudin-Schuhmann Values**

| Particle Size | Cumulative Measured | Cumulative Predicted | Unweighted Residuals | Weighted Residuals |
|---|---|---|---|---|
| 49.8 | 1 | 1.017 | -0.017 | -0.018 |
| 42.9 | 0.99 | 0.949 | 0.0413 | 0.039 |
| 37.1 | 0.98 | 0.886 | 0.0938 | 0.083 |
| 32 | 0.97 | 0.827 | 0.1432 | 0.118 |
| 27.6 | 0.95 | 0.771 | 0.1786 | 0.138 |
| 23.9 | 0.91 | 0.721 | 0.189 | 0.136 |
| 20.5 | 0.87 | 0.671 | 0.199 | 0.134 |
| 17.7 | 0.81 | 0.626 | 0.184 | 0.115 |
| 15.3 | 0.74 | 0.585 | 0.155 | 0.091 |
| 13.2 | 0.67 | 0.546 | 0.124 | 0.068 |
| 11.4 | 0.61 | 0.510 | 0.100 | 0.051 |
| 9.8 | 0.55 | 0.475 | 0.075 | 0.036 |
| 8.5 | 0.48 | 0.444 | 0.036 | 0.016 |
| 7.3 | 0.41 | 0.413 | -0.003 | -0.001 |
| 6.3 | 0.33 | 0.386 | -0.056 | -0.022 |
| 5.4 | 0.26 | 0.359 | -0.099 | -0.035 |
| 4.7 | 0.21 | 0.336 | -0.126 | -0.042 |
| 4.1 | 0.15 | 0.315 | -0.165 | -0.052 |
| 3.5 | 0.11 | 0.293 | -0.183 | -0.054 |
| 3 | 0.08 | 0.272 | -0.192 | -0.052 |
| 2.6 | 0.06 | 0.255 | -0.195 | -0.050 |
| 2.2 | 0.04 | 0.236 | -0.196 | -0.046 |
| 1.9 | 0.02 | 0.220 | -0.200 | -0.044 |
| pan | | | | |

The cumulative fraction passing the size "$x_i$", as measured, is "$y_i$". These values of "$x_i$" and "$y_i$" where fit using the simplex method of non-linear regression to the Gates-Gaudin-Schuhmann function. The response of this function is the predicted fraction passing; "$\hat{y}_i$", at size "i".

The difference between the measured values and those predicted by the Gate-Gaudin-Schuhmann model; $(y_i - \hat{y}_i)$, are the un-weighted residuals. The sum of these un-weighted residuals is minimized by the simplex method. These values, for the Quinto overflow size class data, along with weighted residuals are found in Table 63. Both the measured and predicted fraction finer are plotted against particle size in Figure 114.

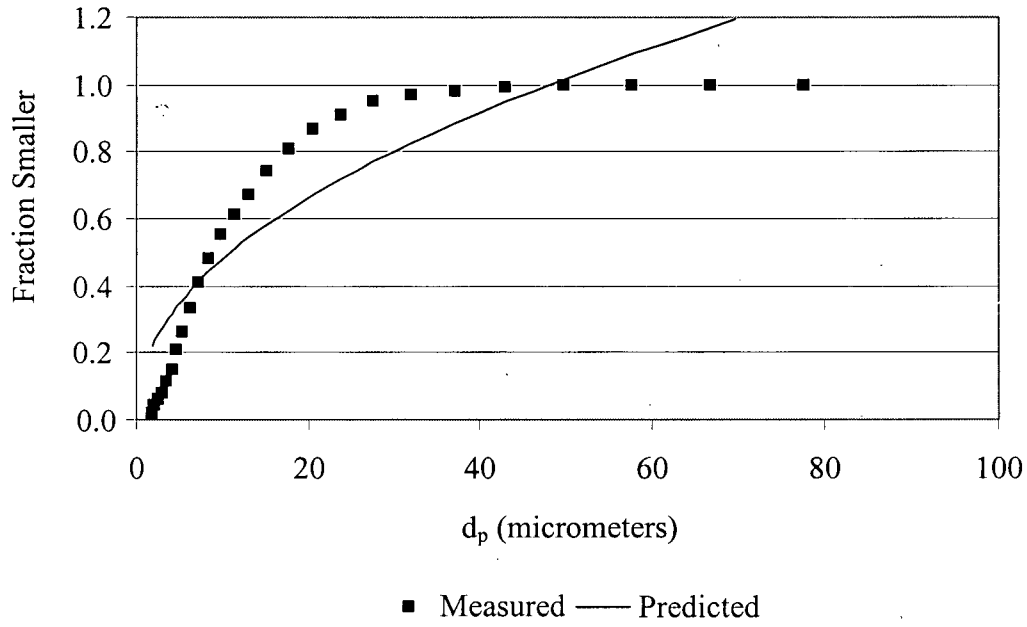


**Figure 114: Quinto overflow size class data and Gate-Gaudin-Schuhmann predicted size distribution**

The residuals produced by the difference between measured and predicted fraction finer are shown in Figure 115. This figure shows that the residuals are not randomly distributed.

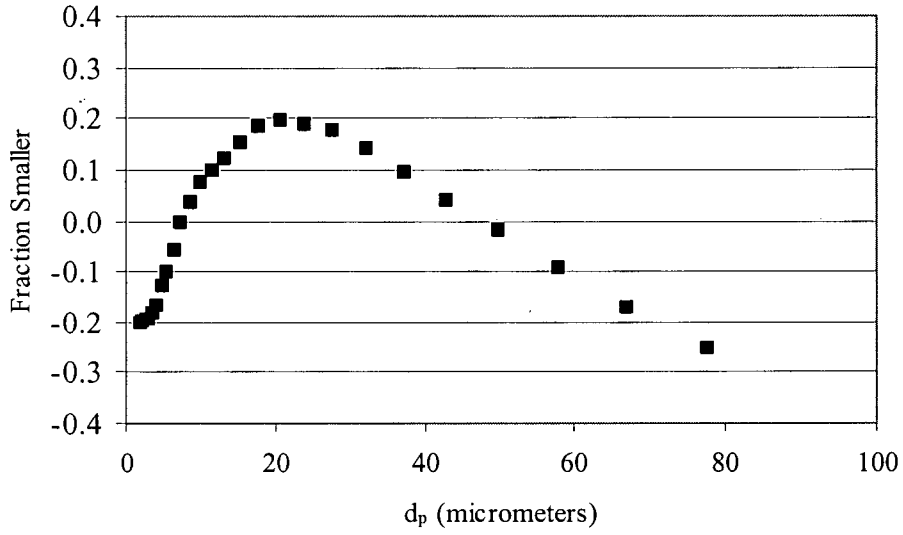


**Figure 115: Quinto overflow size class data Gates-Gaudin-Schuhmann un-weighted residuals**

### 12.1.3 INCO Feed Stream

The INCO feed size distribution was tested using sieves. This information is presented (Table 64) as a particles size; "$x_i$" [micrometers] and the volume of solids, as a fraction, that lie within the band bounded by that size and the size smaller.

**Table 64: INCO feed stream particle size distribution**

| Particle Size $x_i$ | Volume Within Band | Cumulative Measured $y_i$ | Cumulative Predicted $\hat{y}_i$ | Unweighted Residuals $y_i - \hat{y}_i$ | Weighted Residuals $\hat{y}_i(y_i - \hat{y}_i)$ |
|---|---|---|---|---|---|
| 44 | 0.624 | 0.624 | 0.624 | 0.000 | 0.000 |
| 74 | 0.282 | 0.906 | 0.909 | -0.003 | -0.003 |
| 105 | 0.088 | 0.994 | 0.987 | 0.007 | 0.006 |
| 148 | 0.006 | 1.000 | 0.999 | 0.001 | 0.001 |

In Table 64 the cumulative fraction passing the size "$x_i$", as measured, is "$y_i$". These values of "$x_i$" and "$y_i$" where fit using the simplex method of non-linear regression to Equation 80 – the Weibull or Rosin – Rammler function. The response of this function is the predicted fraction

passing; "$\hat{y}_i$", at size "i". The Gates-Gaudin-Schuhmann method was not used since the Rosin-Rammler function resulted in better prediction when using the Quinto data.

Using the non-linear Rosin-Rammler method, the sum of the un-weighted residuals is minimized by the simplex method. These values, for the INCO feed stream size class data, along with weighted residuals are found in Table 64. Both the measured and predicted fraction finer are plotted against particle size in Figure 116. In this non-linear regression, "$\bar{x}_i$" = 44.58 and $\beta$ = 1.312.

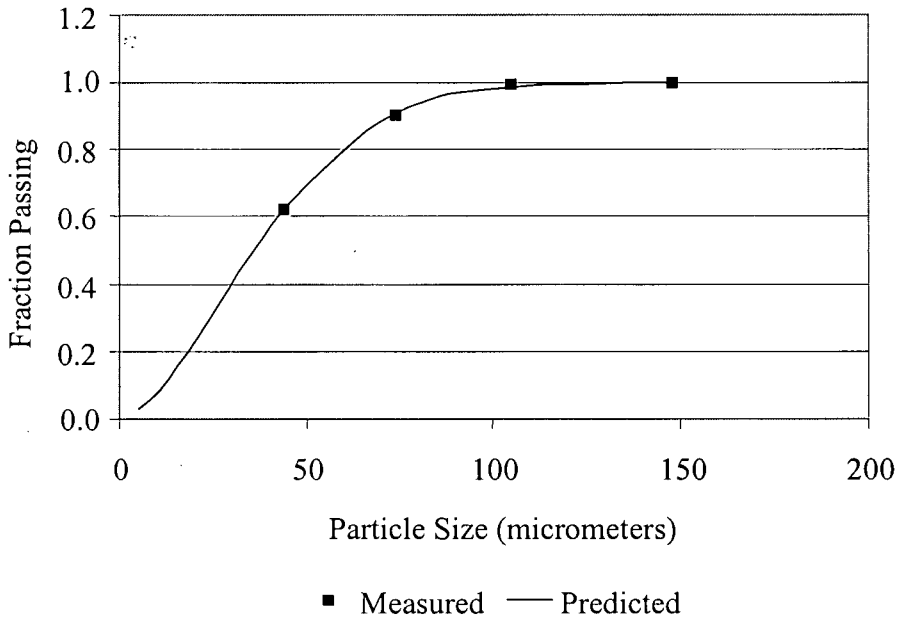


**Figure 116: INCO feed stream size class data and Weibull distribution predicted size distribution**

The un-weighed residuals of this fit are shown in Figure 117. These residuals appear to be randomly distributed.

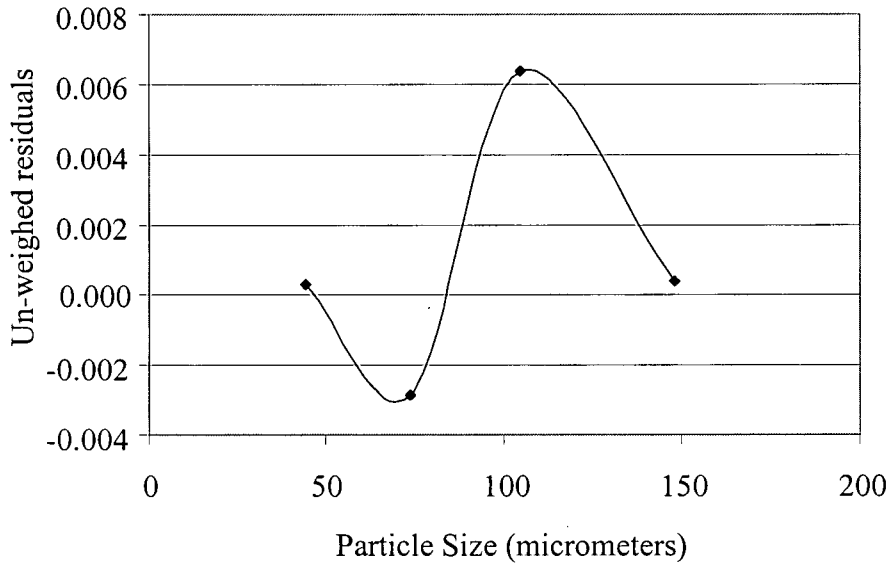


**Figure 117: INCO feed stream size class data Wiebull distribution un-weighted residuals**

The equivalent Rosin-Rammler plot of the INCO feed stream particle size distribution is found in Figure 118.

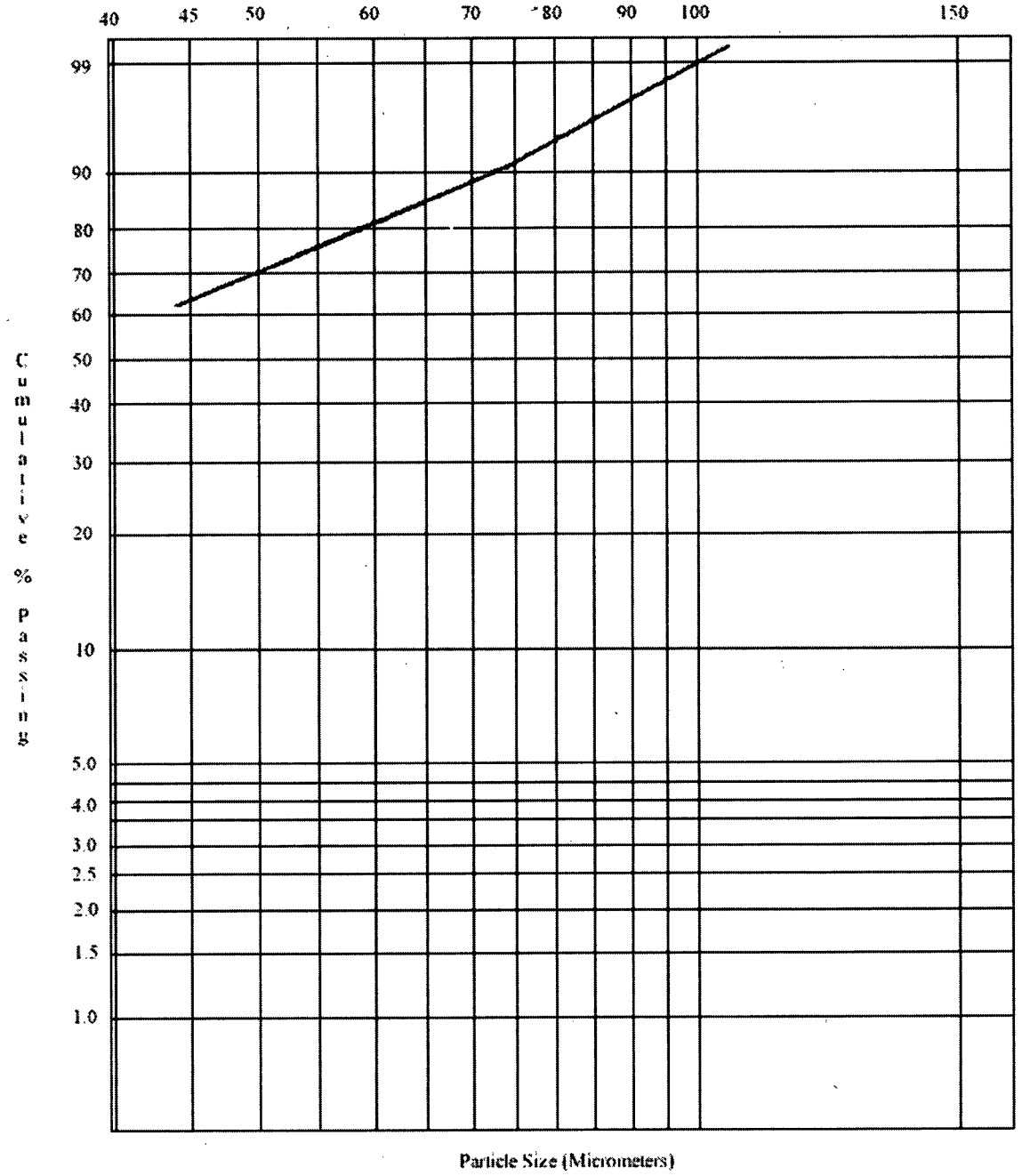


**Figure 118: Rosin-Rammler plot of INCO feed particle size distribution**

## 12.1.4 INCO Overflow Stream

The INCO overflow size distribution was tested using sieves. This information is presented (Table 65) as a particles size; "$x_i$" [micrometers] and the volume of solids, as a fraction, that lie within the band bounded by that size and the size smaller.

**Table 65: INCO overflow stream particle size distribution**

| Particle Size $x_i$ | Volume Within Band | Cumulative Measured $y_i$ | Cumulative Predicted $\hat{y}_i$ | Unweighted Residuals $y_i - \hat{y}_i$ | Weighted Residuals $\hat{y}_i(y_i - \hat{y}_i)$ |
|---|---|---|---|---|---|
| 44 | 0.731 | 0.731 | 0.730 | 0.001 | 0.001 |
| 74 | 0.232 | 0.963 | 0.964 | -0.001 | -0.001 |
| 105 | 0.037 | 1.000 | 0.998 | 0.002 | 0.001 |
| 148 | 0.000 | 1.000 | 1.000 | 0.000 | 0.000 |

The cumulative fraction passing the size "$x_i$", as measured, is "$y_i$". These values of "$x_i$" and "$y_i$" where fit using the simplex method of non-linear regression to Equation 80 – the Weibull or Rosin – Rammler function. The response of this function is the predicted fraction passing; "$\hat{y}_i$", at size "i".

The sum of these un-weighted residuals is minimized by the simplex, non-linear regression, method. These values, for the INCO feed stream size class data, along with weighted residuals are found in Table 65. Both the measured and predicted fraction finer are plotted against particle size in Figure 119. In this non-linear regression, "$\bar{x}_i$" = 37.9 and $\beta = 1.34$.

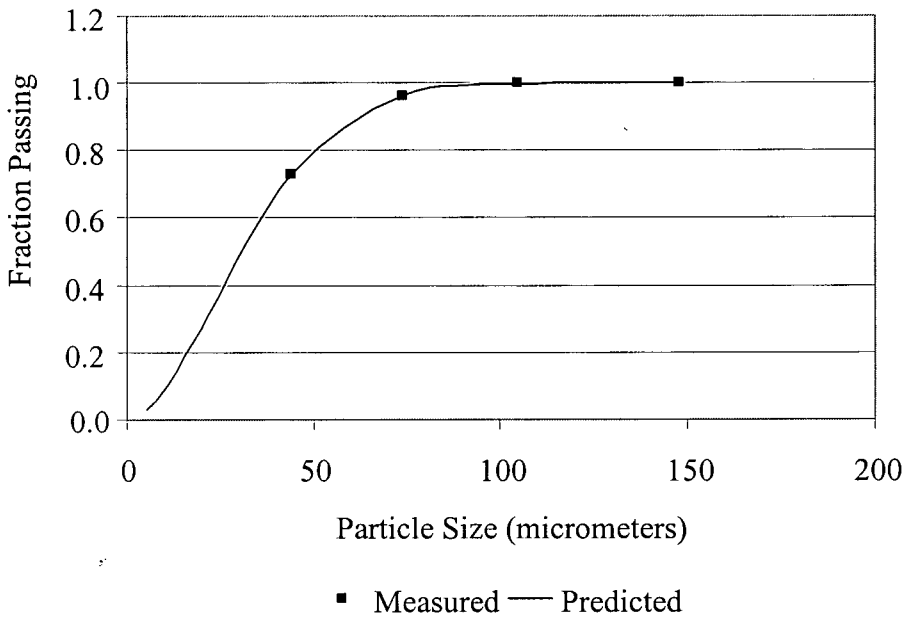


**Figure 119: INCO overflow stream size class data and Weibull distrubition predicted size distribution**

The un-weighed residuals of this fit are shown in Figure 120. These residuals appear to be randomly distributed.

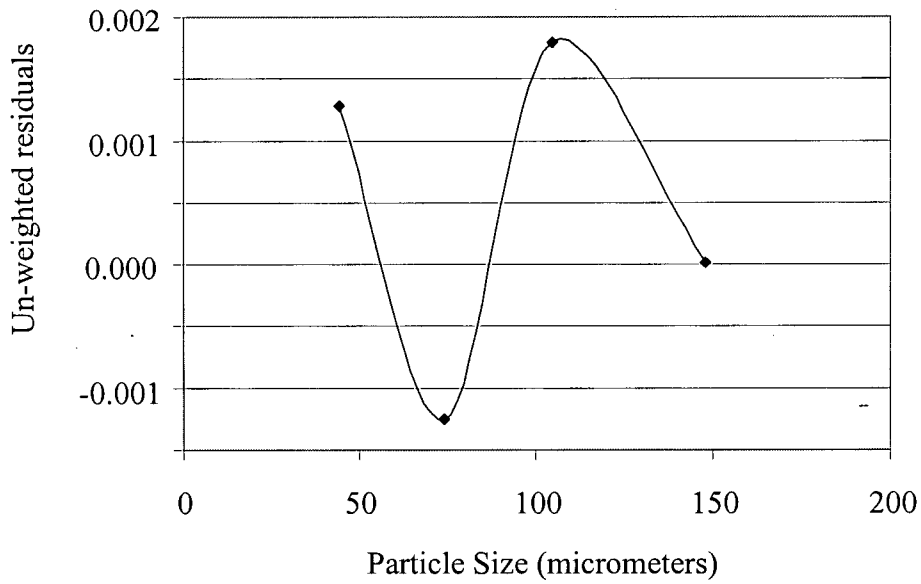


**Figure 120: INCO feed stream size class data Wiebull distribution un-weighted residuals**

The equivalent Rosin-Rammler plot of the INCO feed stream particle size distribution is found in Figure 121.

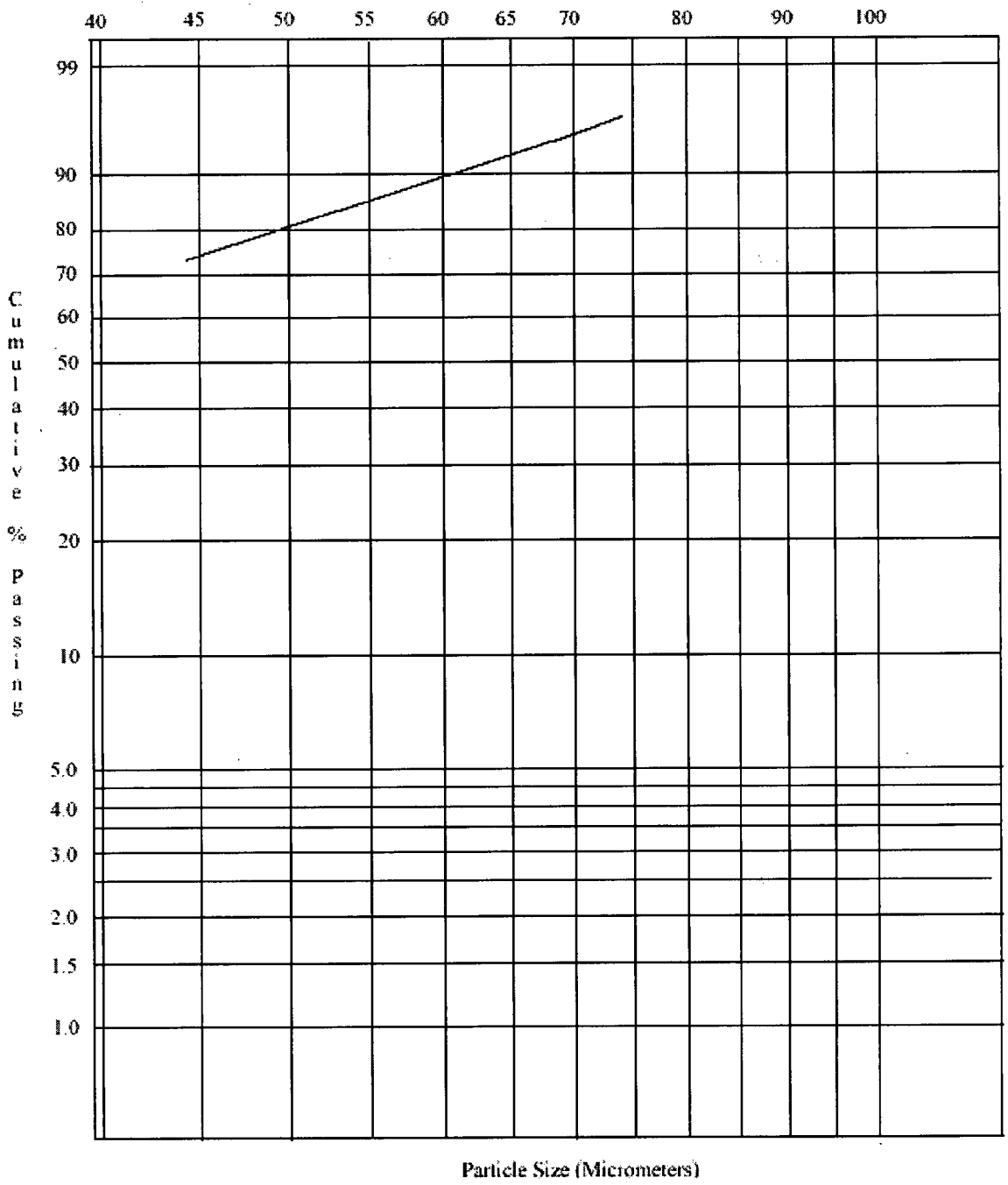


**Figure 121: Rosin-Rammler plot of INCO overflow particle size distribution**

## 12.2 Average Particle Size

### 12.2.1 Introduction

There are a number of methods that are used to characterize average particle size that are not spherical. This work uses the geometric mean, which is the square root of the product of the upper and lower size that bounds a size class as shown in Equation 230. In Equation 230 "$\hat{x}_{gi}$" [cm] is the geometric average of the size class bounded by "$x_i$" [cm] and "$x_{i-1}$" [cm].

$$\hat{x}_{gi} = \sqrt{(x_i x_{i-1})} \qquad \text{Equation 230}$$

An alternative is the Sauter diameter or the specific surface diameter. This diameter is the diameter of a sphere having the same ratio of surface area to volume as the particle. When the particles are spherical this diameter is calculated using Equation 231.

$$\hat{x}_{SMDi} = \frac{\sum_{j=1}^{J} n_j d_j^3}{\sum_{j=1}^{J} n_j d_j^2} \qquad \text{Equation 231}$$

In Equation 231 "$\hat{x}_{SMDi}$" is the Sauter mean diameter of size class "i", "j" is the total number of sizes within the size class, "$n_j$ is the number of particles of each size, and "$d_j$" s the diameter of thoses sizes. This equation can be used if the particle shape is cubic.

When the particles are not spherical, but rather are tabular, volume and surface areas must be used, thus, Equation 231 becomes Equation 232. In Equation 232 "x", "y" and "z" are the axis dimensions of the particles and "d" is the Sauter diameter. In order to calculate the average Sauter diameter the results of Equation 232 must be used in Equation 231.

$$d = \frac{3\sum_{j=1}^{J} n_j x_j y_j z_j}{\sum_{j=1}^{J} x_j y_j + x_j z_j + y_j z_j}$$

Equation 232

Equation 232 is derived from the definition of the Sauter mean diameter as shown in Equation 233. Using the definitions of spherical volume and area, and tabular volume and area, Equation 234 results. Equation 232 is the simplified form of Equation 234

$$\frac{V_{sphere}}{A_{sphere}} = \frac{\sum nV_{particle}}{\sum nA_{particle}}$$

Equation 233

$$\frac{\pi d^3}{6\pi d^2} = \frac{\sum_{j=1}^{J} n_j x_j y_j z_j}{2\sum_{j=1}^{J} x_j y_j + x_j z_j + y_j z_j}$$

Equation 234

Use of the Sauter mean requires information concerning "n" the number of particles at each size. This information may not be known. When narrow size classes are used it may be assumed that each size within the size class has an equal number of particles. However, this can only be used to approximate a Rosin-Rammler or Gates-Gaudin-Schuhmann function when the increments are very small. The continuous nature of the size distribution can be approximated for calculation purposes by assuming a large number of increments within the size class.

The cubic or spherical form of the Sauter mean diameter is often is often used without regard to the shape of the particle. This diameter is termed "$\bar{x}_{(3,2)i}$". This number is not a volume to surface area ratio since the tabular nature, or the short "z" axis is not taken into consideration.

## 12.2.2 Quinto Overflow Stream

Quinto company research indicates that the "z" axis of the mica crystals are between 1 and 4 micrometers in length. The Sauter mean diameters for each size class was calculated assuming that: (1) "$x_i$" = "$y_i$" and "z" = 2 micrometers. Table 66 shows the calculated geometric mean; "$\bar{x}_{Gi}$", Sauter mean; "$\bar{x}_{SMDi}$", and the "$\bar{x}_{(3,2)i}$" diameters for the Quinto overflow particle size distribution.

**Table 66: Comparison of average particle size calculation methods using Quinto data. Both $\bar{x}_{SMDi}$ and $\bar{x}_{(3,2)i}$ where calculated using "J" = 100 and assuming that "$n_j$" is evenly distributed across all particle sizes within the size class.**

| Particle Size $x_i$ | Geometric Mean $\bar{x}_{Gi}$ | Sauter Mean (tabular) $\bar{x}_{SMDi}$ | $d^3/d^2$ Mean $\bar{x}_{(3,2)i}$ |
|---|---|---|---|
| 77.5 | | | |
| 66.9 | 72.01 | 3.79 | 72.46 |
| 57.7 | 62.13 | 3.76 | 62.53 |
| 49.8 | 53.60 | 3.72 | 53.95 |
| 42.9 | 46.22 | 3.68 | 46.52 |
| 37.1 | 39.89 | 3.64 | 40.14 |
| 32.0 | 34.46 | 3.59 | 34.68 |
| 27.6 | 29.72 | 3.53 | 29.91 |
| 23.9 | 25.68 | 3.46 | 25.84 |
| 20.5 | 22.13 | 3.39 | 22.29 |
| 17.7 | 19.05 | 3.31 | 19.17 |
| 15.3 | 16.46 | 3.22 | 16.56 |
| 13.2 | 14.21 | 3.12 | 14.30 |
| 11.4 | 12.27 | 3.02 | 12.34 |
| 9.8 | 10.57 | 2.91 | 10.64 |
| 8.5 | 9.13 | 2.78 | 9.18 |
| 7.3 | 7.88 | 2.66 | 7.93 |
| 6.3 | 6.78 | 2.52 | 6.82 |
| 5.4 | 5.83 | 2.38 | 5.87 |
| 4.7 | 5.04 | 2.23 | 5.07 |
| 4.1 | 4.39 | 2.10 | 4.41 |
| 3.5 | 3.79 | 1.95 | 3.82 |
| 3.0 | 3.24 | 1.80 | 3.26 |
| 2.6 | 2.79 | 1.65 | 2.81 |
| 2.2 | 2.39 | 1.50 | 2.41 |
| 1.9 | 2.04 | 1.36 | 2.06 |

These results indicate that the non-spherical nature of mica makes the Sauter mean a poor choice for characterization of the Quinto average particle size and that there is little difference between the geometric and "$\bar{x}_{(3,2)i}$" diameters.

### 12.2.3 INCO Average Particle Size

The screen sizes; "$x_i$" used to characterize the INCO feed and overflow streams, are shown in Table 67 along with the geometric mean; "$\bar{x}_{Gi}$". Chalcocite, the floating mineral within the INCO feed stream is pseudohexagonal in shape, but at small crystal sizes may be approximated by a cubic representation. Assuming a cubic crystal, the Sauter mean diameter; "$\bar{x}_{SMDi}$" can be calculated with knowledge of the distribution of particles within the size class. Since the INCO size classes are quite wide, the assumption of even distribution to each size of particle may not hold, however, this mean is also shown in Table 67. Since the overall stream particle size distribution is close to the Rosin-Rammler distribution the Sauter mean calculated assuming the same particle distribution within the size class may be more accurate.

**Table 67: Comparison of average particle size calculation methods using INCO feed stream data. The $\bar{x}_{SMDi}$ diameter was calculated using "J" = 100 and assuming that "$n_j$" is evenly distributed across all particle sizes within the size class ($n_j$=$n_{j+1}$) and assuming a Rosin-Rammler distribution.**

| Particle Size $x_i$ | Geometric Mean $\bar{x}_{Gi}$ | Sauter Mean $\bar{x}_{SMDi}$, $n_j = n_{j+1}$ | Sauter Mean (feed) $\bar{x}_{SMDi}$ Rosin-Rammler $n_j$ | Sauter Mean (over) $\bar{x}_{SMDi}$ Rosin-Rammler $n_j$ |
|---|---|---|---|---|
| 148 | | | | |
| 105 | 124.66 | 129.39 | 112.84 | 111.15 |
| 74 | 88.15 | 91.62 | 81.21 | 80.41 |
| 44 | 57.06 | 61.97 | 52.43 | 51.82 |
| 20 | 29.66 | 35.41 | 28.52 | 28.27 |